Local structure/property relationships in functional materials

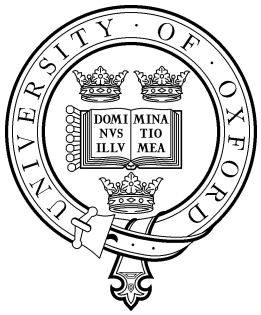

Callum A. Young
The Queen's College
University of Oxford

A thesis submitted for the degree of
Doctor of Philosophy

Trinity 2014

Declaration of Authorship

This dissertation is the result of my own original work, and where it draws on the work of others, this is acknowledged at the appropriate points in the text. This dissertation has not been submitted in whole or in part for a degree at this or any other institution.

Callum Young

Local structure/property relationships in functional materials

Callum A. Young, The Queen's College, University of Oxford

A thesis submitted for the degree of Doctor of Philosophy, Trinity 2014

Abstract

It is increasingly being realised that localised deviations from the average structure can play an important role in a material's properties, and hence an understanding of these deviations is essential when constructing a coherent picture of a system. In this thesis, both neutron and X-ray total scattering data have been collected and used to reveal information on three canonical systems: the high-temperature superconductor $YBa_2Cu_3O_{7-x}$; the parent compound of the colossal magnetoresistive manganites, $LaMnO_3$; and the oldest known magnetic material, Fe_3O_4. Reverse Monte Carlo refinements—using the RMCProfile implementation of the algorithm—have been used as the principal analysis technique, and the functionality of the RMCProfile program has been extended to allow the refinement of magnetic systems involving substitutional disorder. For $YBa_2Cu_3O_{7-x}$, the focus of this thesis is on the apical Cu–O bond length. This is shown to have a bimodal distribution, but correlations in the displacements of both atoms disguise this fact in the average structure, thus resolving the apparent controversy that had existed between local- and average-structure probes. $LaMnO_3$ displays (what was thought to be) a simple order–disorder transition that results in the Jahn-Teller distortion becoming invisible in the average structure above $\sim 750\,\mathrm{K}$. Here it is shown that in fact the transition is more complicated, and involves a change in the symmetry of the Jahn-Teller distortion, whereby the long Mn–O bonds move from being opposite one another in the octahedra to being adjacent to one another. This new distortion still breaks the degeneracy of the system, and is consistent with a wide range of existing observations. Finally the low temperature structure of Fe_3O_4 is examined using the updated RMCProfile code. The refinements show sensitivity to local structure variations, producing a bimodal Fe atom bond valence distribution. In addition, the refined magnetic spin configuration is presented, providing the first detailed description of the low-temperature magnetic structure. It is found to be a canted ferrimagnet, and appears to be consistent with Cc symmetry.

Acknowledgements

I am exceedingly grateful to the numerous people that I have worked with and known during the course of my thesis. First and foremost I would like to thank my supervisor, Prof. Andrew Goodwin. Aside from offering me my place in the department and securing funding for me, he has been an enormous source of knowledge and support throughout my degree, and I have learned a lot from him. This project could not have taken place without him.

Next I would like to thank all those people I have collaborated with during my time here. Prof. David Keen and Dr Matthew Tucker assisted with data collections and processing throughout my thesis, as well as providing their expertise on reverse Monte Carlo refinements as required. My own shortcomings in synthetic ability were more than compensated for by the guidance and support of Dr Michael Hayward, Edward Dixon, and Fabio Denis Romero.

For work relating to $LaMnO_3$, thanks are also due to Edward Beake and Anthony Phillips, for help with analysis; Leigh Connor, for help with X-ray data collection; and Thomas Proffen, for providing his neutron data for comparison. J. Paul Attfield provided his high-quality magnetite sample for the work in Chapter 5, and Martin Dove and Paul Saines assisted with data collection and analysis respectively. Thank you all, I'm very grateful for your efforts.

My time with the Goodwin Group has been made very enjoyable by the company I found there, and my work has undoubtably benefitted by my interactions with its members. The trouble-shooting and proof-reading services provided are too numerous to list, but have not been forgotten, and nor has the encouragement you gave. In particular I would like to

mention Nick, Paul, Ines, Jasper, Andrew C, Matt, Joe, Josh and Peter. Thanks too go to the Quiztallographers, and especially the Quiztallography Secretary, Karim, for ensuring my education was not restricted to the field of Chemistry.

On a more personal note, I would like to acknowledge the support of others I've known during my time in Oxford. I would like to thank my friends at The Queen's College, for the lively lunchtime discussions, and the opportunities provided to test my driving skills. I have also made a great many friends in the OURC, CURA and the NRCofS. With any luck our paths will cross on a regular basis.

Contents

List of Figures

List of Tables

List of Abbreviations and Symbols

ACC	amorphous calcium carbonate
CMR	colossal magnetoresistance
DFT	density functional theory
EPSR	empirical potential structure refinement
EXAFS	extended X-ray absorption fine structure
HTSC	high-temperature superconductivity
JT	Jahn-Teller
NMR	nuclear magnetic resonance
NTE	negative thermal expansion
PDF	pair distribution function
PIA	pressure induced amorphisation
PNR	polar nanoregion
PTE	positive thermal expansion
RMC	reverse Monte Carlo
SQUID	superconducting quantum interference device
T_{c}	critical temperature (superconductors)
T_{JT}	JT transition temperature
T_{V}	Verwey transition temperature
XANES	X-ray absorption near-edge structure
XRPD	X-ray powder diffraction
YBCO	$YBa_2Cu_3O_{7-x}$

Chapter 1

Introduction

As science has rapidly progressed throughout the last century, the scientific community has begun to take for granted the ability to determine the structure of the materials with which we work. This is largely due to the progress made in crystallographic techniques, with the development of direct methods, the huge advances in computing power, and the abundance of advanced laboratory diffractometers meaning that structures (by and large) can now be solved quickly and easily. The structure of a material is key to determining its properties, and we rely on having accurate descriptions of materials on the atomic scale, so that procedures used in the synthesis of materials can be related to patterns in their behaviour: this then informs the iterative improvement process, allowing us to develop substances more suited to our needs.

But some materials defy our standard crystallographic techniques. Where materials contain some degree of disorder the average structure may no longer provide an adequate representation of their key features, and we will struggle to understand their behaviour without greater insight into what is happening on the local scale. Many important classes of functional materials fall into this category; examples include relaxor ferroelectrics [1], high temperature superconductors [2], frustrated magnets [3], colossal magnetoresistance materials [2], and electrode materials [4]. There is therefore a need to employ a wider range of structural characterisation techniques that can identify localised deviations away from the average structure, and then resolve the information gained on both length scales.

This thesis aims to use (and, in part, to develop further) the state-of-the-art experimental and analysis techniques of total scattering and reverse Monte Carlo refinement to examine the structure of three canonical functional materials from both

a local and an average perspective, and then to resolve these two viewpoints in order to gain new insights into these materials. We begin this chapter with an introduction to total scattering, and then follow with a review of some of the main areas of materials chemistry where it has been of use, before finishing by discussing in more detail the structure of this thesis.

1.1 Total Scattering

Broadly speaking, diffraction patterns can be split up into two components: the sharp Bragg peaks that describe any periodic order in the structure of interest; and the diffuse scattering that is caused by any disorder in the sample. It is usual in diffraction experiments to ignore the diffuse scattering contribution, and with good reason: diffuse scattering is tricky to measure accurately,* and most materials are well ordered, or the disorder is of little interest. Total scattering, as the name might suggest, *does* include the diffuse scattering component.

For some materials—*e.g.* liquids and glasses—standard diffraction techniques are simply not an option due to the absence of discrete Bragg peaks. For these materials total scattering is essential. Indeed, the technique was largely developed as a way to study these sorts of materials [6, 7]. But why might one use this technique on other, more ordered materials? Well, at the expense of a more involved data collection and analysis process (which we will discuss further below), it allows us to examine a system in terms of a real-space correlation function. This is the *pair distribution function*, or PDF, a real-space histogram of interatomic distances.

The PDF is arguably the principal route to analysing total scattering data, and the terms "PDF technique" and "total scattering technique" are often used interchangeably. The main feature of the PDF is that it shifts the focus away from long range periodicity, towards local structure and short-range interactions. Effectively the problem is approached from a different direction, which can be of great use.

*Diffuse scattering is generally of low intensity, and often hidden underneath the Bragg peaks. Much diffuse scattering also exists at high scattering angles, often inaccessible to lab-based diffractometers. The analysis of single crystal diffuse scattering, usually using electron diffraction, is however a field in its own right—please see for example Ref. 5 for a further discussion on the subject.

Here we will discuss some of the salient aspects of total scattering experiments, with the focus mainly on neutron scattering due to its predominant use in this thesis.

1.1.1 Theory of Total Scattering

There are many different formalisms used to describe total scattering. Here we will follow those summarised by Keen in Ref. 8. Starting from the central expression of neutron scattering by a material, the definition of the double differential neutron cross section per unit of solid angle, Ω, and energy interval, $\hbar\omega$:

$$\frac{1}{N}\frac{\mathrm{d}^2\sigma}{\mathrm{d}\Omega\mathrm{d}\omega} = \frac{k'}{k}\sum_{i=1}^{n}\overline{b_i^2}S_i^{\mathrm{s}}(\mathbf{Q},\omega) + \frac{k'}{k}\sum_{i,j=1,i\neq j}^{n}\bar{b_i}\bar{b_j}S_{ij}^{\mathrm{d}}(\mathbf{Q},\omega). \tag{1.1}$$

This describes a sample of N atoms of n different types. k and k' refer to the initial and final scattering wavevectors respectively, and the scattering vector, $\mathbf{Q} = \mathbf{k} - \mathbf{k}'$, has length $4\pi\sin\theta/\lambda$ for a neutron with wavelength λ scattered at an angle 2θ. $\bar{b_i}$ is the bound coherent neutron scattering length for atom type i, averaged over its different spin states and isotopes. $S_i^{\mathrm{s}}(\mathbf{Q},\omega)$ and $S_{ij}^{\mathrm{d}}(\mathbf{Q},\omega)$ refer to the self and distinct parts of the structure factor respectively.

As the total scattering cross section is described by $\sigma_i = 4\pi\overline{b_i^2}$, and the coherent scattering cross section is described by $\sigma_i^{\mathrm{coh}} = 4\pi\bar{b_i}^2$, the incoherent scattering cross section is given by $\sigma_i^{\mathrm{inc}} = \sigma_i - \sigma_i^{\mathrm{coh}}$. It is possible to separate Eq. 1.1 into coherent and incoherent scattering terms in the same way:

$$\frac{1}{N}\frac{\mathrm{d}^2\sigma}{\mathrm{d}\Omega\mathrm{d}\omega} = \frac{k'}{k}\sum_{i=1}^{n}(\overline{b_i^2} - \bar{b_i}^2)S_i^{\mathrm{s}}(\mathbf{Q},\omega) + \frac{k'}{k}\sum_{i,j=1}^{n}\bar{b_i}\bar{b_j}S_{ij}(\mathbf{Q},\omega), \tag{1.2}$$

where $S_i^{\mathrm{s}}(\mathbf{Q},\omega)$ denotes the incoherent scattering term, and $S_{ij}(\mathbf{Q},\omega)$ denotes the coherent scattering term. Making use of the static approximation, and considering only systems whose scattering depends purely on the magnitude, and not the direction, of the scattering vector (*e.g.* liquids, glasses, or crystalline powders), then we may integrate over energy and orientation to obtain:

$$\frac{1}{N}\frac{\mathrm{d}\sigma}{\mathrm{d}\Omega} = \sum_{i=1}^{n}(\overline{b_i^2} - \bar{b_i}^2)S_i^{\mathrm{s}}(Q) + \sum_{i,j=1}^{n}\bar{b_i}\bar{b_j}S_{ij}(Q). \tag{1.3}$$

The term $S_i^{\mathrm{s}}(Q)$ is now equal to c_i, the fraction of element i in the material, while

$$S_{ij}(Q) = c_i c_j[A_{ij}(Q) - 1] + c_i\delta_{ij}, \tag{1.4}$$

where δ_{ij} is the Dirac delta function, and $A_{ij}(Q)$ are the Faber-Ziman partial structure factors [9]. Substituting these terms results in the more commonly-seen form of the scattering cross section:

$$\frac{1}{N}\frac{\mathrm{d}\sigma}{\mathrm{d}\Omega} = \sum_{i,j=1}^{n} c_i c_j \bar{b_i}\bar{b_j}[A_{ij}(Q) - 1] + \sum_{i=1}^{n} c_i \overline{b_i^2}. \tag{1.5}$$

This is essentially the main total scattering structure factor equation. Other, equivalent, definitions are in use; for example

$$F(Q) = \sum_{i,j=1}^{n} c_i c_j \bar{b_i}\bar{b_j}[A_{ij}(Q) - 1]. \tag{1.6}$$

As can be easily seen, the only difference between Eq. 1.5 and Eq. 1.6 is the addition of the final summation in Eq. 1.5, which is a constant for a given system.

The data are converted from reciprocal space to real space by Fourier transform. The $A_{ij}(Q)$ are related by Fourier transform to the partial radial distribution functions, $g_{ij}(r)$:[†]

$$A_{ij}(Q) - 1 = \rho_0 \int_0^\infty 4\pi r^2 [g_{ij}(r) - 1] \frac{\sin Qr}{Qr}\,\mathrm{d}r \tag{1.7}$$

and

$$g_{ij}(r) - 1 = \frac{1}{(2\pi)^3 \rho_0} \int_0^\infty 4\pi Q^2 [A_{ij}(Q) - 1] \frac{\sin Qr}{Qr}\,\mathrm{d}Q. \tag{1.8}$$

Here ρ_0 is the average number density of the material and $g_{ij}(r)$ describes the density probability for an atom of species i having a neighbour of species j at a distance r. Likewise, $F(Q)$ can be related to $G(r)$, the total radial distribution function (the function commonly referred to as the PDF):

$$F(Q) = \rho_0 \int_0^\infty 4\pi r^2 G(r) \frac{\sin Qr}{Qr}\,\mathrm{d}r \tag{1.9}$$

and

$$G(r) = \frac{1}{(2\pi)^3 \rho_0} \int_0^\infty 4\pi Q^2 F(Q) \frac{\sin Qr}{Qr}\,\mathrm{d}Q, \tag{1.10}$$

giving

$$G(r) = \sum_{i,j=1}^{n} c_i c_j \bar{b_i}\bar{b_j}[g_{ij}(r) - 1]. \tag{1.11}$$

[†]*N.B.* $g_{ij}(r)$ are explicitly defined as $g_{ij}(r) = \frac{n_{ij}(r)}{4\pi r^2\,\mathrm{d}r\,\rho_j}$, where $\rho_j = c_j\rho_0$, and $n_{ij}(r)$ are the number of atoms of type j at a distance between r and $r + \mathrm{d}r$ from an atom of type i.

Alternative formulations include a differently normalised structure factor, $S(Q)$:

$$S(Q) - 1 = F(Q) \Big/ \left(\sum_{i=1}^{n} c_i \bar{b_i} \right)^2 , \tag{1.12}$$

which gives

$$S(Q) = \left(\sum_{i=1}^{n} c_i \bar{b_i} \right)^{-2} \sum_{i,j=1}^{n} c_i c_j \bar{b_i} \bar{b_j} A_{ij}(Q) \tag{1.13}$$

when rearranged. Likewise other commonly-used variations of the real space correlation function exist, notably

$$D(r) = 4\pi r \rho_0 G(r) \tag{1.14}$$

and

$$T(r) = 4\pi r \rho_0 \left[G(r) + \left(\sum_{i=1}^{n} c_i \bar{b_i} \right)^2 \right] . \tag{1.15}$$

These alternate forms of the PDF differ primarily from $G(r)$ in their behaviour as $r \to \infty$: $G(r \to \infty) = 0$; $D(r)$ scales as $r \times G(r)$, accentuating the peaks at high r values, but still tends to zero at infinity; $T(r)$ scales as $r \times G(r) + r$, again accentuating high r peaks, but tending to $4\pi r \rho_0 \left(\sum_{i=1}^{n} c_i \bar{b_i} \right)^2$ as $r \to \infty$. The practical implications are that different formulations of the real space data are used depending on which region of the data is considered most relevant to the science question being addressed. In practice the functions $G(r)$ and $D(r)$ are the most frequently used.[‡]

We conclude this section by noting that for many years neutron PDF analysis has in some respects been superior to the equivalent X-ray PDF analysis due to the greater ease with which an exact expression for it can be calculated: the neutron PDF is simply a weighted linear combination of the partial PDFs [Eq. 1.11], while the situation for X-rays is complicated by the variations in Q dependence of the scattering factors of different elements. While this poses no problems for single-element systems, approximations have been used to deal with multi-element materials. Recently, work has been carried out to address this deficiency, and an exact and computationally efficient expression for X-ray PDFs has now been published [10]. This should hopefully assist with the growing number of X-ray PDF experiments that are being performed.

[‡] $G(r)$ is somewhat confusingly used as a catch-all term by some groups, and can sometimes refer to the functions denominated here as $D(r)$ or $T(r)$. For example within the PDFGUI community '$G(r)$' is used to refer to a function that scales as the $D(r)$ described here.

1.1.2 Practicalities of Total Scattering

The collection of total scattering data is by no means straightforward. Firstly, there are certain implications for collecting the data that arise because the real-space correlation function is obtained by Fourier transform of the reciprocal space data. Since only a finite region of reciprocal space can be measured, the real space transform of scattering data can be considered to be the true PDF convolved with a sinc function; consequently, the resolution of the PDF is directly dependent on the range of Q-space that is accessed. The wider the region of reciprocal space that can be sampled, the better the resolution of the PDF obtained [7, 11]. This necessitates (i) detectors capable of collecting data over a wide range of angles, and (ii) the use of short wavelength beams to compress as much of reciprocal space into the accessible spread of angles. For effective PDF analysis a $Q_{\max}$ of at least $25\,\text{Å}^{-1}$ is generally necessary; $Q_{\max} \geq 40\,\text{Å}^{-1}$ is strongly preferred [12, 13]. While some laboratory based diffractometers using Mo or Ag X-ray sources are starting to be able to access the lower end of this range [14], it falls to central facilities to provide instruments that can access the top end.

Synchrotrons allow much higher energies to be used, and generally have much faster collection times, which can allow time-resolved studies to be performed [15]. The 11 ID-B beamline at the Advanced Photon Source at Argonne National Laboratory, U.S.A. [16–18], uses an area detector to collect data rapidly over large angles and high energies, and is well established in the total scattering community. Beamlines at the Diamond Light Source, *e.g.* I12 [19], have also been used for total scattering experiments, and a dedicated total scattering beamline, I15-1 or "XPDF", has recently been commissioned there. Neutron sources can also offer shorter wavelengths than standard laboratory based instruments, though collection times are greatly increased! Crucially, however, pulsed (spallation) neutron sources operating in time-of-flight mode can offer access to much larger areas of reciprocal space by virtue of the range of wavelengths used. Instruments such as GEM [20–22] and POLARIS [23] at the ISIS pulsed neutron and muon source, U.K. [Fig. 1.1], and NPDF at the Lujan Neutron Scattering Centre on Los Alamos National Laboratory, U.S.A. [24], can routinely collect data in the range $0.8 < Q < 50\,\text{Å}^{-1}$, and sometimes beyond. This is arguably the contemporary "Gold Standard" of total scattering.

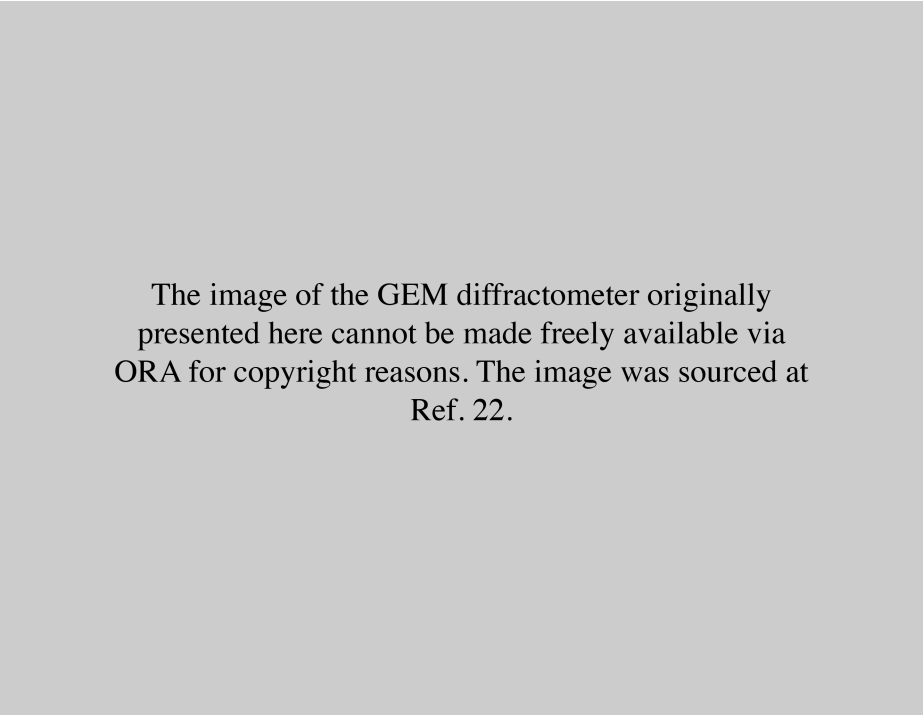

Figure 1.1: The GEM diffractometer, showing the multiple detector banks offering coverage across an extremely wide range of angles [22].

Another requirement concerns the beam energies used. The energy integration implicit in Eq. 1.3 requires detection of both elastic and inelastic scattering events. In turn this implies that the energy of the beam must be greater than the phonon energies in the sample [7]. For pulsed neutron sources this approximation is reasonable.[§]

To ensure that information in the data arises from only the sample, it is important to remove any background scattering that may be present as a result of scattering from the sample environment (*e.g.* sample container, cryostat, furnace) [7, 13, 27]. For a simple Rietveld analysis of Bragg peaks, a basic background subtraction using a smoothly varying polynomial will suffice, but a more rigorous approach is required when low intensity diffuse scattering must also be accurately recorded. Steps must be taken to minimise the background scattering; *e.g.*, by use of vanadium for sample containers during neutron scattering experiments, and precise measurement of the

[§]The contribution of inelastic scattering events to total scattering data is significant and detectable, and it has been shown to be possible to extract phonon dispersion curves from total scattering data—please see Refs 25, 26 for more details.

background [28]. Multiple background measurements are typical of a total scattering experiment, including but not limited to: empty instrument; empty sample container; and empty sample container in furnace/cryostat. It is also important to ensure that collection times are long enough to provide an adequate signal to noise ratio, particularly at high-Q values where the signal is weakest [7]. Typically this results in collection times of the order of hours for neutron scattering experiments, while the greater intensities produced by synchrotron sources mean that collection times are rarely above a few minutes in length for these experiments.

Finally there are a few other corrections that must be applied before the data can be used [7]. These principally concern correctly normalising the measured intensities, so that the data may be put on an absolute scale—essential for proper total scattering analysis. For other techniques, such as Rietveld refinement, this is unnecessary as the scale factors and background functions are allowed to refine freely. Multiple scattering within the sample must also be taken into account: this can be calculated for a sample that scatters only a small amount of the incident beam (less than 20%), so is not normally a problem for neutrons. Neutron sources rarely give a uniform energy spectrum in their incident beams, meaning that measured spectra must be scaled accordingly. This is typically measured by a special detector placed in front of the instrument. The detector efficiencies and solid angles of coverage also need to be accounted for to properly normalise the intensities, which can be done by measuring the spectra obtained from a solid vanadium rod of the same size as the sample. The coherent scattering cross section of vanadium is almost zero, and the incoherent scattering intensity can be calculated quite easily, making normalisation of the measured intensity relatively straightforward [28]. Inelastic scattering causes the wavelength of the scattered beam to be different to that of the incident beam, which is usually insignificant for X-ray scattering but can be quite important for neutron scattering. As detectors do not measure the energy of scattered neutrons there is no way of identifying inelastic neutrons as they arrive, and this can lead to incorrect Q assignments. The Placzek correction takes this into account, as well as adjusting for the fact that detector efficiencies usually scale as the inverse of scattered neutron velocity [29–31]. It is possible to calculate this correction for simple atomic systems, but for more complicated systems it must be modified from these simpler analogues.

1.1.3 Analysis of Total Scattering Data

Once the total scattering data have been successfully obtained and suitably corrected[¶] there are a number of analysis options available to the researcher. For crystalline materials, the PDF is often first analysed within the context of the known average structure. Simple methods might include straightforward peak position and width analysis of the PDF to obtain information on bond lengths and their distributions, or perhaps simply looking for any peak splitting. More advanced methods might include small-box real space refinements, using a program such as PDFGUI [35, 36]. This uses a least-squares method to refine a unit-cell-sized structure against regions of the PDF, and is often referred to as a "real-space Rietveld" method. This can extract more information than by inspection of peak positions alone, and can be used to observe how the structure changes over different length scales. If the local structure substantially deviates from the average structure it can also be difficult to fit the PDF adequately without some other insight into the problem.

The most advanced analysis method for total scattering data remains reverse Monte Carlo (RMC) refinement; this is the principal technique used for this thesis, and will form the subject of the next chapter. Related to RMC is the technique of empirical potential structure refinement [37, 38]. This is more suited for the analysis of liquids and fully amorphous systems, and works by iteratively refining a set of interatomic potentials—which have been used to generate a large-box structural model—against the fit to total scattering data.

1.2 Previous Studies

Having presented an introduction to the theory and practical considerations of total scattering, our emphasis shifts to some of the many areas of science where total scattering has proved useful, drawing on work prepared for a review article published in the *Journal of Materials Chemistry* [39]. These areas are organised into seven subsections, which aim to present a brief overview of the challenges faced, and how they were overcome using PDF techniques. We shall begin with negative thermal

[¶]A number of pieces of software are available to the researcher to assist with data processing, including but not limited to, PDFGETX [32], PDFGETN [33], and GUDRUNN AND GUDRUNX [34].

expansion materials, largely because much work has been done on this topic within our group.

1.2.1 Negative Thermal Expansion

Negative thermal expansion (NTE) is the phenomenon whereby the volume of a material actually decreases on warming [40, 41]. The potential uses for NTE materials are many. For example, they can be used as optical substrates in aerospace engineering materials to avoid the need for mechanical correction of focal lengths as *e.g.* a satellite passes in and out of the earth's shadow; or as components of Bragg diffraction gratings used in optical fibre technology where even small thermal fluctuations in ocean temperatures limit data transfer to less than 100 % of the theoretical fibre capacity.

In these applications, as in many others, the key interest is in using NTE to counteract the more usual positive thermal expansion (PTE) effect of ordinary engineering materials. Consequently there is a strong need to design new NTE materials of increasingly extreme behaviour, in order to increase their efficiency in composite materials. This design brief demands an understanding of the microscopic origin of NTE. Unfortunately, traditional crystallographic analysis is of only limited help, indicating that NTE arises from an unphysical shortening of bond lengths with increasing temperature [42]. In contrast, the use of local structure techniques such as PDF has been crucial in determining the microscopic origin of NTE, revealing how correlated vibrational motion in NTE materials can give rise to a thermally-induced volume contraction even as individual bond lengths increase. Moreover the picture one obtains remains consistent with the results of average structure analysis, producing a coherent description of the phenomenon of NTE.

1.2.1.1 ZrW_2O_8

The archetypal NTE material is zirconium tungstate, ZrW_2O_8 [Fig. 1.2]. It has a notably large and negative linear coefficient of thermal expansion, α, of $-9.07\,\mathrm{MK}^{-1}$ over the range 2–350 K [44], which is comparable in magnitude to the PTE of engineering materials. Its structure consists of a network of ZrO_6 octahedra and WO_4 tetrahedra connected at their vertices [Fig. 1.2(b)]. The crystal symmetry is cubic

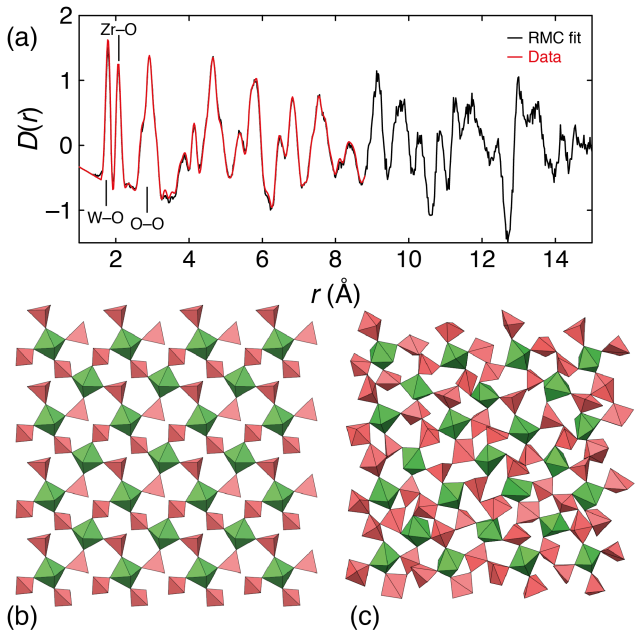

Figure 1.2: Local structure in ZrW_2O_8. The PDF of ZrW_2O_8 (a), with the principal contributions to low-r peaks marked. RMC refinement marked in black, with experimental PDF overlaid in red. The (b) crystalline and (c) amorphous structures of ZrW_2O_8, as produced by RMC refinement. ZrO_6 octahedra are shown in green, while WO_4 tetrahedra are shown in red. Figure adapted from Ref. 43.

and hence the thermal expansivity isotropic. From the very first study of NTE behaviour in ZrW_2O_8, it has been argued that transverse vibrational motion of O atoms in the Zr–O–W linkages might provide a mechanism for the phenomenon [45]. It was quickly pointed out [46] that this type of vibrational motion should occur at a low energy in this particular oxide because the unusual framework topology allowed the O displacements to be correlated throughout the structure in the form of rotations and translations of ZrO_6 octahedra and WO_4 tetrahedra with minimal distortions of either type of coordination polyhedron. This so-called Rigid Unit Mode (RUM) picture of dynamics in ZrW_2O_8 was called into question by a subsequent EXAFS study which argued that the Zr–O–W linkage appeared too stiff for RUMs to play a key role in driving NTE [47].

Neutron PDF measurements of thermal variations in the structure of ZrW_2O_8 settled the debate by providing insight into the correlated displacements of different types of atoms in their structure, and how these correlations are affected by temperature [Fig. 1.2(a)] [43]. Structural refinement of variable-temperature PDF data

using RMC methods allowed extraction of the thermal variation of Zr...W distance distributions, which revealed much greater flexibility than suggested in the EXAFS study of Ref. 47. The atomic displacement ("thermal") parameters of conventional crystallographic refinements characterise the vibrational displacements of *individual* atom types, but here PDF measurements revealed the magnitude of correlated displacements of *pairs* of atoms. Access to atomistic models refined from the PDF data allowed for even more subtle analysis. Using an algorithm with its origins in geometric algebra [43], it was possible to quantify the extent of rotation, translation and deformation of ZrO_6 octahedra and WO_4 tetrahedra evident in RMC configurations and then to demonstrate that these values were actually very similar to those obtained theoretically from the RUM model. Taken together, these results painted a much more complete picture of structure and dynamics in ZrW_2O_8 than would otherwise have been possible and showed that NTE was driven largely by RUM-type vibrational modes.

PDF measurements have played a key role in explaining a second useful and counterintuitive property of ZrW_2O_8, namely that of pressure-induced amorphisation (PIA). Under hydrostatic pressures greater than 1.5 GPa, Bragg peaks are no longer observed in the diffraction patterns (X-ray or neutron) of ZrW_2O_8, which is consistent with the onset of a crystalline–amorphous transition [48]. Such transitions are of enormous current interest, not least because of their central role in data storage for DVD-RAM technologies [49, 50]. Interestingly, PIA and NTE are thought to be connected [51], but the inherent difficulties associated with characterising the structure of an amorphous phase have resulted in a number of wildly contrasting explanations of the phenomenon being proposed. One model was that the "amorphisation" actually involved decomposition into ZrO_2 and WO_3 (Ref. 52)—this was quickly discounted using PDF measurements once it was shown that the observed PDF of amorphous ZrW_2O_8 (*a*-ZrW_2O_8) was inconsistent with all possible linear combinations of the PDFs of the two binary oxides. A second model suggested that the very large density increase (26 %) associated with PIA reflected the formation of new Zr–O–W bonds such that the coordination number of Zr increased from 6 to 7 [53]; and a third model that new W–O–W bonds were formed so that it was the W coordination number that increased instead—in this case from 4 to 5 [54].

In order to distinguish between the various models, a combination of neutron and X-ray PDF data were used to drive RMC refinements that used starting configurations corresponding to each of the models proposed [54]. This use of X-ray and neutron PDF data together is seen as the experimental ideal because it maximises sensitivity for all atom types: an element that is weakly weighted in X-ray data may be more strongly weighted in neutron data, and *vice versa*. Using this approach for *a*-ZrW_2O_8, it was shown that amorphisation most likely proceeds via the mechanism involving formation of new W–O–W linkages. PDF analysis allowed refinement of the "amorphous" structure and showed how this new structure formed via correlated polyhedral rotations and translations within the crystalline precursor of precisely the same type implicated in its NTE behaviour [Fig. 1.2(b),(c)]—a level of analysis that would simply not have been possible using traditional crystallographic approaches. So PDF measurements showed that the process of PIA does not produce a completely random structure, but rather one where the connectivity is derived from that of the original crystalline phase. The implications of such a phenomenology for the fast phase-change kinetics of the chalcogenides used in DVD-RAM technology have not passed unnoticed [55–58].

1.2.1.2 Cyanides

A second family of NTE compounds that has been increasingly widely studied is that of the metal–cyanide frameworks [59–65]. It appears that the metal–cyanide–metal (M–CN–M) structural motif found in these framework materials can give rise to equally unconventional mechanical phenomena to those found in materials involving under-constrained metal–oxygen–metal linkages, such as ZrW_2O_8. Indeed the additional flexibility of M–CN–M linkages means that cyanide-containing materials are more likely to show NTE, and that the effect is likely to have a greater magnitude than found in oxide frameworks [Fig. 1.3(a),(b)] [66].

The archetypal compound in this family is the cubic material $Zn(CN)_2$, and again PDF measurements have played a central role in elucidating the mechanism of its NTE effect. Its structure consists of Zn^{II} ions tetrahedrally coordinated by bridging cyanide anions, to give a pair of interpenetrating frameworks each with identical diamond net topologies [Fig. 1.3(c)] [60]. The material shows the greatest isotropic NTE below

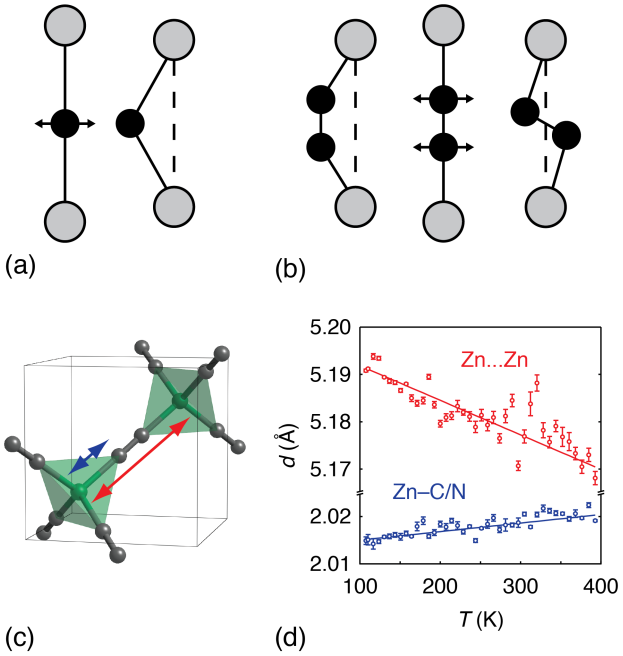

Figure 1.3: Flexibility and NTE in cyanides. Schematic diagrams representing the possible vibrational modes that can result in NTE behaviour for (a) one and (b) two atom linkages. Heavy atoms (*e.g.* metals) are shown by grey circles, with lighter atoms (*e.g.* oxygen) shown by the black circles. Arrows indicate the directions of atomic motion. (c) Unit cell of $Zn(CN)_2$ with key interatomic distances highlighted. (d) Plot showing the PDF-extracted distances. The Zn...Zn distance decreases with increasing temperature despite the increase in the Zn...C/N distance, providing direct evidence of the role of transverse vibrational motion in giving NTE. An average structure refinement produces an unphysical contraction of the Zn...C/N bond length. Figure adapted with permission from Ref. 42.

180 K where $\alpha = -19.8\,\mathrm{MK}^{-1}$ with a subtle reduction in the magnitude of NTE at higher temperatures [42]. Variable-temperature single crystal X-ray diffraction studies revealed a large increase in C and N transverse displacements and a decrease in Zn–C/N bond lengths with increasing temperature, which were interpreted in terms of RUM-type vibrational motion of the $[Zn(C/N)]_4$ coordination tetrahedra [64]. But it was a PDF study that provided direct evidence for this mechanism: in contrast to the picture obtained by traditional crystallographic refinement, PDF refinements showed that the Zn–C/N distances increased with increasing temperature, while the Zn...Zn separations decreased [Fig. 1.3(d)] [42]. This can only be accommodated within the structure if there is a large degree of transverse vibrational motion of the C and N atoms.

In addition to their NTE properties, transition metal cyanide frameworks are of interest from a crystal-chemical viewpoint because they exhibit a number of different types of structural disorder. PDF measurements have helped interpret the very bizarre diffraction patterns of low-dimensional cyanide frameworks such as AuCN and $Ni(CN)_2$, which consist of chains (AuCN) or layers ($Ni(CN)_2$) that are packed in a quasi-periodic arrangement [Fig. 1.4] [62, 63, 67]. These strange packing arrangements, which cannot be characterised using average structure techniques, appear to arise from a combination of structural frustration and weak interactions, and actually further strengthen the NTE behaviour of these materials [62, 63]. A further complication in these structures is the existence of CN orientational disorder, which is common amongst homometallic transition metal cyanides [68]. Because the M–C and M–N bond lengths are expected to be different to each other for a given metal M [69], the average structure reflects only a "smeared" scattering density along the M–C/N vector and it has been all but impossible to resolve this density into its two separate contributions using average structure techniques [61, 64]. However, PDF measurements are sensitive to the different bond lengths and it was shown recently that these could in fact be resolved for $Ni(CN)_2$ even in the presence of the stacking disorder discussed above [67]. Characterising such differences is crucial in the development of *ab initio* and empirical potential models of structure, dynamics and the electronic properties of cyanide-containing frameworks [69].

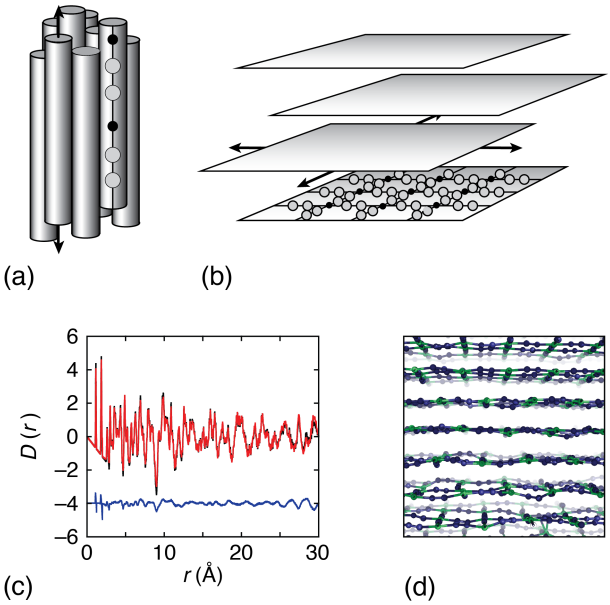

Figure 1.4: (a) The structures of the low dimensional cyanides MCN and (b) $M(CN)_2$, demonstrating the simple linear and planar frameworks respectively. There is no vertical alignment between chains for MCN, and there is no periodic lateral alignment between planes in $M(CN)_2$. (c) RMC-generated PDF of $Ni(CN)_2$ in red, with experimental PDF in black and difference curve plotted beneath in blue. (d) RMC-generated structure showing the disordered layers and large amplitude vibrational displacements. Figure adapted from Ref. 64.

By replacing the linear cyanide ion in these structures by the almost-linear dicyanoargentate $[Ag(CN)_2]^-$ or dicyanoaurate $[Au(CN)_2]^-$ anions it is possible to engineer even more flexible structures that exhibit highly atypical mechanical properties. Silver(I) hexacyanocobaltate(III), $Ag_3[Co(CN)_6]$, is one such material. It exhibits very strong ("colossal") PTE *and* NTE effects along different crystal axes that are an order of magnitude larger than those found in normal materials [70]. The structure itself consists of a highly under-constrained framework of Co–CN–Ag–NC–Co linkages forming the edges of a distorted α-Po cubic net, with three such frameworks interpenetrating [Fig. 1.5(a)] [59]. The anisotropic PTE/NTE expansion behaviour means that there exist particular crystallographic orientations along which the expansion coefficient is zero: these include the directions along which the Co–CN–Ag–NC–Co chains are aligned. So for this material the average structure analysis suggested the framework behaves much as a sheet of "garden trellis" whereby expansion parallel to one axis forces a perpendicular contraction [70]. But what was not clear was what is actually responsible for driving this hinging mechanism as temperature is varied. Atomistic refinement of neutron PDF measurements using the RMCProfile code [71] and subsequent phonon analysis [25, 72] allowed characterisation of the vibrational modes most sensitive to thermal variations. It was found that displacements of Ag atoms, which occupy the vertices of a Kagome net [Fig. 1.5(b)], were very strongly anharmonic; at higher temperatures, where the phonon contribution to free energy becomes increasingly important, the system is able to recover sufficient free energy by increasing the Ag...Ag separation (hence reducing the vibrational energy of Ag displacements) to overcome the energy cost associated with large-scale deformation of the network geometry [Fig. 1.5(c)] [73, 74]. The point to be emphasised here is that even in systems where there are not significant discrepancies between local and average structure—as is the case for $Ag_3[Co(CN)_6]$—PDF methods are able to provide significant insight into the atomic-scale mechanisms responsible for macroscopic phenomena of interest.

1.2.2 Zeolites and Metal–Organic Frameworks

The structural disorder and low-energy dynamics found in NTE materials arises primarily from the geometric flexibility of under-constrained linkages—the existence of

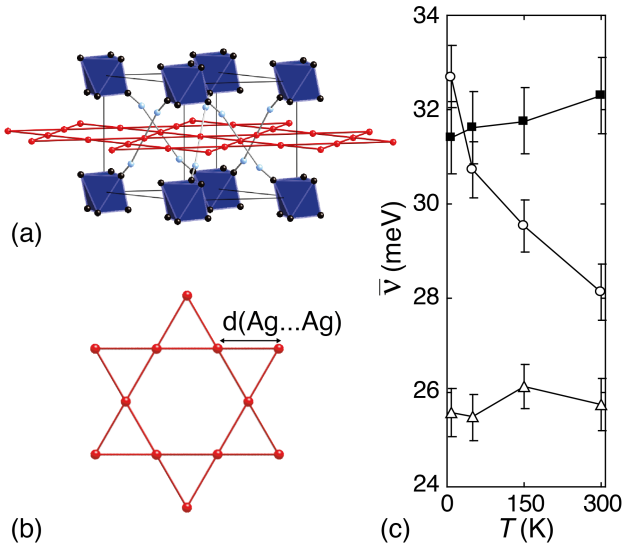

Figure 1.5: (a) The crystal structure of $Ag_3[Co(CN)_6]$ with the Kagome net of Ag atoms shown in red. (b) Plan view of the Kagome net. (c) Plot of the average partial phonon frequencies for the different species in $Ag_3[Co(CN)_6]$, with Ag atoms shown as open circles, C/N as filled squares and Co atoms as open triangles. The reduction in Ag phonon frequencies at higher temperatures allows the enthalpic cost of deforming the network structure to be overcome. Figure adapted from Ref. 70.

which is of course a common feature of all framework materials, including zeolites and metal-organic frameworks (MOFs). The structural flexibility of this broad group is well established [75], and this gives rise to phenomena that are well-suited to local structure PDF investigations: gas sorption and storage properties [76, 77], pressure- and temperature-induced amorphisation [78, 79] and catalytic activity [80].

Given the difficulty in synthesising zeolites and the strong industrial interest in overcoming this difficulty, one fundamental question has always been how the phases actually grow from their amorphous seed nuclei. Spectroscopic techniques show that there exist strong similarities between product and precursor on a local scale, but because they cannot give any information about structures on an intermediate length scale, it is not possible to develop an understanding of *e.g.* how specific zeolite ring motifs evolve during crystal growth. In a landmark PDF study of zeolite A [81], it was shown that different ring structures evolved at different points in the growth process [Fig. 1.6(a)]. This insight was obtained from analysis of RMC configurations obtained by fitting to synchrotron X-ray PDF data. In the models based on data from the amorphous precursor material there existed a similarly broad distribution of even-numbered rings to that found in zeolite A itself; there was, however, no structural coherence in their arrangement. The actual distribution of rings was also different, with increasingly many of the highly-strained double 4-membered rings as zeolite crystallisation occurs. This established for the first time that formation of strained ring motifs takes place at the final stages of precursor organisation for crystallisation.

The reverse process—namely zeolite amorphisation—is also of considerable interest, since there is scope for these phases to be used as hosts for radioactive waste containment. It is crucial for such applications to know whether structural integrity (and hence waste containment) is maintained under large changes in pressure or temperature. By its very nature, amorphisation is an inherently difficult process to study. Spectroscopic studies of PIA in hydrated Na-A zeolite, for example, had suggested that some aspects of the zeolite structure were less deformable than others [82]. A recent PDF study was able to shed new light on this important problem [78]. Simply by comparing experimental PDFs for hydrated Na-A zeolite measured at different points in the amorphisation process with the calculated partial PDFs, it was possible to show which components of the structure deformed most strongly under pressure and which

retained their structural integrity. This revealed that again the double 4-membered rings were crucial in the transition between amorphous and crystalline phases in this material. These rings deformed under pressure, while other units remained rigid, placing the results of the earlier spectroscopic study within a well-defined structural context [78]. The combination of PDF measurements and RMC modelling has since been used to produce even more detailed structural descriptions of the amorphisation process. In silicalite-1-F, for example [Fig. 1.6(b)], it was shown that amorphisation occurs without disruption of the network connectivity: flexing of the Si–O–Si bonds allows for a network collapse that causes the drastic volume reduction associated with the process [83].

Zeolitic imidazolate frameworks (ZIFs) are a family of MOFs whose structures assume the same topologies as zeolites [76]. They have recently been shown to share also the same propensity for anomalous mechanical properties, including amorphisation [79, 84], NTE [85] and negative compressibility [86]. Despite the prominence of MOFs in the materials chemistry literature, local structure studies are relatively few. The process of thermal amorphisation and recrystallisation of one such framework, known as ZIF-4, provides a good example of the potential role that PDF measurements can be expected to play in the field.

Heating a polycrystalline sample of ZIF-4 to 300 °C under ambient pressure causes an irreversible transition to an amorphous phase (*a*-ZIF) [Fig. 1.6(c)]. This amorphous phase is recoverable to room temperature, and can be converted into another, denser, crystalline phase (ZIF-zni) when heated to 400 °C [79]. Importantly, the composition remains constant throughout both structural transitions. RMC refinements of neutron and X-ray PDF data showed that not only was the local coordination environment of the Zn atoms identical in all three phases, but that the network connectivity of the amorphous intermediate was distinct to that found in either crystalline phase [Fig. 1.6(c)]. Indeed the best refinements corresponded to the use of a continuous random network model for *a*-ZIF, similar to that used to describe the Si–O–Si connectivity in silica glass. Just as ZIFs are MOF analogues of zeolitic silica frameworks, so too does it seem that *a*-ZIF is the MOF analogue of silica glass. Taken together with the results of pressure-induced amorphisation in zeolites and ZrW_2O_8, these studies have illustrated the huge variation in amorphous topologies

and amorphisation mechanisms possible.

Amorphisation is by no means the only property of framework materials of practical importance. There is particularly strong interest in the use of framework materials as catalysts and in gas storage and sequestration. For all these applications it is of fundamental importance to understand the interaction between host framework structure and guest molecules (*e.g.* the catalytic substrate or gas molecule to be stored). Characterisation of gas-storage sites, for example, has helped improve the design of frameworks with increasingly attractive storage capabilities [77]. It is no surprise that there has been quite some effort within the community to study binding phenomena using traditional crystallographic techniques. The relatively low concentration of adsorbed species makes conclusive interpretation of average structure models difficult; the existence of multiple binding sites complicates the analysis further. An important breakthrough in the field is the use of differential PDF techniques to study guest–guest and guest–host interactions [87, 88]. If the PDF from an unloaded structure is subtracted from that of the corresponding loaded structure then it is possible to obtain simply those correlations that relate to the adsorbed species. This so-called "differential PDF" analysis then provides important information regarding the correlations among adsorbed species and those between the adsorbate and atoms in the framework structure. With a knowledge of these correlations the preferred binding sites can usually be identified. In some cases the effect of sorption can be even more profound: the framework structure itself can be affected during adsorption, and these effects are also amenable to characterisation using PDF analysis. As an example, it was found using PDF measurements that gas sorption changed the ligand binding geometries in so-called "YO-MOF" [89]. These structural changes resulted in a hysteretic effect upon loading and unloading of CO_2, and produced a "gating effect" for adsorption of N_2 and Ar that potentially allowed for selective CO_2 sorption in gas mixtures.

1.2.3 Ferroelectrics and Relaxors

The study of structural disorder in more conventional framework structures—specifically perovskites and their derivatives—has a long and colourful history. Relaxor ferroelectrics are a particularly good illustration of a class of perovskite materials where

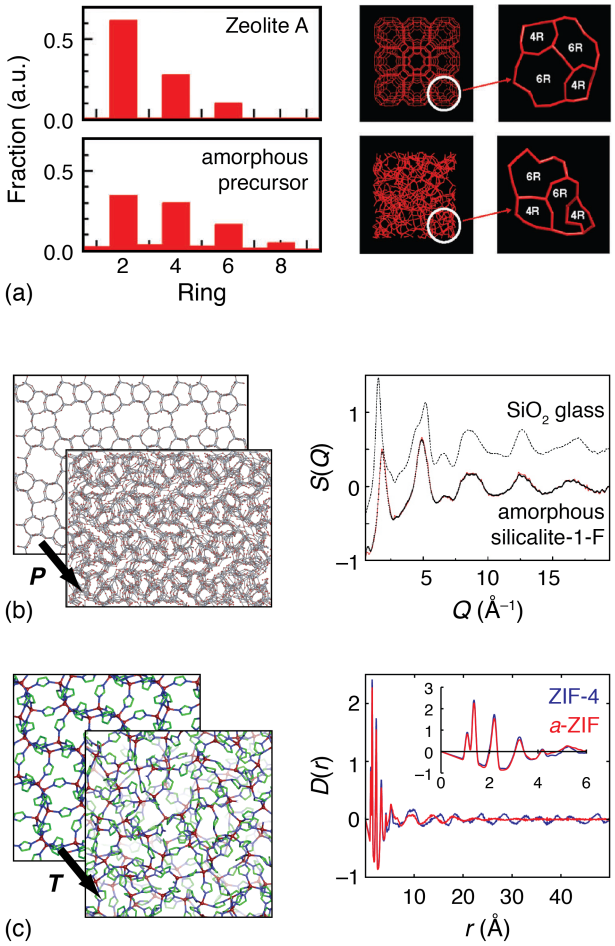

Figure 1.6: Amorphous-crystalline relationships in zeolitic materials. (a) Ring structures and their fractional amounts for Zeolite-A and its amorphous precursor, showing how the population changes during crystallisation. Adapted with permission from Ref. 81. © 2006 Royal Society of Chemistry. (b) Silicalite-1-F transforms to an amorphous structure under pressure, shown in the left hand panel. The right hand panel compares the $S(Q)$ for SiO_2 glass with that for amorphised silicalite-1-F, with the best RMC fit overlaid in red. The best fit is obtained for a model that retains the connectivity of the original structure, rather than one that resembles a-ZIF. Adapted with permission from Ref. 83. © 2009 American Chemical Society. (c) ZIF-4 transforms to an amorphous structure upon heating, but in contrast to silicalite-1-F it does not retain the connectivity of the original structure. The PDF shows that while the immediate environment around each atom does not appear to change much (*i.e.* bond lengths are unchanged), but the long range structure changes significantly. Figure adapted from Ref. 79.

PDF analysis has helped characterise this structural disorder and bridge the gap between local structure and macroscopic function. For example, PDF measurements provided the first direct experimental evidence for the existence of polar nanoregions (PNRs) in the prototypical relaxor ferroelectric material $Pb(Mg_{1/3}Nb_{2/3})O_3$ (PMN) [90]. The bulk material possesses cubic symmetry, but the symmetry within each PNR is lower and generates a local polarisation via off-centre displacements of the Pb atoms. PDF measurements were sensitive to the volume fraction of these domains (each of which has dimensions 5–50 Å); so by measuring neutron PDF data at various temperatures it was possible to explain a number of bulk properties of PMN in terms of the statistical likelihood of interactions between neighbouring PNRs. As temperature decreases, the volume fraction of PNRs in the material increases; this continues until at $T \sim 200\,\mathrm{K}$ the percolation threshold is reached. There is no other method available for measuring PNR volume fraction and so this information was truly pivotal in understanding the origin of the field-induced rhombohedral phase transition observed at 220 K [91] and the dielectric anomaly observed on field heating after zero-field cooling [92]. This type of analysis proved general to the related relaxor ferroelectric $Pb(Zn_{1/3}Nb_{2/3})O_3$, where the PNRs were even more strongly evident in the PDF data [93]. More recently, much smaller (and possibly itinerant) PNR formation has been observed using PDF techniques in a non-relaxor perovskite, $SrSnO_3$ [Fig. 1.7] [94]. The particular interest here is that this material has no available mechanism for cation disorder and it had always been assumed that PNR formation was dependent on local cation clustering [95].

The archetypal room temperature ferroelectric is $BaTiO_3$, and both it and its solid solutions have been the focus of a number of PDF studies [96–98]. One particularly interesting study compared Nb-substituted $BaTiO_3$ and $SrTiO_3$ to try to determine why $SrTiO_3$ displays metallic behaviour for small doping levels but $BaTiO_3$ requires far greater levels [97]. The authors used a combination of supercell and single-cell models to fit their PDF data, and found that the average structure description only deviated from the experimental PDF at small r ranges. Here one of the $BaTi_{1-x}Nb_xO_3$ peaks becomes bimodal while the equivalent $SrTi_{1-x}Nb_xO_3$ peak does not. This distortion was likened to the rhombohedral distortion in $BaTiO_3$ itself, and it was speculated that the Nb doping on a small fraction of the Ti sites was enough to

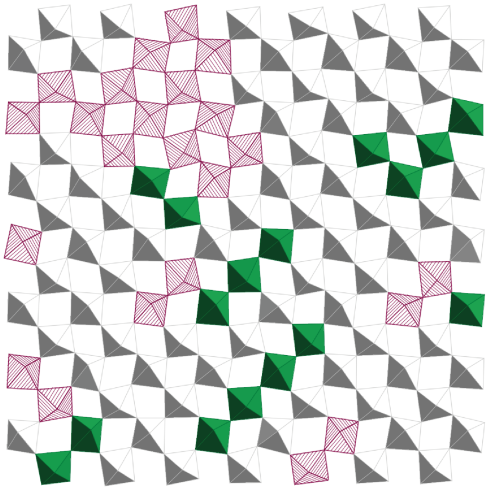

Figure 1.7: Polar nanoregions in strontium stannate, as generated by RMC refinement. Octahedra in which the Sn atoms are displaced in the same directions are shown in the same colours. This correlated displacement behaviour strongly resembles that of polar nanoregions found in relaxor ferroelectrics. It can be seen that the correlations present are very short range, and would not show up in an average structure model.

disrupt the long-range ordering. This gave the appearance of a cubic crystal structure and altered the electronic structure preventing the higher conductivity found in the $SrTi_{1-x}Nb_xO_3$ structure [97].

Doping at the Ti site of $BaTiO_3$ with Zr actually leads to the onset of relaxor behaviour [98]. The transition has been studied using PDF measurements by following the effect of composition on local structure across the $BaTi_{1-x}Zr_xO_3$ family [98]. For $BaTiO_3$ itself, the local structure is different from the average in all but its rhombohedral phase; in contrast the local structure of $BaZrO_3$ is well described by the average structure. PDF analysis of neutron scattering data is ideal for probing the local structure of the solid solution of these two compounds, especially as the neutron scattering lengths of Ti and Zr are of opposite sign, which allows the two elements to be distinguished readily. Comparison of experimental PDFs with those obtained from the average-structure models showed the most significant differences for the intermediate compound ($x = 0.32$); the observed difference PDF was consistent only with either a distortion of the oxygens in the Ti/Zr coordination shell or concerted displacements of the cations away from their crystallographic sites [98]. Good agreement was found between the experimental PDFs for intermediate compounds and PDFs calculated from an appropriately weighted combination of those of the end-members, suggesting that nearest neighbour bonds are not affected by the overall composition [98]. The obvious implication is that the local structure of the relaxors is in fact very different from the average structure—certainly a recurring theme for these materials. Moreover, it was found that only the Ti^{4+} cations are responsible for the ferroelectric behaviour, and hence it is really only the extent of correlation in cation displacements that distinguishes between relaxor and "ordinary" ferroelectric behaviour in this family [98].

Related compounds have attracted recent interest as part of the search for lead-free piezoelectrics, as industry strives to find a suitable replacement for lead zirconate titanate. Bi^{3+} would appear to be a possible replacement for the Pb^{2+} cation on the A site, but it has proved difficult to stabilise under ambient conditions, and a greater understanding is required. As expected, PDF techniques have proved useful for observing cation displacements that are not apparent in the average structure. $Na_{0.5}Bi_{0.5}TiO_3$ was investigated using both small- and large-box refinement methods

and combined X-ray and neutron total scattering data [99]. By fitting to different regions of the PDF using PDFGUI—the so-called "box-car fitting" approach—it was clear that the environments around the *A*-site cations were locally distorted away from the average environments. This small-box approach was unable to differentiate between the Na^{+} and Bi^{3+} cations, so the RMC method was employed as this allows more freedom of movement. This permitted the distinctions in the bonding environments to be discerned, showing that in fact the Bi–O partials were more asymmetric, which carries implications for possible ferroelectric domain formation [99].

RMC refinements were also applied to neutron total scattering data to investigate the Bi local structure in $Bi(Ti_{3/8}Fe_{2/8}Mg_{3/8})O_3$, and revealed the presence of correlated displacements, forming monoclinic domains of up to 15 Å in size [100]. The refined structure also produced more chemically-sensible bonding conditions for the Ti^{4+}, Fe^{3+} and Mg^{2+} cations, giving them each distinct environments, while they were constrained to be identical in the average structure model [100]. This once again demonstrates the ability of local structure methods to bring new insights to materials, and paint a more consistent picture than that which the average structure may on occasion present.

1.2.4 Jahn-Teller Active Materials

Whereas in relaxors the short-range correlations of key interest involve dipole ordering, in the family of colossal-magnetoresistance (CMR) manganites the correlations involve orbital ordering. Jahn-Teller (JT) active metals (*e.g.* Mn^{3+} in the CMR manganites) lower the symmetry of their coordination environment in order to remove orbital degeneracy. In terms of their local structure, this means that metal–ligand bond lengths that would otherwise be identical are no longer equal; for example, in $LaMnO_3$ each Mn has two "long", two "medium" and two "short" Mn–O bonds. If the arrangement in space of these different bonds is strongly correlated for each JT active metal atom within a sample then the macroscopic symmetry will reflect the same JT distortion. In this case the JT distortion will be detectable using traditional X-ray (or neutron) crystallographic techniques. However if the bond orientations are only correlated over small length-scales then the average symmetry will be higher

Figure 1.8: Plots displaying the longest Mn-O distance (a measure of the magnitude of the J-T distortion) as a function of the temperature and composition for the chemical series $La_{1-x}Ca_xMnO_3$. Panel (a) shows the data obtained using Rietveld analysis, and panel (b) shows that obtained using PDF analysis. Only the PDF measurements are sensitive to the CMR transition. Solid curves indicate T_{JT} and T_c phase boundaries [105].

than the local symmetry. The experimental characterisation of orbital (dis)ordering mechanisms is one of the key challenges in the field [101].

Perhaps the highest-profile of the JT active compounds investigated using PDF techniques is the series of CMR manganite perovskites $La_{1-x}Ca_xMnO_3$. Magnetoresistive materials are those that have an electrical conductivity that varies depending on the applied magnetic field; the term "colossal" distinguishes those materials which display the effect to an abnormally large extent—greater even than the so-called "giant" magnetoresistors. The end members [102, 103] and other compositions in the series [104–107] have been studied using PDF measurements, with the primary emphasis placed on how the structure changes as a function of temperature and/or composition. The average structure is largely unaffected by each of the various electronic/orbital transitions implicated in CMR behaviour, but it was shown that the electronic phase diagram was actually replicated by local correlations extracted from the PDF data [Fig. 1.8]. In addition to mapping out the local-structure "phase diagram", it was also observed that the end members show very contrasting local $\leftrightarrow$ average structure relationships: $LaMnO_3$ formed locally-ordered clusters of JT distorted domains $\sim$16 Å wide [102], whereas $CaMnO_3$ possessed a very simple structure where the average and local structures are indistinguishable [103]. In this thesis the structure of the La end member is revisited using a more advanced analysis method—namely, RMC refinement—to explore in greater detail this intriguing material.

Of course, Jahn-Teller distortions need not involve perovskite frameworks. A

quite different example of PDF measurements of a JT active system is given by a recent study of distortions of tetrahedral Cu^{2+} and octahedral Mn^{3+} in $CuMn_2O_4$ spinel [108]. In this study, neutron total scattering data were used to drive RMC refinements, from which a quite extraordinary breadth of structural information about $CuMn_2O_4$ was obtained. In addition to the usual bond length and bond angle distribution analysis that is often performed with RMC configurations, in this case the Cu/Mn occupancy on tetrahedral and octahedral sites was also determined. Quite unexpectedly a relatively large (*ca* 30 %) site inversion was observed. Moreover, from the corresponding metal–oxygen bond lengths it was possible to use bond valence sum (BVS) calculations to estimate the formal charge of each metal ion on the two different sites. What was found was that the site inversion was associated with disproportionation for both metal ions:

$$\begin{aligned} 2Cu_t^{2+} &\rightarrow Cu_t^{+} + Cu_o^{3+} \\ 2Mn_o^{3+} &\rightarrow Mn_t^{2+} + Mn_o^{4+} \end{aligned}$$

where the subscripts "t" and "o" indicate cations occupying tetrahedral and octahedral sites, respectively [Fig. 1.9]. Initially cautious of the supposed formation of Cu^{3+} in this system [109, 110], the authors confirmed this result using X-ray photoelectron spectroscopy. It was noted that disproportionation removes the JT activity of both ions and so might be favoured in this particular compound because the spinel tetrahedral sites form a diamond lattice, for which it is notoriously difficult to support local distortions [111].

The propensity for Bi^{3+} cations to move off centre within their coordination polyhedra essentially reflects a second order Jahn Teller (SOJT) distortion [112] and is considered responsible for the attractive dielectric properties of Bi-containing pyrochlore frameworks [113]. The pyrochlore lattice (general formula $A_2B_2O_6O'$) is generally described in terms of two interpenetrating sublattices: an "anti-cristobalite" A_2O' sublattice which is strongly disordered, and an ordered BO_3 sublattice consisting of corner-sharing BO_6 octahedra. Bi atoms occupy the A site, for which the average crystallographic symmetry imposes O′–Bi–O′ angles of 180 °. The SOJT distortions reduce this angle around the Bi^{3+} ions, which in turn produces a local dipole moment parallel to the direction of Bi displacements. These local dipole moments

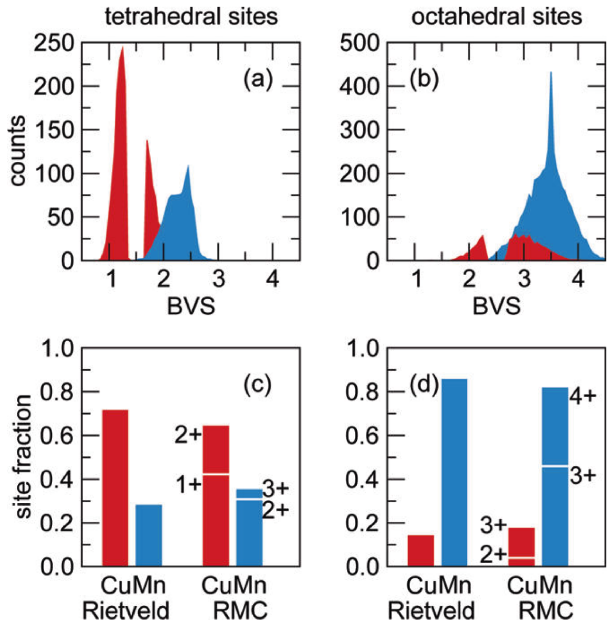

Figure 1.9: Many–atom RMC configurations allow information such as bond valence sums to be calculated, as shown here in panels (a) and (b). Cu data is given in red, and Mn in blue. In (c) and (d) the site occupancies are given as obtained from Rietveld refinement and RMC for comparison. Of note in this case is the tendency for ions to disproportionate away from Cu^{2+} and Mn^{3+} in the RMC configurations [108].

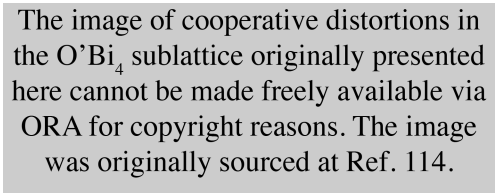

Figure 1.10: Cooperative distortions in the O′Bi_4 sublattice can occur in a zigzag pattern, as shown here for the ideal structure. In reality these distortions are correlated only over short distances [114].

are the structural features implicated in the dielectric properties of this family, and so the question of how the local Bi distortions are correlated is fundamental. A recent PDF/RMC study of Bi displacements in $Bi_2Ti_2O_7$ was able to characterise these correlations [114]. A weak but persistent preference was found for correlated Bi displacements that preserved Bi...Bi distances [Fig. 1.10] [114], a result that was also obtained using RMC analysis of diffuse scattering patterns in electron diffraction patterns of the related system $Bi_2Ru_2O_7$ [115]. Interestingly, there exists a mapping between this Bi displacement pattern and the hydrogen atom positions in cubic ice, which lead to the proposal that these bismuth-containing pyrochlores might be considered as "charge ices" [114].

1.2.5 Spin glasses, spin ices and magnetic structure

It is now well established that when a suitable magnetically-active metal ion occupies the pyrochlore *A* site a frustrated magnetic ground state is possible where the spin orientations can also be mapped onto the hydrogen atom positions of cubic ice: these are the so-called "spin ices" [116–119], especially topical for their role in "magnetricity" [120]. While it is the case that PDF methods are less well developed for describing magnetic disorder than structural disorder, there are certainly strong parallels between the underlying phenomenology. Spin ices possess a well-defined local magnetic structure but magnetic Bragg peaks are not observed in their neutron diffraction patterns: their local magnetic order neither requires nor produces long-range magnetic order. Such materials do, however, exhibit a characteristic magnetic diffuse scattering pattern; just as for nuclear diffuse scattering, RMC modelling can be used to fit this diffuse scattering pattern and hence to probe local magnetic structure in spin disordered systems [118, 121–123]. In materials such as $Y_2Mo_2O_7$ [124], the situation

is even more complex because structural disorder is coupled to spin frustration—this combination is thought to be pre-requisite for the so-called "spin glass" ground state [125]. For such materials even non-magnetic PDF refinements still provide very useful insight into the magnetic structure simply because of this link between structural and magnetic degrees of freedom [124].

Work in the field is advancing rapidly, and recently significant progress has been made to increase the scope of local structure and RMC analysis of frustrated magnets, such that it is now possible to calculate a three dimensional magnetic structure from one dimensional powder data [3]. Single-crystal magnetic scattering poses several challenges, not least sample preparation and data collection times, so the ability to extract the same information from a powder sample greatly assists the study of these materials. This approach has the added benefit of yielding a large structural model of the magnetic moments, which can be examined in detail to obtain a greater understanding of local interactions. For example, for the spin ice $Ho_2Ge_2O_7$ the ice rules defect densities were calculated from the RMC-refined structures, and compared to the densities obtained from other sources [126]. Of course, where single crystal scattering data *are* available, in-depth information can still be obtained—a detailed set of magnetic interactions for Co-doped β-Mn were extracted from magnetic single crystal fitted using RMC methods [127].

But magnetic systems need not be frustrated for total scattering to be of use. A simple example is that of the canonical antiferromagnet MnO. When heated above its Néel temperature, T_N, of 118 K MnO assumes the cubic rocksalt structure and is paramagnetic; at temperatures below T_N antiferromagnetic ordering results in a rhombohedral distortion to this structure [128–130]. Because the spin alignment axis is perpendicular to the rhombohedral axis it has long been realised that the true symmetry can be no higher than monoclinic [131]; however none of the implied peak splitting has ever been observed in traditional Bragg diffraction patterns. It was perhaps unexpected then that a recent total scattering study found the local structure to be actually much more sensitive to this symmetry lowering than is the average structure. In this way a monoclinic structure solution was proposed based on *ab initio* magnetic structure refinements of these total scattering data using RMCProfile [130]. Earlier variable-temperature total scattering measurements on MnO also

probed the degree of magnetic fluctuations at temperatures above and below T_N and showed that correlated spin excitations persisted to temperatures as high as 1100 K [132]. Finally, just as nuclear PDF measurements provide some constraints on vibrational energies, so too was it found that some degree of quantitative information about the spin-wave dispersion in spin ordered systems (*e.g.* antiferromagnetic MnO) could be extracted from magnetic RMC configurations [133]. It is perhaps worth emphasising that spin wave measurements usually require large single crystal samples, and so the ability to access similar data from a powder-based technique such as PDF—as for the analysis of frustrated magnets—is not insignificant.

1.2.6 Nanoparticles

We now move on to a discussion of "nanostructured" materials [134], by which we mean systems which exhibit structural order over short length scales but which do not give rise to sharp Bragg reflections in their diffraction patterns. Such materials are intrinsically difficult to characterise using traditional crystallographic techniques and so PDF methods are uniquely positioned to provide insight into their structure. Of course PDF methods have long been closely associated with the related problem of studying structure in glasses, so it is unsurprising that many of the tools developed for characterising glasses are now finding application in "nanocrystalline" materials [135].

There are a number of structural characteristics of nanoparticles that can be extracted directly from the PDF. Irrespective of the particular chemical system, the length scale over which sharp correlations are observed provides a measure of the nanoparticle size distribution and is also sensitive to their shape [24, 96, 136, 137] [Fig. 1.11]. Recent developments in solid state X-ray detectors mean that PDF data can now be measured sufficiently quickly that it is even possible to monitor the growth of nanoparticles *in situ* [136], which has provided a wealth of information about the growth process and reaction kinetics [136, 138, 139]. By extracting lattice parameters from the PDF (*e.g.* via PDFGUI refinement) one can identify any differences in lattice spacing from the bulk phase and any relaxation effects at the nanoparticle surface can also be probed in this way [24]. Variable-temperature PDF measurements allow for nanoparticle thermal expansion coefficients to be calculated [24]; differential PDF

measurements can help characterise interactions between nanoparticles and species adsorbed onto their surface [96, 140].

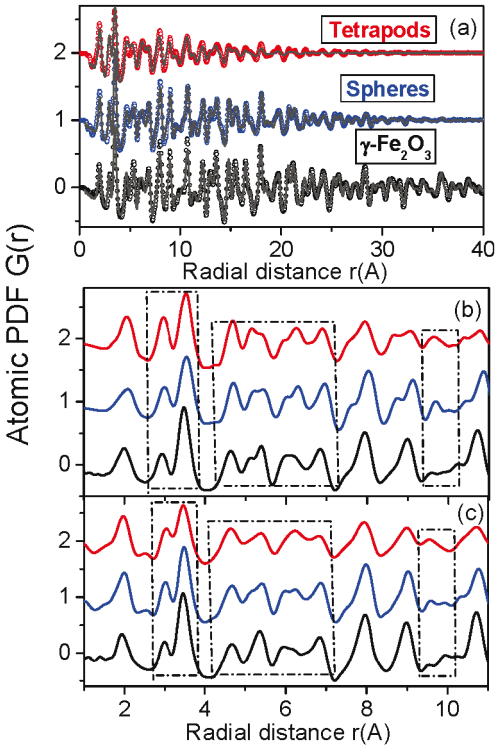

Figure 1.11: (a) Experimentally derived PDFs of γ-Fe_2O_3 showing the effects of particle shape. Calculated model PDFs, (b), for the low r region are then compared to experimental PDFs, (c). The broken black lines highlight peaks whose intensities depend on the particle shape. Sufficient differences are present to be able to distinguish between different particle shapes [137]. © 2009 American Chemical Society.

Local structural distortions within the nanoparticle still maintain a signature in the PDF; this has been exploited in, for example, studies of $BaTiO_3$ nanoparticles where it was found that local ferroelectric displacements occurred (as for bulk $BaTiO_3$) but that the degree of correlation in these displacements reduced as particle size decreased, such that smaller particles appeared increasingly cubic in symmetry [96].

As for the various crystalline systems discussed in earlier sections, it is also the case that large-box RMC modelling can help provide a more detailed structural model for nanostructured materials. A recent example involves local structure determination in amorphous calcium carbonate (ACC) [141]. This is a long-studied system where the fundamental question had always been how the amorphous phase is re-

lated structurally to the various crystalline phases into which it transforms *in vivo* [142, 143]. It was clear from EXAFS measurements that a well-defined short range order is present in ACC, at least within the first Ca coordination shell [144]. RMC refinements of X-ray PDF data yielded an unexpected biphasic structural model: ACC appeared to consist of a Ca-rich framework and Ca-deficient channels, which contain only carbonate and water and percolate through the framework structure [141]. The arrangement of Ca atoms within the framework component was essentially an "average" of that found in the various crystalline polymorphs, which may be responsible for the existence of multiple crystallisation pathways. The existence of mobile anionic channels might also be important for ion transport during crystallisation and/or for ion exchange in biostabilisation of the amorphous phase [141].

Amorphous and nanoparticulate systems are becoming increasingly relevant to the pharmaceutical industry. Many pharmaceutical products are intrinsically very poorly soluble in water, and this means that absorption of the drugs via ingestion can be ineffectually slow. The industry as a whole has taken to improving solubility by preparing products in amorphous or poorly-crystalline forms [145]. The imperfect packing characteristic of these forms facilitates solubilisation in the gut and hence accelerates incorporation of the product into the bloodstream. Occasionally the compounds are inherently amorphous, but most times crystallinity has to be intentionally destroyed through melt-quenching or high-pressure ball milling. In all cases, the final product is subject to the same stringent purity controls imposed by consumer law that apply to crystalline products; the onus is on the supplier to prove the structural integrity and purity of each compound. Consequently the absence of crystallinity in the products presents a number of challenges: (i) characterisation of the product and assurance of its structural purity is difficult, (ii) patent protection is consequently problematic, and (iii) eventual conversion back to the original crystalline form usually occurs, but the rate at which this happens (and hence the shelf-life of the product) varies enormously and is not well understood.

A recent study has shown how PDF analysis might provide the long-needed means of addressing these issues [146]. In particular, it was found that PDF data were sensitive to different types of amorphous and nanocrystalline forms of key pharmaceuticals, and could be used to relate the packing of amorphous ingredients to that found in

their known crystalline polymorphs. Like much of PDF science, this is a nascent approach to studying pharmaceutical compounds. Rapid progress can be expected as increasingly sophisticated experimental and analytical PDF methods are employed [147].

1.2.7 Recent developments

Now that the field is reasonably established, it is likely to be increasingly used for industrial applications—indeed the beginning of this can be seen already. The global research effort into energy storage materials is an obvious candidate for future local structure analysis using PDF. In terms of gas storage materials, one would expect not only to characterise the binding sites of gas molecules but also to understand better the sorption/desorption processes and hence address issues such as reversibility and sorption kinetics. For example, one study has used synchrotron X-ray total scattering data to monitor defect formation during hydrogenation/dehydrogenation cycling in $V_{1-x}Ti_x$ alloys, finding a correlation between the increase in dislocation density and the reduction of hydrogen capacity [148]. With further work in this area it should be possible to design longer lasting storage materials.

Battery materials often see very large structural changes during charge and discharge, and understanding these changes and the way in which they are coupled with conduction processes will be crucial in developing next-generation materials. Similarly, a knowledge of ion conduction pathways and mechanisms is of fundamental importance for developing materials for fuel cells: here there are already a handful of studies that illustrate the potential gains that PDF techniques may bring. For example, Ref. 149, which uses RMC refinement to investigate the superionic conductor lithium lanthanum titanate. The results are shown in Fig. 1.12, demonstrating that the identification of conduction pathways and structural "bottlenecks" is possible, which could assist in intelligent design of battery materials. RMC refinement of neutron diffraction data has also proved useful for the superionic conductors $\beta-SrBr_2$ [150] and $\delta-Bi_2O_3$ [151], uncovering local correlations within the anion positions. TiO_2 [152] and other electrode materials [153], have been examined using PDF, revealing details of the structural connectivity upon Li insertion [152], and defect regions—undetected by average structure probes—have been revealed in

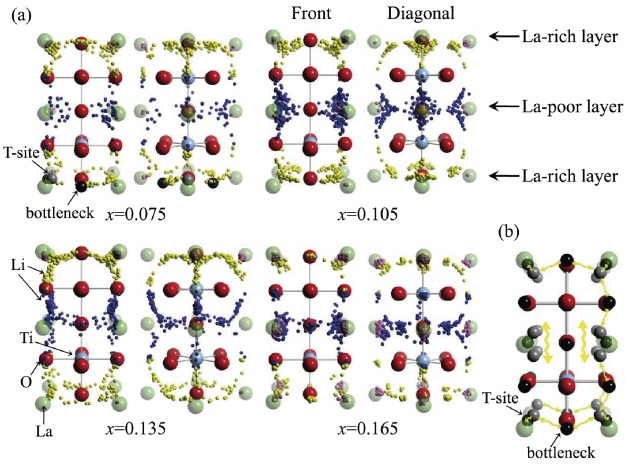

Figure 1.12: (a) Unit cells for the material $La_{2/3-x}Li_{3x}TiO_3$ for four different values of x produced by RMC modelling. Li atoms from the configurations have all been collapsed onto a single unit cell to show their distribution of positions. Li atoms in a La-rich layer are coloured yellow; those on a La-poor layer are coloured blue. (b) diagram indicating possible Li ion conduction pathways. Reproduced with permission from Ref. 149. © IOP Publishing.

$Ce_{1-x}Gd_xO_{2-x/2}$ electrolytes [154]. Steps are now being taken to develop a diffraction cell that will allow *in situ* measurements to be made of the structural changes that occur during charge/discharge cycles in battery materials [155]. All these cases help establish the ability of local structure techniques to provide valuable information on the inner workings of these functional materials.

The drive for increased efficiency is encouraging the development of improved catalysts, and work has begun to improve our understanding of their structures through the use of PDF techniques. Two recent PDF studies have characterised domain formation in water splitting catalysts with X-ray PDFs: the first examined cobalt oxide films, finding the data able to easily discriminate between different candidate structures, with some suggestion of distorted oxygen geometries around the domain edges [156]; the second concerned iridium oxide, and had success fitting the domains with a five iridium cluster based on the rutile structure, again with suggestions of distorted regions at the periphery [157]. The next step must surely be to combine these measurements with *in situ* catalysis experiments, with the aim of obtaining accurate information regarding the catalyst-reactant interactions.

The techniques for reliable measurement and analysis of total scattering data

are constantly being refined, with improvements to instruments and software alike. Aspects of theory are being developed [10], data reduction processes are being re-evaluated [158], and there is a move to incorporate data from other sources, such as EXAFS, to improve the reliability of results [159, 160]. Three-dimensional PDFs are even being discussed [161], which have the potential to increase dramatically the information available to researchers, albeit at the cost of increased computational demands. There have also been some developments over the past few years of techniques aimed at using the PDF to "solve" the local structure of amorphous or nanocrystalline materials [162, 163]. The driving force behind these developments is the realisation that the establishment of "crystallographic" methods for nanostructured materials would be of enormous value to a very large number of science areas: for example, to the pharmaceutics industry as a means of characterising and patenting their amorphous ingredients, in the study of biomineralisation processes and the design of bioactive glasses, in developing nanoparticles including quantum dots and the pursuit of "superatom" states, in functionalising amorphous metal–organic frameworks, and in developing data storage technology built on phase change chalcogenides.

There is no doubt that total scattering techniques are an area with huge potential for growth, which promises to benefit many areas of science in the coming years.

1.3 Project Overview

We return now to the topic of this thesis. As mentioned above, total scattering combined with RMC refinements have been used to examine three functional materials that exhibit a degree of disorder. These were the high temperature cuprate superconductor, $YBa_2Cu_3O_{7-x}$; the parent compound of several families of colossal magnetoresistive compounds, $LaMnO_3$; and the oldest known magnetic material, Fe_3O_4—commonly referred to as magnetite. Each was chosen for being in some respect 'canonical', and because questions still remain regarding their structures, despite extensive study. For $YBa_2Cu_3O_{7-x}$ the debate concerns a particular bond length implicated in charge localisation; for $LaMnO_3$ the question is one of orbital ordering across different length scales; for magnetite the interest lies in the structural transition known as the Verwey transition, and any charge ordering that may exist, along

with the undetermined magnetic structure. Hopefully this thesis will show that despite the extensive work already carried out on these well-known materials, it is still possible to gain new insight by applying advanced analysis methods as outlined here.

The next chapter details the RMC refinement method at the heart of this study, and the various alterations made to the RMCProfile code in the process of this thesis are also outlined. The three results chapters are presented in order of increasing complexity: $YBa_2Cu_3O_{7-x}$, then $LaMnO_3$, and finally Fe_3O_4. An introduction to each system and the challenges faced will be presented at the beginning of the respective chapters. The thesis concludes with a summary of the main results of this study and a discussion of the implications for related problems in the condensed matter sciences.

Chapter 2

RMCProfile Code Development

2.1 Introduction/A Brief Description of RMC

Standard crystallographic techniques work well for ordered materials, but fail when it comes to disordered materials, as these cannot be represented adequately by a repeating unit cell. It is this gap that reverse Monte Carlo refinement tries to fill. This technique fits a large box of atoms directly to experimental data through an iterative trial and error process [see § 2.3.1], producing a physically realisable structure that is consistent with the information provided. The large number of atoms included ($\sim 10^4$) allows all the various structural elements involved to be represented, particularly those that might not be described by a smaller repeating unit. RMC refinement can also provide useful information about correlated atomic motion in crystalline materials, which again cannot be obtained using average structure methods.

The stochastic nature of the RMC process results in a certain amount of noise in the atomic positions, creating the most disordered configurations that are still consistent with the data, so the process tends to overestimate the disorder present in the system. This means that the results can only indicate general trends or features present in the structures, and the positions of individual atoms cannot be assigned much meaning when considered on their own. In general a degree of care is required to ensure that a refined structure is chemically sensible and consistent with other information.

The extra effort and attention required to successfully perform an RMC refinement when compared to a Rietveld refinement—as well as the more specialised conditions involved in the collection of total scattering data—means that an RMC refinement

should not be undertaken lightly. It can however, if done properly, provide a useful insight into complex systems that other techniques cannot.

This chapter will continue with a brief review of the history of RMC refinement, before discussing the algorithm used, and specific details of the RMCProfile code. Finally it will finish with a discussion of the changes made to the RMCProfile code as part of this thesis.

2.2 A Brief History of RMC

As was mentioned in the preceding chapter, the total scattering technique was largely developed with fully disordered materials—liquids and glasses—in mind. The first ISIS diffractometer, LAD,* was designed (and named) for this purpose [164]. There was a need however, of analysis techniques that could fully utilise the total scattering data, and the reverse Monte Carlo refinement technique was developed some 26 years ago in response to this [165].

There are several reviews that chart the progress of the method in the early days: please see Refs [166–169] for in-depth contemporary accounts of the field. In brief, the technique was soon expanded beyond simple atomic liquids, and it was quickly realised that RMC methods could be used to fit to data forms other than purely total scattering data, for example, EXAFS, NMR, and single-crystal scattering. From the point of view of this thesis, the biggest breakthrough came with the realisation that the technique could also be applied to predominantly crystalline structures, which happened quite early on [170, 171].

Initial work on crystalline structures used unmodified versions of the code written for amorphous systems, and it was soon realised that for well-ordered systems resolution issues limited the potential of the technique. There then followed a series of modifications to the code designed to overcome these issues and improve the ability to fit data from polycrystalline samples [172, 173], culminating in the development of the RMCProfile code [71], the innovative feature of which was the explicit fitting of the Bragg peak profiles, allowing all information contained in the Bragg peaks to be utilised.

**Liquids and Amorphous Diffractometer*; first installed at the Harwell Linac neutron source 1982, and subsequently moved to the new ISIS facility prior to first neutron production in 1984. This was the predecessor to the GEM diffractometer.

RMCProfile is the implementation of the RMC method used in this thesis, and it will be discussed further in the next section. For now though it is worth explicitly mentioning the existence of other RMC programs, written by a variety of people across numerous institutions. RMCA—alluded to above—is perhaps the earliest, written for amorphous systems but sometimes applied to rather disordered crystals [165]. RMCX followed shortly afterwards, which extended the functionality to allow fitting to single crystal diffuse scattering [174]. RMCPOW adapted RMCX to allow basic fitting to Bragg data for powder samples [168, 172]. A successive improvement to Bragg fitting, RMCBragg [173], started from the RMCA code, and was subsequently superseded by the RMCProfile code currently used [71]. While improvements to functionality have been made in recent years, more attention has been given to improving ease of use for the operators: RMC++ has been created as an open-source program, designed to allow greater flexibility for the user [175], while the RMCProfile code has been given a graphical user interface and rechristened RMCGui [176]. We should note for completeness that RMC is now being used proportionately less for liquids and glasses than was once the case, and EPSR [38, 177] is now the more widely-used code in this area.

2.3 The RMC Algorithm, and RMCProfile in particular

2.3.1 The Algorithm

RMC is so named as it is a variation on the Metropolis Monte Carlo algorithm [178, 179]—random moves are evaluated against some merit index, and accepted or rejected based on criteria that allow for some 'bad' moves. But while conventional (direct) Monte Carlo algorithms start with a set of local interaction potentials, and run to minimise the overall energy, the *reverse* Monte Carlo method replaces the energy term with a fit-to-data. RMC earns the epithet 'reverse' as while the conventional MC algorithm starts from local interactions and produces a larger structure, the RMC algorithm starts with larger structural information and produces a model that can provide information about local interactions.[†]

[†]It should be noted that in some cases local interactions may be applied in order to encourage the refinement to follow a sensible path. Please see the following section for more details.

The refinement process starts with the coordinates of a large configuration of atoms. Typically this is an ordered model based on the average structure (assuming a crystalline material is being studied), and for RMCProfile this should be a supercell of the individual unit cell.[‡] Then the expected pattern that this structure would produce is compared to the pattern that has actually been measured experimentally, and a numerical merit index, χ^2_{initial}, is calculated to assess the quality of the fit. Typically total scattering data of some form will be used, often in conjunction with other data forms.

An atom in the configuration is then randomly selected and moved by a small amount in a random direction. Moves are typically translational, with a fixed maximum move distance, though other types of move are possible, as will be discussed later. The fit to the data for this altered structure is then calculated, and the merit indices for the two models are compared. If the fit is improved in the new structure then the move is accepted unconditionally; if the fit is degraded by the move then it may be accepted, with a probability P dependent on how much worse the fit is made. If $\Delta\chi^2$ describes the change in the merit indices, $\chi^2_{\text{final}} - \chi^2_{\text{initial}}$, where a lower χ^2 is desired, then the situation may be summarised as follows:

$$\text{for } \Delta\chi^2 \leq 0 \quad : \quad P = 1 \tag{2.1}$$

$$\text{for } \Delta\chi^2 > 0 \quad : \quad P \propto \exp(-\Delta\chi^2). \tag{2.2}$$

For refinements where multiple data sets are used, the $\Delta\chi^2_{\text{Total}}$ term should be a suitably weighted sum of the individual $\Delta\chi^2_i$ for each data set.

The reason for accepting 'bad' moves is to prevent a refinement becoming stuck in a local minimum, allowing it to find the global minimum. In practice this arrangement must be monitored closely: typically restrictions may be made to prevent the (albeit very small) possibility of accepting a very unfavourable move, and the acceptance rates are adjusted by use of weighting terms for each data set.[§]

The process of making a trial move, evaluating it, and then accepting or rejecting it is iterated many thousands of times, depending on the number of atoms and how

[‡]An approximately cubic supercell of side $\sim 50\,\text{Å}^{-1}$ is reasonable.

[§]These weighting terms function much like the 'temperature' in conventional MC simulations—where MC may use an energy term divided by temperature, $\frac{E}{kT}$, to evaluate a model, RMC may divide its merit indices by the weighting terms, $\frac{\chi^2}{\sigma^2}$, when evaluating a move.

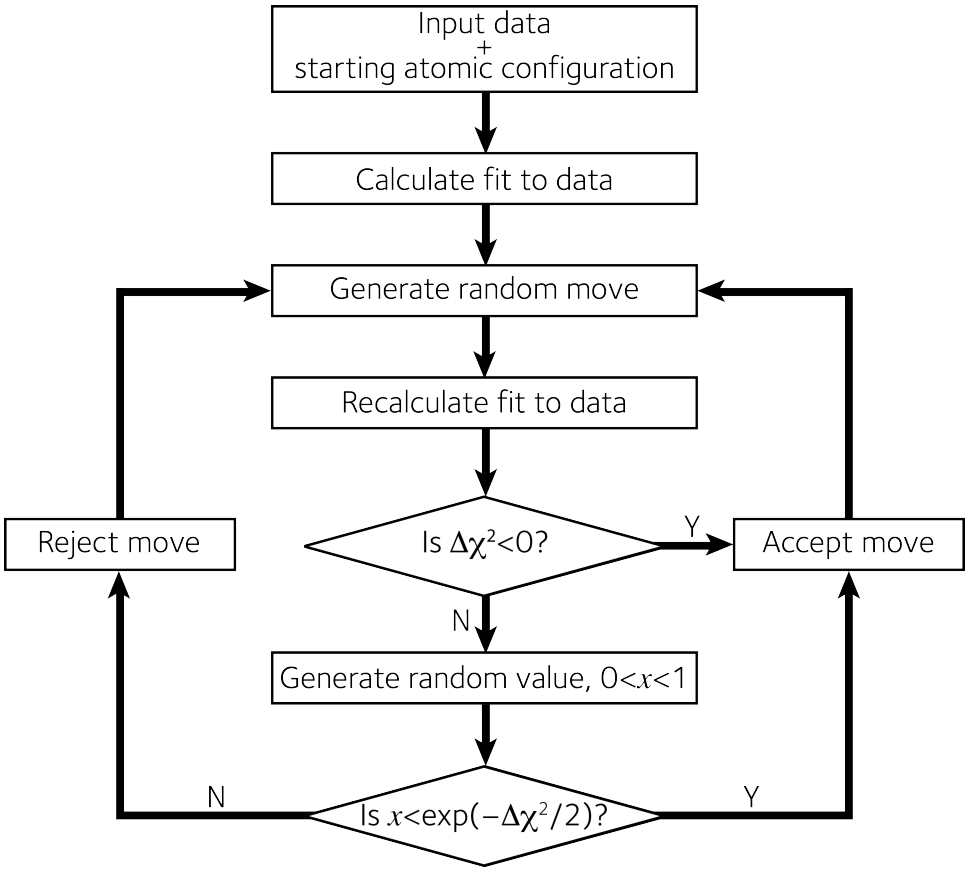

Figure 2.1: A flow diagram outlining the RMC process.

appropriate the starting structure was. It is at the user's discretion how long the refinement is left to run, though monitoring the χ^2_{Total} throughout the refinement will provide an indication of when the refinement is approaching convergence. The process is summarised in Figure 2.1. As any move made in the refinement process depends purely on the current state, and not on any previous state, the process possesses the Markov property, and RMC belongs to the Markov chain Monte Carlo class of algorithms. As such it is a stochastic process that samples a probability distribution—the probability of the refined structure fitting the data. This has some important implications. The refinement will move towards the most likely state it can find within the time allowed for it to converge, which is often the state with the greatest entropy. This means that the final refined atomic configuration cannot be thought of as *the* 'solution', but more as *a* possible solution, that is consistent with the supplied data. It is best to think of it as a possible 'snap-shot' in time of the dynamic structure, not as a unique answer—there will be many equivalent structures

that can fit a particular PDF adequately well.

The desire for increased entropy also drives all refinements—to a greater or lesser extent—towards amorphisation, and additional constraints (besides the data) may be required to ensure that refinements remain physically sensible. Above all, structures produced should be scrutinised carefully to ensure that only reasonable trends and patterns are being inferred from the results. The technique is not without its limitations, but can provide extremely useful insights into the inner workings of unusual materials if used properly, and results are in good agreement with other techniques.

2.3.2 Particulars of RMCProfile

RMCProfile [71] is a sophisticated implementation of the RMC algorithm, which has been extended and improved on numerous occasions. As outlined above, the principal modification is that it deals explicitly with Bragg scattering data, meaning that it is sensitive to the average distribution of atoms as well as the local correlations between them. Other forms of total scattering data in both real and reciprocal space can be treated simultaneously with this Bragg data. Other modifications include: the incorporation of molecular constraints, which act to reduce the likelihood of a refinement causing excessive distortions to certain features of the structure; the ability to model the spin distribution of magnetic materials; the ability to model materials that include an element of site disorder, for example cation disorder or vacancy inclusion, through the addition of a 'swapping' move; the ability to fit to a variety of data types, such as neutron, X-ray and XAFS data; and the ability to calculate bond valence sums, and include them in the refinement process [71, 180].

Here we will provide an introduction to the main files, commands and options available when running a refinement, in order that the reader will have a basic understanding of the program when it is referred to in future chapters. For a full description of the program and how to run it please refer to the RMCProfile User Manual.

2.3.2.1 Essential Components

Below are outlined the principal files and commands involved in a refinement.

Input File This file, with extension '.dat', contains all the input commands required to run a refinement, as well as some metadata.

Configuration File The configuration file contains the coordinates of the all the atoms present in the refinement, and the cell dimensions. It provides the starting coordinates at the beginning of the refinement, and is updated as the refinement progresses.

Data File(s) The data files provide the data sets utilised during the refinement. These may be for real or reciprocal space data. Generally a simply x–y format will suffice. The refinement of Bragg data requires additional information about the background and instrument parameters, provided in separate files.

Out Files The calculated fits to the experimental data sets are printed in two files: the Bragg fit in one file, and all others in a separate file. Partial structure factors and PDFs are also printed where relevant.

Log File A summary of the refinement progress will be printed to screen. Alternatively this is written to a log file for future reference. Information including refinement duration, χ^2s, number of moves accepted and time per move is updated regularly to allow the user to track the progress of a refinement.

Key Commands The `TIME_LIMIT` keyword sets the duration for which the refinement is allowed to continue.[¶]

Atoms are prevented from moving too close to one another by setting the closest approach distances for each pair of atom types.

The maximum distance that an individual atom may travel during a single move is set using the `MAXIMUM_MOVES` keyword. This prevents improbably large moves disrupting a refinement. It may be sensible to vary the maximum move distance for each atom such that heavy elements do not travel as far as light elements, to replicate the expected variation in atomic displacement parameters.

The significance attributed to each data set is set by the weightings commands. These act like the error associated with each data set, so that the larger the value, the less significance ascribed to the fit to that data set.

[¶]When monitoring a refinement, however, it is better to think in terms of the number of moves that have been accepted in relation to the total number of atoms.

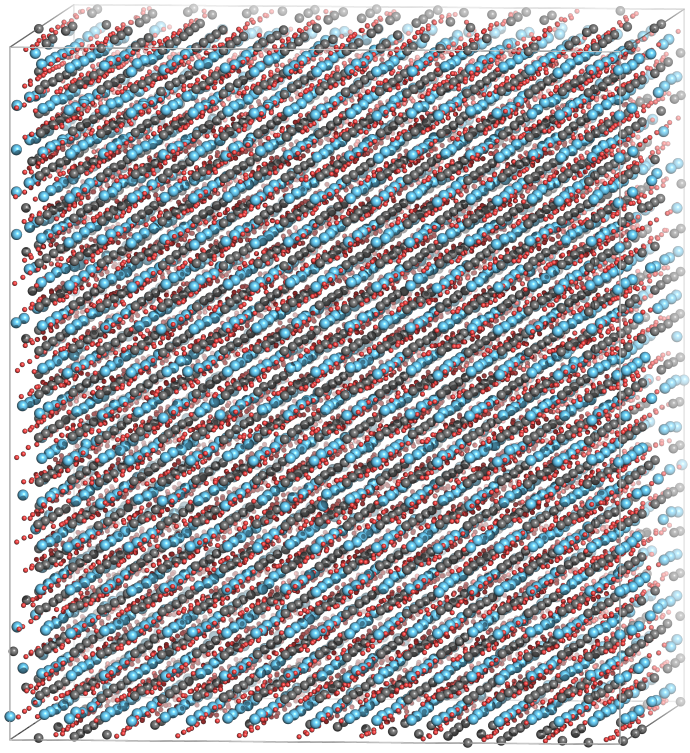

Figure 2.2: An example of a refined RMC configuration to demonstrate the typical size of a structural model. Here $LaMnO_3$ at 753 K is shown, with La atoms coloured in blue, Mn atoms in grey, and O atoms in red. The $10 \times 10 \times 8$ supercell has a side length of roughly 55 Å, a volume of 1.96×10^5 Å^3, and contains 16 000 atoms.

2.4 RMCProfile Code Development

As outlined above, RMCProfile includes many features, including the ability to model magnetic scattering, and to model substitutional disorder. These features had not, however, all been extensively used, and the magnetic and substitutional features had not been used together. In fact it was realised that the code had not been properly written to allow substitution of different magnetic atoms. There was a need to modify the code to allow this, and to test this on a real system. This was carried out as part of this thesis, and Fe_3O_4 was used to check that the program performed as expected.

There follows in this section an explanation of the formalisms used in both magnetic refinements and refinements that include substitutional disorder, and then a discussion of the changes made to allow both to be used simulataneously.

2.4.1 Magnetism

The magnetism code works by maintaining an ordered list of spin vectors that correspond to the list of atomic coordinates used for the rest of the refinement. In other words, the n^{th} spin vector listed corresponds to the n^{th} atom listed. An implication of this is that the magnetic atoms in the structure must be listed first in the refinement files.

Magnetic spins are represented as a point on the surface of a sphere of unit radius (they are scaled appropriately when fitting to data). Spin moves occur in the refinement by adding a randomly generated vector to this point, and then projecting the resultant vector back onto the surface of the sphere, to produce a new spin orientation. The maximum size of the randomly generated vector is defined by the user, and it is sensible for this value not to exceed 0.1 in order to prevent overly large moves from occurring.

The magnetic contribution to the total scattering, S_{mag}, can be obtained from a spin configuration using the following equation [121, 181]:

$$\begin{aligned} S_{\text{mag}}(Q) =& \frac{2}{3} c_{\text{M}} \left[\frac{e^2 \gamma}{2 m_{\text{e}} c^2} \mu f(Q) \right]^2 + 4\pi\rho c_{\text{M}} \left[\frac{e^2 \gamma}{2 m_{\text{e}} c^2} f(Q) \right]^2 \\ & \times \int r^2 \left\{ A(r) \frac{\sin Qr}{Qr} + B(r) \left[\frac{\sin Qr}{(Qr)^3} - \frac{\cos Qr}{(Qr)^2} \right] \right\} \mathrm{d}r. \end{aligned} \tag{2.3}$$

Here c_{M} refers to the concentration of the magnetic species, μ is the magnitude of the magnetic moment, $f(Q)$ is the magnetic form factor, ρ is the number density of magnetic atoms, e is the electronic charge, m_{e} is the mass of an electron, c is the speed of light, and γ is the magnetic moment of a neutron. $A(r)$ and $B(r)$ are real space correlation functions, defined as:

$$A(r) = \langle \mu_y(\mathbf{0}) \cdot \mu_y(\mathbf{r}) \rangle \tag{2.4}$$

$$B(r) = 2\langle \mu_x(\mathbf{0}) \cdot \mu_x(\mathbf{r}) \rangle - \langle \mu_y(\mathbf{0}) \cdot \mu_y(\mathbf{r}) \rangle. \tag{2.5}$$

Essentially these describe the magnitude of the spin–spin correlation functions perpendicular and parallel to the vector between two atoms at $\mathbf{0}$ and $\mathbf{r}$, respectively. They can be easily calculated from the spin configuration used in the RMC refinement, and are analogous to the conventional pair distribution function.

The magnetic contribution to the Bragg scattering is obtained using another standard equation [182]:

$$I(\mathbf{Q}) = \frac{1}{N}\left|\sum_j \mathbf{q}_j p_j(Q)\langle\exp\left(i\mathbf{Q}.\mathbf{r}_j\right)\rangle\right|^2, \tag{2.6}$$

where N is the total number of atoms, and $\mathbf{q}_j$ is the magnetic interaction vector, given by

$$\mathbf{q}_j = \frac{\mathbf{m}_j}{m_j} - \frac{\mathbf{Q}(\mathbf{Q}\cdot\mathbf{m}_j)}{Q^2 m_j}. \tag{2.7}$$

Here $\mathbf{m}_j$ is the spin vector of magnetic species j. $p_j(Q)$ describes the magnetic scattering amplitudes, which are related to the the magnetic form factors, $f_j(Q)$, according to the following equation:

$$p_j(Q) = \frac{e^2\gamma}{2m_e c^2}\mu_j f_j(Q). \tag{2.8}$$

The magnetic Bragg intensities thus calculated can be easily combined with the nuclear Bragg intensities, and used to fit to the experimental data.

Refinement of magnetic data requires some modifications to the RMC process, besides simply the calculation of magnetic scattering intensities. Generation of a spin move will have no impact on the nuclear scattering contribution to the fit, so will not require this to be recalculated. Generation of a translational move of a non-magnetic atom will similarly not affect the magnetic scattering pattern. However, a translational move of a magnetic atom will require the magnetic scattering to be recalculated, as the distances between spins will have changed. An efficient RMC program should be sensitive to these distinctions, to ensure the necessary calculations are performed for a successful fit to be achieved, without processor time being taken up by unnecessary steps.

2.4.2 Substitutional Disorder

The modelling of substitutional disorder is achieved by introducing a third type of move into the refinement process—a 'swap' move. For this move, an atom is randomly selected from the first of two user-defined atom types and swapped with a randomly selected atom of the second type. The atom histograms and neighbour lists must then be appropriately updated. If the move is not accepted then everything must be

returned to its initial state. The nature of the process means that no new formalisms are introduced, it is simply careful bookkeeping that is required.

We note in passing that the swap move has the potential to be quite disruptive to a refinement, especially if the two atom types involved have quite different scattering strengths, and consequently it is not uncommon for very few swap moves to be accepted. As a result, both the initial distribution of different atom types as well as the refinement strategy need to be considered carefully.

2.4.3 Unification of Magnetism and Substitutional Disorder

Updating the code to allow successful swapping of magnetic atoms required extensive iterations of testing and modifying the code. Simple refinements were tried first, building up in complexity, in order to isolate the effects of different parts of the code. The refinements were kept short–of the order of a few hours at most—and the time per generated move was monitored, together with the χ^2 value, the accuracy of numerical values, and the scaling of data sets. Where errors occurred, they were traced back to source by printing the appropriate values before and after each section of code, allowing the cause to be identified.

Simple refinements of magnetic systems were tried first, using parallel refinements of Fe_3O_4 and MnO data sets as a consistency check. Once it was established that these performed as expected, the process moved on to refining the magnetic structure of these systems. Next simple refinements using swap moves without any magnetism were tested to ensure the correct treatment of histograms and neighbour lists. A useful check was that the acceptance rate for swap moves involving the same type of atom was 100 %. Finally, refinements involving the swapping of magnetic atoms were tried.

A simplified schematic of the RMCProfile refinement process is shown in Fig. 2.3, with modified sections of the code highlighted in red. The changes made to each section will now be described.

Magn_write_bragg_form_facs subroutine This was adapted so that the same peak cutoff used for nuclear scattering is used for magnetic scattering too. Previously this had calculated magnetic peaks to much higher Q values. This change prevents

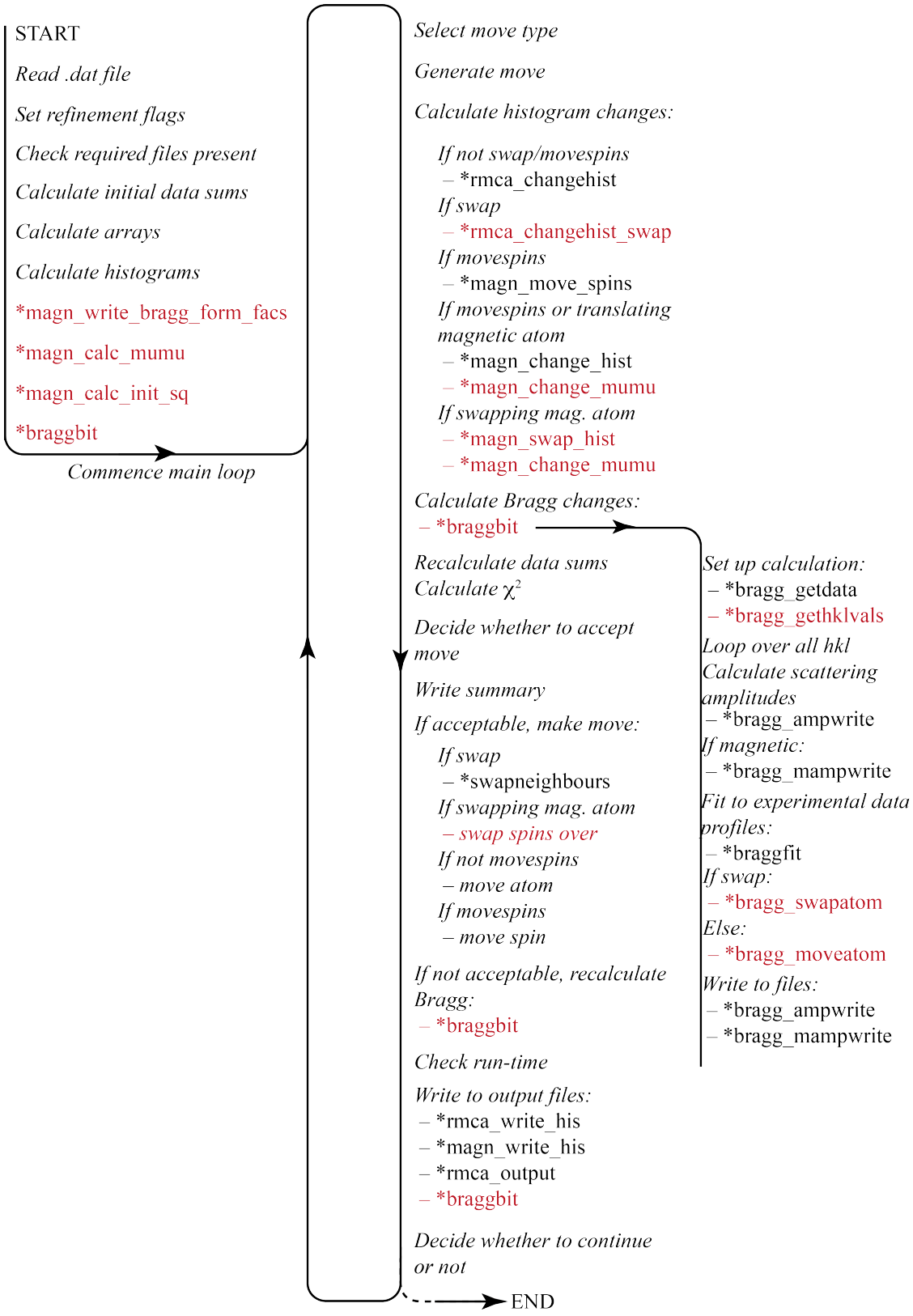

Figure 2.3: Simplified schematic of changes made to RMCProfile code. Subroutines denoted by Roman font and asterisk. Altered sections coloured red.

an excessive number of magnetic peaks being calculated, which can slow down a refinement.

Magn_calc_mumu and Magn_change_mumu subroutines These were altered so that they correctly handle multiple types of magnetic atom.

Magn_calc_init_sq subroutine This subroutine was created to increase the speed of a refinement, by calculating and storing certain values once at the start of the refinement, so that they do not have to be read in or calculated at future points of the refinement by the "Magn_calc_sq" subroutine.

Rmca_changehist_swap subroutine Alterations were made to ensure that the correct protocol was in place to deal with swapping magnetic or non-magnetic atoms, as well as to speed up the refinement process.

Magn_swap_hist subroutine Corrections were made to process for updating magnetic histograms during swapping moves, and to increase the precision of calculations.

Bragg_gethklvals subroutine This was extended to include the calculation of magnetic form factors.

Bragg_swapatom subroutine Previously this subroutine did not include any consideration of magnetic scattering: this was added, and steps taken to improve the calculation precision.

Bragg_moveatom subroutine This subroutine was altered to increase the precision and efficiency of the calculations.

Main loop Changes were made here to the way in which magnetic atoms are swapped—in particular, regarding whether spin orientations should be swapped as well as atom positions. It was decided that spins should remain attached to the atom site rather than the atom type, because— as mentioned above—the large disruption often associated with swap moves can mean that few are accepted. This decision

regarding the spins was in part an attempt to minimise this disruption to the magnetic scattering functions, as well as recognition that spin orientations are heavily influenced by their neighbours.

The result of these changes is that the code will now successfully refine magnetic systems where substitutional disorder is involved, and in particular, where substitutional disorder of magnetic atoms is involved. This updated program has been used to perform a refinement of Fe_3O_4, described in detail in Chapter 5.

Chapter 3

Apical Oxygen bonding in $YBa_2Cu_3O_{7-x}$

We start the experimental section of this thesis with a system that demonstrates the sensitivity of the RMC technique to subtle structural distortions, and its ability to produce structural models consistent with a variety of results that may at first seem incompatible.

3.1 HTSC and YBCO

Superconductivity is the unusual phenomenon whereby a material conducts electricity without any energy loss. First observed in mercury below 4 K by Kamerlingh Onnes in 1911 [183–185], the field has been growing ever since, incentivised by the prospect of a new era of efficient devices. The obstacle has always been the low temperatures normally required for this behaviour to be allowed—below ∼130 K—and the goal has been to produce materials with ever higher transition temperatures. The biggest jump came with the discovery of the cuprate superconductors. These were first observed by Bednorz and Müller in 1986 [186][†], and they have received much attention ever since. $YBa_2Cu_3O_{7-x}$ has become in many ways the canonical high temperature superconductor, largely because it was the first material to be discovered that had a critical temperature above the boiling point of liquid nitrogen [187], which brought huge practical benefits. Even amidst the rise of the pnictide superconductors [188],

[†]For this work they were awarded the Nobel Prize in Physics in 1987, a remarkably short time period between discovery and award, reflecting the significance of this class of materials.

it is still of significance in the condensed matter physics community today, with a recent resurgence of interest in the cuprates [189–191].

So far the only microscopic theory of superconductivity to emerge is that of Bardeen, Cooper and Schrieffer [192–194]. The main premise is that an attractive force causes electrons to pair up into so-called 'Cooper pairs', which then behave as composite bosons, and may condense into the ground quantum state. This creates a gap in the allowed energy states, preventing small excitations that cause scattering of electrons, and the phenomenon of superconductivity is observed. This theory works well for conventional superconductors, where the attractive force is brought about by electron–phonon coupling, but fails to describe certain features of the cuprates (often described as 'unconventional' superconductors), for example the unusual isotope effect observed [195–197]. While it is generally believed that Cooper pairs are still responsible for mediating superconductivity in these materials [198], the cause of the attractive force is still being investigated [199–201].

Many mechanisms have been proposed, including charge localisation (*e.g.* in the form of "stripes") [202], electron-phonon coupling [203], or bipolaron formation and condensation [204]. Crucial to establishing a suitable model for this behaviour is to have a well developed model of the structure. Local structure probes, such as EXAFS and PDF methods, would be expected to help in this effort, and in particular could bring sensitivity to any lattice distortions that might be present. However previous studies have often presented results that appear contradictory to other average structure studies, causing controversy.

For the specific case of YBCO the controversy has centred on the Cu2–O4 bond, significant in the structure as it connects the Cu–O "planes"—thought to be important for conduction—with the Cu–O "chains"—thought to be important as charge reservoirs [Fig. 3.1] [205]. X-ray absorption studies [206–211] suggested that this apical oxygen sits in a double well potential, which has clear implications for charge localisation and electron-lattice coupling. However this has been in clear disagreement with both single crystal [212, 213] and powder diffraction [214–217] experiments, which do not find any evidence of site splitting for either the Cu2 or O4 atoms, and while neutron PDF studies could obtain improved fits for models that included a bimodal distribution of Cu2 atoms, they dismissed a splitting on the O4 site [218, 219].

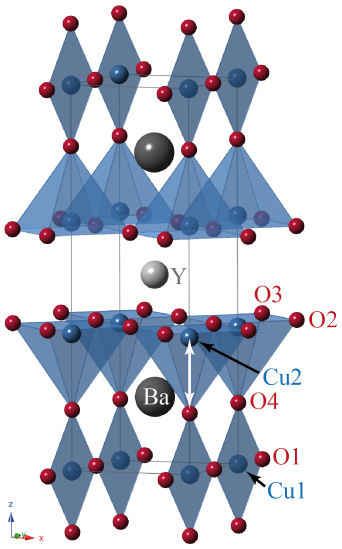

Figure 3.1: The unit cell of $YBa_2Cu_3O_{7-x}$, with the key Cu2–O4 bond highlighted in white.

Ab initio calculations [220] also tried to replicate the double well potential, but failed, although inelastic neutron scattering studies have observed increased sensitivity of the dynamic scattering function $S(Q, E)$ in the region of T_c and attributed it to structural instabilities involving the Cu2-O4 bond [221].

The work presented here attempts to reconcile these apparent contradictions. The RMC refinement method is used, distinguishing this work from the previous PDF studies of Refs. 218, 219 by including average structure data in the refinement process, which automatically results in a structure consistent with all length scales, and by allowing more sophisticated multi-atom correlations to be investigated. The principal result is that a bimodal Cu2–O4 bond length distribution is present in the structure, but correlations in the displacements of these atoms mean that each site remains unimodal. This explains the double well potential observed by EXAFS studies, while still being consistent with the average structure studies.

3.2 Experimental

3.2.1 Sample Preparation

A 2.5 g sample of $YBa_2Cu_3O_{7-\delta}$ was prepared using the citrate gel method described in Ref. 222. Y_2O_3 (99.999%, dried at 900 °C), $BaCO_3$ (99.997%) and CuO (99.9999%)

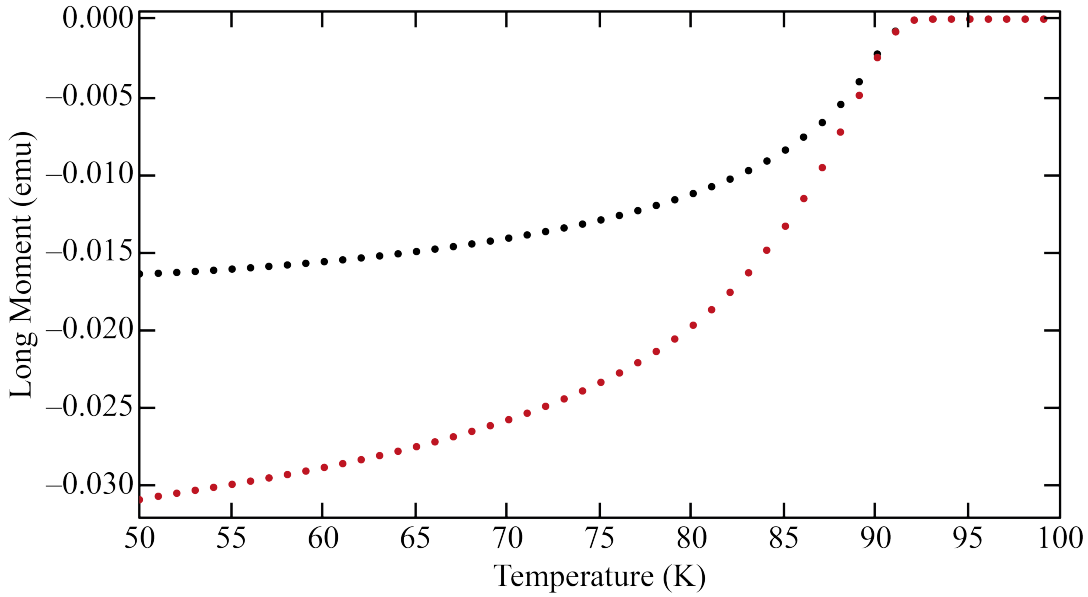

Figure 3.2: SQUID magnetometry data for $YBa_2Cu_3O_{6.93}$, showing field-cooled (black) and zero-field-cooled (red) curves. Collected in a 100 Oe field.

were combined in a suitable stoichiometric ratio, and dissolved in a minimum volume of 6 M nitric acid. Four mole equivalents of citric acid, together with 4 ml of ethylene glycol, were added and the resultant mixture heated with continuous stirring. Once the reaction was complete the gel formed was ground to a fine powder, placed in a Ni foil-lined crucible, and pyrolysed in air at 600 °C. Ni foil was used to line all alumina ovenware for subsequent heat treatment to prevent sample contamination. The powder was then reground and pressed into 13 mm diameter pellets under a weight of 5 tonnes, then heated to 920 °C under flowing O_2 before being cooled to room temperature at a rate of 1 °C min^{-1}; this process was repeated three times. Finally the sample was reground and fired for 12 hours at 600 °C under flowing O_2 to produce a sample with as high an oxygen content as possible. Iodometric analysis established that $\delta = 0.07(3)$, giving a final stoichiometry of $YBa_2Cu_3O_{6.93}$.

X-ray powder diffraction was used to confirm phase purity, and refined lattice parameters were found to be in good agreement with previously published values. SQUID magnetometry was used to determine the superconducting transition temperature, which was measured as $T_c = 92(1)$ K [Fig. 3.2].

3.2.2 Data Collection

Total scattering data were collected on the GEM diffractometer at the ISIS pulsed neutron and muon source [20–22]. 1.8 g of the sample described above was placed in a thin-walled, 3 mm diameter vanadium can of 5.8 cm height, and a closed cycle helium refrigerator was used to cool the sample to 50 K, *i.e.* below the critical temperature. Total scattering data were collected over a wide range of scattering vectors, covering $0.7 \leq Q \leq 50\,\text{Å}^{-1}$. This corresponds to a real space resolution of approximately $\Delta r \simeq 3.791/Q_{\text{max}} \simeq 0.08\,\text{Å}$.

Standard data correction methods were applied, which accounted for the effects of background scattering, multiple scattering within the sample, absorption, beam intensity variations, and the Placzek inelasticity correction [7]. These were implemented using the Gudrun software package [223]. The corrected data were converted into experimental $F(Q)$ and $G(r)$ functions, as described in § 1.1.1. A Q_{max} of $40\,\text{Å}^{-1}$ was selected, as it was found that this value gave the most reliable $G(r)$ function. Three sets of Bragg profile functions were extracted for use with the GSAS rietveld refinement program [224], corresponding to detector banks centred on scattering angles of $2\theta = 63.62°, 91.37°$ and 154.46°. The data fitting processes used are described in full in the following section.

3.2.3 Structure Refinements

Rietveld average structure refinements were performed using the General Structure Analysis System (GSAS) package [224] using the structural model published in Ref. [225] as a starting point. The primary purpose of the Rietveld refinements was to confirm that our data produced a sensible average structure, with lattice parameters, atomic coordinates and anisotropic displacement parameters that are consistent with previously published results. The secondary purpose was to use this sensible average structure—consistent with our data—as a starting point for our RMC refinements. Three instrument banks were used in the refinements to provide coverage of all the principal structural peaks, while also including an adequate amount of the higher angle peaks. The final fit gave residuals $wR_p = 0.0207$ and $R_p = 0.0218$. The fits to the separate banks are shown in Fig. 3.3, and the refined cell parameters are listed in Table 3.1.

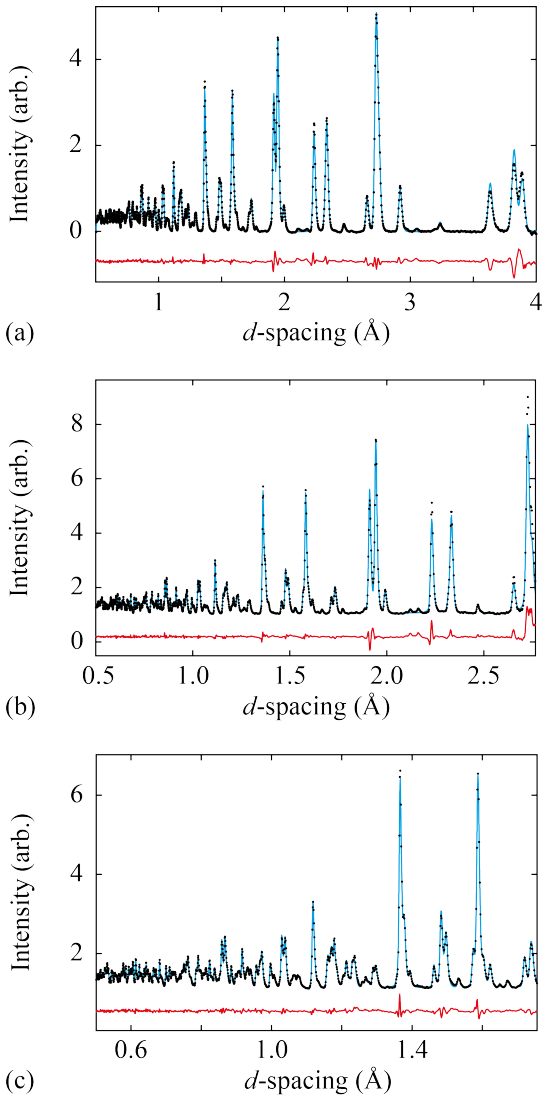

Figure 3.3: Rietveld refinement fits for the three separate GEM detector banks used. (a) Bank 4, $2\theta = 63.62°$; (b) Bank 5, 91.37°; (c) Bank 6, 154.46°. Instrument resolution is reduced at the low-angle end of the bank, leading to poorer fits of the high d-spacing peaks in some cases. In each instance, data are shown as filled black circles, fits as blue lines, and the difference curves (data–fit) as red lines shifted vertically for clarity.

Table 3.1: Crystallographic parameters, atomic coordinates and isotropic equivalent displacement parameters determined from Rietveld refinement.

Crystal system		Orthorhombic		
Space group		$Pmmm$		
a (Å)		3.81412(5)		
b (Å)		3.87694(6)		
c (Å)		11.63970(22)		
V (Å^3)		172.117(3)		
Z		1		
T (K)		50		
Atom	x	y	z	U_{iso} (Å^2)
Y	0.5	0.5	0.5	0.0031(4)
Ba	0.5	0.5	0.18377(12)	0.00092(26)
Cu1	0	0	0	0.0038(4)
Cu2	0	0	0.35535(9)	0.0019(8)
O1	0	0.5	0	0.0115(7)
O2	0.5	0	0.37837(13)	0.0045(4)
O3	0	0.5	0.37727(15)	0.0020(4)
O4	0	0	0.15879(11)	0.0047(4)

RMC refinements were carried out using the program RMCProfile [71]. Starting configurations were created from $24 \times 24 \times 8$ supercells of the final GSAS-refined structure. These contained 59 904 atoms and were approximately cubic with a side of roughly 90 Å in length. As the value of δ in the sample was small, and to avoid the risk of introducing bias to the model, no oxygen vacancies were created in the structure, and the refinements assumed a stoichiometry of $YBa_2Cu_3O_7$, *i.e.* $\delta = 0$.

To prevent the formation of amorphous regions in the refinement, distance window constraints were employed: these are listed in Table 3.2. Structures were refined against Bragg, $F(Q)$, and $G(r)$ data sets, with an additional $G(r)$ data set covering the first 7 Å used to increase the importance of this region during the fitting process. Example fits are shown in Fig. 3.4. The weightings attached to each data set are shown in Table 3.3. The detector bank number 4 data set was selected for use as the Bragg component of the RMC refinement, as this provided the largest d-spacing peaks for constraining the average structure during the refinement.

The "save_configurations" option was used to collect multiple configurations from each refinement, with a print period of every 333 334 moves used to ensure that

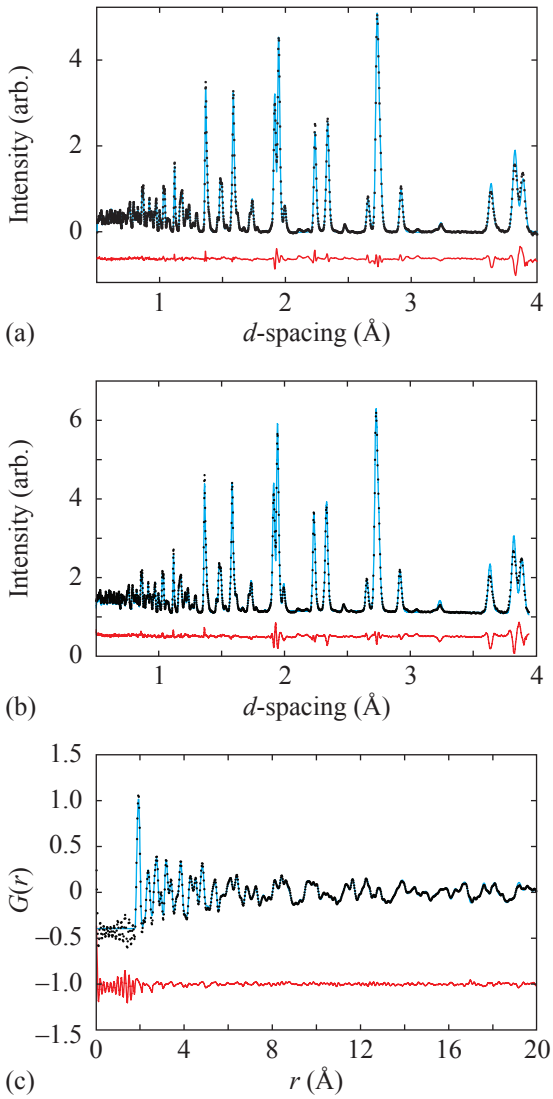

Figure 3.4: Fits obtained for neutron powder diffraction data for (a) Rietveld refinement, and (b) RMC refinement. The corresponding RMC fit to $G(r)$ data is shown in (c). In each instance, data are shown as filled black circles, fits as red lines, and the difference curves (data–fit) as blue lines shifted vertically for clarity.

Table 3.2: Distance window parameters $d_{\min}$ and $d_{\max}$ used in RMC refinements of $YBa_2Cu_3O_7$. The final refined peak positions and standards deviations are given by $\bar{d}$ and $\sigma(d)$ respectively.

Atom pair	d_{min} (Å)	d_{max} (Å)	$\bar{d}$ (Å)	$\sigma(d)$ (Å)
Y–O2,3	2.10	2.56	2.38	0.07
Ba–O	2.50	3.50	2.76	0.13
Cu1–O1	1.73	2.10	1.93	0.06
Cu1–O4	1.73	2.50	1.84	0.04
Cu2–O2	1.73	2.10	1.93	0.06
Cu2–O3	1.73	2.10	1.93	0.06
Cu2–O4	1.73	2.50	2.29	0.06

Table 3.3: The weighting parameters attached to each data set used in RMC refinements, as described in § 2.3.2.1.

Data set	Weighting
Bragg	0.005
$F(Q)$	0.005
$G(r)1$	0.005
$G(r)2$	0.002

each configuration saved was distinct. The total run time for each refinement was 8 000 mins, allowing between 7 and 10 configurations to be saved[‡].

3.3 Results

3.3.1 Average Structure

The first analysis of the results consisted of checking the average structures produced by both Rietveld and RMC refinements, to ensure consistency both between the two and with external studies. The structural parameters and coordinates of the GSAS refinement are given in Table. 3.1, and agree well with previously published studies of near-stoichiometric YBCO [213, 216, 225]. The GSAS refined structure is shown in Fig. 3.6(a), alongside the RMC refined structure in section (b). As can be seen, there is good consistency between the atom positions and distributions between the

[‡]The exact number depended on the $Q_{\max}$ used. For reasons that will be discussed shortly, multiple refinements were run using $Q_{\max}$ values other than the optimum value of 40 $Å^{-1}$. Reducing the $Q_{\max}$ speeds up the calculation time, allowing more moves to be completed within the time limit, and hence more configurations to be saved; increasing $Q_{\max}$ has the opposite effect.

two refinements.

Some details of the Rietveld refinement should be mentioned here. It was possible to achieve a stable refinement of anisotropic displacement parameters for all atoms except Ba, for which an unconstrained refinement consistently produced non-positive values for the U_{22} parameter. This was consequently fixed at $0.001\,\text{Å}^2$. It is also noted that the O1 atoms (the 'chain' oxygens) have rather elongated ellipsoids in the x-direction. This has been reported previously in many studies [213, 219, 226] and is thought to be related to low-energy correlated displacements of the square CuO_4 units.

As the focus of this study is the Cu2–O4 bond distribution, further Rietveld refinements were performed to investigate the stability of split sites on either one or other or both of these atom positions. In agreement with previous attempts made by other studies [214–217], it was found that not one of these three refinements provided a stable refinement or gave an improved fit to the data.

The distribution of atoms in a RMC-refined structure is not constrained to follow an ellipsoidal pattern, allowing the atoms to take any form required by the data. This can act as a useful check to the presence or otherwise of site-splitting. In this case, by projecting the atom site distribution for the Cu2 and O4 atoms it is clear that both sites are unimodal, and well-fitted using a single Gaussian function, not two [Fig. 3.5]. This confirms that it is not necessary—or appropriate—to describe these atom positions in terms of split sites. An examination of the RMC-refined structure in Fig. 3.6(b) suggests that there may in fact be some site splitting for the O1 site. This is related to the elongated ellipsoids observed in the Rietveld refinement, and is likely associated with the postulated low-energy displacements.

3.3.2 Local Structure

Having ascertained that the average structure produced by the RMC refinements was sensible, attention was turned to what could be revealed about the local structure. The focus remained on the Cu2–O4 bonds, and the bond length distribution was calculated from the refined configurations. These were clearly bimodal, and well fitted using two Gaussian functions [Fig. 3.7(a), left]. The positions of these Gaussian functions implied the presence of 'short' Cu–O bonds of length 2.167 Å, and 'long'

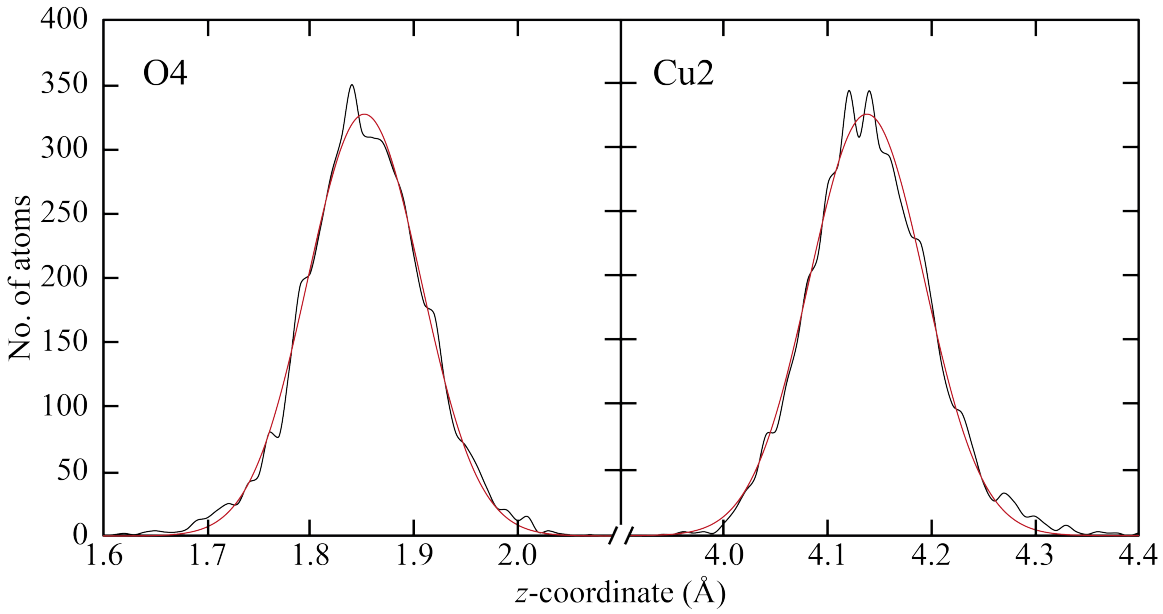

Figure 3.5: Atom site distributions (black) as a function of z-coordinate for the Cu2 and O4 atoms. The distributions are fitted with Gaussian curves (red), showing good agreement. Attempts to fit the distributions using two Gaussians always resulted in one Gaussian having essentially zero area.

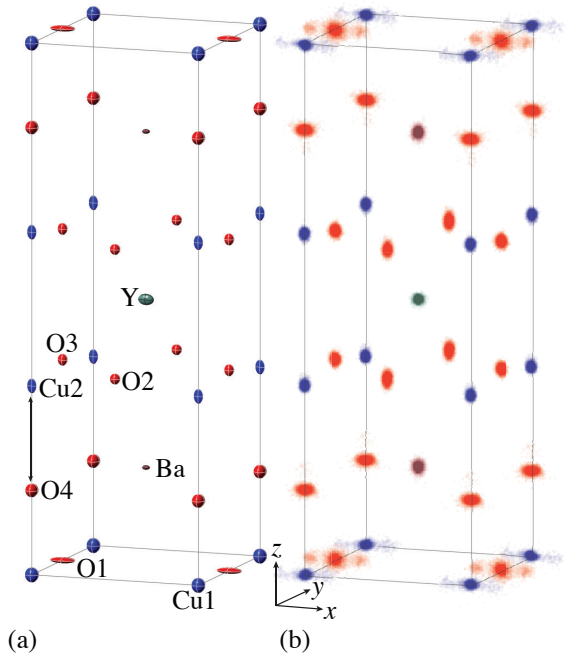

Figure 3.6: Refined structural models of $YBa_2Cu_3O_{6.93}$, produced from (a) Rietveld refinement, and (b) RMC refinement. The crucial Cu2–O4 bond is indicated by an arrow. Thermal ellipsoids in (a) are shown at 80% probability. The representation in (b) is produced by projecting an entire RMC configuration onto a single unit cell and building intensity where most atoms are found.

bonds of length 2.307 Å, which agrees remarkably with the values obtained in the EXAFS study of Ref. 210, of 2.220 Å and 2.337 Å.

The experimental $G(r)$ function was examined to determine the origin of this splitting in the refinement. A clear peak can be observed at the appropriate distance, and an examination of the partial pair distribution functions shows that only the $g_{\mathrm{Cu2,O4}}(r)$ function is non-zero in this region [Fig. 3.8(a)]. All other Cu–O bonds are much shorter—contributing to the main peak at around 1.9 Å—and do not stray into this area. While there is some overlap at larger distances with the Y–O2/Y–O3 partial PDFs, they have essentially zero intensity for $r < 2.20$ Å, despite the distance window constraints allowing them to occupy the regions as low as 2.10 Å. This establishes that—providing this feature in the data is real—the intensity in this region of the PDF is correctly attributed as a separate distribution of short Cu2–O4 bonds.

This now required a demonstration that this feature *was* real, the concern being that its magnitude is comparable to that of Fourier truncation ripples often found at low r values. While such ripples are strongest at the very lowest r values (and most noticeable in the region before the first peaks appear) they are found throughout the PDF to a greater or lesser extent, and it is inescapable that a RMC refinement will fit some intensity that has no physical origin. Generally these ripples are small compared to the principal peaks in the PDF, and the presence of other data sets in the fitting process helps to reduce their significance in the overall refinement. However in a situation such as this, where a small feature of the pattern is of great importance, it is worth assessing the impact that Fourier truncation ripples have. This was achieved by performing a series of refinements using different values of Q_{max}, the highest value of Q used when calculating the $G(r)$ function. Q_{max} has a strong influence on the positions and magnitudes of Fourier ripples, but does not greatly affect real features in the same way, though a lower value of Q_{max} will result in a lower resolution.

Eleven sets of refinements were performed using Q_{max} values at evenly-spaced intervals ranging from 30 Å^{-1} to 50 Å^{-1}. The modified $G(r)$ data sets are shown in Fig. 3.8(b). At least seven independent configurations[§] were collected for each Q_{max} value using the `SAVE_CONFIGURATIONS` option.

[§]Configurations used were separated by at least $140\,000 = 59\,904 \ln 10$ accepted moves.

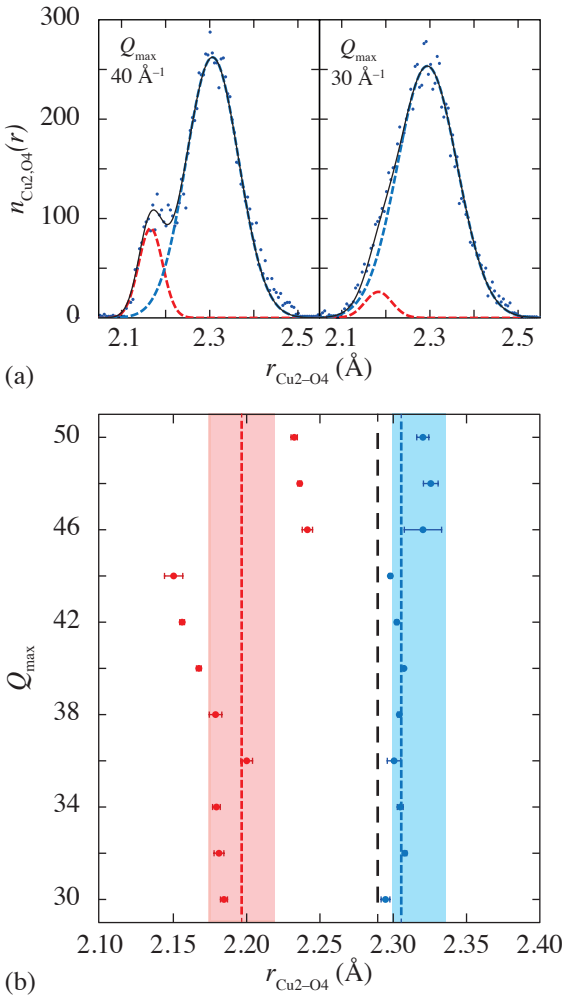

Figure 3.7: (a) Cu2–O4 bond histograms (solid points) determined by RMC refinements against $G(r)$ functions generated for maximum scattering vectors of (left) $Q_{\mathrm{max}} = 40\,\mathrm{Å}^{-1}$ and (right) $Q_{\mathrm{max}} = 30\,\mathrm{Å}^{-1}$. These two distributions correspond respectively to the most and the least convincing bimodal distributions obtained for the 11 different Q_{max} values investigated. Calculated fits using a pair of Gaussian curves are shown as a solid line, with the two individual Gaussian contributions shown as red and blue dashed lines. (b) Q_{max}-dependence of the 'short' and 'long' Cu2–O4 bond lengths (red and blue circles, respectively), determined as the midpoints of the corresponding Gaussian fits. Error-weighted averages are plotted as vertical red and blue dashed lines. The range of values obtained using EXAFS in Refs. 208, 210 are shown as shaded regions, with the Rietveld Cu2–O4 bond length value shown as a bold black dashed vertical line.

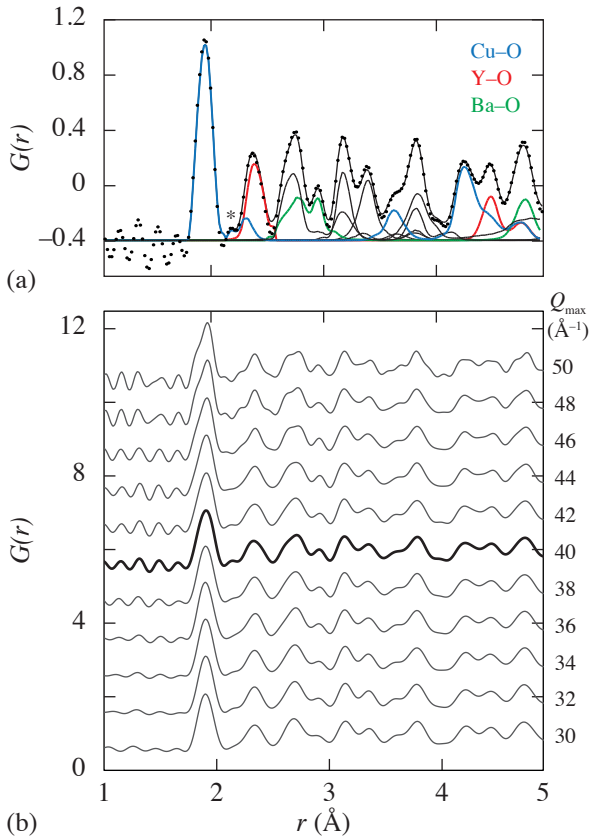

Figure 3.8: (a) Experimental $G(r)$ function (filled circles) and corresponding RMC fit (solid black line). The relative contributions to the RMC fit arising from the various partial pair distribution functions are included, with those corresponding to the Cu–O, Y–O and Ba–O pairs highlighted in blue, red and green, respectively. The experimental feature responsible for splitting the Cu2–O4 distribution is highlighted with an asterisk. (b) Experimental $G(r)$ functions generated using a range of Q_{max} values $30 \leq Q_{\mathrm{max}} \leq 50\,\mathrm{\AA}^{-1}$; the bold curve is that shown in (a).

Cu2–O4 bond length distributions were calculated for each of the eleven sets of refinements produced, and fitted with Gaussian curves as before. It was found that two Gaussian peaks were always required to adequately fit the distribution, and the peak positions never varied greatly from the EXAFS results of Refs. 208 & 210 [Fig. 3.7(b)]. Examples of this Gaussian fitting are given in Figure 3.7(a), where the most (left) and least (right) convincing fits are shown to demonstrate the variation observed. Good consistency was also found in the widths and areas of the peaks, with variation of less than 10% across the set. It should be noted though that values obtained for both the highest and lowest values of $Q_{\max}$ are expected to be less reliable than those in the middle of the set. For low values of $Q_{\max}$ the resolution is reduced, while for high values the PDF is greatly affected by Fourier ripples, diminishing the data quality.

The average bond lengths obtained from this analysis are presented in Table 3.5 and compared to the EXAFS results of Ref. 210. An error-weighted average across all eleven configurations gives the fraction of short Cu2–O4 bonds as being 12.3±2.8%.

To ensure consistency with previous PDF studies, further refinements were performed using PDFGUI, a small-box modelling program, often described as a 'real-space Rietveld' method. Split sites for either the Cu2 or O4 atoms in a single unit cell were refined against the $G(r)$ function for two different $r_{\max}$ values. Different $r_{\max}$ values were used as often short-range correlations have little impact in the PDF at larger distances, which can affect the success of a refinement. Four different values of $Q_{\max}$ were also used to establish the sensitivity of these results to the Fourier ripples. The results of this are given in Tables 3.4 & 3.5, and an example fit using $Q_{\max} = 25\,\text{Å}^{-1}$ data is shown in Fig. 3.9.

The previous study of Ref. 219 found that split sites could be refined for the Cu2 atom, but not the O4 position, and equated this to a difference Δd(Cu2–O4) between the short and long bonds of 0.18(6) Å. Here we also find that it is possible to refine split sites for the Cu2 atoms, with improved fits being obtained only when low values of $r_{\max}$ were used. In addition to this, it was also possible in some cases to refine a split site for the O4 atom, though this never resulted in a bond length difference greater than 0.05 Å.

Table 3.4: Free atom position parameters and Cu2–O4 bond lengths determined using various experimental techniques and refinement strategies.

	Rietveld		PDFGui		RMC	EXAFS
	this work	Ref. 213	this work	Ref. 219	this work	Ref. 210
z_{Ba}	0.18377(12)	0.18369(12)	0.1836(9)	0.1840(2)	0.18398(9)	–
z_{Cu2}	0.35535(9)	0.35464(8)	0.3570(49)	0.3548(2)	0.35580(7)	–
z_{O2}	0.37837(13)	0.37808(7)	0.378(3)	0.3780(3)	0.37701(11)	–
z_{O3}	0.37727(15)	0.37808(7)	0.378(2)	0.3782(3)	0.37805(8)	–
z_{O4}	0.15879(11)	0.15919(10)	0.15998(95)	0.1599(2)	0.15951(9)	–
$\langle d(\mathrm{Cu2–O4})\rangle$	2.2879(17)	2.2860(15)	2.268(14)	2.280(3)	2.2849(13)	–
$d(\mathrm{Cu2–O4})_{\mathrm{short}}$	–	–	2.20(10)	2.19(3)	2.197(10)	2.220(5)
$d(\mathrm{Cu2–O4})_{\mathrm{long}}$	–	–	2.29(10)	2.37(3)	2.306(3)	2.337(5)

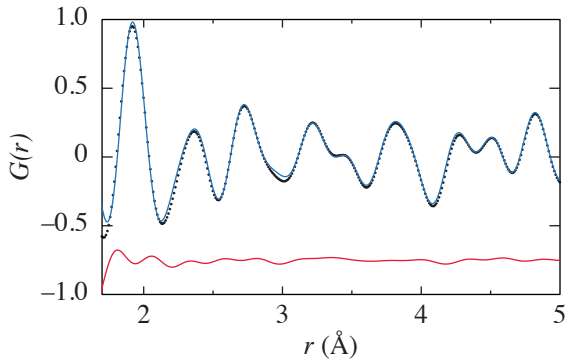

Figure 3.9: A typical fit to $G(r)$ data using PDFGUI, in this case using a $Q_{\max}$ value of 25 Å^{-1}.

Table 3.5: Differences Δd(Cu2–O4) between short and long Cu2–O4 bond lengths determined using r-dependent PDFGUI refinement of the experimental $G(r)$ functions generated for various $Q_{\max}$ values.

$Q_{\max}$ (Å^{-1})	$r_{\max}$ (Å)	Δd(Cu2–O4) (Å)	R_{ws}	R_{wu}
25	5	0.08(7)	0.0908	0.0935
	15	0.03(5)	0.0883	0.0901
30	5	0.089(26)	0.1224	0.1406
	15	0.03(6)	0.0941	0.0951
40	5	0.099(28)	0.1207	0.1267
	15	0.065(26)	0.1261	0.1276
50	5	0.093(22)	0.1863	0.1888
	15	0.008(4)	0.2146	0.2157

3.4 Discussion

The most significant result of this study is that a large-box RMC refinement fitting to both local and average structure data is able to account for a number of seemingly contradictory results:

i. That single crystal and powder diffraction experiments assert that the Cu2 and O4 atom sites are unimodal [212–217].

ii. That Cu K-edge EXAFS spectra are best fitted using a double well potential, implying two Cu2–O4 bond lengths [207–211].

iii. That PDFGUI refinements are best fitted using a split Cu2 site when $r_{\max}$ is small ($\simeq 5\,\text{Å}$), though this splitting disappears for larger $r_{\max}$ values [219].

iv. That the magnitude of the splitting is much larger than the U_{33} displacement parameter of the Cu2 atom.

In order to have consistency between both unimodal atom sites and a bimodal bond length distribution, it is necessary that the displacements of the Cu2 and O4 atoms are correlated during long and short bond formation. Specifically, formation of a long bond must involve displacement of the Cu atom in the $+z$ direction and the O atom in the $-z$ direction (with respect to the axes and highlighted bond in Fig. 3.6), and formation of a short bond requires coordinated displacements in the opposite directions. A model involving both split Cu2 and O4 atom sites would not be supported by a Rietveld refinement as the required displacements would be smaller than the magnitude of thermal motion, and so indistinguishable. Such a model would also produce a trimodal Cu2–O4 bond length distribution unless correlations were taken into account, and so would not be supported by the PDF results.

While the PDFGUI refinements successfully produce a bimodal bond length distribution, they do so in a way that cannot easily be resolved with the average structure results—having the Cu2 atom take up the entirety of the displacement would result in an unfeasibly large U_{33} parameter. The RMC refinement however, manages to resolve this issue by dividing the required displacement between the two sites, producing a structural model that is consistent with the average structure information.

To explore whether any spatial correlations were present amongst short Cu2–O4 bonds in the structure—for example, whether any tendency to cluster was present—a correlation function was defined as

$$\chi(r) = \frac{a_{\text{eff}}}{Nr} \sum_i \sum_j u_i u_j(r), \tag{3.1}$$

where

$$u_i = \begin{cases} +1 & d(\text{Cu2–O4})_i > d_{\text{c}} \\ -1 & d(\text{Cu2–O4})_i < d_{\text{c}} \end{cases}, \tag{3.2}$$

$a_{\text{eff}} = \sqrt{ab}$, the distance d_{c} is the critical Cu2–O4 bond length below which a bond is considered to be 'short', N is the number of Cu2 centres in a configuration, and the sums in Eqn. 3.1 are taken over all Cu2 centres i, j within the same [CuO_2] layer and separated by the distance r.

The unequal ratio of long and short bonds will lead to $\chi(r)$ being non-zero even for random distributions of short bonds, which could be misleading. To counter this a second correlation function was calculated, $\chi_{\text{rand}}(r)$, using the same set of u_i values as for $\chi(r)$, but with a randomised distribution. The difference function

$$\Delta\chi(r) = \chi(r) - \chi_{\text{rand}}(r) \tag{3.3}$$

was then used to examine the extent to which short Cu2–O4 bonds are more ($\Delta\chi(r) > 0$) or less ($\Delta\chi(r) < 0$) likely to cluster at a distance r than in a random configuration.

$\Delta\chi(r)$ was calculated for eight configurations and averaged to produce the final correlation function plotted in Fig. 3.10. As can be seen the variation in the function between data sets is of the same order of magnitude as the peaks themselves, meaning that little significance can be attached to them—indeed few peaks lie more than two standard deviations away from zero. This is shown clearly in Fig. 3.11. It is perhaps worth commenting though that any tendency for short Cu2–O4 bonds to cluster into pairs (hinted at by the positive peak at $r/a_{\text{eff}} = 1$) could be consistent with a bipolaron model of superconductivity, if accompanied by charge localisation [204, 227].¶

¶While it may be tempting to associate the two different Cu2–O4 bond lengths observed here with a change in valence state—and a difference in bond length of 0.11 Å may well be consistent with a change in Cu oxidation state—the neutron scattering data used here can give no information on the electronic structure of the material, so no further comment can be given in this regard.

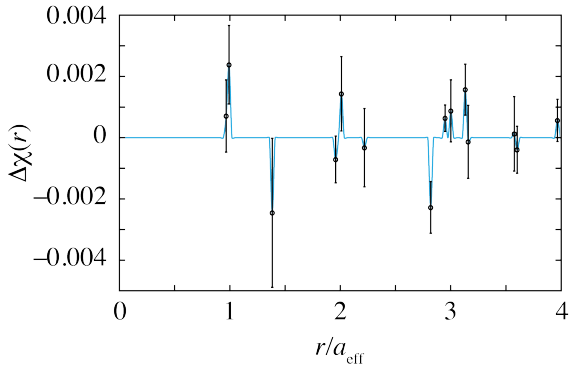

Figure 3.10: The short-bond/short-bond correlation function $\Delta\chi(r)$ calculated for eight RMC configurations and then averaged. For ease of interpretation, the horizontal axis corresponds to interatomic distances scaled relative to the average in-plane lattice parameter. The positive peak at $r/a_{\mathrm{eff}} = 1$ indicates that short apical Cu2–O4 bonds may prefer to form neighbouring pairs.

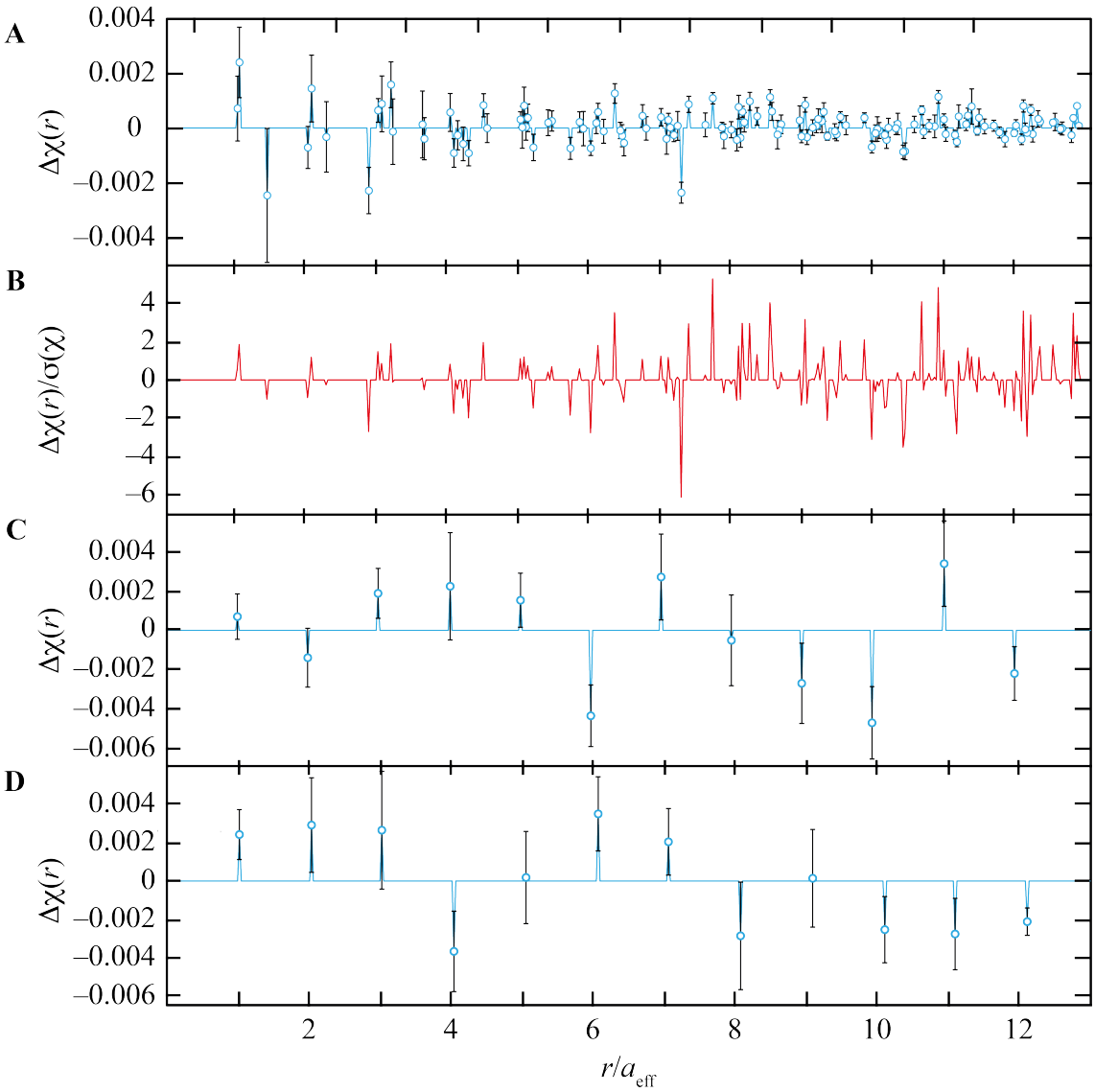

Figure 3.11: A: The correlation function $\Delta\chi(r)$ plotted out to $r/a_{\text{eff}} = 13$. B: A plot of the correlation function divided by its standard error, to give an indication of the significance of each peak. To investigate whether any significant anisotropy was present the equivalent one-dimensional correlation function was calculated along (C) the x-direction, and (D) the y-direction.

3.5 Conclusions

In conclusion, neutron total scattering data collected for a sample of $YBa_2Cu_3O_{6.93}$ have been used to drive a combination of Rietveld average structure refinements, and both large- and small-box local structure refinements. The results have been shown to be consistent with previously published work across all length scales. RMC refinements benefit from fitting a large structural model to both local and average structure data sets simultaneously, and in doing so have managed to resolve seemingly contradictory results in the literature. The sensitivity of the RMC technique to subtle structural features linked to charge disproportionation has also been demonstrated, though the potential hazards of artefacts in the data, such as Fourier truncation ripples, have been highlighted.

Two lengths of apical Cu2–O4 bonds have been identified: a short bond of length 2.197(10) Å, and a long bond of 2.306(3) Å. No strong evidence of clustering of the short bonds within layers has been found.

Future work could involve trying to introduce vacancies into the refinement configuration, to better replicate the stoichiometry of the sample, and the effects of these vacancies on the location of long and short bonds could also be explored. A variable composition study could provide interesting information on how the structure changes with oxygen content. The behaviour of the CuO_4 chain units could also be investigated, to try to identify the cause of the elongated displacement parameters of the chain oxygens.

Chapter 4

Jahn-Teller Symmetry Switching in $LaMnO_3$

We move on now to a more complicated system involving an orbital order–disorder transition.

4.1 CMR and $LaMnO_3$

The story of $LaMnO_3$ in the field of solid state physics is inextricably linked to that of the doped manganites, and their unusual magnetic behaviours. Chief among these is the phenomenon of colossal magnetoresistance (CMR), whereby the electrical resistivity of a material undergoes an order of magnitude change upon application of an applied magnetic field [Fig. 4.1]. $LaMnO_3$ is the parent compound of several CMR families, including the series $La_{1-x}A_xMnO_3$, where A = Ca, Sr, Ba. Indeed when CMR was first discovered back in the 1950s, it was in doped lanthanum manganites [228], and they have remained the focus of a large proportion of the subsequent work on CMR [229–233].

The material has the perovskite structure, with an array of corner-sharing MnO_6 octahedra surrounding the larger La^{3+} cations [Fig. 4.2] [235]. Tilting of the octahedra results in an orthorhombic structure of space group *Pbnm* under ambient conditions. At low temperatures it has an antiferromagnetic structure with a Néel temperature of 141 K [236]; however it is the higher temperature phase transitions that are the focus of this study, and in particular the orthorhombic–pseudocubic transition that occurs at ~ 750 K, widely viewed to be the canonical orbital order–disorder transition [102, 235, 237]. Such a transition precedes CMR itself within the doped manganites [105,

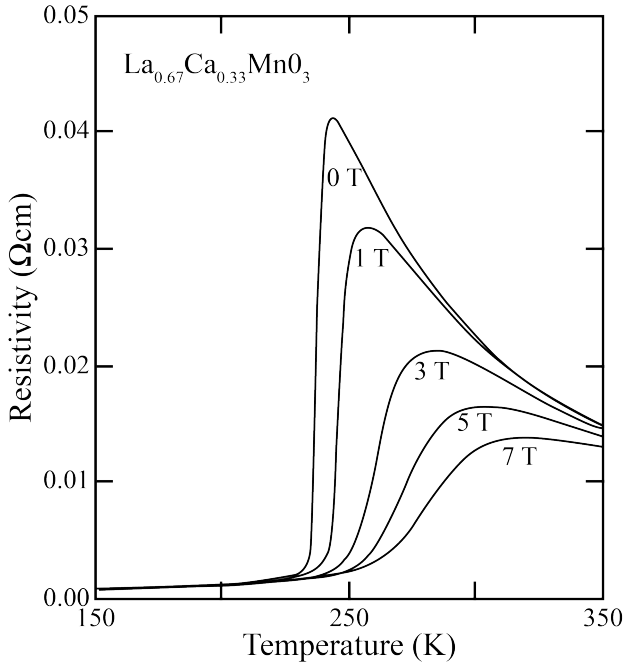

Figure 4.1: When optimally-doped $La_{1-x}Ca_xMnO_3$ is subjected to strong magnetic fields, the resistivity changes dramatically. Figure adapted from Ref. 234.

238, 239], and is implicated more generally in charge and orbital ordering processes in a variety of other functional condensed phases [240–242].

The issue of orbital order in $LaMnO_3$ arises fundamentally from the degeneracy of the Mn^{3+} t^3e^1 d-electron configuration [237]. This degeneracy is lifted by a JT distortion of the $[MnO_6]$ coordination environment, which acts to couple Mn–O bond displacements with orbital occupancies, and hence structural and electronic degrees of freedom [243]. Crystallographic measurements of $LaMnO_3$ performed under ambient conditions indicate that these distortions (and consequently orbital occupancies) are ordered throughout the crystal lattice, with a periodicity that coincides with that imposed by the octahedral tilt system also present [Fig. 4.2A,B] [235]. The presence of orbital order also affects the conductivity and magnetic properties of ambient $LaMnO_3$ [237, 244]: the material is an insulator with strongly anisotropic magnetic interactions, as evidenced by a Weiss constant $\Theta = 52\,\mathrm{K}$ that represents a compromise between ferromagnetism within the (a, b) plane and antiferromagnetic interactions between adjacent (a, b) planes (*i.e.* along c). The disappearance of long-range orbital order on heating to $T_{\mathrm{JT}} = 750\,\mathrm{K}$ is observed experimentally by a convergence of the crystallographic Mn–O bond lengths from three distinct values in the ambient

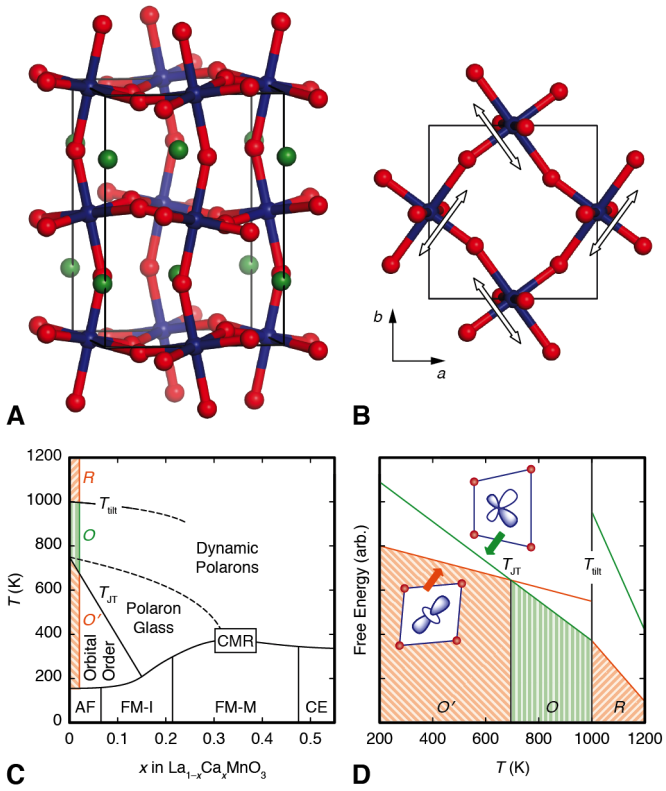

Figure 4.2: A: The ambient (O') structure consists of a framework of corner sharing MnO_6 octahedra (Mn atoms blue; O atoms red), with La atoms (green) occupying 12-coordinate extra-framework sites. The presence of octahedral tilts confers orthorhombic *Pbnm* symmetry, with the **c** crystal axis (here shown vertical) approximately $\sqrt{2}$ times larger than the **a** and **b** axes. B: Axial JT distortions are arranged with the same periodicity as the octahedral tilts. Long Mn–O bonds (indicated by arrows) are confined within the (a, b) planes; this particular arrangement results in small difference between a and b lattice parameters. C: On heating to $T_{JT} = 750\,K$ there is an isosymmetric structural transition to the so-called O phase, with the same octahedral tilts as in O' but with no discernible JT distortion; the a and b lattice parameters of this phase are essentially the same. On hole doping, the value of T_{JT} decreases such that CMR (*e.g.* in $La_{1-x}Ca_xMnO_3$) emerges from the disordered phase. A discontinuous octahedral tilt transition occurs at $\sim$1000 K to give a rhombohedral (R) phase that persists until decomposition. D: Centric (orange) and acentric (green) JT distortions compete in $LaMnO_3$. Centric distortions are enthalpically favoured because they minimise anion–anion repulsions. Acentric distortions give rise to large configurational entropies by virtue of an increased degeneracy of orbital orientations and low strains associated with orbital disorder. The O'/O transition corresponds to the temperature at which the free energies of these competing states cross.

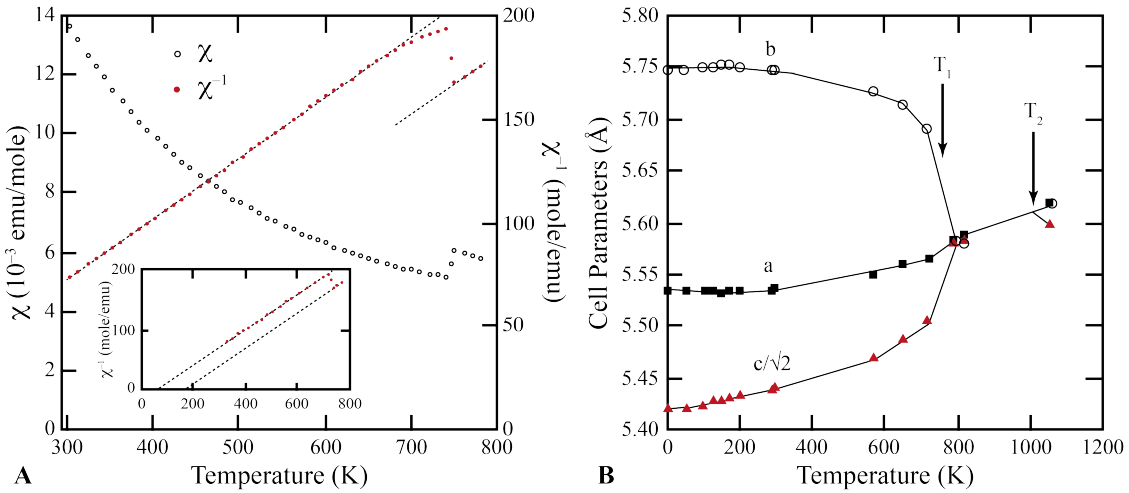

Figure 4.3: A: Magnetic susceptibility data, $\chi(T)$ and $\chi^{-1}(T)$ for a single crystal sample of $LaMnO_3$, showing the transition at 750 K, and the change in magnetic behaviour. Adapted from Ref. 237. B: Unit cell parameters obtained from neutron powder diffraction, showing the O'/O transition at 750 K (T_1) and the O/R transition at 1010 K (T_2). Lines act as guides to the eye. Adapted from Ref. 235.

phase (d(Mn–O) = 1.91, 1.97, 2.18 Å) to a single effective value (1.99 < d(Mn–O) < 2.04 Å) above T_{JT} [235]. Because the same octahedral tilt systems remain active across this transition there is no change in unit cell symmetry, but the reduced unit cell dimensions become pseudocubic within the disordered phase [Fig. 4.3B]; these ordered and disordered orthorhombic phases are usually denoted by the labels O' and O, respectively. Also associated with the O'/O transition are changes in conductivity and magnetism: resistivity falls by two orders of magnitude, and the Weiss constant increases to a value Θ = 177 K [Fig. 4.3A] that is now consistent with isotropic ferromagnetic interactions [237, 244]. A second structural transition occurs on further heating to T_{tilt} = 1010 K to give a rhombohedral phase (denoted R) with a different set of octahedral tilts [235], and which also supports orbital disorder [102] [Fig. 1(C)].

It is the O phase, however, that is of greatest scientific relevance to CMR. On doping $LaMnO_3$ with certain alkaline earth elements, the O'/O transition temperature falls rapidly, such that for the key CMR compositions the disordered O phase is stabilised at temperatures immediately above the crucial metal–insulator transition [Fig. 4.2C] [238]. Consequently, a microscopic understanding of orbital disorder—even in the insulating end-member $LaMnO_3$—has always been considered one of the

fundamental challenges of CMR science [233]. The current generally-held view is that orbital disorder in the O phase is accommodated by dynamic fluctuations of local JT distortions, which in the doped manganites are probably best described in terms of dynamic polarons [105, 242]. Experimental evidence for the persistence of JT distortions in O phase $LaMnO_3$ comes primarily from neutron pair distribution function (PDF) and X-ray absorption fine structure (EXAFS) measurements, both of which indicate negligible variation in local Mn–O bond lengths across the O'/O transition [102, 245, 246]. The interpretation of these data at distances beyond the nearest Mn–O separation differs between, on the one hand, a picture of $\sim$2 nm clusters with structures related to that of the ambient O' phase [102] and, on the other hand, an antiferrodistortive three-state Potts model in which long Mn–O bonds are not confined to the (a, b) planes [245, 247]. These two models have different implications for understanding the configurational entropy, electronic structure, magnetic interactions, and microscopic strain in $LaMnO_3$—yet they cannot easily be discriminated by average structure methods or by using local structure techniques that focus on Mn–O separations alone. In fact it will be shown here that neither model accurately represents the O phase.

4.2 Experimental

4.2.1 Sample Preparation

A polycrystalline sample of $LaMnO_3$ (6.5 g) was prepared via the citrate gel route, as follows. A stoichiometric mixture of La_2O_3 (Alfa Aesar, 99.999%) and MnO_2 (Alfa Aesar, 99.997%) was dissolved in a minimum quantity of 6 M nitric acid. An excess of citric acid and 4 ml of ethylene glycol were then added and the solution heated with constant stirring. The resulting gel was dried and ground to a fine powder, placed in a crucible, and heated in air to 1000 °C for 10 h. The powder was then re-ground and pressed into 13 mm pellets under a force of 5 t. The pellets were fired at 1350 °C under flowing O_2 for 40 h, re-ground and pressed, and finally fired at 1350 °C under flowing Ar. Phase purity was confirmed by X-ray powder diffraction [Fig. 4.4]; the refined lattice parameters were found to be in good agreement with previously published values—$a = 5.53451(6)$, $b = 5.73624(6)$ and $c = 7.69431(7)$ *c.f.* $a = 5.5358(1)$, $b = 5.7363(1)$ and $c = 7.6994(2)$ from Ref. 248.

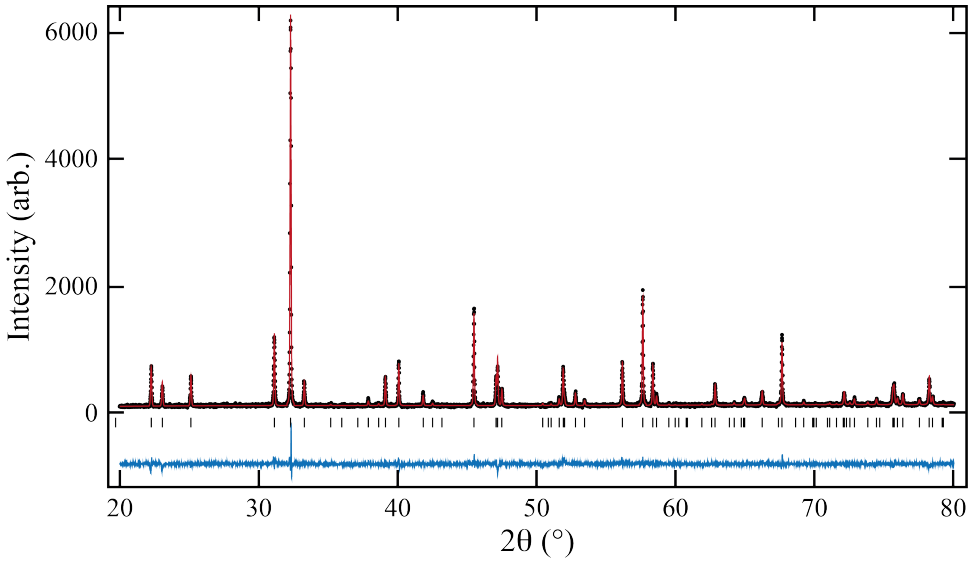

Figure 4.4: X-ray powder diffraction was used to confirm sample purity.

4.2.2 Data Collection

4.2.2.1 X-ray Total Scattering Measurements

X-ray total scattering data were obtained on the I12 beamline at the Diamond Light Source. A beam size of 1.5 mm × 1.5 mm using 0.14577 Å (85.05 keV) wavelength radiation was selected, and a Thales Pixium RF4343 2D detector (CsI scintillator, 430 mm × 430 mm) mounted 474 mm from the sample collected the data. Only the top half of the detector was used to avoid problems caused by pixel mismatch at the connection between the two halves. The beam was centred in the corner of this half to allow scattering to be detected to as high an angle as possible.

The finely ground sample was packed into a 1 mm quartz capillary; this was mounted vertically and rotated about the vertical axis during collection. A hot air blower was used to heat the sample to the required temperatures, and a thermocouple was used to confirm that the upper temperature limit corresponded to the desired temperature. Temperature calibration between X-ray and neutron total scattering measurements (discussed below) was made possible by matching lattice parameter evolutions and the two phase transition temperatures T_{JT} and T_{tilt}. Background measurements were collected using an empty quartz capillary in an otherwise identical experimental configuration.

For each temperature point, 600 one-second exposures were collected and then

averaged. Data were collected at 50 °C intervals between 50 °C and 250 °C, then at 10 °C intervals from 260 °C to 750 °C. Background measurements were similarly collected at 50 °C intervals between 50 °C and 250 °C, but then at 25 °C intervals from 275 °C to 750 °C. Beam downtime disrupted certain collections, though an adequate range of temperatures was still obtained.

The program Fit2D was used for initial data processing [249, 250]. A custom mask was used to remove dead pixels in the detector, and each image was integrated to give a one dimensional scattering pattern. Background subtractions and further corrections were performed using GudrunX [34]. The data were converted to the form

$$F_{\mathrm{X}}(Q) = \rho_0 \int_0^{\infty} 4\pi r^2 G_{\mathrm{X}}(r) \frac{\sin Qr}{Qr}, \tag{4.1}$$

where

$$G_{\mathrm{X}}(r) = \sum_{i,j} c_i c_j f_i(Q) f_j(Q) [g_{ij}(r) - 1], \tag{4.2}$$

$$g_{ij}(r) = \frac{n_{ij}(r)}{4\pi r^2 \mathrm{d}r \rho_0 c_j}. \tag{4.3}$$

The notation used is that of Ref. 8. For the latter stages of RMC refinement, the Q-weighted version $QF_{\mathrm{X}}(Q)$ was used.

4.2.2.2 Neutron Total Scattering Measurements

Neutron total scattering data were collected on the GEM diffractometer at the ISIS pulsed neutron and muon source [22]. The powdered $LaMnO_3$ sample was loaded into a cylindrical thin walled vanadium can, of 8 mm diameter and 5.8 cm tall, which was in turn placed in a furnace inside the instrument. Data were collected for 6 hours at each of 8 temperatures: 523, 653, 753, 823, 903, 973, 1023, and 1103 K. Room temperature data were measured during a separate (preliminary) experiment, making use of a smaller sample volume. In that particular case the sample was loaded into a cylindrical thin-walled vanadium can of 4 mm diameter; no furnace was used. Standard background and normalisation collections were performed in all cases [8, 22]. The data collected span a wide range of scattering vectors, with magnitudes $0.7 \leq Q \leq 40\,\text{Å}^{-1}$.

Following collection the data were corrected using standard methods [34], taking into account the effects of background scattering, absorption, multiple scattering within the sample, beam intensity variations, and the Placzek inelasticity correction.

The corrected data were converted to experimental $F(Q)$ and $G(r)$ functions of the form:

$$F_{\mathrm{N}}(Q) = \rho_0 \int_0^{\infty} 4\pi r^2 G(r) \frac{\sin Qr}{Qr}, \tag{4.4}$$

$$G_{\mathrm{N}}(r) = \sum_{i,j} c_i c_j \bar{b}_i \bar{b}_j [g_{ij}(r) - 1], \tag{4.5}$$

where

$$g_{ij}(r) = \frac{n_{ij}(r)}{4\pi r^2 \mathrm{d}r \rho_0 c_j}. \tag{4.6}$$

In the latter stages of refinement the models were fitted using $QF_{\mathrm{N}}(Q)$ and $D_{\mathrm{N}}(r) = 4\pi r \rho_0 G_{\mathrm{N}}(r)$ to emphasise local structure features in the data. Once again the notation used is that of Ref. 8.

4.2.3 Structure Refinements

4.2.3.1 Rietveld Refinements

The average structure of the sample was refined using the GSAS software package [224]. The structure was refined in the orthorhombic space group *Pbnm* for both the orthorhombic and pseudocubic phases, while the space group $R\bar{3}c$ was used for the rhombohedral phase, in accordance with a previous study [235]. Atomic displacements were modelled using isotropic atomic displacement parameters. No positional constraints were employed beyond those required by the space groups employed. Banks 3–6 of the neutron data collected on the GEM diffractometer were used preferentially to the X-ray data, being of higher resolution and with a better characterised peak shape.

4.2.3.2 RMC Refinements

RMC refinements were performed using the RMCProfile code [71]. For each of the temperatures 300, 523, 653, 753, 823, 903, 973, 1023, and 1103 K, four sets of experimental data were used to drive RMC refinements: the neutron Bragg diffraction pattern, the X-ray and neutron reciprocal-space scattering functions, and the neutron PDF. The X-ray PDF $D_{\mathrm{X}}(r)$ was fitted only indirectly (*i.e. via* the X-ray total scattering function) in order to avoid assuming equivalence in the X-ray form factor Q-dependence for La, Mn, and O [8]. An ensemble of eight starting configurations were prepared for each temperature point, formed from supercells produced

Table 4.1: Weightings used for data sets in RMC refinements.

Data set	300 K Weighting	Weighting for all others
$G_{\mathrm{N}}(r)/D_{\mathrm{N}}(r)$	0.0005	0.005
$F_{\mathrm{N}}(Q)/QF_{\mathrm{N}}(Q)$	0.001	0.01
$F_{\mathrm{X}}(Q)/QF_{\mathrm{X}}(Q)$	0.005	0.005
Neutron Bragg	0.0002	0.01

from the GSAS average structure refinements. $10 \times 10 \times 8$ supercells were used for the orthorhombic and pseudocubic phases, while for the rhombohedral phase the $R\bar{3}c$ unit cell was converted to a larger, orthorhombic cell, of which a $10 \times 6 \times 4$ supercell was formed. The relationship between $R\bar{3}c$ (hexagonal setting) and RMC cells is described by the transformation

$$\begin{bmatrix} \mathbf{a} \\ \mathbf{b} \\ \mathbf{c} \end{bmatrix}_{\mathrm{RMC}} = \begin{bmatrix} 10 & 0 & 0 \\ -6 & 12 & 0 \\ 0 & 0 & 4 \end{bmatrix} \begin{bmatrix} \mathbf{a} \\ \mathbf{b} \\ \mathbf{c} \end{bmatrix}_{R\bar{3}c} . \tag{4.7}$$

In all cases the refinements were allowed to proceed until all structural parameters converged.

The four datasets used were weighted as in Table 4.1. Weightings were chosen after a period of testing, to allow excellent fits to each data set. The 300 K neutron data was collected under slightly different conditions to the rest of the temperatures, and consequently the RMC refinements required different weightings to achieve comparable fits.

Closest approach distances were set to prevent atoms encroaching on each other, and distance windows were employed to prevent certain atom pairs moving too far apart [72]. Slight variations were used for each temperature to reflect the evolving structure. Details of minimum and maximum distances allowed for each pair of atoms at each temperature are given in Table 4.2. The maximum distance applies to pairs of atoms that start the refinement within that cut off—these are defined as "neighbours" for the remainder of the refinement.

Table 4.2: Hard distance constraints used during RMC refinements, with all values given in units of Å. For each atom pair, the given value (or first number if two are given) corresponds to the minimum allowed separation; the second number (if present) corresponds to the maximum allowed separation, where this was constrained. In some instances an initial distance was used to define the neighbours, while a slightly larger distance was used as a constraint during the refinement. The relevant entries are marked by an asterisk; the initial maximum separation used was equal to either 3.20 Å (653 K) or 3.30 Å (all other temperatures).

T / K	La–La	La–Mn	La–O	Mn–Mn	Mn–O	O–O
300	3.00	2.00	2.28	3.00	1.70 / 2.27	2.20 / 3.20
523	3.00	2.00	2.29	3.00	1.78 / 2.28	2.20 / 3.20
653	3.00	2.00	2.28	3.00	1.78 / 2.27	2.20 / 3.30*
753	3.00	2.00	2.26	3.00	1.78 / 2.25	2.20 / 3.40*
823	3.00	2.00	2.25	3.00	1.78 / 2.24	2.20 / 3.40*
903	3.00	2.00	2.25	3.00	1.78 / 2.24	2.20 / 3.50*
973	3.00	2.00	2.27	3.00	1.78 / 2.26	2.20 / 3.50*
1023	3.40	2.00	2.10	3.00	1.78 / 2.70	2.20 / 3.50*
1103	3.40	2.00	2.10	3.00	1.78 / 2.70	2.20 / 3.50*

4.3 Results

4.3.0.3 Data Resolution

Before discussing the results of the analysis performed, it is worth examining the total scattering data collected. By employing state-of-the-art total scattering measurements, the real-space resolution accessed in the $D(r)$ functions used here is far superior to that on which the PDF studies of Refs. 102 and 105 are based. This improved resolution enables new insight into the physics of the O'/O transition in $LaMnO_3$ by revealing a clear discontinuity in $D(r)$ over distances substantially shorter than the crystallographic unit cell dimensions [Fig. 4.5(C,D)]. This has not been reported previously, and in itself this result rules out a simple order/disorder interpretation of the transition, which would require that $D(r)$ remains essentially unchanged for values of r less than some finite multiple of unit-cell lengths.

A direct comparison between the neutron $D(r)$ functions for the disordered O phase measured using the NPDF instrument at LANL, and the GEM instrument data used in this study is shown in Fig. 4.6. While the qualitative features of both functions are similar, the detailed features are more easily discernible in the GEM data

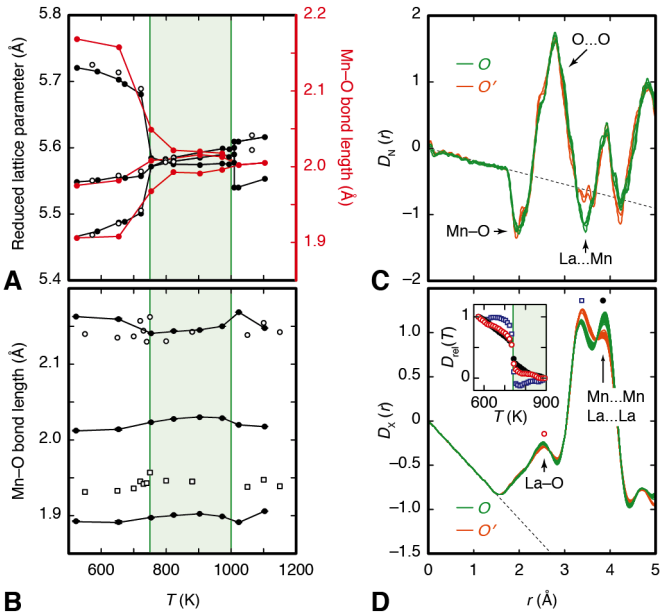

Figure 4.5: (A) The reduced lattice parameters $a' = a, b' = b, c' = c/\sqrt{2}$ determined by Rietveld fits to neutron total scattering data (filled black circles) converge at $T_{\rm JT} = 750\,{\rm K}$, in agreement with the data of Ref. 235 (open black circles). The Mn–O bond lengths determined from the corresponding average structure models (filled red circles) reflect the existence of a JT distortion in the O' phase, but are all equivalent within the O and R phases. (B) Local Mn–O separations extracted from our RMC refinements (filled black circles) show the persistence of a JT distortion in all three phases, in accord with the neutron PDF analysis of Ref. 102 (long Mn–O bond-lengths shown as open black circles; average over short and medium Mn–O bond lengths shown as open black squares). Using this metric, there is no obvious discontinuity in local structure at $T_{\rm JT}$. (C) High real-space resolution neutron PDF data show subtle but reproducible distinctions in local structure over the range $2 < r < 5\,$Å between O' (orange lines; 3 data sets superimposed) and O (green lines; 4 data sets superimposed) phases. The dashed line indicates the PDF baseline; contributions involving Mn atoms can deviate below this line by virtue of the negative neutron scattering length of Mn. (D) A similar discontinuity is observed in the PDFs extracted from our X-ray total scattering data. In both cases the variations observed at $T_{\rm JT}$ are many times larger than the Fourier truncation ripples (which have not been removed) and the differences between PDFs within a given phase. The most obvious changes in these raw data are observed at distances that correspond to pairwise terms involving in La and Mn atoms; normalised intensities $D_{\rm rel}(T) = [D_{\rm X}(T) - D_{\rm X}(573\,{\rm K})]/[D_{\rm X}(893\,{\rm K}) - D_{\rm X}(573\,{\rm K})]$ for peaks corresponding to La–O (2.43 Å; open red circles), La. . .Mn (3.33 Å; open blue squares) and Mn. . .Mn/La. . .La (3.81 Å; filled black circles) separations are given in the inset. For each of these features, the O'/O transition involves a discontinuous change in $D(r)$ intensities. Consequently there is a switching in local geometry that takes place over interatomic separations less than the unit cell dimensions.

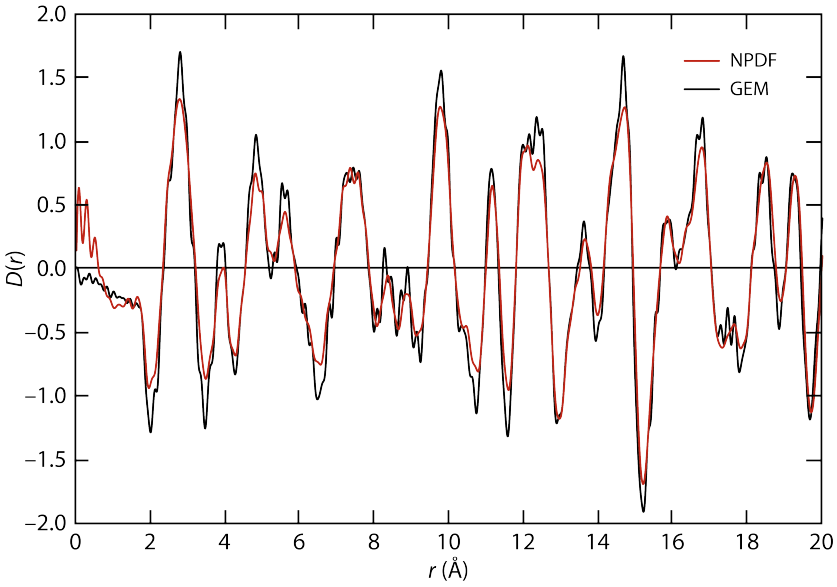

Figure 4.6: Comparison between NPDF (800 K) and GEM (823 K) neutron $D(r)$ functions for O-phase $LaMnO_3$.

(*e.g.* the shoulder on the peak near $r = 3$ Å), and also the data normalisaton is more robust for these same data. Normalisation is particularly important for RMC studies since the absolute areas under each peak are accounted for in terms of a physical number of interatomic separations derived from the atomistic configurations.

4.3.1 Average Structure

4.3.1.1 Rietveld refinements

The resultant Rietveld fits are shown in Figs. A.1–A.9 in Appendix A. As can be seen, a good fit is achieved in each case. The refined lattice parameters for each temperature point are given in Table 4.3, the positional and atomic displacement parameters summarised in Table 4.4, and the corresponding Mn–O bond lengths listed in Table 4.5. All values are in good agreement with previously published results, *e.g.* Ref. 235, as can be seen in Fig. 4.5A.

Table 4.3: Unit cell parameters determined by Rietveld refinement of neutron scattering data.

T / K	Space Group	a / Å	b / Å	c / Å
300	$Pbnm$	5.52744(3)	5.73484(4)	7.68113(5)
523	$Pbnm$	5.54801(4)	5.72072(4)	7.73080(7)
653	$Pbnm$	5.55559(5)	5.70290(5)	7.75978(8)
753	$Pbnm$	5.57204(18)	5.58482(13)	7.8791(3)
823	$Pbnm$	5.58503(16)	5.57448(11)	7.8910(2)
903	$Pbnm$	5.59239(9)	5.57446(7)	7.89888(18)
973	$Pbnm$	5.59864(9)	5.57592(8)	7.90448(18)
1023	$R\bar{3}c$	5.60938(3)	–	13.57268(11)
1103	$R\bar{3}c$	5.61647(3)	–	13.60048(11)

Table 4.4: Positional and atomic displacement parameters determined by Rietveld refinement of neutron scattering data. For the *Pbnm* phases atom positions are as follows: La (x,y,0.25); Mn (0,0.5,0); O1 (x, y, 0.25); O2 (x, y, z). For the $R\bar{3}c$ phases atom positions are as follows: La (0,0,0.25); Mn (0,0,0); O (x, 0, 0.25).

T / K	x_{La}	y_{La}	x_{O1}	y_{O1}	x_{O2}	y_{O2}	z_{O2}	U(La) / Å^2	U(Mn) / Å^2	U(O1) / Å^2	U(O2) / Å^2
300	0.99198(8)	0.04884(7)	0.07395(9)	0.48790(9)	0.72564(8)	0.30654(7)	0.03852(5)	0.00520(12)	0.00227(19)	0.00679(17)	0.00603(12)
523	0.99317(10)	0.04397(8)	0.07258(12)	0.48869(12)	0.72703(10)	0.30435(7)	0.03790(6)	0.00365(12)	0.00058(19)	0.00647(18)	0.00482(12)
653	0.99376(12)	0.04041(10)	0.07183(13)	0.48973(14)	0.72800(12)	0.30211(8)	0.03726(6)	0.00420(13)	0.0013(2)	0.0087(2)	0.00649(14)
753	0.9959(5)	0.02522(17)	0.0691(5)	0.4905(3)	0.7259(3)	0.2844(3)	0.0381(2)	0.00610(18)	0.0038(3)	0.0152(5)	0.0130(3)
823	0.9964(3)	0.02136(12)	0.0692(3)	0.4902(3)	0.7242(2)	0.27975(19)	0.03774(14)	0.01381(19)	0.00874(19)	0.0228(4)	0.0210(3)
903	0.9977(5)	0.02026(14)	0.0708(4)	0.4921(3)	0.7244(2)	0.2759(2)	0.03616(19)	0.01595(13)	0.01020(17)	0.0266(5)	0.0238(3)
973	0.9986(3)	0.01703(14)	0.0675(3)	0.4911(3)	0.7270(2)	0.27589(18)	0.03753(14)	0.0162(2)	0.0111(2)	0.0274(5)	0.0253(4)
1023	–	–	0.44134(6)	–	–	–	–	0.01748(17)	0.0098(2)	0.03061(13)	–
1103	–	–	0.44212(6)	–	–	–	–	0.0184(3)	0.0111(3)	0.0329(2)	–

Table 4.5: Mn–O bond lengths extracted from Rietveld refinements of neutron scattering data.

T / K	short	medium	long
300	1.9022(4)	1.96453(11)	2.1757(4)
523	1.905830(10)	1.97525(2)	2.168790(10)
653	1.9080(6)	1.98143(15)	2.1579(5)
753	1.9680(19)	2.0078(5)	2.049(2)
823	1.9924(14)	2.0110(4)	2.0219(14)
903	1.99185(2)	2.01534(5)	2.02014(2)
973	1.9964(13)	2.0126(4)	2.0174(13)
1023	2.00241(6)	2.00241(6)	2.00241(6)
1103	2.00473(6)	2.00473(6)	2.00473(6)

4.3.1.2 RMC Refinements

Good fits are obtained for all data sets, shown in Figs. A.10–A.18. To confirm that the RMC-refined structures were still in good agreement with the Rietveld-refined average structures, average atomic coordinates and thermal displacement parameters were extracted from RMC configurations for the O' and O phases according to the following procedure. First, the configuration supercell was collapsed onto a single unit cell and the extent of configurational drift established by the deviation of Mn positions away from the 4*b* Wyckoff positions. The symmetry operations of *Pbnm* were then applied in order to determine the average atomic coordinates in the asymmetric unit.

The thermal displacement tensors **U** were then calculated for each crystallographically independent species from the covariance of displacements away from the average positions. The atomic coordinates and U_{ij} values so determined are given in Table 4.6. A similar procedure was followed for the two refinements in the R phase, except that (i) the deviation of the Mn positions away from the 6*b* Wyckoff position was used to determine drift, and (ii) the symmetry operations of $R\bar{3}c$ were used to determine average atomic coordinates within the asymmetric unit.

Again these values are consistent with the literature values.

Table 4.6: Average structure coordinates and anisotropic displacement parameters from RMC refinements. Values of U_{ij} terms are given in units of Å^2.

T / K	Atom	x	y	z	U_{11}	U_{22}	U_{33}	U_{12}	U_{13}	U_{23}
300	La	0.9904	0.0493	0.2500	0.0060	0.0077	0.0056	−0.0011	0.0000	0.0000
	Mn	0.0000	0.5000	0.0000	0.0075	0.0081	0.0088	0.0005	0.0011	0.0006
	O1	0.0732	0.4890	0.2500	0.0056	0.0135	0.0089	−0.0027	0.0000	0.0000
	O2	0.7236	0.3056	0.0387	0.0068	0.0102	0.0099	−0.0019	−0.0001	−0.0030
523	La	0.9911	0.0483	0.2505	0.0260	0.0295	0.0151	−0.0050	0.0000	−0.0020
	Mn	0.0000	0.5000	0.0000	0.0111	0.0146	0.0130	−0.0002	0.0000	−0.0033
	O1	0.0695	0.4965	0.2509	0.0076	0.0191	0.0085	−0.0009	−0.0003	−0.0004
	O2	0.7243	0.2968	0.0365	0.0084	0.0120	0.0110	−0.0042	−0.0004	−0.0013
653	La	0.9918	0.0493	0.2505	0.0381	0.0433	0.0204	−0.0067	−0.0007	−0.0005
	Mn	0.0000	0.5000	0.0000	0.0165	0.0248	0.0143	−0.0007	0.0004	0.0017
	O1	0.0687	0.4991	0.2490	0.0110	0.0181	0.0062	−0.0004	0.0002	−0.0003
	O2	0.7278	0.2907	0.0365	0.0109	0.0156	0.0098	−0.0060	0.0006	−0.0022
753	La	0.9965	0.0390	0.2500	0.0240	0.0933	0.0188	−0.0083	0.0000	0.0001
	Mn	0.0000	0.5000	0.0000	0.0119	0.0675	0.0063	0.0014	0.0000	0.0035
	O1	0.0670	0.5121	0.2498	0.0184	0.0190	0.0062	−0.0008	−0.0002	−0.0004
	O2	0.7323	0.2681	0.0387	0.0117	0.0159	0.0156	−0.0013	0.0008	−0.0008
823	La	0.9909	0.0406	0.2503	0.0700	0.0771	0.0392	−0.0124	−0.0010	−0.0007
	Mn	0.0000	0.5000	0.0000	0.0426	0.0251	0.0169	−0.0021	0.0000	−0.0047
	O1	0.0714	0.5112	0.2507	0.0274	0.0316	0.0085	0.0014	0.0000	0.0000
	O2	0.7299	0.2659	0.0367	0.0202	0.0207	0.0235	−0.0074	0.0032	−0.0045
903	La	0.9917	0.0358	0.2497	0.0831	0.0698	0.0509	−0.0125	0.0007	−0.0004
	Mn	0.0000	0.5000	0.0000	0.0485	0.0135	0.0252	−0.0018	−0.0004	−0.0001
	O1	0.0692	0.5109	0.2497	0.0323	0.0363	0.0113	0.0023	−0.0009	−0.0006
	O2	0.7316	0.2654	0.0376	0.0258	0.0239	0.0287	−0.0119	0.0043	−0.0056
973	La	0.9950	0.0344	0.2499	0.0686	0.0742	0.0498	−0.0091	−0.0005	0.0000
	Mn	0.0000	0.5000	0.0000	0.0321	0.0349	0.0229	−0.0001	−0.0003	0.0029
	O1	0.0664	0.5112	0.2498	0.0326	0.0271	0.0115	0.0010	−0.0001	−0.0002
	O2	0.7346	0.2615	0.0386	0.0207	0.0220	0.0293	−0.0081	0.0018	−0.0035
1023	La	0.0000	0.0000	0.2500	0.0523	0.0523	0.0126	0.0000	0.0000	0.0261
	Mn	0.0000	0.0000	0.0000	0.0303	0.0303	0.0079	0.0000	0.0000	0.0151
	O	0.2313	0.3333	0.0833	0.0311	0.0268	0.0388	−0.0149	−0.0075	0.0134
1103	La	0.0000	0.0000	0.2500	0.0231	0.0231	0.0157	0.0000	0.0000	0.0115
	Mn	0.0000	0.0000	0.0000	0.0209	0.0209	0.0095	0.0000	0.0000	0.0104
	O	0.2296	0.3333	0.0833	0.0360	0.0300	0.0348	−0.0129	−0.0065	0.0150

4.3.2 Local Structure

4.3.2.1 Mn–O Bond Lengths

The first stage of the local structure analysis was concerned with once again checking consistency with previous studies, such as Ref. 102. To that end, the average (local) Mn–O bond distances were determined by averaging over the two longest, the next two longest, and finally the two shortest Mn–O bond lengths for each Mn centre. These values are given in Table 4.7, and a comparison with Ref. 102 is shown in Fig. 4.5B.

An example of the partial structure factors is shown in Fig. 4.7 as a visual depiction of the local bond distributions in a refined configuration.

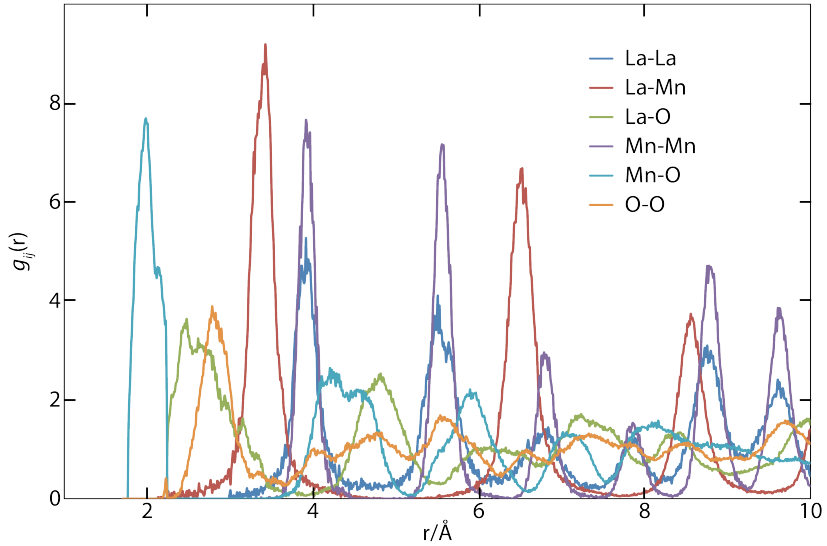

Figure 4.7: Representative partial pair correlation functions $g_{ij}(r)$, extracted from an RMC configuration refined against data collected at 823 K.

4.3.2.2 O–Mn–O Angles

As the focus of this study is the JT-distorted MnO_6 octahedra, the next stage of the analysis involved checking the distortion of these octahedra by looking at the orientations of the two longest Mn–O bonds. The established understanding of orbital order and disorder in this material suggests these bonds should be antiparallel for all three phases. For the orbitally ordered O' phase the bond angle histograms show, as

Table 4.7: Mn–O bond lengths determined from RMC refinements (values given in units of Å).

T / K	short	medium	long
300	1.88960(7)	1.99843(9)	2.17661(7)
523	1.8925(2)	2.0120(4)	2.1627(2)
653	1.8914(10)	2.0141(12)	2.1595(15)
753	1.8973(3)	2.02334(13)	2.1407(5)
823	1.9007(2)	2.02756(18)	2.14351(14)
903	1.9024(3)	2.0300(3)	2.1451(3)
973	1.89898(18)	2.0286(2)	2.1501(4)
1023	1.8910(2)	2.0199(2)	2.1688(4)
1103	1.90565(13)	2.01781(16)	2.14778(18)

expected for a *trans** arrangement of long bonds, a peak at an angle of 180° [Fig. 4.8A]. What is more, the spatial distribution of these long bonds within the configuration reflects the expected chequerboard ordering pattern [Fig. 4.8C].

However, for the orbitally 'disordered' O phase, the maximum in the histogram instead occurs at 90°, indicating an unexpected *cis* arrangement of the two long bonds. Now, as there are twelve possible ways to orient an octahedron in the *cis* arrangement, but only three in the *trans* arrangement, a purely statistical distribution would appear to favour the *cis* arrangement over the *trans*. With this in mind, the ratio of *cis*:*trans* octahedra was calculated for each temperature [Table 4.8], and compared to the value expected for a random distribution [Fig. 4.8B]. The results show a large preponderance for the *cis* arrangement in the O phase, which disappears again in the R phase, demonstrating that this feature of the refinement is driven by the data. It is also noted that there appears to be a certain tendency for *cis* octahedra to cluster with other octahedra of the same orientation [Fig. 4.8D].

This basic trend is also observed when the refinements are repeated using the neutron PDF data of Ref. 102 [Fig. 4.9]. Thus the first unexpected result to emerge from this study is that the local symmetry of the JT distortion appears to change across the O/O' transition.

*In this thesis, the term *trans* is used to describe an arrangement of long bonds in an octahedron where the bonds are found 180° apart. The other possible situation, where the bonds are to be found at 90° is referred to as a *cis* arrangement.

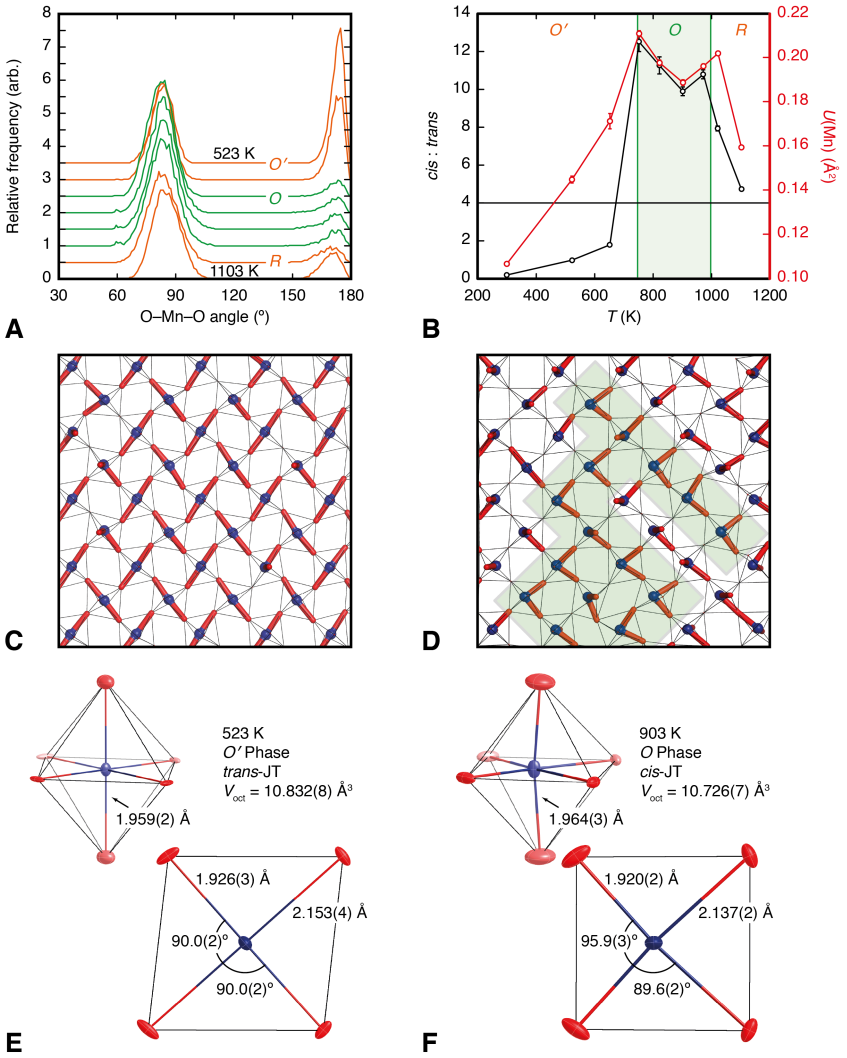

Figure 4.8: (A) O–Mn–O angle histogram functions, calculated using the two longest Mn–O bonds associated with each Mn centre in the RMC configurations. The maximum switches at T_{JT} from ∼180° (*trans*-JT distortion) to ∼90° (*cis*-JT distortion). (B) The ratio of *cis*-to-*trans*-JT distortions (black circles) within the *O* phase is many times larger than the statistical limit (black horizontal line). The mean-squared magnitude of Mn off-centre displacements (red circles) also varies discontinuously across the O'/O transition. (C), (D) Representative regions of RMC configurations refined against data collected at (C) 523 K and (D) 903 K reveal the spatial correlation between JT distortions in the O' and *O* phases: Mn atoms are shown as dark blue spheres, long Mn–O bonds as red cylinders, and MnO_6 coordination polyhedra as thin black lines. At 523 K, *trans*-JT distortions are correlated according to the checkerboard ordering pattern given in Fig. 1(B); there are a minority of *cis*-JT defects. In the *O* phase, however, *cis*-JT distortions dominate, forming correlated nano-domains (shaded region) with ferroelectric Mn displacements. All 12 possible *cis*-JT orientations are sampled; some shown here involve Mn–O bonds that lie perpendicular to the plane of the diagram. (E), (F) Local MnO_6 coordination geometries at (E) 523 K and (F) 903 K extracted from the RMC configurations, taking into account octahedral tilts and JT distortion orientations.

Table 4.8: Average numbers of *cis*- and *trans*-JT MnO_6 octahedra in RMC configurations.

T / K	Number of *cis*	Number of *trans*	Ratio *cis*:*trans*
300	523	2677	0.195(2)
523	1583	1617	0.980(12)
653	2049	1151	1.79(6)
753	2961	239	12.5(5)
823	2936	264	11.3(4)
903	2906	294	9.9(2)
973	2928	272	10.8(3)
1023	2557	323	7.94(14)
1103	2377	503	4.73(3)

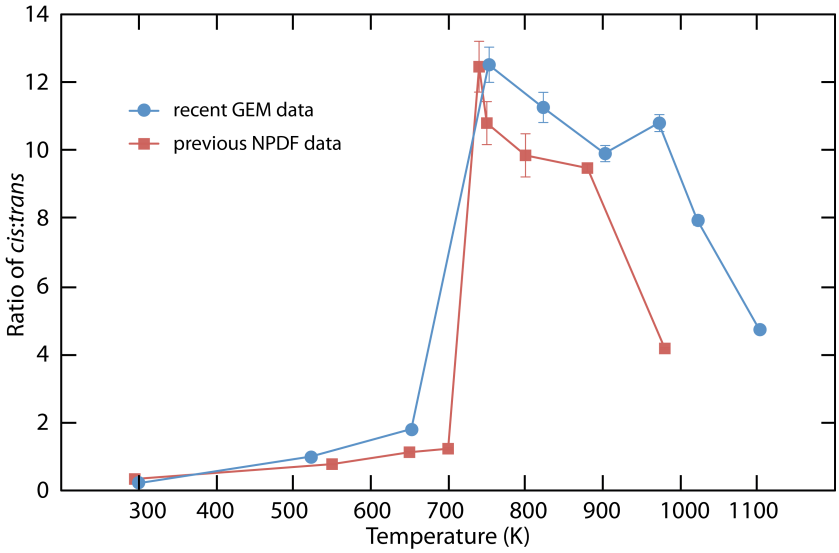

Figure 4.9: Ratio of *cis*:*trans* distorted octahedra for refinements using the current data collected on the GEM diffractometer, ISIS, and the older data from Ref. 102, collected on the NPDF diffractometer, LANL. It should be noted that a different sample of $LaMnO_3$ was used for the NPDF data collection, which explains the slightly different temperature dependence observed.

4.3.2.3 Local MnO_6 Structure

Having established the presence of *cis* octahedra as well as *trans*, it was desirable that these distortions should be described by a local coordinate system centred on each Mn atom, to allow comparisons to be made easily. The local geometries of each type were obtained by averaging over the ensemble of refinements for each temperature, using the following process.

First, the two longest Mn–O bond vectors $\mathbf{r}_1, \mathbf{r}_2$ were determined. For a *cis*-JT geometry, the two Mn–O bond vectors $\mathbf{r}_3, \mathbf{r}_4$ corresponding to those Mn–O bonds opposite these longest bonds were identified next; for a *trans*-JT geometry, $\mathbf{r}_3$ was taken to be the shortest Mn–O bond vector, and $\mathbf{r}_4$ to be the remaining Mn–O bond vector contained within the plane described by $\mathbf{r}_1, \mathbf{r}_2, \mathbf{r}_3$. The LAPACK Fortran library DSYEVX was then used to fit a plane to the four vectors $\mathbf{r}_i$; the normal to this plane was identified as the local $\mathbf{z}$ axis. For a *cis*-JT geometry, the local $\mathbf{x}$ axis is determined according to

$$\mathbf{x} = \frac{\mathbf{r}_1 + \mathbf{r}_2}{|\mathbf{r}_1 + \mathbf{r}_2|}; \tag{4.8}$$

whereas for a *trans*-JT geometry the equation

$$\mathbf{x} = \frac{\mathbf{r}_1 + \mathbf{r}_3}{|\mathbf{r}_1 + \mathbf{r}_3|}. \tag{4.9}$$

was used. In both cases, $\mathbf{y}$ is defined as $\mathbf{y} = \mathbf{z} \times \mathbf{x}$. It should be noted that the local coordinate system used here automatically accounts for octahedral tilts, and also that—because the $\mathbf{x}, \mathbf{y}$ plane is fitted to the $\mathbf{r}_i$ vectors—a reduced apparent mean squared displacement of these atoms in a direction normal to this plane is expected.

Having established a local coordinate system for each Mn centre, the average O positions were determined for each RMC configuration for each of the two JT geometries. Effective thermal displacement parameters were determined from the covariance of the local displacements away from the average positions, having taken into account the change of axis system described above. Absolute coordinates (Å) and atomic displacement parameters relative to these local axes for each temperature in this study are listed in Tables **??**–**??**, and examples of each type are shown in Fig. 4.8E,F.

While the average *trans*-distorted octahedron has a geometry essentially identical that observed in the average structure of the O' phase, the geometry of the *cis* phase

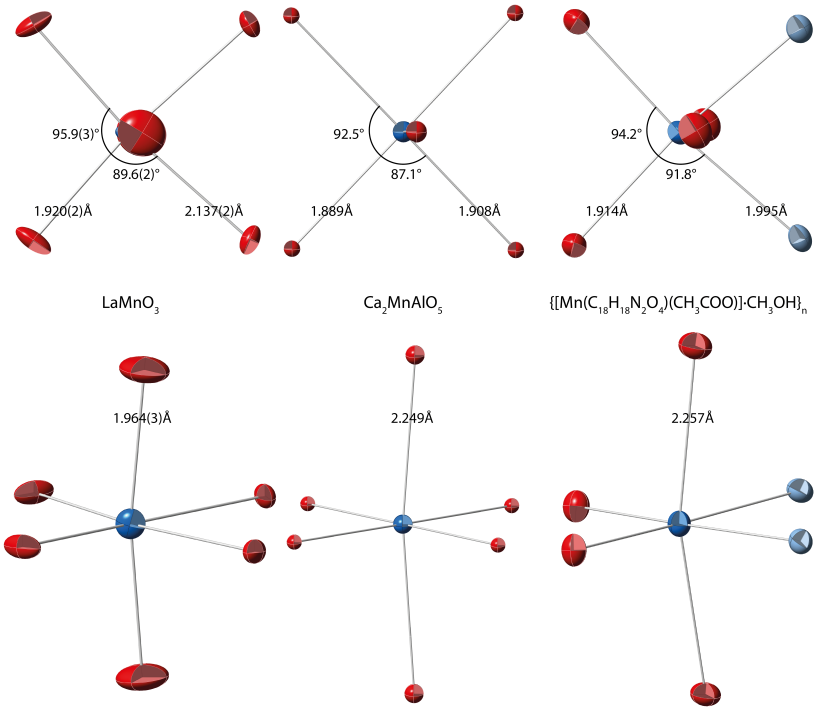

Figure 4.10: A visual comparison between the MnO_6 octahedra found in $LaMnO_3$ (left hand side), Ca_2MnAlO_5 (centre), and $\{[Mn(C_{18}H_{18}N_2O_4)(CH_3COO)]CH_3OH\}_n$ (right hand side), with a view from above (top row) and oblique view (bottom row). Key bond angles and lengths are indicated. The larger atomic displacement parameters in the $LaMnO_3$ diagrams are a result of some disorder that is inevitable in RMC refinements, and the flattening of the ellipsoids is due to the way the octahedra are extracted from the configuration and averaged.

is rather different: the centre of symmetry is lost, and while the individual Mn–O bond lengths remain similar to those observed within the ordered phase, their relative arrangement is modified. These *cis*-distorted octahedra are not without precedent: they do in fact bear close resemblance to the handful of established systems with acentric Mn^{3+} environments [251, 252]. An illustration of the similarities between the *cis*-JT octahedra we observe in $LaMnO_3$, and the MnO_6 octahedra in Ca_2MnAlO_5 and MnN_2O_4 octahedra in the compound $\{[Mn(C_{18}H_{18}N_2O_4)(CH_3COO)]CH_3OH\}_n$ is included in Fig. 4.10.

Table 4.9: Mean-squared off-centre displacement of Mn atoms determined from RMC refinements.

T / K	Displacement / Å^2
300	0.1063(3)
523	0.1446(16)
653	0.171(3)
753	0.2110(13)
823	0.1978(13)
903	0.1888(13)
973	0.1962(11)
1023	0.2021(6)
1103	0.1593(4)

4.3.2.4 Mn Displacements

The acentric Mn environment results in a larger than expected Mn displacement parameter, meaning that these displacements can also be used to monitor the presence of *cis*-distorted octahedra. Mean squared manganese off-center displacements $\mathbf{u}$(Mn) were calculated by first determining for each MnO_6 coordination polyhedron the centroid of the O_6 cage:

$$\bar{\mathbf{x}} = \frac{1}{6}\sum_{i=1}^{6}\mathbf{x}(\mathrm{O}_i), \tag{4.10}$$

where $\mathbf{x}(\mathrm{O}_i)$ is the position of O vertex i in absolute coordinates. We then have

$$\mathbf{u}(\mathrm{Mn}) = \frac{1}{N}\sum_{j}\left(\mathbf{x}_j(\mathrm{Mn}) - \bar{\mathbf{x}}_j\right)^2, \tag{4.11}$$

where the sum is taken over all Mn centres (of which there are N). The values so determined are listed in Table 4.9. It can be seen that the magnitudes of the displacements rise and fall in the same manner as the *cis*:*trans* ratio.

4.3.2.5 Comparison of JT Geometries

Having obtained descriptions of the average JT distortions of each type, more detailed comparisons can now be made between the two. Here follows some discussion of the volumes, axial variances, and similarity to the Mn^{4+} geometry of the two distortions.

Volume Calculations Effective MnO_6 octahedron volumes were calculated from the local atomic coordinates determined using the approach described in section 4.3.2.3. The six O atom positions were used as input for the convex hull determination program QHULL [253]. This program computes the convex hull volume, which is exact for an octahedral geometry. Computed volumes for the *trans*- and *cis*-JT states (523 and 903 K, respectively) are 10.832(8) Å^3 and 10.726(7) Å^3. The uncertainties quoted here correspond to the standard deviations in octahedral volumes calculated across the eight independent RMC configurations refined for each temperature.

Axial separation variance The extent to which JT distortion axis re-orientations introduce local strain can be estimated from the variance in axial O...O separations. Making use of the local geometries extracted from configurations as described above, we determined that the variance observed in the *trans*-JT geometry (523 K) is equal to 0.0401(4) Å^2, and that of the *cis*-JT geometry (903 K) is 0.0042(2) Å^3. The uncertainties quoted here correspond to the standard deviations in variances calculated across the eight independent RMC configurations refined at each temperature. The ratio of *cis*:*trans* variance terms is equal to 0.105(6); hence there is an order of magnitude difference in variances between the two distortion geometries.

Comparison with Mn^{4+} geometry The comparison to the MnO_6 geometry in $CaMnO_3$ was determined in a similar manner, except that the variance term

$$\mathrm{Var(O\ldots O)} = \frac{1}{3}\sum_i [r(\mathrm{O\ldots O})_i - \bar{r}]^2 \tag{4.12}$$

is modified such that $\bar{r}$ is no longer the average O...O separation, but rather the average axial dimension of the MnO_6 octahedra in $CaMnO_3$. The corresponding value $\bar{r} = 3.805$ Å gives variances of 0.0887(5) and 0.0450(6) Å^2 and for the *trans*- and *cis*-JT, respectively. The ratio of *cis*:*trans* variance terms is equal to 0.507(7); hence there is a factor of two difference in variances between the two distortion geometries and the Mn^{4+} coordination environment.

4.3.2.6 Quadrupolar Order Parameters

JT distortions generate localised quadrupolar moments in a structure, which, if quantified can be used to monitor or assess the extent of the distortion present. This has

been used previously for this system in Ref. 254, where a combination of neutron total scattering and geometric modelling is used to argue that the quadrupolar distortions present in the O' phase persist into the orbital disordered O phase. Taken at face value, this result appears to contradict the results of the present study. However it is shown below that the analysis performed in that former study obfuscates the *trans*- to *cis*-JT distortion.

The approach taken in Ref. 254 was to determine for each MnO_6 octahedron the following quadrupole moments

$$q_1 = 2\sum_{i=1}^{6} x_i y_i, \tag{4.13}$$

$$q_2 = 2\sum_{i=1}^{6} y_i z_i, \tag{4.14}$$

$$q_3 = 2\sum_{i=1}^{6} z_i x_i, \tag{4.15}$$

$$q_4 = \sum_{i=1}^{6} (x_i^2 - y_i^2), \tag{4.16}$$

$$q_5 = \frac{1}{\sqrt{3}} \sum_{i=1}^{6} (2z_i^2 - x_i^2 = y_i^2), \tag{4.17}$$

where x_i, y_i, z_i are the cartesian components of the six Mn–O bond vectors. A normalised magnitude of the total quadrupole moment is then defined as

$$P^2 = \frac{3}{16(b^2 - a^2)^2} \left(\sum_{j=1}^{5} q_j^2 \right), \tag{4.18}$$

where a and b correspond to the average lengths of "short" and "long" Mn–O bonds, respectively. This particular formulation was chosen such that a configuration in which all MnO_6 octahedra adopted the average-structure *trans*-JT geometries would correspond to a mean quadrupole moment $P = 1$. The inference was made that the absence of *trans*-JT distortions would give rise to a zero value of P. The key result of Ref. 254 was to show that the distribution of P values for atomistic configurations refined against neutron scattering data were peaked near $P = 1$ for temperatures in all three phases O', O, and R.

In order to compare the results of this study with those of Ref. 254 the quadrupole moment for each octahedron in these refinements was calculated, and the probability

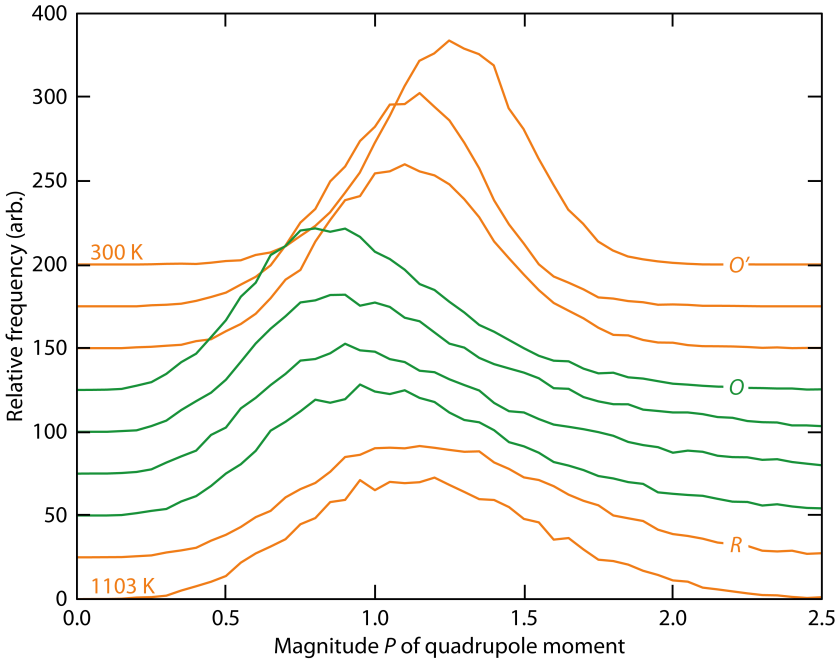

Figure 4.11: Probability distributions of quadrupole magnitudes, P, at different temperatures.

distributions of the quadrupole magnitudes, P, for each temperature were plotted [Fig. 4.11]. It is found that the histograms of this study are centred on a value of $\sim$1.2 for the O′ and R phases, and near $\sim$0.9 in the O phase. The difference in P values between O' and O phases that is observed is almost identical with that reported in Ref. 254, and so what is found here is that the particular quadrupolar normalisation used in that study is not particularly sensitive to the type and extent of Jahn Teller distortion.

4.3.2.7 3-State Potts Model

The transition at 750 K in $LaMnO_3$ is a well known example of an order disorder transition, and many attempts have been made to describe it. One of these is the modified three-state Potts model proposed by Ahmed *et al.*, also known as the anisotropic Potts model [247].

The Potts model is effectively an extension of the Ising model to higher dimensions, which allows a more varied phase structure. The three-state Potts model discussed here is based on a cubic lattice, with three equivalent choices of axis for the distortion,

Table 4.10: Distance window constraints employed to maintain the three-state Potts model during RMC refinement.

Atom pair	Minimum separation / Å	Maximum separation / Å
Mn1–O1	2.08	2.28
Mn1–O2	1.70	2.08
Mn1–O3	1.70	2.08
Mn2–O1	1.70	2.08
Mn2–O2	2.00	2.28
Mn2–O3	1.70	2.08
O1–O1	2.20	3.40
O1–O2	2.20	3.40
O1–O3	2.20	3.40
O2–O2	2.20	3.40
O2–O3	2.20	3.40
O3–O3	2.20	3.40

and where the interactions depend on the relative orientation of the orbitals as well as the vector joining them. Essentially this potential acts to avoid the situation where the JT axes of neighbouring MnO_6 octahedra coincide on the same O atom, *i.e.* to avoid having two adjacent long Mn–O bonds. For further details please see Ref. 247.

In order to compare the refined structures of the present study with this model, RMC refinements were set up that were suitably constrained to conform to the three-state Potts model. These were allowed to refine to the data, and then the fits were compared. A Monte Carlo algorithm was used to create a starting structure that obeyed the proposed interactions, and distance window constraints prevented the atoms from straying too far during the refinement. In order to achieve this, two separate groups of Mn atoms had to be defined, as well as three groups of O atoms. The distance window constraints used are described in Table 4.10, and a cross section of the structure is shown in Fig. 4.12.

A representative set of fits is shown in Fig. 4.13. As is evident when compared to those fits in Figs A.10–A.18, the fits obtained using the Potts model constraints are inferior to those obtained without the constraints. It is also noted that if one of the Potts model refined structures has its constraints removed and it is allowed to refine freely it returns to a *cis*-distorted structure like those obtained previously.

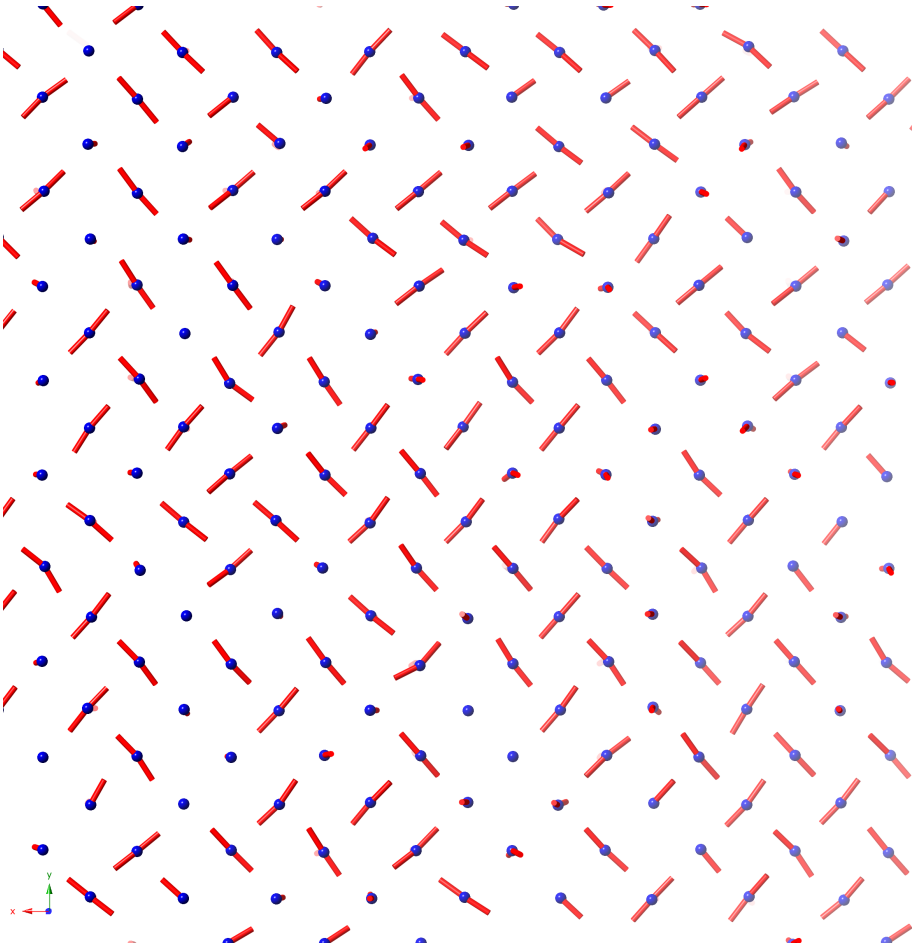

Figure 4.12: A cross section through a three-state Potts-constrained model, with long Mn-O bonds highlighted.

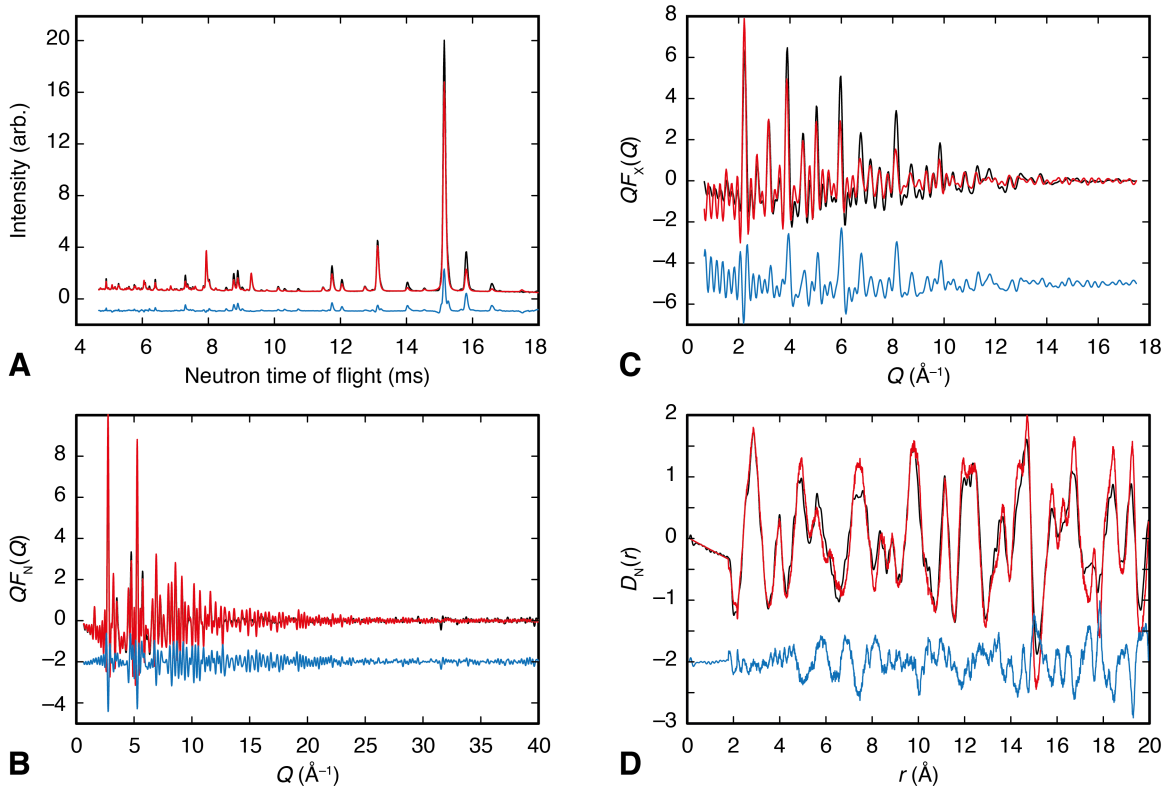

Figure 4.13: Representative fits to data for an RMC refinement performed using Potts model constraints. A) Neutron Bragg data; B) neutron $QF(Q)$ data; C) X-ray $QF(Q)$ data; D) neutron $D(r)$ data. Data collected at 753 K.

4.3.2.8 PDFGUI refinements

Some simpler refinements—using far fewer parameters than in the RMC refinements—were performed as a precaution against the hazards of over-fitting data. PDFGUI [36] was chosen for this task, as it uses much smaller structural models (typically only one unit cell) to fit to PDF data, resulting in far fewer degrees of freedom.

The two extracted JT geometries were used to generate structural models described using only a single JT distortion parameter, u: in one set of refinements this parameter described a *trans*-JT distortion; in the other a *cis*-JT distortion. The octahedral tilts, lattice parameters, and average Mn–O bond lengths were taken from conventional Rietveld refinements. The oxygen coordinates are described in Table 4.11 as a function of u, the average bond length r, the octahedral tilt angles θ and φ, and the lattice parameters a, b and c.

Both models were fitted to neutron PDF data in the range 1.5 Å–6.0 Å at each temperature in the O′ and O phases, and for each case the same parameters were refined. Only the oxygen coordinates were allowed to refine (*via* the 'u' parameter); the La and Mn positions were kept fixed on their average positions. Scale, damping and broadening factors were also refined, as were U_{iso} values. The reduced χ^2 was compared to establish which model gave the better fit. The results are presented in Fig. 4.8B and Table 4.12 below.

It was found that for temperatures below 750 K, *i.e.* in the O′ phase, the *trans*-distorted model fitted the data better, while for temperatures covering the O phase the *cis*-distorted model was superior. This demonstrates that the data favour the *cis*-distortion whether refined using large-box or small-box methods, and the feature observed in the RMC refinements is not simply an artefact of the process resulting from over-fitting.

4.3.2.9 EXAFS calculations

As a final consistency check against previously published local structure data, Mn K-edge EXAFS signals were calculated from the RMC configurations using the FEFF7 code [255] in order to compare these against experimental EXAFS data [246]. As in that publication, the primary interest in this case was in assessing the difference between calculated EXAFS spectra across the O'/O transition. The comparison

Table 4.11: Oxygen positions in the distorted unit cells, described in the form $A+Bu$, where u is a parameter describing the extent of the distortion, r is the average Mn-O bond length, θ and φ are the octahedral tilt angles, and a, b and c are the lattice parameters. The other oxygen positions may be easily obtained by applying suitable symmetry operations.

Atom(coordinate)	A	B
trans-distorted		
O1(x)	$0.5+\frac{\tan\theta}{2\sqrt{2}}$	0
O1(y)	$\frac{\tan\varphi\sin\theta}{2\sqrt{2}}$	0
O1(z)	$\frac{3}{4}$	0
O2(x)	$0.5+\frac{\cos\theta\cos\varphi-\sin\varphi}{4\cos\theta\cos\varphi}$	$\frac{\cos\theta\cos\varphi-\sin\varphi}{4r\cos\theta\cos\varphi}$
O2(y)	$\frac{\cos\theta\sin\varphi+\cos\varphi}{4\cos\varphi}$	$\frac{\cos\theta\sin\varphi+\cos\varphi}{4r\cos\varphi}$
O2(z)	$0.5-\frac{\tan\theta}{4\sqrt{2}}$	0
cis-distorted		
O1(x)	$\frac{r(\cos\theta\cos\varphi-\sin\varphi)}{\sqrt{2}a}$	$\frac{0.143\cos\theta\cos\varphi-0.008\sin\varphi}{a}$
O1(y)	$\frac{r(\cos\theta\sin\varphi+\cos\varphi)}{\sqrt{2}b}$	$\frac{0.143\cos\theta\sin\varphi+0.008\cos\varphi}{b}$
O1(z)	$0.5-\frac{r\sin\theta}{\sqrt{2}c}$	$-\frac{0.143\sin\theta}{c}$
O2(x)	$0.5+\frac{r(\cos\theta\cos\varphi+\sin\varphi)}{\sqrt{2}a}$	$\frac{0.143\cos\theta\cos\varphi+0.008\sin\varphi}{a}$
O2(y)	$\frac{r(\cos\theta\sin\varphi-\cos\varphi)}{\sqrt{2}b}$	$\frac{0.143\cos\theta\sin\varphi-0.008\cos\varphi}{b}$
O2(z)	$0.5-\frac{r\sin\theta}{\sqrt{2}c}$	$-\frac{0.143\sin\theta}{\sqrt{2}c}$
$O3_{up}$(x)	$0.5+\frac{r\sin\theta\cos\varphi}{a}$	$\frac{0.143\cos\theta\cos\varphi}{a}$
$O3_{up}$(y)	$\frac{r\sin\theta\sin\varphi}{b}$	$\frac{0.143\cos\theta\sin\varphi}{b}$
$O3_{up}$(z)	$0.5+\frac{r\cos\theta}{c}$	$-\frac{0.143\sin\theta}{c}$
$O3_{down}$(x)	$0.5-\frac{r\sin\theta\cos\varphi}{a}$	$\frac{0.143\cos\theta\cos\varphi}{a}$
$O3_{down}$(y)	$-\frac{r\sin\theta\sin\varphi}{b}$	$\frac{0.143\cos\theta\sin\varphi}{b}$
$O3_{down}$(z)	$0.5-\frac{r\cos\theta}{c}$	$-\frac{0.143\sin\theta}{c}$

Table 4.12: Results for PDFGUI refinements showing the reduced χ^2 for both the *cis* and *trans* refinements. Below 750 K the *trans* refinements have the lower χ^2, but above the transition it is the *cis* refinements that provide the better fit.

Temperature / K	*trans*	*cis*
300	0.499	0.895
523	0.413	0.638
653	0.299	0.381
753	0.470	0.419
823	0.503	0.430
903	0.445	0.365
973	0.414	0.367

between EXAFS spectra determined from our RMC models for temperatures of 653 and 753 K is shown in Fig. 4.14. It should be noted that it is well established that FEFF7 calculations making use of RMC configurations give rise to EXAFS spectra with broadened features [141], so the absolute differences between calculated and experimental data are not particularly meaningful. What is important is that the periodicity of the difference function $\Delta\chi(k)$ is well represented by the variations in local Mn environments in these RMC configurations. Consequently the local JT geometry transition observed is consistent not only with the scattering data that have been collected, but also with EXAFS measurements carried out independently.

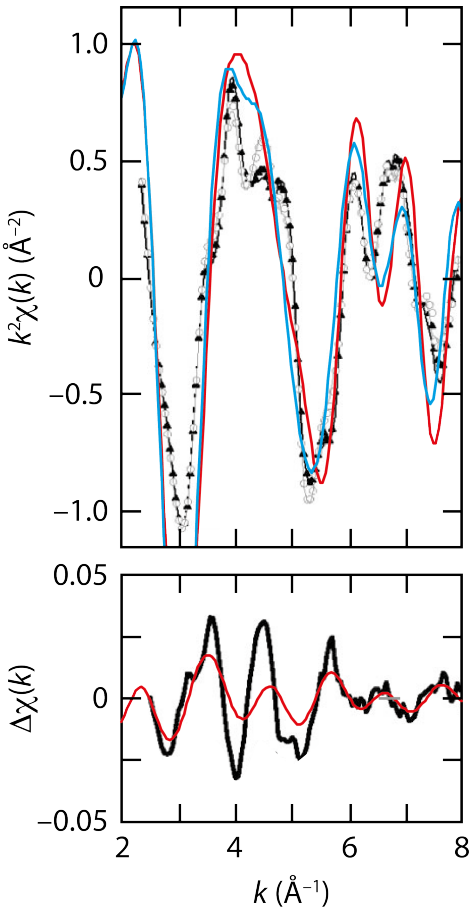

Figure 4.14: Comparison between RMC (coloured lines) and experimental EXAFS spectra (symbols and black lines) of Ref. 246. In the top panel, the k^2-weighted spectra are shown for temperatures in the O' (blue lines; filled symbols) and the O (red lines; open symbols) phases. The lower panel shows the difference function calculated from the RMC configurations (red line) and as reported in Ref. 246. Quantitative overlap is not to be expected for atomistic FEFF7 calculations. What is important is that the periodicity of the difference function (which arises from the changes in the real-space scattering pathways) is well matched.

4.3.3 Other

4.3.3.1 Comparative Energetics of the JT Distortions

In the absence of first principles techniques capable of calculating electronic and lattice enthalpies for orbital disordered states, the enthalpy difference between *trans*- and *cis*-JT distortions has been estimated by considering separately the symmetry-adapted crystal field stabilisation and lattice energies. Crystal field energies were calculated using the generic coordinate approach described first in Ref. 256, taking into account symmetry-allowed mixing of $3d$, $4s$ and $4p$ states. Local atom coordinates were taken from the RMC refinements near T_{JT}; the specific values used are summarised in Table 4.13. The ligand field strength parameter Δ was adjusted to give a crystal field stabilisation near the experimental value of between 1.5 and 2 eV (Ref. 257). The final difference in crystal field stabilisation energies scales linearly with this value; in these calculations $E_{\mathrm{JT}} = 1.71$ eV. The corresponding orbital energies are listed in Table 4.14, which also documents the effect of $3d/4p$ mixing on the *cis*-JT state. The corresponding crystal field terms for the E_{JT} value given above are 1.71 and 1.55 eV for *trans*- and *cis*-JT geometries respectively.

The volume discontinuity at T_{JT} also gives rise to a change in lattice enthalpy at the transition. This discontinuity occurs in the counterintuitive direction: the high-temperature, disordered, state actually has a lower molar volume than does the low-temperature orbital ordered state [258]. Consequently the change in lattice enthalpy favours the disordered state and will act to balance the cost in crystal field energy determined above. In order to estimate the lattice enthalpy difference between O' and O phases the GULP simulation code [259] was used. The input consisted of atomic coordinates taken from the Rietveld refinements of neutron scattering data together with point (Mulliken) charges determined from *ab initio* calculations described below.

Mulliken charges were allocated on the basis of a spin-polarised DFT calculation using the Perdew-Burke-Ernzerhof (PBE) exchange-correlation functional [260] as implemented within CASTEP 6.11 [261]. The geometry was optimised starting from experimental values with an antiferromagnetic spin configuration. The resulting configurations agreed well with experimental data; unit cell lengths and Mn–O bond distances were 13% larger than experimental values, as expected for this functional. Charges for subsequent calculations were assigned from the final electron density.

Table 4.13: Local O atom coordinates used in crystal field energy calculations. The first six rows describe a typical *trans*-JT geometry and the subsequent six rows describe a typical *cis*-JT geometry.

Mn–O bond vector	x (Å)	y (Å)	z (Å)
1	1.925	0	0
2	0	1.959	0
3	0	0	2.153
4	−1.925	0	0
5	0	−1.959	0
6	0	0	−2.153
1	1.586	−1.433	0
2	−1.282	−1.426	0
3	−1.282	1.426	0
4	1.586	1.433	0
5	0.134	0	1.960
6	0.134	0	−1.960

Table 4.14: Crystal field stabilisation energies for $3d$ states in *trans*- and *cis*-JT MnO_6 geometries; all values are given in units of eV relative to the distortion-free $3d$ energy. Mixing of $3d$ and $4p$ states is forbidden for the *trans*- geometry but is symmetry-allowed for the *cis*-JT state.

Orbital symmetry	*trans*-JT	Orbital symmetry	*cis*-JT no d/p mixing	*cis*-JT d/p mixing
B_{3g}	−0.958	A_1	−0.795	−0.914
B_{2g}	−0.828	B_1	−0.620	−0.712
B_{1g}	−0.293	A_2	−0.688	−0.688
A_g	0.370	B_2	0.894	0.760
A_g	1.709	A_1	1.209	1.209

Table 4.15: Mulliken charges and corresponding lattice enthalpies (in eV) for the O' and O structures at T_{JT}. The first row contains the values determined in the DFT calculations, and the subsequent rows correspond to ±5% fluctuations in those values in order to explore the sensitivity of ΔH_{latt} values.

La charge	Mn charge	$H_{\mathrm{latt}}(O')$	$H_{\mathrm{latt}}(O)$	ΔH_{latt}
1.47	0.84	−95.4368	−95.5515	0.1147
1.42	0.89	−95.2437	−95.3582	0.1144
1.52	0.79	−95.7787	−95.8937	0.1151

Ultrasoft pseudopotentials were generated on-the-fly using the default CASTEP parameters. The plane-wave basis set was truncated at 21.6 Ha, and the Brillouin zone was sampled using two equally-weighted k-points equivalent to a $2 \times 2 \times 2$ Monkhorst-Pack grid. At these values the total energy had converged to within 15 meV, which is well within the error of subsequent calculations. A Hubbard U potential of 4 eV was applied to the Mn atoms; this value was based on literature fits to experimental enthalpies of oxidation of manganese oxides [262] and has been used in previous studies of $LaMnO_3$ [263]. As a check, the calculations were repeated with a potential of 8 eV [264]; the charges varied by less than 6%. The calculations were similarly repeated using the local density approximation (LDA); here the charges varied by less than 7%.

Lattice enthalpy changes were then calculated using the Mulliken charges taken from the first principles calculations. In Table 4.15 these are compared with the values obtained for 5% variation in the charges in order to determine the sensitivity of the enthalpy difference obtained to errors in the DFT results. In all cases the difference between O' and O lattice enthalpies was equal to 0.115 ± 1 eV, corresponding to a total enthalpy cost of roughly 40 meV and a transition temperature of 884 K. Given the robust nature of the lattice enthalpy calculations, the greatest uncertainty in these calculations is likely the ligand field parameter used in crystal field calculations together with estimation of the extent of d/p mixing. We explored the effect of perturbations in these values on the final transition temperature obtained: a ±10% change in parameters gives transition temperatures between 500 and 1270 K. While this range is large, it nonetheless demonstrates that the balance of energy terms is appropriate for a transition that takes place at temperatures of the order of 1000 K.

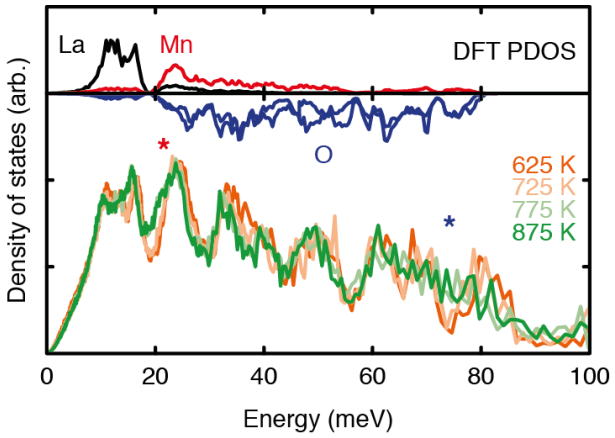

Figure 4.15: Normalised phonon densities of states at 625, 725, 775 and 875 K obtained using inelastic neutron scattering measurements. The DFT partial densities of states (PDOS) are shown in the top part of the figure, from which it is clear that the largest discontinuity observed across the orbital order/disorder transition occurs in a region of the phonon spectrum dominated by Mn displacements (marked by a red asterisk). The feature that dominates discussion in Ref. 265 is the broadening of O atom displacements between 60 and 80 meV (marked by a blue asterisk). Figure adapted from Ref. 265.

4.3.3.2 Inelastic Neutron Scattering

Ref. 265 reports the results of a recent high-temperature inelastic neutron scattering study of $LaMnO_3$, where the authors interpreted their results with reference to a series of first principles DFT calculations. The phonon densities of states measured in this study are given in Fig. 4.15. For the most part there is relatively little change in the phonon spectrum across the order/disorder transition other than subtle shifts in peak positions arising from thermal expansion effects; this is pointed out by the authors. There are however discontinuities within two main regions of the phonon spectrum: near 20 meV and again near 75 meV. The former is not discussed in Ref. 265 whereas the latter is attributed to broadening of the MnO_6 coordination polyhedra accompanying orbital disorder. It should be noted however, that the changes in the density of states between 725 K and 775 K in these regions is much larger than the changes observed for either 265–725 K or 775–875 K and hence they cannot be ascribed to anharmonicity effects. The authors' DFT calculations allow coarse assignment of the density of states. Taking into account the slight mismatch in energies, the region near 20 meV for which there is a discontinuous change is dominated by displacements of

the Mn atoms. In an earlier paper, Ref. 266 the same group made use of this DFT model to predict a number of thermodynamic properties, including the atom-specific displacement parameters. That the Mn displacements were severely underestimated within the disordered phase is consistent with the shift to lower energies for the Mn-dominated phonon density of states. Taken together, these observations are consistent with a microscopic structural model in which the Mn coordination environment changes symmetry across the orbital order/disorder transition.

4.4 Discussion

4.4.1 Enthalpic Considerations

Having observed this unexpected alteration in local symmetry across the transition, it now comes to us to consider why such a fundamental change might occur—especially given the large ($\sim 1.7\,\mathrm{eV}$) JT stabilisation of the electronic ground state. Based on the coordination geometries discussed above, it is possible to calculate the difference in crystal field and lattice energies for the *trans*- and *cis*-JT states. The corresponding crystal field splittings for the two geometries are shown in Fig. 4.16; both configurations are stabilised with respect to the undistorted octahedral case (*i.e.* they are both valid JT distortions), but the *cis*-JT geometry lies *circa* 150 meV higher in energy. The energy difference is balanced, however, by a 115 meV decrease in lattice enthalpy that arises from the (anomalously) smaller volume of the MnO_6 coordination geometry in the high-temperature *cis*-JT state [§ 4.3.3.1]. The volume of the *cis*-JT geometry is smaller than that of the *trans*-JT by around 1.5%, corresponding to a unit cell volume reduction of comparable magnitude to that observed in experiment—$0.6\,\text{Å}^3$ compared to $0.9\,\text{Å}^3$ [267]. This leaves a sufficiently small ($\sim$35 meV) total enthalpy change ΔH_{JT} associated with the *cis*/*trans* switching that the process may be driven by entropy.

4.4.2 Configurational entropy

Specific heat measurements indicate an entropy change $\Delta S_{\mathrm{JT}} = 0.515(\pm 0.02)R$ associated with the orbital disordering process in $LaMnO_3$ [245]. Taking this value alongside the enthalpy change listed above, calculations predict a crossover in free

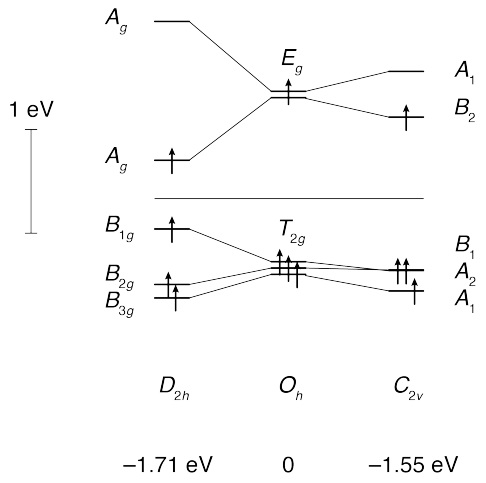

Figure 4.16: The crystal field splittings for the two different JT distortions, labelled according to their approximate symmetry. The effects of d/p mixing are included where relevant, but $4p$ states have been omitted for clarity.

energies for the two JT states at a critical temperature $T_c = 880\,\mathrm{K}$—surprisingly close to the experimental value of 750 K. This level of agreement is probably quite serendipitous, though even with significant perturbations the calculations still return a T_c of order 1000 K.

Considering now the origins of the observed entropy change, if this value can be interpreted entirely in terms of configurational entropy, then the various descriptions of orbital order presented in the literature can be summarised in the following way.

1. **Orientationally-disordered nanodomains of *O′*.** The configurational entropy within an individual nanodomain is vanishingly small, so in this model the configurational entropy arises from the number of possible nanodomain orientations. For nanodomains of average dimension L (in units of Mn–Mn separations), one obtains

$$\Delta S = L^{-3} \ln 6, \tag{4.19}$$

since each domain has six degrees of freedom. The experimental value of ΔS requires $L = 1.5$, which suggests that most "nanodomains" would not persist beyond a single MnO_6 octahedron. The formulation in Eq. (4.19) breaks down in this case, because not all six degrees of freedom (translational and rotational) are realistically available to every MnO_6 octahedron.

2. **Decoupled static or dynamic disorder of *trans*-JT distortions.** In this model, each MnO_6 octahedron samples any one of the three possible axial arrangements of *trans*-JT distortions; the strain associated with coupled distortions is neglected [245]. The corresponding configurational entropy $\Delta S = R \ln 3 = 1.098R$ is larger than that observed experimentally, but it is widely accepted that strains will be too large for this model to provide a realistic description of orbital order.

3. **Three-site antiferrodistortive Potts model on a cubic lattice.** In this model, the three *trans*-JT states interact via an effective Hamiltonian that penalises like orientations on neighbouring sites. In this way, the model crudely accounts for the lattice strain that arises were neighbouring MnO_6 octahedra to be joined by two consecutive long Mn–O bonds [245, 247, 268]. The ground state of this system has a configurational entropy $\Delta S \simeq \frac{1}{2} R \ln 2 = 0.347R$, which is too small to account for the experimental value.

4. **Orientationally-disordered nanodomains of a three-site antiferrodistortive Potts model.** This hybrid approach was proposed in Ref. 245, and involves accounting for the difference between experimental and three-site Potts entropies by including an additional $L^{-3} \ln 6$ term associated with orientational disorder of decoupled three-state Potts regions. The requisite value of L is then 2.3, which suggests that coherent three-state Potts correlations persist only over pairs of neighbouring MnO_6 octahedra. Consequently, the strain term associated with this model is unlikely to be realistic.

5. **Anisotropic three-site antiferrodistortive Potts model.** This modification of the Potts model takes into account the relationship between orbital orientations and the vector joining adjacent sites [269]. The point is that like orientations of *trans*-JT distortions on neighbouring sites only give rise to large strains if the distortion axis is parallel to the vector joining the two sites. This model has a configurational entropy close to $R \ln 2 = 0.69R$, but is not strain-free because Mn centres joined by, say, a pair of Mn–O bonds where one is long and one is short are assumed to adopt an equivalent separation to two centres joined by a pair of short Mn–O bonds.

A transition to a *cis*-JT distortion as observed in these RMC refinements might be expected to exhibit a positive value of ΔS_{JT} for a couple of reasons. Firstly, there are twelve possible distortions axes for a given octahedron, compared to only three for the *trans* distortion, and secondly, the variance in octahedral axis dimensions [§ 4.3.2.5] is an order of magnitude lower than for a *trans* arrangement, minimising the strain involved in sampling different JT orientations and favouring dynamical nano-domain evolution.

A model of uncorrelated distortion orientations for the *cis*-JT distortion would predict a large configurational entropy ($R \ln 12 = 2.48R$) that is clearly inconsistent with the experimental value. But two empirical correlations were observed to occur between neighbouring MnO_6 octahedra that act to reduce this value: first, there is a strong tendency for long-bond avoidance on shared sites; and, second, there is evidence of ferrodistortive coupling between neighbouring octahedra. Taking the first of these correlations by itself, it can be shown that the resultant configurational entropy is close to $R \ln 8 = 2.08R$. Ferrodistortive coupling with a coherence length of *ca* 6 Å reduces this value to $0.6R$, which is close to the experimentally observed value. Consequently, it would seem that the driving force responsible for ferrodistortive correlations is likely to be electronic in nature.

To summarise, the emerging picture is one of an entropy-driven 'excited' JT state that is stabilised relative to the ground state JT distortion at sufficiently high temperatures [Fig. 4.2], in a situation that mirrors that of the thermally-driven symmetry lowering in lead chalcolgenides [270]. Of relevance to the doped manganite compounds is the observation that the geometry of the O_6 octahedral shell in the *cis*-JT distortion deviates 50% less markedly from the Mn^{4+} environment in $CaMnO_3$ [103] than does the *trans* geometry. Consequently the negative value of $\mathrm{d}T_{\mathrm{JT}}/\mathrm{d}x$ likely reflects the effect of reduced strain on the value of ΔH_{JT} as x increases. Finally it is noted that a return to *trans*-JT distortions in the higher temperature R phase suggests that the situation is finely balanced between the free energies of competing distortions, the lattice symmetry and the activation of different octahedral tilt systems.

4.4.3 Other Considerations

The JT-switching model presented here also helps to rationalise a number of other observations concerning this transition. Firstly, Mn K-edge EXAFS measurements have previously suggested a change in the Mn environments across the transition, beyond nearest-neighbour Mn–O distances [245, 246, 271]—it has already been seen that the refinements presented here can reproduce these features [§ 4.3.2.9]. XANES measurements have presented the results that Mn $3d/4p$ mixing occurs at the transition [246], a process that is forbidden unless the Mn environment becomes acentric, making these results difficult to interpret under the established order/disorder model of the transition.

This $3d/4p$ mixing, combined with the changes in Mn. . .Mn distances and Mn–O angles that occur, will renormalise the electronic bond structure, and could therefore account for the resistivity anomaly observed at T_{JT} [237].†

Off-centering of the Mn atom in the *cis*-JT distorted octahedra would lead to the creation of a dipole moment, meaning one would expect to see evidence of this in dielectric spectroscopy. Indeed a relaxor-like dielectric anomaly has been measured in Ref. 272, with the suggested explanation being the emergence of a nanoscale polar domain structure. The results of this study show that this observation and interpretation would in fact be consistent with neutron and X-ray scattering data.

As demonstrated above, the measured value of ΔS_{JT}—too large to be accounted for by previous models of orbital disorder (*e.g.* three-state Potts [268])—can now be quantitatively explained. The statistical sampling of all twelve possible *cis*-JT orientations can account for both the emergent isotropy in ferromagnetic interactions and the pseudocubic metric of the O phase $Pbnm$ cell [235].

The discontinuity in cell volume at the transition reflects the change in the MnO_6 coordination geometry, and consequent volume reduction [§ 4.3.2.5]. The discontinuity in the Mn atomic displacement parameters reported here [§ 4.3.2.4] and elsewhere [235, 266] can be explained by Mn off-centering. This could also suggest an origin for the anomalous shift in phonon energies associated with Mn displacements recently measured using inelastic neutron spectroscopy [§ 4.3.3.2 and Ref. 265].

†Unfortunately the understanding required to perform accurate density functional calculations on states that are both excited and extensively disordered is not currently available, so supporting *ab initio* calculations cannot be provided at the present time.

The implications of a JT symmetry transition reach beyond the specific case of $LaMnO_3$. At the heart of functional oxide science are the possibilities available for exploiting the complex relationships between structural, electronic, magnetic and orbital degrees of freedom. The discovery that orbital transitions can be associated with finely balanced shifts between fundamentally different electronic states hints at the possibility that orbital switching transitions could play a key role in manganite physics. Certainly it seems likely that any polaronic phase that emerges upon doping will be more complex than was perhaps previously envisaged, with the potential for coupling between hole localisation and Mn off-centering. If nothing else, then the observation of an unexpected local structure within orbital-disordered $LaMnO_3$ serves to highlight the importance of characterisng fully the disordered states of matter from which so much of contemporary condensed matter physics is found to emerge.

4.5 Conclusions

Rietveld average structure refinements, and both small- and large- box local structure refinements have been performed using newly-collected neutron and X-ray total scattering data. RMC refinements, using the RMCProfile code, have produced large atomistic configurations, consistent with both average and local structural information, and form the backbone of this study. They have been shown to be consistent with previously published results from a range of sources covering both average and local structure techniques.

The key finding from the work is that the local symmetry of the JT distorted MnO_6 octahedra changes from a centrosymmetric to an acentric arrangement when moving from the orbitally ordered phase to the pseudocubic phase. This demonstrates that in fact the established view of the transition as a simple change from long-range to short-range order is incorrect, or at best, incomplete.

The two different JT distortions have been characterised, and compared in detail. The transition from *trans*- to *cis*-distortions has been shown to explain a number of other previously unaccounted for observations, including dielectric, X-ray absorption, and volume anomalies at T_{JT}. Again this illustrates the benefit of taking an holistic approach to structural modelling.

The interplay between orbital and structural degrees of freedom would appear to be quite finely balanced. This suggests that there could be more unexpected results found for doped phases, *e.g.* $La_{1-x}Ca_xMnO_3$, particularly in the dynamic polaron region of the phase diagram. This could provide a further opportunity to test the ability of the RMC technique, particularly with regard to modelling substitutional disorder.[‡] Finally, this unexpected result in what was thought to be a straightforward and well-understood order-disorder transition hints at the possibility that other seemingly uncomplicated order-disorder transitions may in fact be masking some hidden complexity.

[‡]It should be noted of course that the techniques used here are not directly sensitive to dynamics.

Chapter 5

Magnetism and charge ordering in Fe_3O_4

Having looked at a system concerned primarily with charge ordering, and one concerned primarily with orbital ordering, we now move on to a more complicated system concerned with both charge and magnetic ordering—magnetite, or Fe_3O_4.

5.1 Magnetite and the Verwey Transition

The study of magnetite goes back a remarkably long time. As the naturally magnetic mineral commonly referred to as lodestone, it was the first known magnetic material, and indeed references to it date back more than 2500 years.* Early uses included primitive compasses for maritime navigation [273]; nowadays it is far more likely to be found as a catalyst [274]. Some organisms have also made use of the mineral [275]: magnetotactic bacteria such as *Magnetospirillum magnetotacticum* [276] use magnetic alignment of carefully grown crystals to navigate towards more favourable conditions, while pigeons are thought to achieve remarkable navigational ability through the use of magnetic material located in their necks [277, 278].

The room temperature structure of magnetite [Figure 5.1] is well known and understood—it has the AB_2O_4 inverse spinel structure with cubic $Fd\bar{3}m$ symmetry, where tetrahedral (A) sites are occupied by Fe^{3+} ions, and equal numbers of Fe^{2+} and Fe^{3+} ions are distributed across the octahedral (B) sites—however the low temperature structure is an area of contention. The extensive amount of research that

*One of the first references occurs in Aristotle's *De Anima* 1.2, 405a19, though the author of this text concedes he has not read it himself.

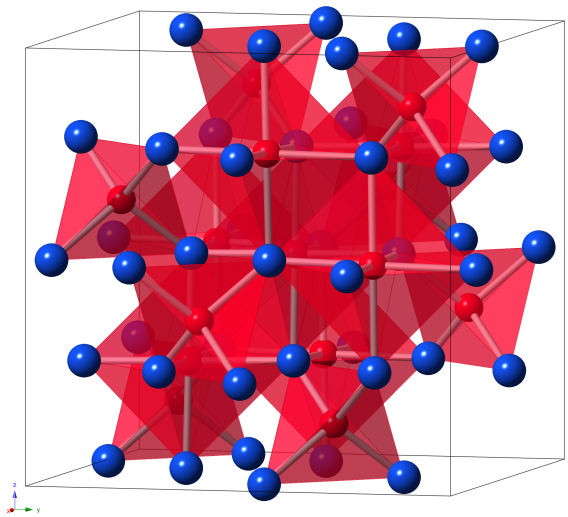

Figure 5.1: The room temperature structure of Fe_3O_4. Iron atoms are coloured red, and oxygen atoms blue.

has been done on this system makes a complete review of the literature here unmanageable. Instead some of the more salient points in the story will be covered, and the reader is referred to published review articles for a complete discussion [279, 280].

In 1939, prompted by an earlier heat capacity study [281], Verwey observed that magnetite exhibits a strong discontinuity in its conductivity at around 120 K [282] [Fig. 5.2]. This led to extensive attempts to explain the phenomenon, and understand the accompanying structural distortion, sparking the huge interest in the material that has continued until this day. It was originally postulated that charge ordering of the Fe^{2+} and Fe^{3+} ions on the octahedral sites was the origin [283], and while some studies at first seemed to confirm this model [284], it was later shown to be incorrect [285]. This left open the question of what was the low temperature structure of magnetite, and did it exhibit any charge ordering?

Early studies were hampered by certain obstacles that stood (and still stand) in the way of what might otherwise have been a relatively straightforward process. The non-stoichiometry of Fe_3O_4 is arguably the biggest challenge, and it was not until the Mott conference in 1979 that the need for extreme care during sample preparation and quality control was widely recognised [279]. The structural distortion lowers the symmetry from cubic to what is generally believed to be a monoclinic symmetry, causing extensive twining to occur, adding to the difficulties of single crystal work.

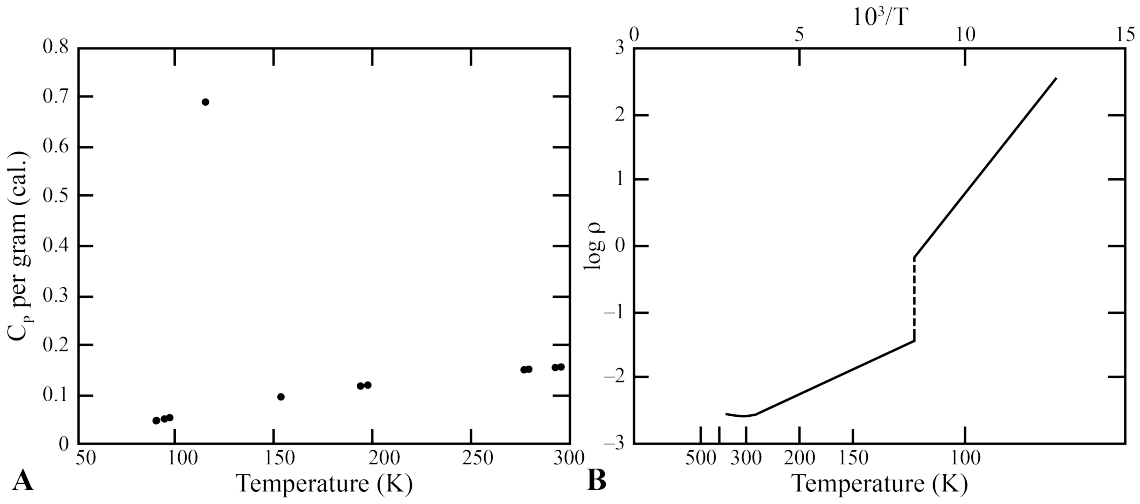

Figure 5.2: Early evidence for the Verwey transition in magnetite. A: A heat capacity anomaly at around 115 K was reported in Ref. 281. B: Verwey observed a discontinuity in the resistivity of magnetite. Panel adapted from Ref. 282.

Finally, the distortion away from cubic symmetry is very subtle, making accurate measurement difficult, even with modern instruments. The combination of these challenges means that early progress was slow, and it is only comparatively recently that significant advances have been made.

Diffraction has arguably been the principal technique in this search, with a high quality single crystal study of a stoichiometric single domain sample being the ultimate goal. A great many other techniques have been applied to the problem: Mössbauer spectroscopy [286–289] and ^{57}Fe NMR [290–292]—both of which are sensitive to the local Fe environments—EXAFS [293], and resonant diffraction [294, 295]. Many charge ordering schemes have been proposed [296–298], some of which satisfy the Anderson criterion for minimising electrostatic repulsion [299], and yet no single model has been universally accepted.

A number of more recent studies have obtained reliable structure solutions from high quality samples: Iizumi *et al.* used neutron single crystal scattering and a detwinned crystal [300]; Wright *et al.* used a combination of high resolution neutron and synchrotron data and a highly stoichiometric powder sample, avoiding the twinning issue [251, 301]; and Senn *et al.* used high energy synchrotron scattering to perform a single crystal study on an individual 40 μm grain, also neatly avoiding the twinning problem [302]. These all concluded that the low temperature structure was best de-

scribed by a monoclinic Cc symmetry unit cell four times larger than the $Fd\bar{3}m$ unit cell [Fig. 5.3]; however, in some cases the refinement was performed using a higher symmetry approximation. Other studies using different techniques have ruled out any symmetry higher than triclinic [303–305]; however, a Raman and infrared study subsequently ruled out all spacegroups lacking an inversion centre [306]. It is clear that this is not a straightforward system to study, and it is certainly not as straightforward as the initial model suggested by Verwey. For one thing, it has been shown repeatedly that charge ordering of Fe^{2+} and Fe^{3+} ions is not present—any charge ordering observed consists of intermediate charge states [280, 307, 308].

As may be expected, the magnetic structure of magnetite has also received much attention over the years—indeed it was one of the first compounds to be studied in the early days of magnetic neutron scattering [309, 310]. Néel was the first to suggest a ferrimagnetic arrangement of the magnetic moments on the Fe sites [311, 312], and this was soon corroborated [310]. The simplest spin model assumes integral charges, where the A site Fe^{3+} ions have a moment of $-5.0\,\mu_B$, and the B site Fe^{3+} and Fe^{2+} ions have moments of $+5.0\,\mu_B$ and $+4.0\,\mu_B$. The orbital moments are quenched, and the moments on the Fe^{3+} ions cancel, giving a net spin moment of $+4.0\,\mu_B$.

This simplified picture may not be representative of the true situation. While it is well accepted that this ferrimagnetic model fits the data well, there is a paucity of neutron diffraction studies where the moments are explicitly refined. Iizumi *et al.* hoped to derive the charge ordering in the low temperature structure from magnetic scattering measurements, but failed to refine the B site moments with reasonable uncertainties [300]. The study by Wright *et al.* did present refined moments, but constrained all moments to lie along the c axis, with a single magnitude for all A sites and a second magnitude for all B sites ($+4.44(3)\,\mu_B$ and $-4.17(2)\,\mu_B$ respectively) [251].

Most studies have measured instead the average moment for the bulk sample, through for example X-ray magnetic circular dichroism (XMCD) or spin-polarized Compton scattering, which are then interpreted as the net moment from the octahedral Fe^{2+} ions—the Fe^{3+} ions having cancelled out. These have not always agreed with one another, particularly on the issue of the orbital contribution. Some studies reported negligible orbital contributions [313–317], while others reported larger val-

ues, such as $0.65\pm0.07\,\mu_B$ [318] or $0.51\pm0.05\,\mu_B$ [319]. This has perhaps now been resolved, with the publication of a further study revealing the presence of large orbital moments of $>1\,\mu_B$ per atom on both the A and B sites, but which cancel out making them invisible to methods that average over the whole cell [320]. This cancellation is quite sensitive to oxygen stoichiometry, with any deviation from perfect stoichiometry potentially leading to an imbalance, which could explain why an orbital contribution has previously been observed in some cases.

Returning to the spin moments that have been observed, there has been some variation in the reported values: these range from $3.54\pm0.05\,\mu_B$ [319], to $3.68\pm0.09\,\mu_B$ [318], $3.90\pm0.09\,\mu_B$ [313], and $3.98\pm0.03\,\mu_B$ [316]. As can be seen these are reasonably close to the expected value of $+4.0\,\mu_B$. It is worth mentioning that these data have been collected at a range of temperatures and magnetic fields, but that no anomalies have been observed in the magnetic behaviour across the transition [316], other than the switch in the magnetic easy axis from $\langle 111\rangle$-type directions above T_V to parallel to the c-axis at low temperatures [321–323].

There is certainly still scope for further research to be performed on magnetite, and the apparent discrepancy between conventional diffraction [251, 300–302] and magnetoelectric [303, 304] studies hints at the possibility of localised symmetry lowering. It would be reasonable to expect that local structure probes may be well suited to this problem, as they will not be troubled by the difficulties faced by average structure probes as outlined previously, and are specifically sensitive to localised distortions. RMC methods have also proved sensitive to complex magnetic structural features in previous studies, such as MnO [130, 133] and FeO [324], so it is possible that total scattering methods may be able to provide some insight into this system as well. As in the preceding chapters of this thesis, this study is based around RMC refinements of total scattering data. The main distinction is that in this case there is a magnetic contribution to the scattering intensity, requiring the magnetic moments of the iron atoms to be included in the refinement. Two different magnetic moments are included, representing the "Fe^{2+}" and "Fe^{3+}" ions, and these two different moments are allowed to swap positions across different sites. This combination of magnetic refinement and swapping atoms between sites explores new territory for the RMCProfile code, and acts as a testing ground before these features are required

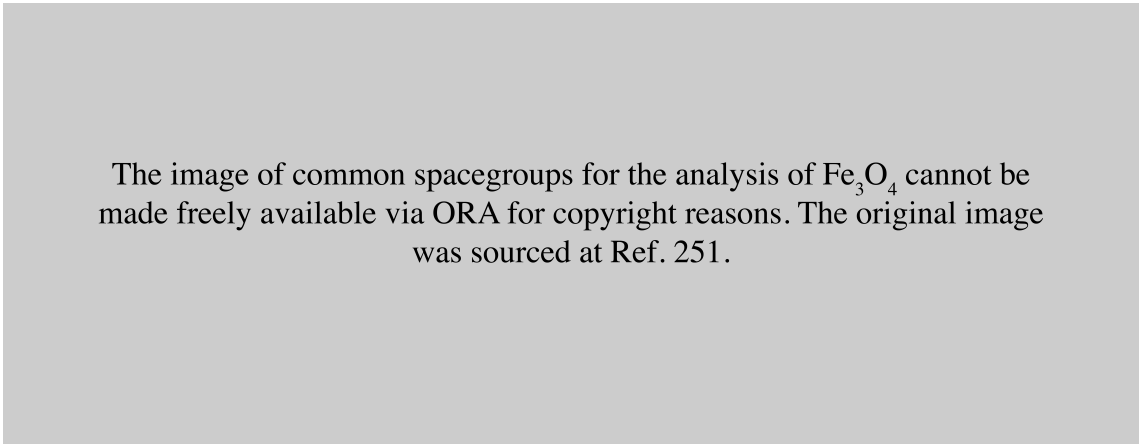

Figure 5.3: Some common space groups used during the analysis of Fe_3O_4, showing the relationships between them [251].

for analysis of the $La_{1-x}Ca_xMnO_3$ series (which will be carried out by a subsequent student).

5.2 Experimental

5.2.1 Sample Preparation

The sample[†] is a highly stoichiometric polycrystalline sample of $Fe_{3-3\delta}O_4$, where $\delta < 0.0001$, produced using the skull melter technique [325], and is the same sample that has been used in Refs. 251, 301, 302, 326, 327. Hence it is of reliable quality, and there are no concerns over its purity.

5.2.2 Data Collection

Neutron total scattering data were collected on the GEM diffractometer at ISIS, at a temperature of 10 K. The collection spanned scattering vectors in the range $1 > Q > 50\,\text{Å}^{-1}$, giving real-space resolution of the order $\Delta r \simeq 0.08\,\text{Å}^{-1}$. Appropriate corrections were performed using standard methods to account for the effects of background scattering, absorption, beam intensity variations, multiple scattering, and the Placzek inelasticity correction [7, 34]. The data were then transformed into the function $F(Q)$ (as described in Eqn. 1.9) and the Bragg intensities were extracted. No conversion into a real-space function was performed, as the magnetic component

[†]Kindly provided by Prof. J. Paul Attfield.

of the scattering could not be separated from the nuclear component, meaning that an accurate pair distribution function could not be produced.

5.2.3 Structure Refinements

Rietveld average structure refinements were first performed using the GSAS software package [224]. The purpose of carrying out these refinements was to obtain a reliable set of lattice parameters for use with the subsequent RMC refinements, and to check for consistency with previous studies, rather than to gain any unique insight into the problem. The subtlety of the structural distortion makes a stable refinement of Fe_3O_4 at low temperatures somewhat difficult. To simplify the process a $P2/m$ unit cell was used, rather than the larger and more complex Cc cell reported elsewhere, and additional $Fd\bar{3}m$ symmetry constraints were added to improve the robustness. This approximation has been used previously in other powder refinement studies [251]. Isotropic displacement parameters were used, and were constrained to be the same for all atoms, again to improve the stability of the refinement. Magnetic moments were constrained such that tetrahedral Fe atoms all had the same magnitude of moment, and pointed along the c-axis in the positive direction, while octahedral Fe atoms were also constrained to share the same magnetic moment (but distinct from that of the tetrahedral sites), and had moments fixed along the negative c-axis. This constraint has also been used previously [251].

The fits produced are shown in Figure 5.4. It can be seen that not all the intensities are well reproduced, but the peak positions are good: this is sufficient to fulfil requirements. Refined lattice and atom parameters are displayed in Table 5.1 alongside values from Ref. 300. It can be seen that there is good agreement between the two.

RMC refinements were performed using the RMCProfile code. Starting configurations were produced from $8 \times 8 \times 6$ supercells of the GSAS refined $P2/m$ cell (10 752 atoms, $\sim$50 Å width). This size was chosen as it is roughly cubic, and so maximises the useful volume, and because this is equivalent in size to a $4 \times 4 \times 3$ supercell of the Cc unit cell setting, allowing easy comparison with previous studies that used this cell.

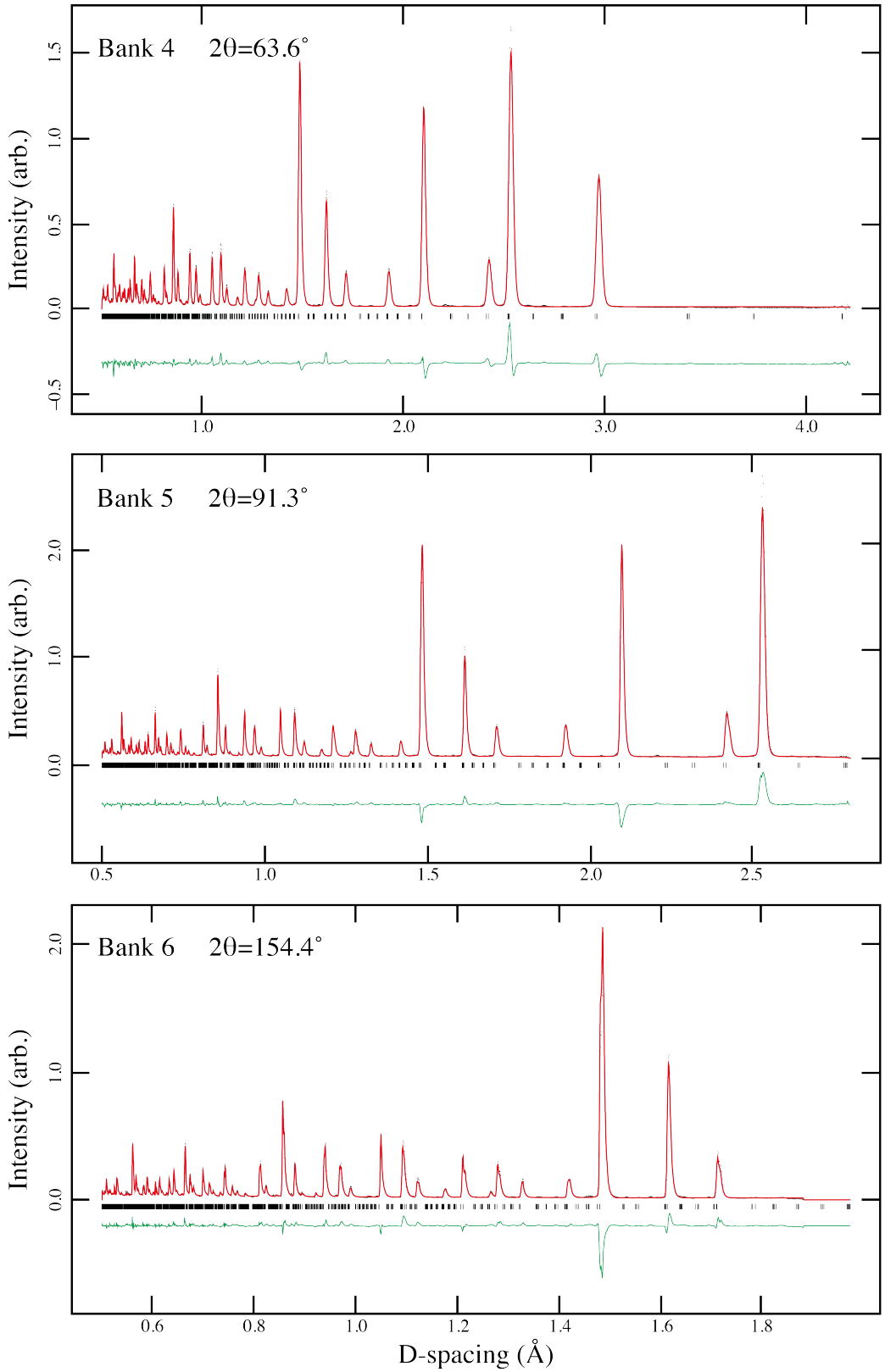

Figure 5.4: Shown above are the GSAS Rietveld refinement fits to the Fe_3O_4 neutron scattering data collected on the GEM diffractometer. Data are represented as black dots; the calculated fits by red lines; and the difference curves are plotted in green. Reflection positions are indicated by black tick marks.

Table 5.1: The results of the Rietveld refinement are displayed in the table below. Atom parameter entries in *italics* denote results from Ref. 300.

	This study			Ref. 300	
Crystal system	Monoclinic			Monoclinic	
Space group	$P2/m$			Cc	
a (Å)	5.9346(5)			5.934(2) (*equivalent*)	
b (Å)	5.9169(4)			5.926(2) (*equivalent*)	
c (Å)	8.3844(6)			8.376(4) (*equivalent*)	
β (°)	90.242(6)			90.20(3)	
V (Å^3)	294.414(7)			294.5(8) (*equivalent*)	
Z	4			4 (*equivalent*)	
T (K)	10			10	
Atom	x	y	z	U_{iso} (Å^2)	Mult.
FeA1	0.25	0.5	0.375	0.00132(5)	2
	0.25	*0.5067(2)*	*0.3774(1)*	*0.0006(4)*	
FeA2	0.25	0	0.125	0.00132(5)	2
	0.25	*0.0049(3)*	*0.1270(1)*	*0.0006(4)*	
FeB1	0.25	0.75	0.75	0.00132(5)	4
	0.25	*0.7549(5)*	*0.7492(2)*	*0.0001(3)*	
FeB2	0	0.5	0	0.00132(5)	1
	0	*0.5*	*0*	*0.0016(5)*	
FeB3	0	0	0.5	0.00132(5)	1
	0	*0.0099(3)*	*0.5*	*0.0018(5)*	
FeB4	0.5	0.5	0	0.00132(5)	1
	0.5	*0.5*	*0*	*0.0016(5)*	
FeB5	0.5	0	0.5	0.00132(5)	1
	0	*0.0099(3)*	*0.5*	*0.0018(5)*	
O1	0.01173(11)	0.5	0.75586(5)	0.00132(5)	2
	0.0067(6)	*0.4950(3)*	*0.7512(1)*	*0.0014(5)*	
O2	0.25	0.76173(11)	0.50586(5)	0.00132(5)	4
	0.25	*0.7696(6)*	*0.5054(2)*	*0.0025(5)*	
O3	0.48827(11)	0.5	0.75586(5)	0.00132(5)	2
	0.4933(6)	*0.5050(3)*	*0.7512(1)*	*0.0014(5)*	
O4	0.25	0.73827(11)	−0.00586(5)	0.00132(5)	4
	0.25	*0.7477(6)*	*−0.0009(2)*	*0.0016(6)*	
O5	0.51173(11)	0	0.25586(5)	0.00132(5)	2
	0.5116(6)	*0.0089(3)*	*0.2590(2)*	*0.0022(5)*	
O6	−0.01173(11)	0	0.25586(5)	0.00132(5)	2
	−0.0116(6)	*0.0089(3)*	*0.2590(2)*	*0.0022(5)*	

Configurations were refined against Bragg and $F(Q)$ data sets. As mentioned above, no PDF data could be used due to the presence of magnetic scattering. Magnetic moments on Fe atoms were included in the refinement to allow fitting of the magnetic scattering components in the data. Two magnitudes of moment were included, to allow for some Fe sites being nominally "Fe^{2+}" and others "Fe^{3+}". Several types of move were allowed during refinements: standard translational moves; rotations of magnetic moments on Fe atoms; and swapping moves. Swapping moves were only allowed between different Fe atoms, to permit the "Fe^{2+}" and "Fe^{3+}" moments to explore varying arrangements throughout the configuration.

The ratio of each type of move generated can be controlled. Experience suggests that best results are obtained by alternating between only allowing translational moves, and allowing magnetic moment and swap moves together. This iterative approach allows the refinement to focus on improving the fit to the nuclear scattering, and then focus on the fit to the magnetic scattering. Allowing all three moves simultaneously leads to predominantly translational moves being accepted, with almost no successful swap moves.[‡]

Standard refinements (which we shall call type A) began with only translational atom moves allowed. Magnetic moments were initially set to the GSAS-refined values and positions, *i.e.* tetrahedral sites with a moment of $4.625\,\mu_B$ aligned in the positive c-direction, and octahedral sites with a moment of $4.130\,\mu_B$ aligned in the negative c-direction. Refinements were continued in this manner until little further improvement in χ^2 was made. Typically this was found to occur after 17 000 minutes had elapsed. After this process was complete, the moments were changed so that tetrahedral sites were now $5.0\,\mu_B$ and octahedral sites were 50 % $5.0\,\mu_B$ and 50 % $4.0\,\mu_B$. Refinements were then continued, allowing spin moves and swapping to take place with equal probability of generation, but without any translational moves. This stage proceeded until little further improvement was made to the χ^2, or until few swapping moves were accepted—whichever occurred first. Finally, the configurations were refined once again using translational moves only until the χ^2 reached a steady state, which typically occurred after a further 4 000 minutes.

[‡]Swap moves are generally far less likely to be accepted than the other two types of move, as they can often lead to substantial (negative) changes in the fit.

To explore the effects of the initial conditions on the refined magnetic structure, three other variations of refinement were set up. These started with (i) magnitudes as above, but random orientations (type B); (ii) orientations as above, but 4.0/5.0 μ_B locations randomised (type C); and (iii) both random orientations and 4.0/5.0 μ_B locations (type D).

Example fits from the RMC refinements are shown in Fig. 5.5. As can be seen, good fits were obtained for the principal features in each data set, however it should be noted that the low intensity details in the Bragg data set were not adequately fitted. This is a consequence of the fitting process used in the RMC refinement, and the implications of this will be discussed later.

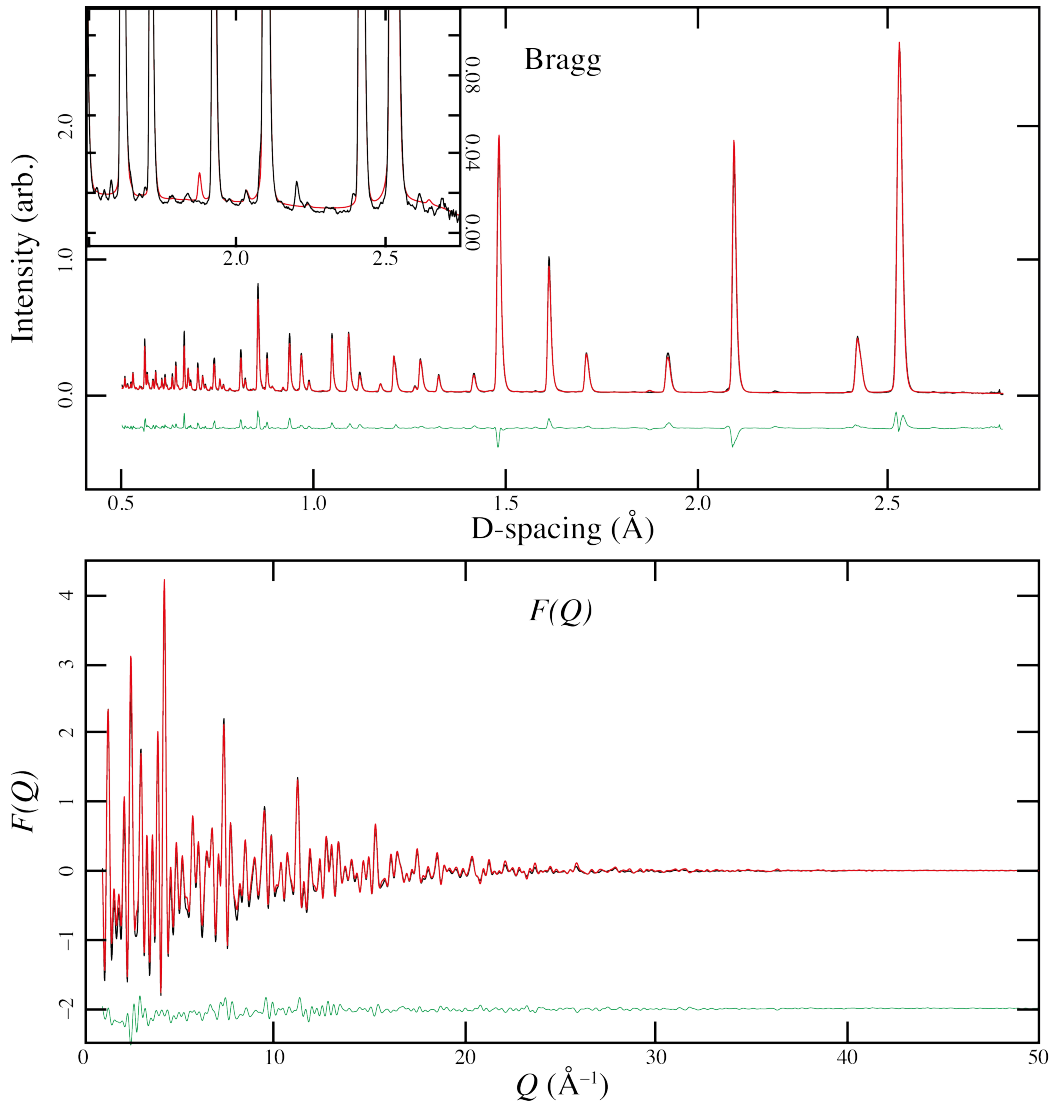

Figure 5.5: Shown above are the RMC refinement fits to the Fe_3O_4 neutron total scattering data collected on the GEM diffractometer. Top: fit to Bragg profile. Top inset: close up of low intensity peaks, showing poor fit. Bottom: fit to $F(Q)$ data. Data are shown in black; the calculated fits by red lines; and the difference curves are plotted in green.

5.3 Results & Discussion

5.3.1 Average Structure

As outlined in § 5.2.3, the Rietveld refinement carried out was a simple one, designed primarily to obtain reliable lattice parameters, and act as a reasonable starting point for the subsequent RMC refinement. As such we cannot expect any new insights to come from this refinement, but can confirm that so far our work is consistent with previous studies. It is quite possible that the RMC refinement may reveal something, however, and it is certainly sensible to check the average structure produced by the refinement to ensure it is realistic. This can be achieved by collapsing the refined configuration down onto a single unit cell and applying the symmetry operations of the appropriate space group. This also allows the positional variation for each atom site to be easily seen. A refined configuration that has been collapsed onto a $P2/m$ unit cell is shown in Figure 5.6. It can be seen that the sites have narrow positional distributions, as might be expected for low temperatures.

The FINDSYM online web program [328] was used to try to extract a space group from several collapsed configurations, after obtaining the average position for each site. This was attempted first using Cc cell settings, but it was found that the program could not cope with so large a cell, so a $P2/m$-sized unit cell was used instead. This reduced cell size meant that no information could be obtained regarding the suitability of the Cc unit cell in the average structure data. The results may be summarised as follows: for low tolerances the space group $P1$ was returned, as expected; for higher tolerances, higher-symmetry space groups were found, with some variation between refinements; above a threshold tolerance only spacegroup $Pma2$ was returned. The disorder inherent in RMC refinements will inevitably lead to a structure without any symmetry—if the allowed tolerances are low—producing a $P1$ spacegroup. This disorder will naturally lead to small variations between separate refinements, hence the variation present in the intermediate-tolerance regime. The spacegroup Pm occurred frequently, however, which may suggest a certain sensitivity to the mirror symmetry present in the Cc cell. By the time the $Pma2$ cell is returned, the tolerances are too high for the result to have much significance.

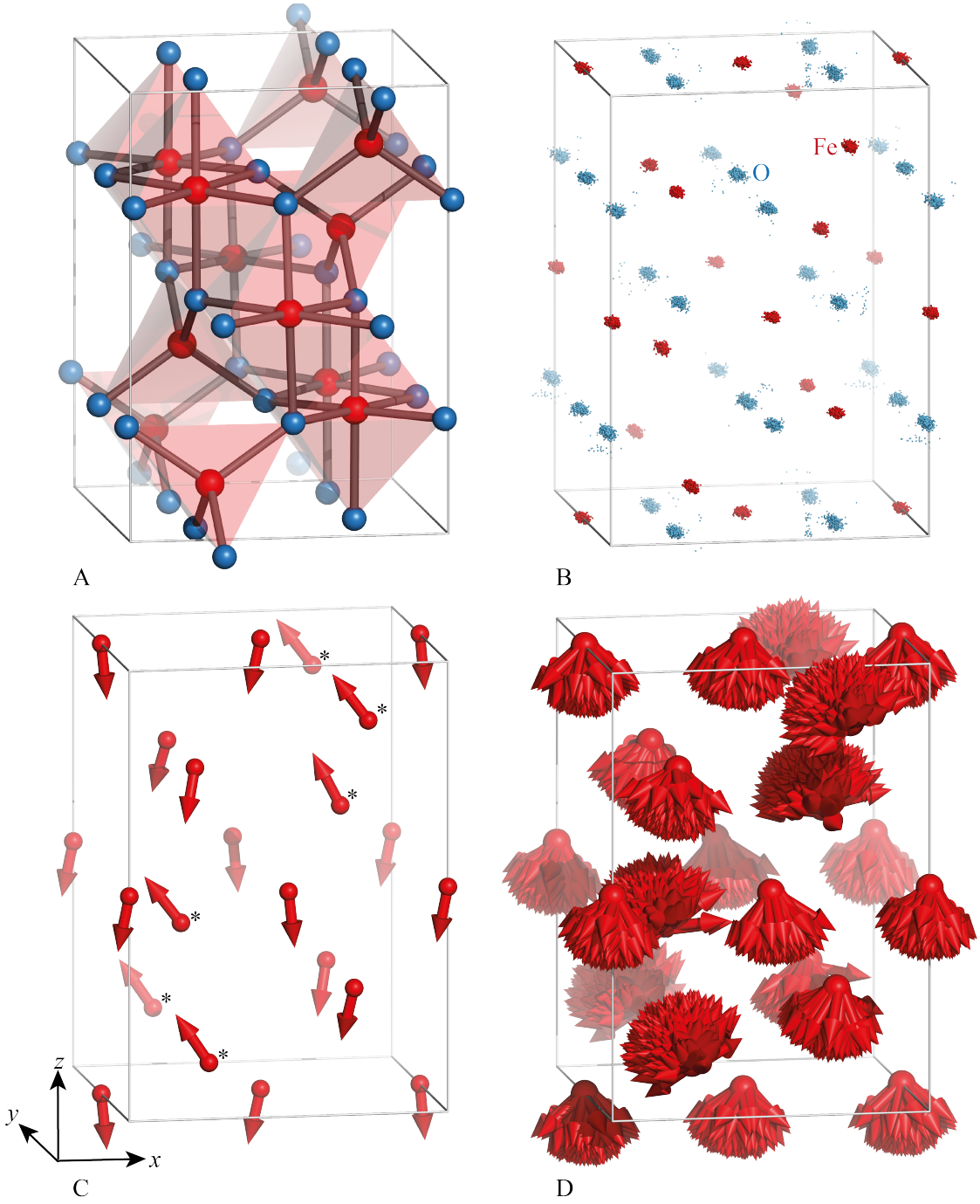

Figure 5.6: Refined $P2/m$ unit cells of Fe_3O_4. A: The GSAS–refined structure, highlighting the tetrahedra and octahedra present in the structure. *NB*: only complete polyhedra have been shown. B: The RMC–refined structure, collapsed down on to a $P2/m$ unit cell. C: The average magnetic structure obtained from RMC refinement. Tetrahedral sites are indicated by an asterisk. D: A complete RMC refinement of the magnetic structure, collapsed onto a single unit cell to show the variation on each site. Iron atoms are coloured red, and oxygen atoms blue.

The result of this is that no significant contribution can be made regarding the average (nuclear) structure of the low temperature phase of magnetite based on these RMC refinements. The disorder present in the refined structures is too large for the subtle distortions involved in the transition to be seen. Further confirmation of this comes from close examination of the fit to Bragg data for the RMC refinements [Figure 5.5, top inset]. Many small peaks and shoulders can be seen, evidence of symmetry lowering distortions present in the structure. Their small size in comparison to the main peaks (∼0.5 %) means that they are essentially ignored during the refinement process, leading to poor or nonexistent fitting by the model. To address this issue would require changes to be made to the RMCProfile code, and is beyond the scope of this project. Possible solutions might be to fit the Bragg data using a logarithmic intensity scale, to increase the significance of the low intensity peaks, or a fitting mechanism using the inverse of the intensity. These solutions are not simple and would require much further work to establish the best operating procedures.

5.3.2 Magnetic Structure

The RMC spin configurations were collapsed onto $P2/m$ unit cells to view the variation in spin orientation for each site. This was well-ordered, with the majority of spins pointing within a narrow distribution [Fig. 5.6 D]. The magnetic moments were also averaged for each site to give the structure shown in Figure 5.6 C. Certain features are clearly apparent. The tetrahedral sites align approximately ferromagnetically to one another, as do the octahedral sites, though the alignment between the two groups is roughly antiferromagnetic, and canted.

Considering first the orientations of the magnetic moments, there is good consistency in the final orientations of each site between refinements that start from the GSAS-refined orientations (types A & C). Not all octahedral sites point in exactly the same direction, but pairs of sites exist that do have very similar directions. These pairs are consistent across different refinements, though small variations in the orientation do occur between refinements. The coordinates of these pairs are listed below:

Group 1	$(\frac{3}{4}, \frac{1}{4}, \frac{1}{4})$	&	$(\frac{1}{4}, \frac{3}{4}, \frac{3}{4})$
Group 2	$(\frac{1}{4}, \frac{1}{4}, \frac{3}{4})$	&	$(\frac{3}{4}, \frac{3}{4}, \frac{1}{4})$
Group 3	$(\frac{1}{2}, 0, \frac{1}{2})$	&	$(0, \frac{1}{2}, 0)$
Group 4	$(0, 0, \frac{1}{2})$	&	$(\frac{1}{2}, \frac{1}{2}, 0)$.

As can be seen, these pairs are all separated by a vector $(\frac{1}{2}, \frac{1}{2}, \frac{1}{2})$.

For refinements that began with random spin orientations there is greater variability in the final absolute orientations for each site, though the relative orientations between octahedral and tetrahedral sites are reasonably consistent at about 130 ° [Table 5.2]. Octahedral sites are still paired up in the same combinations, though the distinctions between the pairs is less clear. Taken together, these results suggest that the most robust aspect of the refinement is the relative orientations between octahedral and tetrahedral sites, rather than the absolute orientations. Another implication is that, starting from a random set of spin orientations, it is much easier to reorient the spins such that they are correct with regard to one another, than it is to reorient them to a correct absolute orientation. This result was also found for MnO [130].

In contrast, when the distribution of $4.0/5.0\,\mu_\mathrm{B}$ spin magnitudes is examined, no patterns or features of note are observed. This suggests either that there is perhaps not enough information available to control the swapping moves of the different magnitudes and encourage some sort of ordering to form, or that any variation in magnitude for each site is accounted for by adjusting the spread of orientations for the sites in question, as a wider spread will tend to lower the average moment on that site—the presence of $4.0\,\mu_\mathrm{B}$ *versus* $5.0\,\mu_\mathrm{B}$ moments would then be of no consequence. Indeed when looking at the average magnetic moments on each site it is clear that there is minimal variation between different sites. The greatest variation is seen for the refinements that started from the fully ordered GSAS orientations, where the octahedral sites had an average moment of $4.18\,\mu_\mathrm{B}$, while the tetrahedral sites had an average moment of $3.45\,\mu_\mathrm{B}$.

The refined structures have also been investigated in the Cc unit cell setting; however, there is insufficient evidence that there is any distinction between that and an expanded $P2/m$ cell, so only the results for the latter cell have been presented here.

It is notable that the average net moment per formula unit is always significantly larger than the value expected based on previous studies, where values of $\lesssim 4\,\mu_\mathrm{B}$ are

Table 5.2: A summary of the refined magnetic moments. Average vectors for different sites are not presented for type B & D refinements, as large variations in orientation between refinements lead to deceptively small values.

Type A refinements				
Average net moment		$6.121(12)\,\mu_B$		
Average angle		$136.6(5)^\circ$		
Group	$m_x(\mu_B)$	$m_y(\mu_B)$	$m_z(\mu_B)$	$\lvert m\rvert(\mu_B)$
1	−0.958	1.042	−3.966	4.212
2	−0.865	−1.014	−3.983	4.202
3	0.415	0.130	−4.175	4.200
4	−0.892	0.072	−3.987	4.089
Tet.	−1.961	0.147	2.802	3.447
Type B refinements				
Average net moment		$5.93(4)\,\mu_B$		
Average angle		$130.8(11)^\circ$		
Group				$\lvert m\rvert(\mu_B)$
1				3.876
2				4.151
3				3.949
4				3.873
Tet.				3.886
Type C refinements				
Average net moment		$5.779(31)\,\mu_B$		
Average angle		$134.8(3)^\circ$		
Group	$m_x(\mu_B)$	$m_y(\mu_B)$	$m_z(\mu_B)$	$\lvert m\rvert(\mu_B)$
1	−0.554	1.713	−3.746	4.199
2	−0.674	−1.738	−3.769	4.249
3	−0.435	−0.023	−3.991	4.083
4	−0.176	−0.040	−4.202	4.262
Tet.	−2.577	−0.402	3.281	4.196
Type D refinements				
Average net moment		$5.787(29)\,\mu_B$		
Average angle		$135(5)^\circ$		
Group				$\lvert m\rvert(\mu_B)$
1				3.961
2				4.031
3				3.865
4				3.859
Tet.				3.665

reported for the spin moments. While little has been reported on the orbital moment, it is perhaps presumptuous to attribute the full value of the difference to their contributions, especially when they are expected to cancel for a stoichiometric sample. It is possible that the spin moments used in the refinement were too large, though it is expected in this case for the refinement to respond by increasing the angular variation for each site, in order to lower the net moment. Considering only the component along the c-direction, the magnitude is closer to what we might expect—$5.25\,\mu_{\mathrm{B}}$ for type A refinements, and $4.57\,\mu_{\mathrm{B}}$ for type C—though still too large, especially when compared to the net moment produced by the GSAS refinement, $3.635\,\mu_{\mathrm{B}}$.

The average spin vectors for each site in type A refinements were used in a GSAS refinement to confirm that the RMC model did in fact fit the data better, and was not simply an artefact of the refinement process. The directions of the spins were fixed, but the magnitudes of the spins were allowed to refine, with the octahedral sites allowed to scale independently of the tetrahedral sites. The GSAS-refined atomic structure was used, but with symmetry reduced to $P1$, and non-magnetic atom parameters fixed. This was compared to an otherwise identical refinement that constrained the spins to lie along the c-axis. It was found that the canted spins model obtained from the RMC refinement gave an improved fit, with a reduced χ^2 of 154.6, compared to 162.9 for the c-axis-confined model. It is worth noting that—though allowed to scale freely—the overall magnitude of the moment for the canted spins model remained large, at $5.925\,\mu_{\mathrm{B}}$.

When considering the symmetry of the refined magnetic structure, we shall confine ourselves to the type A and C refinements, as the overall orientations of the magnetic moments in type B and D refinements are inconsistent. It can be seen that predominantly, the spin components lie within the ac plane. For the tetrahedral sites, and groups 3 and 4 of the octahedral sites, the m_y components are small. The notable exceptions to this are the groups 1 and 2 of the octahedral sites, which have large m_y components that are approximately equal but opposite.

Considering first the expected symmetry of a $P2/m$ cell, there are mirror planes at b equals 0, $\frac{1}{2}$, and 1, with two-fold rotation axes parallel to the b-axis. Inversion centres exist where the rotation axes intersect the mirror planes. The magnetic atoms that lie within the mirror planes are the tetrahedral sites and groups 3 and 4 of the octahedral

sites, and have their spins lying approximately within the mirror plane. The groups 1 and 2 octahedral Fe atoms lie outside of the mirror planes, but are mapped onto one another by the planes. The fact that their m_y components are approximately equal and opposite now means that they are consistent with this symmetry element. However, the large m_x components held by many sites violates the two-fold rotation axis, meaning that $P2/m$ is not an appropriate description of the space group. This is not unexpected: as detailed above, many studies have concluded that magnetite has a lower symmetry Cc structure, and we cannot expect the symmetry of the magnetic structure to be any higher than that of the atomic structure.

Now considering the Cc space group, there are c-glide planes at b equals 0, $\frac{1}{2}$, and 1, and diagonal glide planes at b equals $\frac{1}{4}$ and $\frac{3}{4}$. However, when translating this into the metrically smaller cell used in the present analysis, we must consider c-glide planes at 0 and 1, and a diagonal glide plane at $\frac{1}{2}$. The translational element of the glide can also be ignored, as a translation of half of the larger unit cell equates to a translation of the complete smaller cell, returning the atom or spin to its starting position. There are no other symmetry elements to consider, and we have already established that the magnetic structure outlined here is consistent with mirror planes at 0, $\frac{1}{2}$, and 1. Therefore, the RMC-refined magnetic structure appears to be consistent with a Cc-symmetry unit cell.

5.3.3 Local Structure

Investigation of the local structure must come purely from the RMC refinements. The widespread interest in charge ordering in magnetite led us to explore bond valence sums first. These were calculated using the formula and coefficients presented in Ref. 329,

$$V_i = \sum_j \exp\left(\frac{R_{ij} - d_{ij}}{b}\right) \tag{5.1}$$

where V_i is the valence of species i, bonded to species j; R_{ij} is termed the bond valence parameter, with a value of 1.759 Å for Fe^{3+} bonded to oxygen; d_{ij} is the bond length between species i and j; and b is a constant equal to 0.37 Å.

Strictly speaking, the bond valence parameter varies with valence state, however in this case we do not know in advance what the valence state of a particular atom is meant to be. In addition, there is extensive evidence that the valence states in

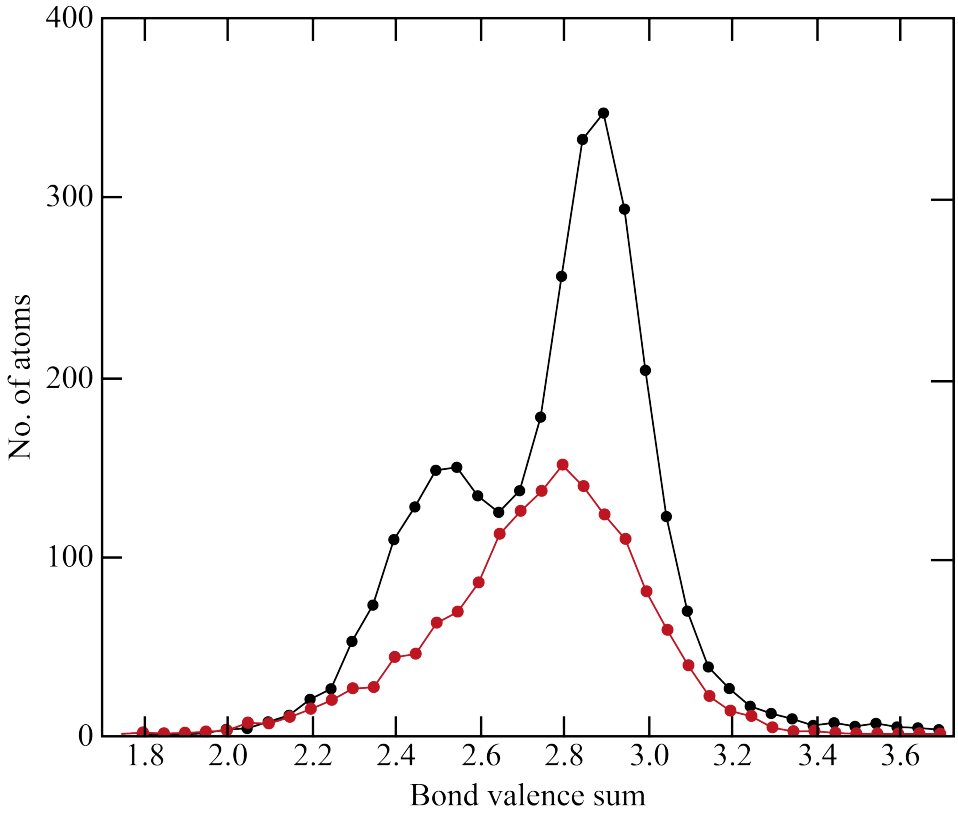

Figure 5.7: Histogram of bond valence sums for octahedral (black) and tetrahedral (red) Fe atoms in refined configurations (average over six refinements).

Fe_3O_4 below the Verwey transition are non-integral (for which there are no tabulated bond valence parameters) [280]. For this reason we have simply used the parameter for Fe^{3+} throughout, noting that doing so will give a higher calculated BVS than expected for iron in a lower valence state.

Figure 5.7 shows the calculated BVS distributions for both the octahedral and tetrahedral sites. Considering first the octahedral iron atoms, the distribution of bond valence sums can be seen to be bimodal, showing that the RMC refinements are sensitive to some form of change in local environment. The two Gaussian peaks are centred at BVS values of 2.51 and 2.89, with an unequal division—the ratio of peak areas is approximately 1.8:1, with a greater weighting to the higher valence states. This uneven splitting goes against the traditional model of charge ordering proposed, where there should be equal numbers of Fe^{2+} and Fe^{3+} ions on the octahedral sites. There is however a Mössbauer study that finds much the same ratio of valence states—1.88:1—in its analysis [289], which lends some support to this observation.

Now considering the BVS distribution for the tetrahedral sites, a single peak is observed in almost the same position as the higher peak found in the octahedral distribution—centred at a valence of 2.8 rather than 2.9 [Fig. 5.7]. This is consistent with expectations, which would be for the tetrahedral sites to be occupied by Fe^{3+} ions, the higher valence species. The average BVS on octahedral sites is 2.78, while for tetrahedral sites it is 2.74. This gives a total valence sum per formula unit of 8.30, reasonably close to the expected value of 8.00, and as mentioned previously our use of the Fe^{3+} bond valence parameter for all Fe atoms will have overestimated the BVS in some cases.

No ordering is immediately discernible among the different valence states of the octahedral iron atoms upon visual inspection. The following correlation function $\chi(r)$ was defined and calculated to assess this more rigorously:

$$\chi(r) = \frac{a_{\text{eff}}^2}{Nr^2} \sum_i \sum_j u_i u_j(r) \tag{5.2}$$

where

$$u_i = \begin{cases} +1 & v_i \geq 2.7 \\ -1 & v_i < 2.7 \end{cases} ; \tag{5.3}$$

a_{eff} is the effective lattice parameter, $\sqrt{ab}$; N is the total number of atoms involved; and v_i is the BVS of atom i. This function is plotted in Figure 5.8, and shows that there does appear to be a slight tendency for dissimilar valence states to be nearest neighbours, while there is a tendency to find the same valence state at twice this distance. As can be seen from the error bars, this is a very weak tendency, limiting its significance when considered in isolation.

The next stages of the investigation were prompted by the most recent of the high resolution diffraction experiments [302]. A key result of this study was the observation of so-called 'trimerons'—linear three atom clusters formed from a central Fe^{2+} ion surrounded by two Fe^{3+} ions. These are distinguished in the structure (which could otherwise be considered to hold a great many of these clusters) by shorter than expected Fe–Fe distances, and form a network throughout the structure connected mostly by the ends of the trimerons [Fig. 5.9].

The RMC refined structures were probed in search of similar trimerons by looking for closer-than-normal Fe atom clusters, but no evidence was found for clusters of

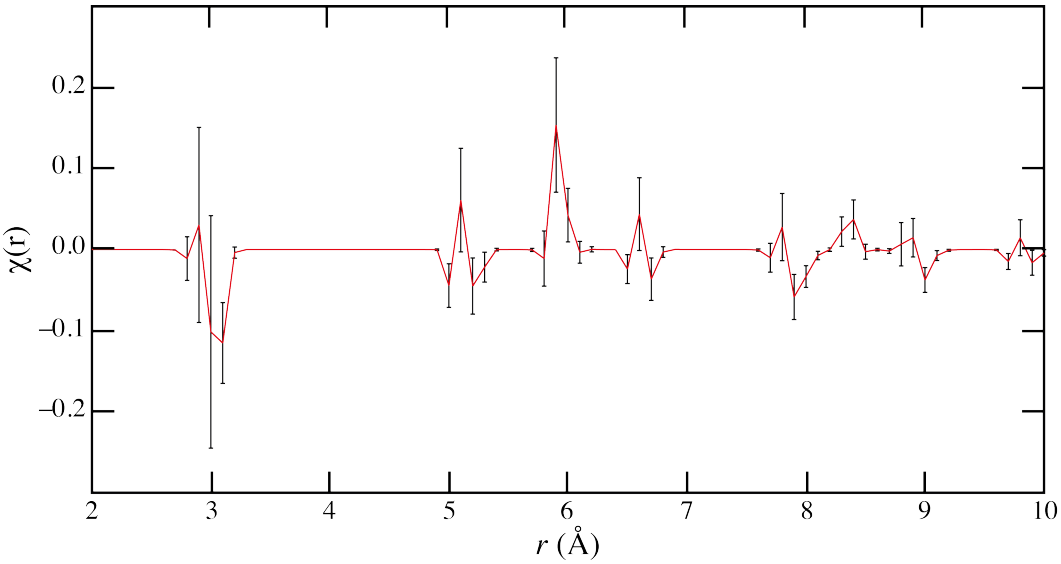

Figure 5.8: Correlation function describing the likelihood of finding different valence states of octahedral Fe atoms at a distance r. A positive peak implies likelihood of finding similar valence states at that distance.

this kind. In fact very little intensity is present in the Fe–Fe bond length histogram at the required distances, and the peak is not bimodal [Figure 5.10]. Nonetheless, the average Fe–Fe distance among octahedral iron atoms is 2.963 Å, which is in good agreement with the average value found in Ref. 302, 2.967 Å. In the absence of the results of Ref. 302 these findings would not be unexpected, and indeed, still seem reasonable.

The next attempt again sought out possible trimerons, but this time using bond valence sums to distinguish the ends and centres, rather than the Fe–Fe distances. This proved somewhat more successful: as noted earlier the ratio of Fe^{3+}:Fe^{2+} ions on the octahedral sites is roughly 2:1, which fits well with the trimeron model of one central Fe^{2+} and two peripheral Fe^{3+} ions. The small correlations that favour dissimilar atoms at a distance of ∼3 Å but similar atoms at ∼6 Å could also support the trimeron model.

Suitable three atom clusters could be identified in great numbers, though no particular patterns or trends could be seen. It is hard to discern between the observed arrangement, and what might be observed for a purely random arrangement of valence states. Applying the short bond length requirement on top of the BVS to identify the trimerons leaves a negligible quantity remaining.

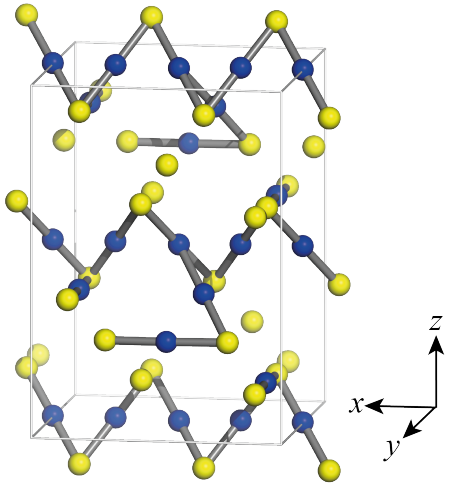

Figure 5.9: Ref. 302 reported a network of 'trimeron' structures below the Verwey transition in magnetite, which are shown above. Trimerons are indicated by grey bonds, while atoms designated as Fe^{2+} and Fe^{3+} are shown in blue and yellow, respectively.

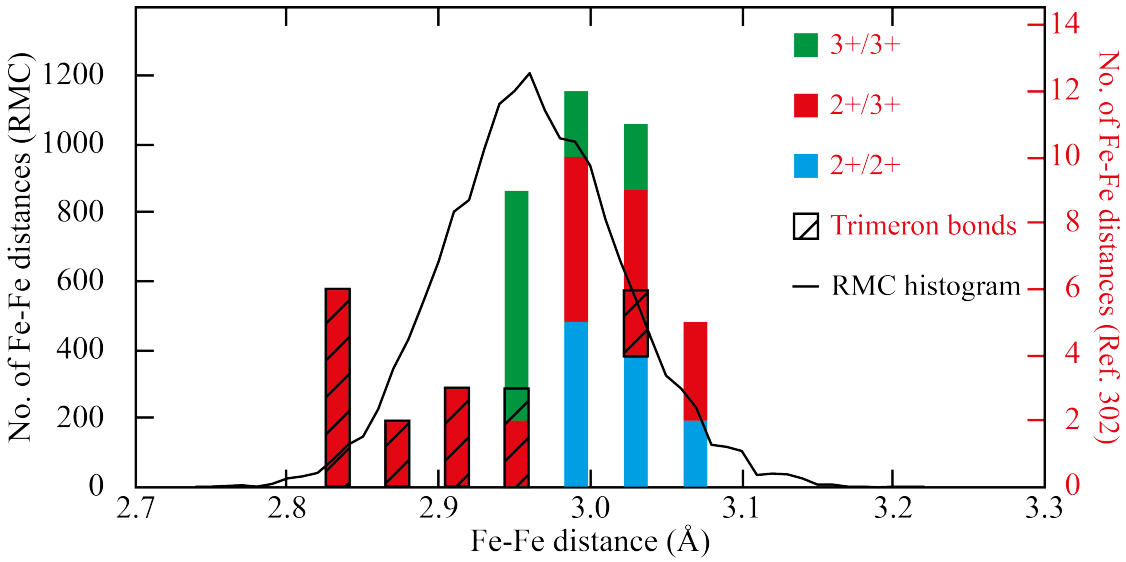

Figure 5.10: Histograms of octahedral Fe–Fe distances in Fe_3O_4. The distribution of octahedral Fe–Fe distances obtained from RMC refinement is shown as a black line, while the distribution obtained in Ref. 302 is shown as coloured bars. The distribution is broken down according to the valences of the Fe atoms involved, as indicated by the key, and those involved in trimeron formation are indicated by hatching. The distribution from Ref. 302 has significant intensity at low distances, while the RMC distribution does not, though they are both centred about the same distance.

Ref. 302 also quantified the distortions present in FeO_6 octahedra in terms of a tetragonal JT mode and a radial breathing mode, termed Q_{JT} and Q_{Rad} respectively. These were chosen for their apparent sensitivity to charge and orbital ordering. The radial breathing mode, Q_{Rad}, is defined simply as:

$$Q_{\mathrm{Rad}} = \frac{d_{+x} + d_{-x} + d_{+y} + d_{-y} + d_{+z} + d_{-z}}{6} - d_{\mathrm{av}} \tag{5.4}$$

where d_{+x} refers to the Fe–O bond length in the positive x-direction, *etc.* and d_{av} is the average Fe–O bond length for the octahedral sites. The tetragonal distortion mode, Q_{JT} is obtained from the following process. First, three E_g symmetry amplitudes, Q_x, Q_y and Q_z are calculated using:

$$Q_x = \frac{2(d_{+x} + d_{-x}) - (d_{+y} + d_{-y} + d_{+z} + d_{-z})}{2\sqrt{3}}, \textit{ etc.} \tag{5.5}$$

These are ranked in order of increasing magnitude, such that $|Q_1| > |Q_2| > |Q_3|$, to identify the unique axis. The distortion will fall somewhere between two limits, designated Q_{T} ($= Q_{\mathrm{JT}}$) and Q_{O}, and can be described as a linear combination of the two. For Q_{T}, $Q_1 = Q_{\mathrm{T}}$, and $Q_2 = Q_3 = -Q_{\mathrm{T}}/2$, while for Q_{O}, $Q_1 = -Q_2 = Q_{\mathrm{O}}$ and $Q_3 = 0$. From these, Q_{JT} can be calculated.

In Ref. 302 the distributions can be easily separated, such that the 8 sites with the larger Q_{Rad} values are also the 8 sites with the smallest Q_{JT} values [Figs. 5.11,5.12]. Q_{Rad} is clearly related to the BVS, as both depend on the Fe–O bond lengths, so a division can also be made in the BVS distribution. There then seems to be a correlation between the BVS and the distortion of the site, with the lower valence sites having the higher magnitude of distortion, which may be consistent with the trimeron model.

The distortion magnitudes were calculated as outlined above for RMC-refined configurations. Fig. 5.11 shows a plot of Q_{Rad} *vs* Q_{JT} for the octahedral Fe atoms in one refined configuration, while Fig. 5.12 shows a similar plot for a Cc-sized unit cell produced by averaging over 12 configurations (without applying any symmetry operations). The results of Ref. 302 are also included in both figures for comparison. As can be seen from Fig. 5.11, the distribution is much larger for individual atom sites than for the 16 Cc atom sites of Ref. 302. This is to be expected, as RMC refinements always produce a more disordered structure than an average structure

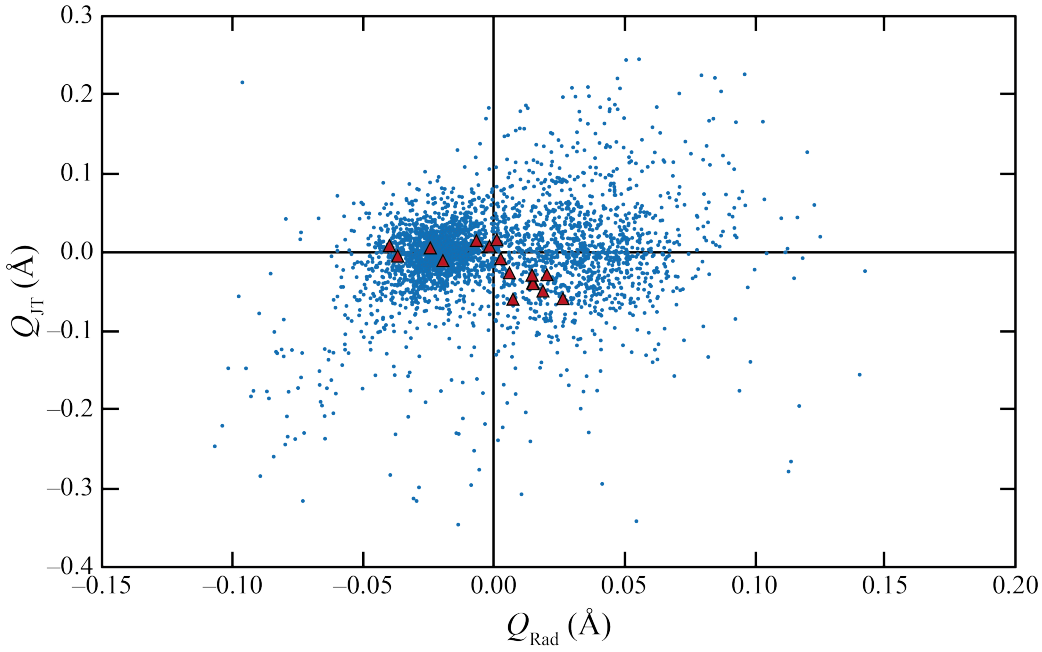

Figure 5.11: The distribution of Q_{JT} and Q_{Rad} values for each octahedral Fe atom in a refined configuration (blue circles). The results reported in Ref. 302 are shown as red triangles for comparison.

model, though it should be noted that the majority of atom sites have distortion magnitudes comparable to those of Ref. 302.

In contrast, the distribution of the RMC-refined structure found in Fig. 5.12 is much smaller than that of the aforementioned study, particularly for the Q_{Rad} distribution. This suggests that while individual Fe octahedral sites have reasonable magnitudes of distortion (and BVS), there is insufficient long range order of suitable symmetry in the RMC-refined configurations for these distortions to be found in the averaged structure. This does not necessarily imply that (i) the distortions described in Ref. 302 are not present, or that (ii) the symmetry of the low temperature structure is not Cc, as it is likely that the RMC refinements are not sensitive to subtle features of the data, as outlined in § 5.3.1.

Quadrupole moments q_1–q_5 (as outlined in § 4.3.2.6) were calculated for Fe atoms as a more in-depth investigation of octahedral distortions. The magnitude of the total quadrupole moment was defined as

$$P = \left(\sum_{j=1}^{5} q_j^2 \right)^{\frac{1}{2}}, \tag{5.6}$$

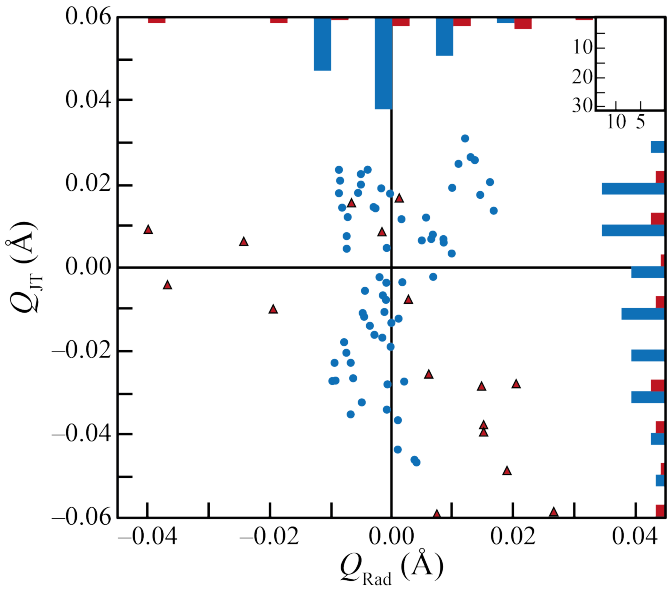

Figure 5.12: The distribution of Q_{JT} and Q_{Rad} values for each octahedral Fe atom in a Cc unit cell produced by averaging the sites from a collection of standard refinements. The results reported in Ref. 302 are shown as red triangles for comparison, and are fewer in number due to symmetry elements rendering certain sites equivalent. Histograms of the distributions are presented along the sides of the chart. While the results of Ref. 302 can be divided into two separate, equal regions by both Q_{JT} and Q_{Rad}, the results of this study cannot.

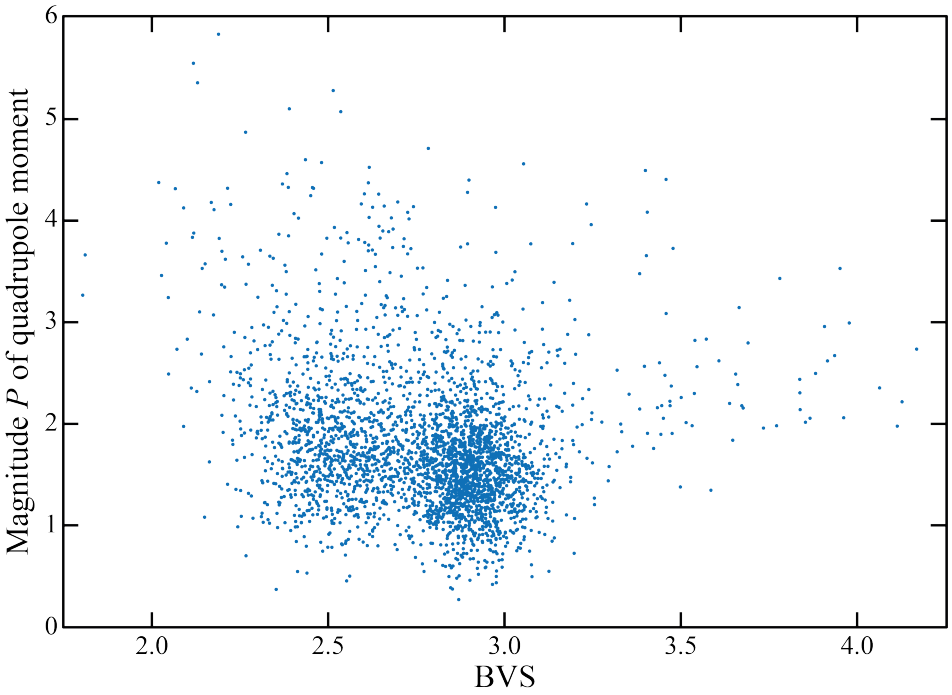

Figure 5.13: Distribution of total quadrupole moment P against BVS. There is a slight tendency for lower valence Fe sites to be have a larger quadrupole moment.

and plotted against BVS for each site in a refined configuration, to establish whether or not there was any correlation, like that seen between Q_{Rad} and Q_{JT} in Ref. 302. The result is shown in Fig. 5.13. The distribution is quite wide, though again the majority of sites have moderate values. There appears to be a slight tendency for lower valence sites to have larger quadrupole moments, though no significant conclusions can be drawn, and this does not appear to be a suitable method for identifying ordering amongst Fe sites.

5.4 Conclusions

In conclusion, previously collected neutron total scattering data were used to drive a RMC refinement of the 10 K structure of magnetite. Both nuclear and magnetic structures were refined, with varying results.

A previously unrecognised limitation in the RMC technique has been identified, namely, the failure to adequately fit to low-intensity features in the diffraction pattern. The result of this is that an accurate description of the average structure of the low temperature phase of magnetite could not be obtained in this study. For a system

such as magnetite, with a very subtle distortion away from cubic symmetry, the program is not sensitive enough to respond to the small signals involved, with slight variations in atomic position being lost amongst the noise. The disorder inherent in RMC refinements will always make precise identification of atomic coordinates difficult, though alternative fitting processes (as outlined in § 5.3.1) could ameliorate the problem. However, the inclusion of additional data sets could assist with this particular system—the use of only Bragg and $F(Q)$ data sets was fewer than might ordinarily be desired, as the inability to separate nuclear and magnetic scattering components from one another precluded the use of a PDF data set. Other options that might greatly assist a future refinement would be the inclusion of X-ray data sets, either as total scattering or single crystal patterns. Currently this study can find no evidence to contradict previous reports presenting a Cc symmetry unit cell.

The magnetic structure was analysed using a small cell of the size of the $P2/m$ cell used for the initial Rietveld refinement. Reasonably narrow distributions of spins were obtained, with certain key features being observed: octahedral sites align approximately ferromagnetically within themselves, as do tetrahedral sites, though the two sites align themselves at $\sim 130^\circ$ to one another; pairs of sites separated by a $(\frac{1}{2}, \frac{1}{2}, \frac{1}{2})$ vector can be identified that have similar spin vectors; and the net moment produced by these refined structures is higher than expected, with a value $\sim 6\,\mu_\mathrm{B}$ rather than $\sim 4\,\mu_\mathrm{B}$. These features are present regardless of the starting arrangement of spins. The overall orientation of the magnetic spins *is* however dependent on the initial conditions. If the refinement starts from an ordered arrangement then a final structure consistent with Cc symmetry is reliably obtained, while refinements starting from random arrangements cannot (within reasonable timescales) reorient themselves suitably to achieve this. Rietveld refinements confirm that the RMC-produced magnetic structure gives an improved fit in comparison to a simpler magnetic structure confined to be parallel to the c-axis.

The local structure was also investigated. An analysis of the valence states of the Fe atoms reveals an unequal bimodal distribution on the octahedral site. This suggests that the RMC refinement is sensitive to certain aspects of local structure, and that some sort of charge disproportionation may exist. This unequal distribution, in a roughly 2:1 ratio, may be consistent with an earlier Mössbauer study [289],

though it is not immediately obvious why this ratio should be found. Examination of the distribution of different valence states shows no evidence for strong charge order; however, calculation of the correlation function implies a weak tendency for dissimilar valence states to be neighbours.

Much comparison has been made with a recent high-profile X-ray single crystal study [Ref. 302], in particular regarding the trimeron structures reported. This study finds no evidence for shortened Fe–Fe distances in the structure, or trimerons described by such distances, though appropriate three-atom clusters may be identified using BVS. The ordering scheme reported in Ref. 302 cannot be observed in this refinement. FeO_6 octahedral distortions were characterised by different distortion modes, again to compare with the specified study. Here again the same behaviour could not be observed in the RMC refinement.

Overall, some good contributions have been made to this field. The first detailed magnetic structure for the low temperature phase has been presented, and while there are still questions that remain, the model presented here should provide a useful starting point for future work. This could involve an examination of why the refined moments are larger than expected, and an appraisal of the magnetic symmetry—which cannot be higher than the atomic symmetry. While no contribution has been made here towards better understanding the average nuclear structure, a deficiency in the RMC method has been identified, which—once addressed—should assist in the refinement of systems with similarly subtle distortions. Finally, the determination of the BVS distribution may prove useful in further explorations of charge ordering. Aside from the progress made on this system, this work has also proved useful in expanding the scope of RMC refinements to disordered magnetic systems, which will open up other areas of research to this technique.

Chapter 6

Conclusions

In this thesis, it has been shown how high quality total scattering data may be used in combination with reverse Monte Carlo refinements to elucidate detailed structural information about complex systems. We began with an introduction to the theory and practicalities of total scattering data collection and processing, before reviewing some of the main areas and systems for which it has been of use. The RMC algorithm was introduced, and some details of the RMCProfile program [71] discussed. The changes made to the RMCProfile code during the course of this research project were then outlined.

The first of three canonical systems to be examined in detail was the high-temperature cuprate superconductor, $YBa_2Cu_3O_{7-x}$. Using Rietveld, RMC and small-box PDF refinement of neutron total scattering data, the apical Cu–O bonds were investigated. These bonds—important for charge transfer—were the subject of an apparent disagreement between average structure diffraction experiments [212–216] and local structure techniques such as EXAFS [206–211], but this was resolved by demonstrating the presence of correlated displacements of the atoms involved.

$LaMnO_3$, part of the CMR manganite family, and the host of a well-known orbital order–disorder transition followed. A combination of state-of-the-art high resolution X-ray and neutron total scattering revealed that in fact this transition was not as straightforward as previously thought, but in fact involved changes to the symmetry of the octahedral distortions involved. Though unexpected, this result was shown to help explain a number of other inexplicable observations.

Finally Fe_3O_4 was discussed, the oldest known magnetic material, and well-studied even in recent years since the discovery of the Verwey transition [282]. A sensitivity

to different valence states was found, and much progress made into ascertaining the magnetic structure of the low temperature phase.

Through these studies, some of the abilities of the RMC technique have been demonstrated. It has handled a variety of different systems (albeit all metal oxides) displaying charge, orbital and magnetic ordering, and some combinations thereof. Its ability to refine to multiple data sets of different types has been proven, along with the clear benefit of this—producing a final structure that is consistent with the data provided, helping to resolve any apparent conflict between different data sets. Another advantage that is perhaps understated is that the refinement process makes no assumptions about the final symmetry of the structure, leaving it free to accept whatever configuration best fits the data. While still partly influenced by the initial conditions of the refinement, this reduces the effect of any bias (whether conscious or unconscious) that the researcher may have.

Nevertheless, there are still certain limitations to the process, as has been discussed in this thesis. Artefacts in the data, such as Fourier truncation ripples, can lead to spurious results if not treated appropriately. Over-fitting of data is a danger too, as a large refinement will inevitably have more degrees of freedom than there are data points used. One solution that we have exploited is to use a small-box refinement program such as PDFGUI in tandem to confirm a key results extracted from the RMC solution. The focus on larger peaks at the expense of smaller features in the data is another problem we have encountered, which can prove problematic in cases that involve subtle global symmetry lowering. A further aspect not highlighted previously is the consequences of the periodic boundary conditions employed: any repeating pattern or unit found within a refinement will have a size and/or repeat distance set by the box size used, which may bear no relation to the size of these features found in the physical material.

Certain themes have run through this thesis as well. The principal one is that of the need to combine local and average structure information when investigating a material. In many respects, these are two sides of the same coin: both the small-scale detail and how this comes together to create the bigger picture are required to gain a full understanding of a complex system.

Related to this local structure–average structure theme is an order–disorder theme. For example, in the O phase of $LaMnO_3$ the *cis*-JT distorted octahedra are locally ordered into nanoscale domains, but the lack of long range order means that the average structure does not see this, and the distortions are lost from view. The $YBa_2Cu_3O_{7-x}$ system could be thought about in a different way: the average structure gives the impression of a well-ordered material, with no evidence of site splitting, while the local structure reveals the variations in bond lengths present. Where disorder is present on one length scale, there may be order present on the other—further support for the notion that both length scales are required.

Similarly the theme of unifying disparate data sets or results has also been present. In $YBa_2Cu_3O_{7-x}$ the average structure data sets were in conflict with the local structure ones; $LaMnO_3$ also had further unusual results to take into account, such as dielectric spectroscopy and the measured entropy change. It would seem that for well-studied systems such as these, there is often a great deal of information available already, and the challenge is simply to unify it.

These things point towards some possible future directions for the area. First and foremost will be the requirement to include a greater variety of data sets in an analysis. In the case of programs like RMCProfile this could include regular use of EXAFS and/or single crystal diffraction data beside the 'standard' total scattering and Bragg data sets. A further goal must also be to maximise the information extracted from the available data—I refer here to situations like that found for the Fe_3O_4 Bragg data, where subtle low intensity features were not properly fitted during the refinement.

Systems related to those discussed here, such as other cuprate superconductors [330–332], or the Ca-doped lanthanum manganites [104, 333–335] could present good opportunities for future work. Other systems, such as the spin glass $Y_2Mo_2O_7$ [336, 337], that shows interesting spin and orbital degrees of freedom, would also be worthy of study. In almost all these cases, an RMC refinement would have to allow for swapping of magnetic species, and an additional outcome of this thesis is that this has now been enabled. The results presented here show that even well studied systems can still hold some secrets, which means that there is scope—especially now that we have improvements in instrumentation and software packages—to revisit other archetypal systems. It may be possible that other surprises await us.

Appendix A

Appendix: Fits to Data for $LaMnO_3$

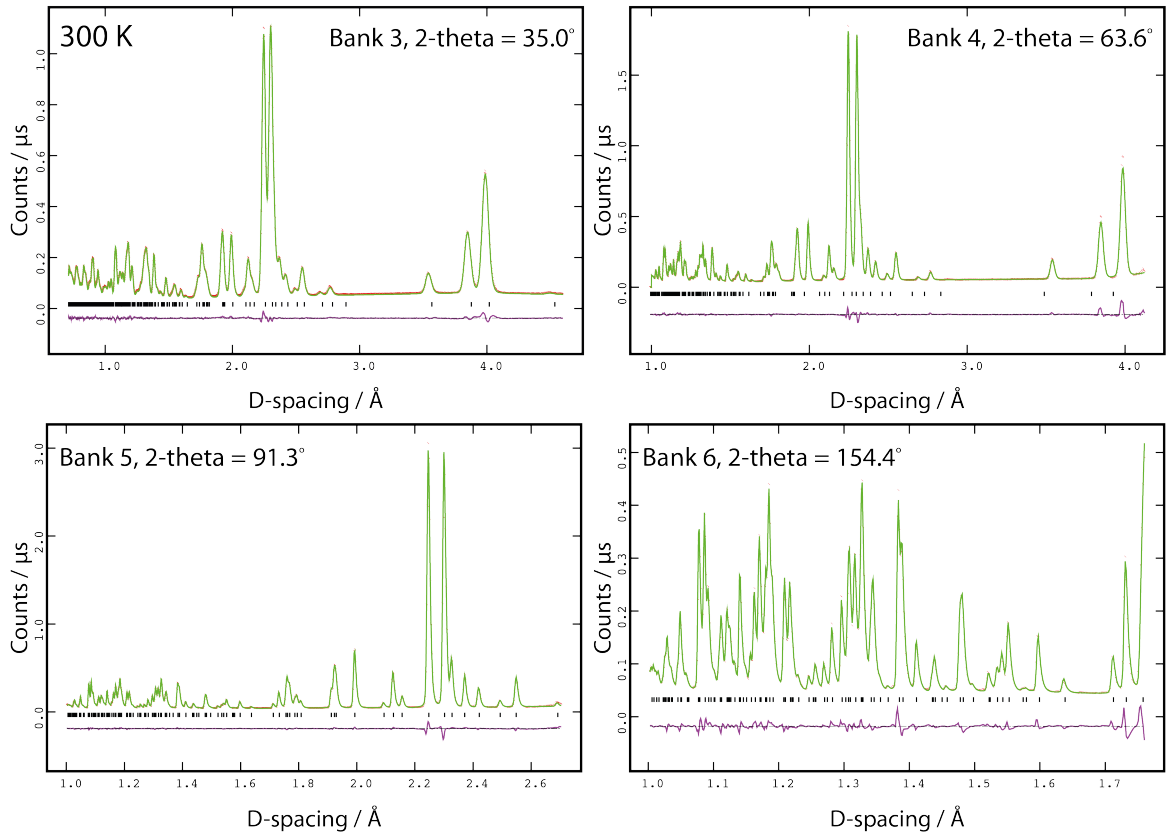

Figure A.1: Rietveld refinement of 300 K neutron powder diffraction data.

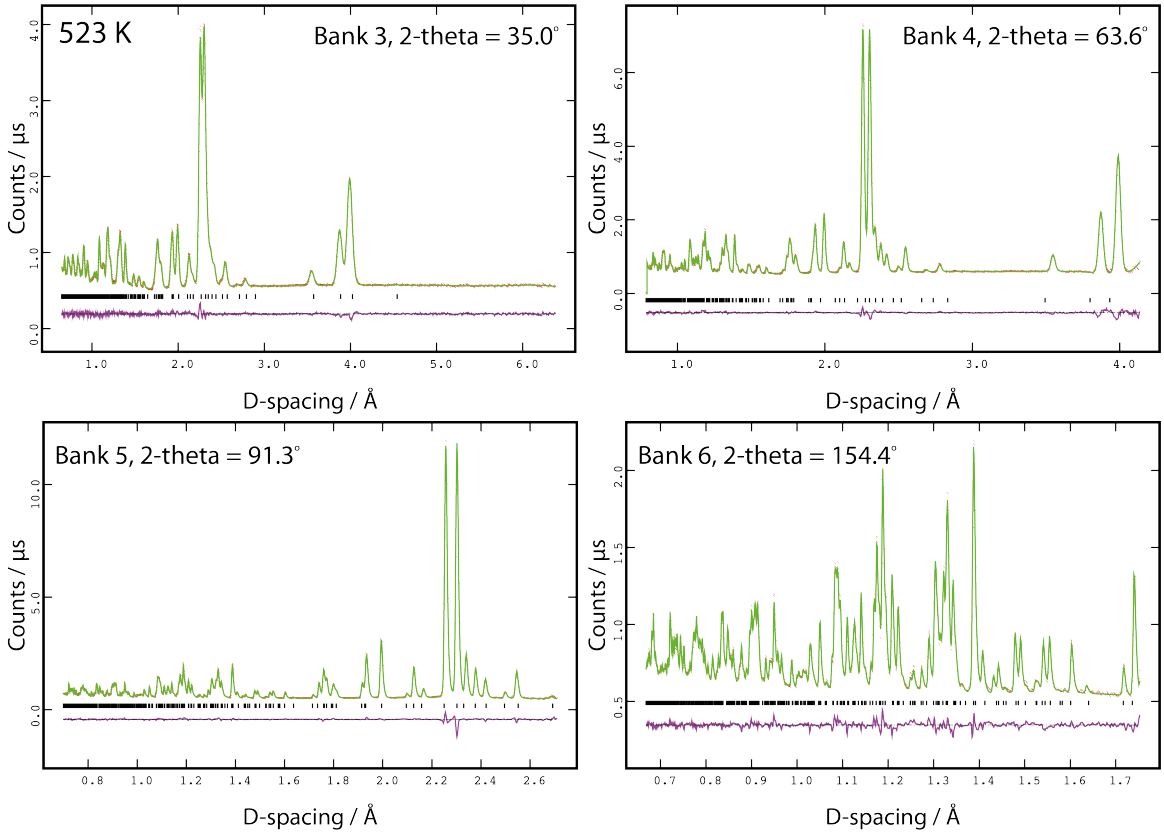

Figure A.2: Rietveld refinement of 523 K neutron powder diffraction data.

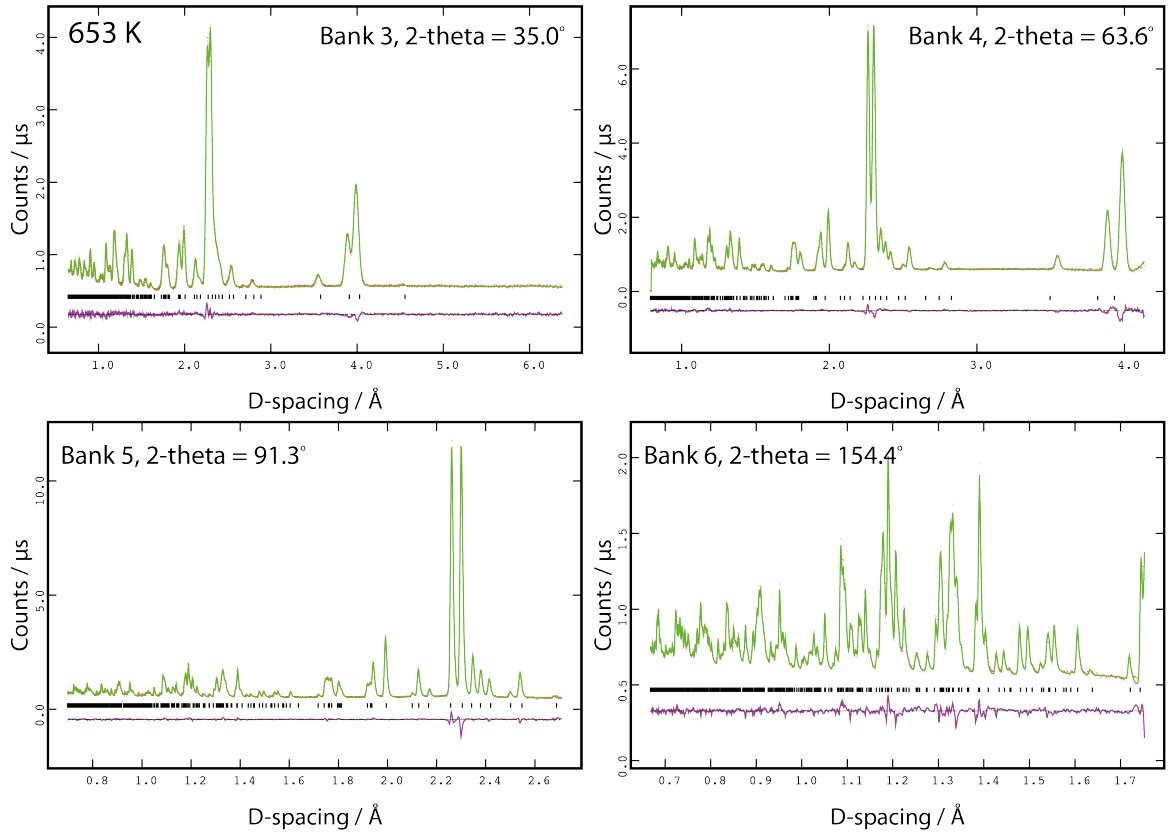

Figure A.3: Rietveld refinement of 653 K neutron powder diffraction data.

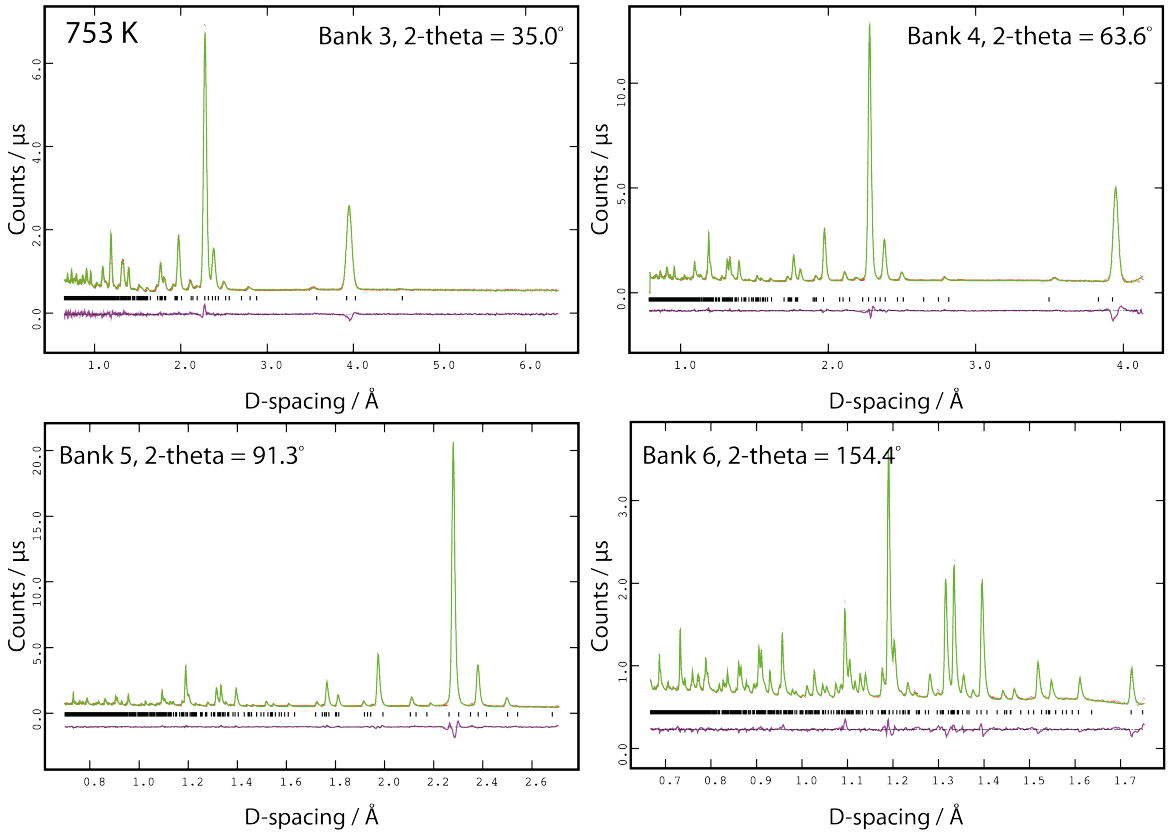

Figure A.4: Rietveld refinement of 753 K neutron powder diffraction data.

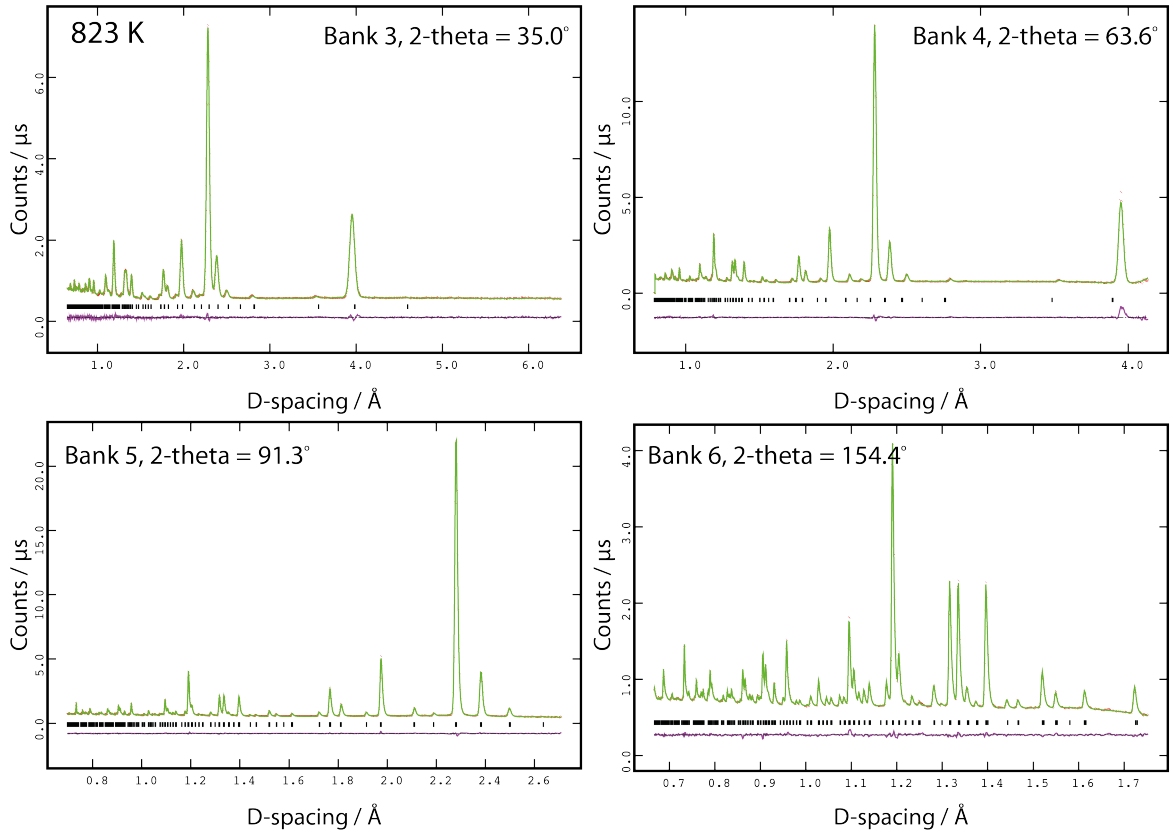

Figure A.5: Rietveld refinement of 823 K neutron powder diffraction data.

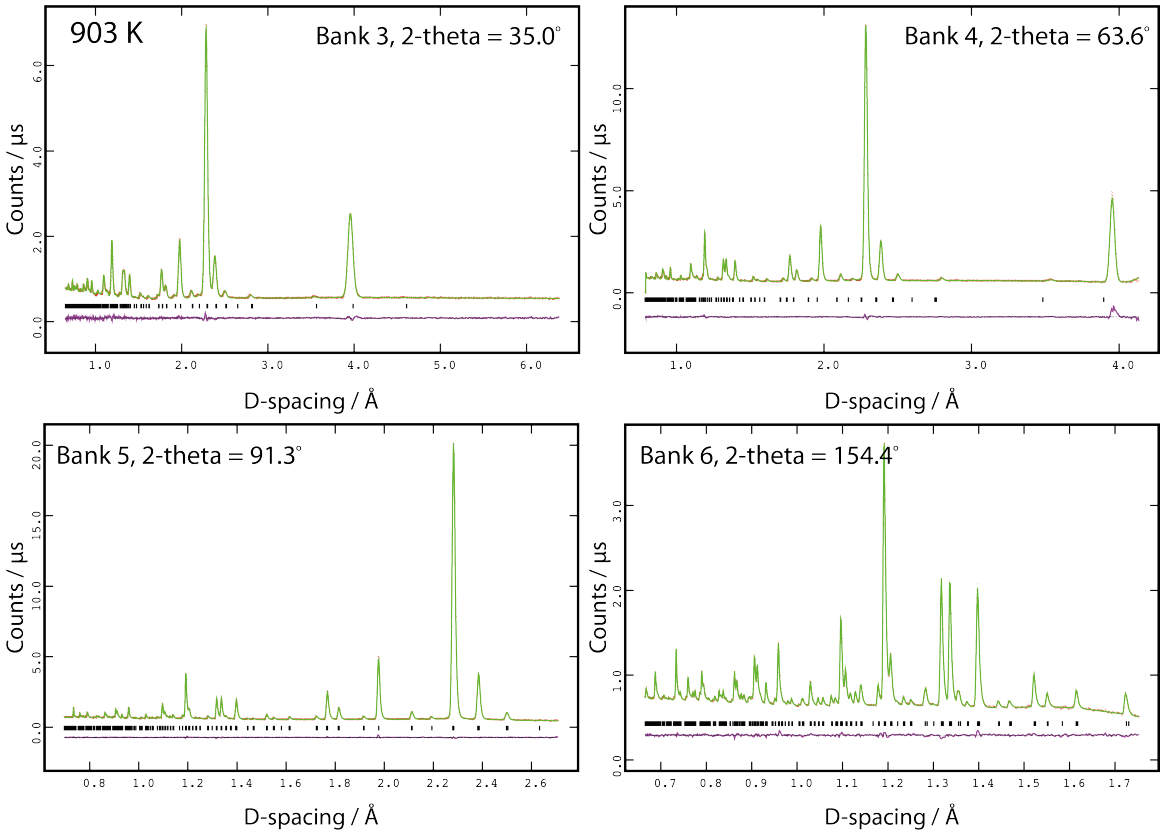

Figure A.6: Rietveld refinement of 903 K neutron powder diffraction data.

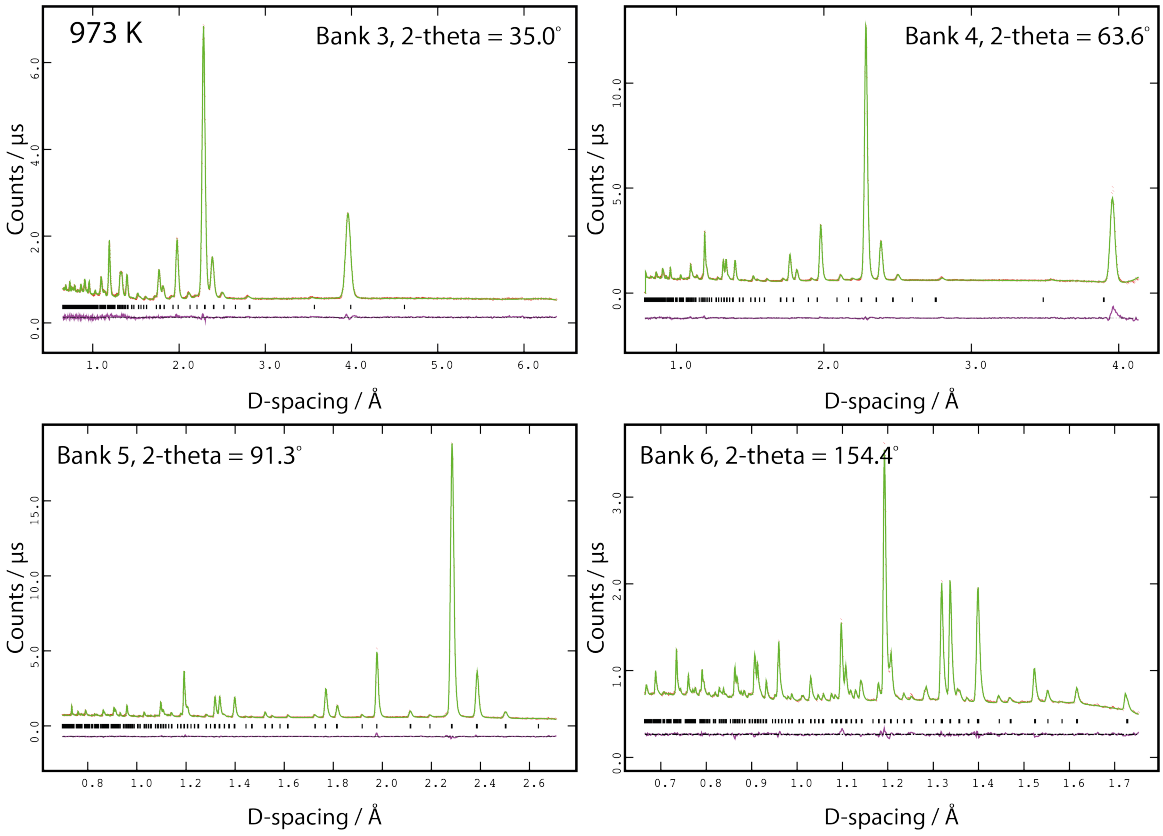

Figure A.7: Rietveld refinement of 973 K neutron powder diffraction data.

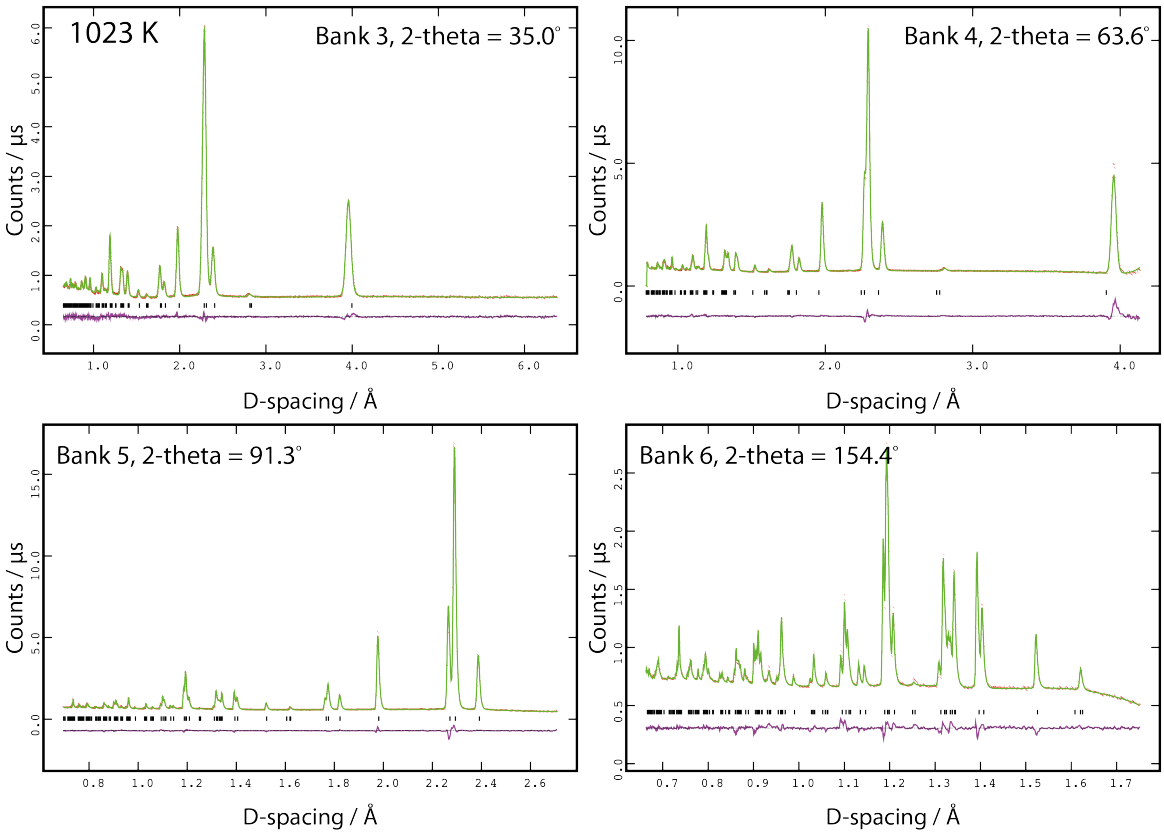

Figure A.8: Rietveld refinement of 1023 K neutron powder diffraction data.

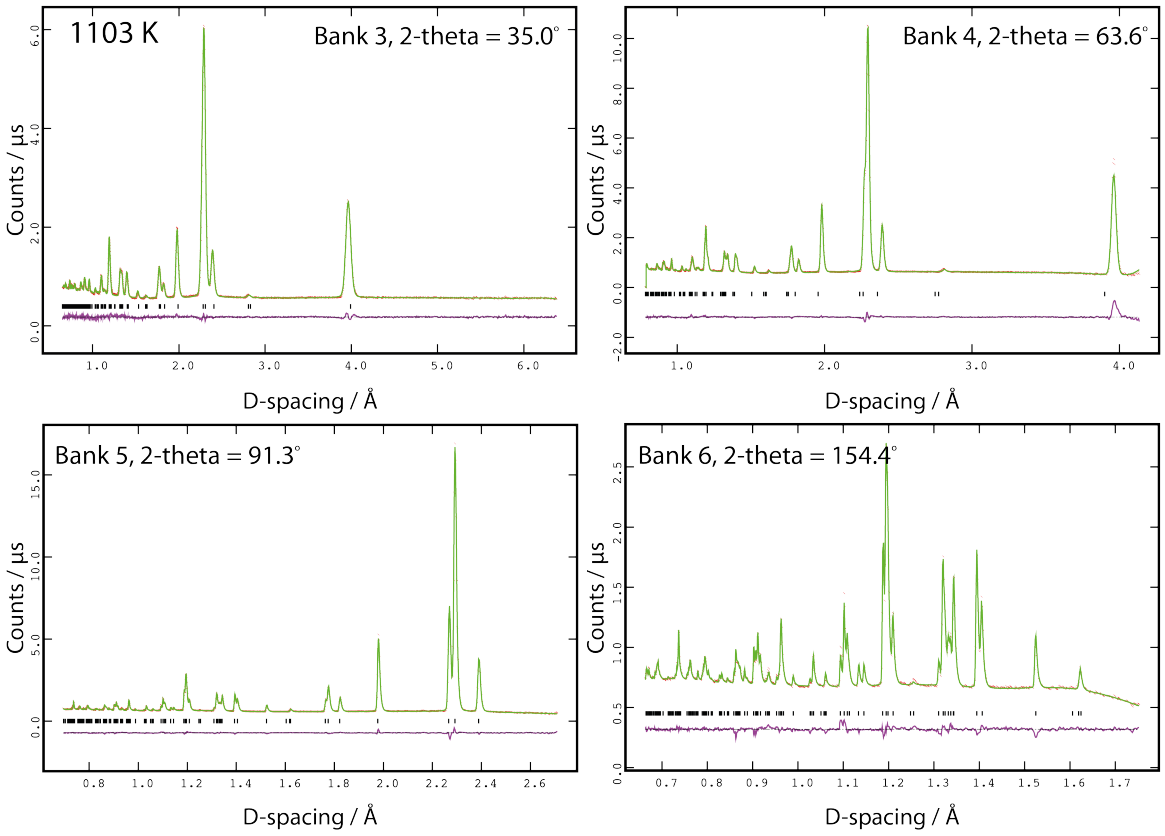

Figure A.9: Rietveld refinement of 1103 K neutron powder diffraction data.

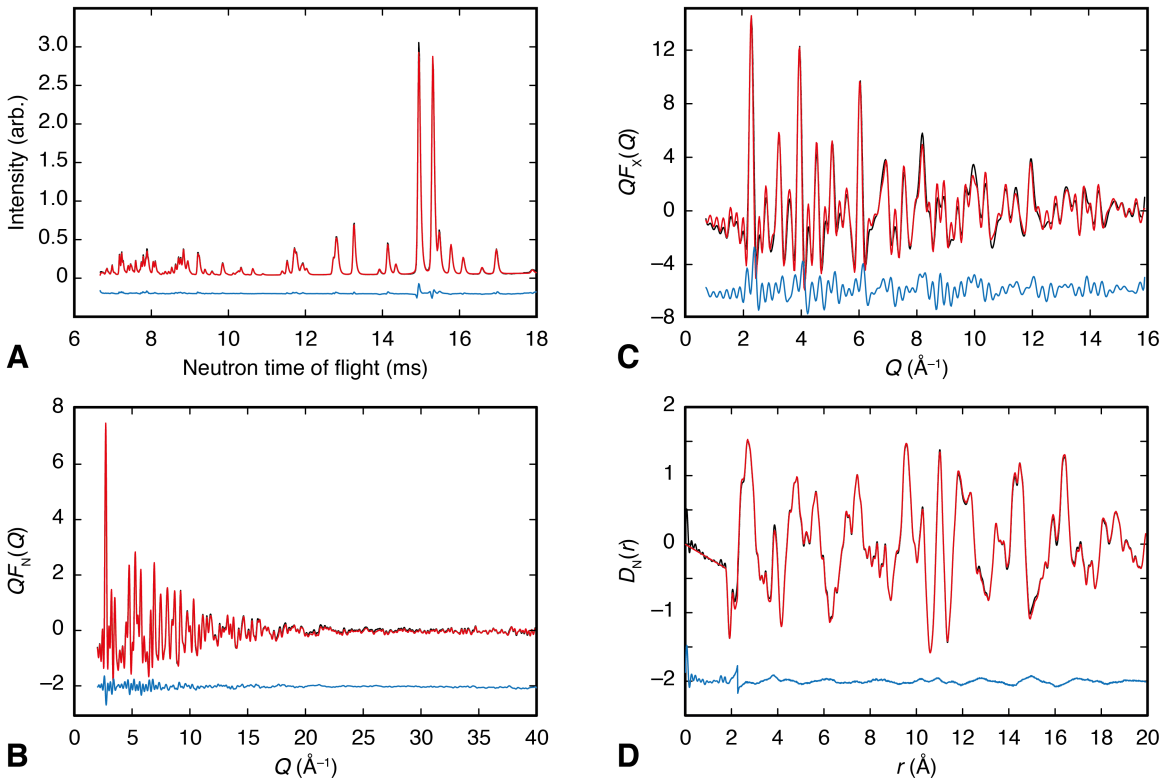

Figure A.10: RMC fits to data for the 300 K refinement: A) neutron Bragg, B) neutron $QF(Q)$, C) X-ray $QF(Q)$, and D) neutron $D(r)$.

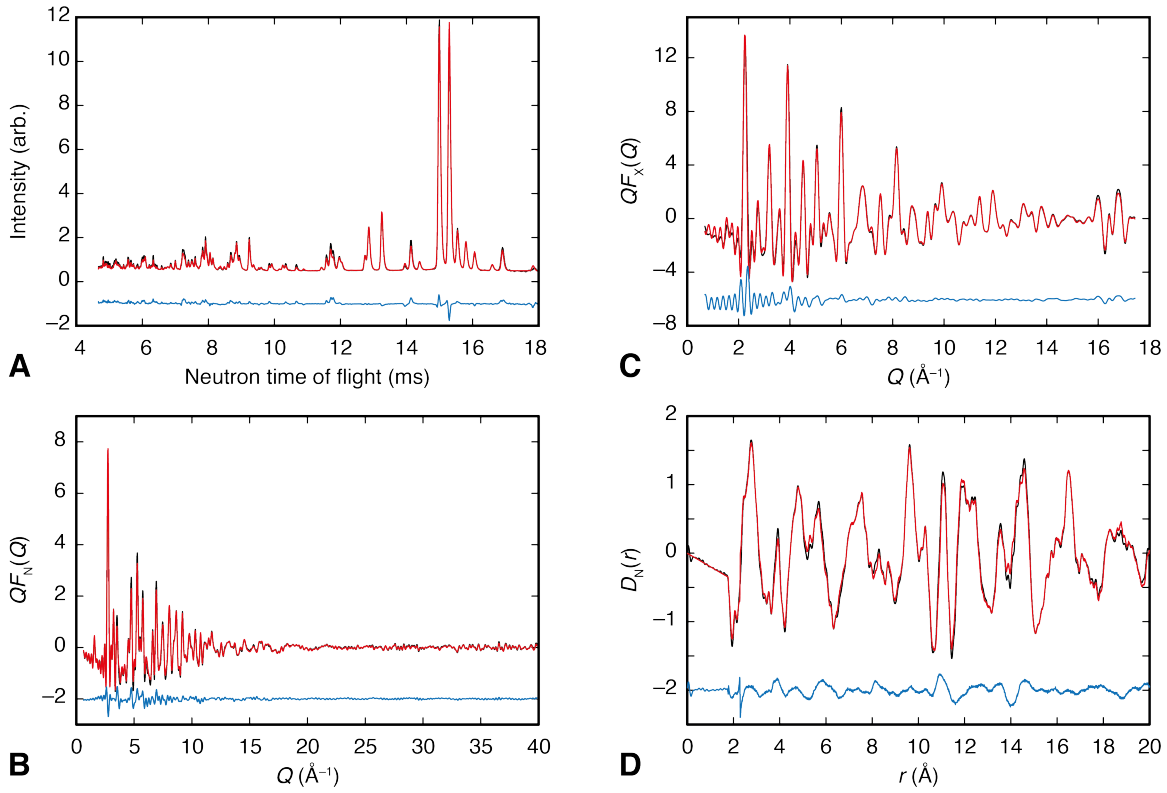

Figure A.11: RMC fits to data for the 523 K refinement: A) neutron Bragg, B) neutron $QF(Q)$, C) X-ray $QF(Q)$, and D) neutron $D(r)$.

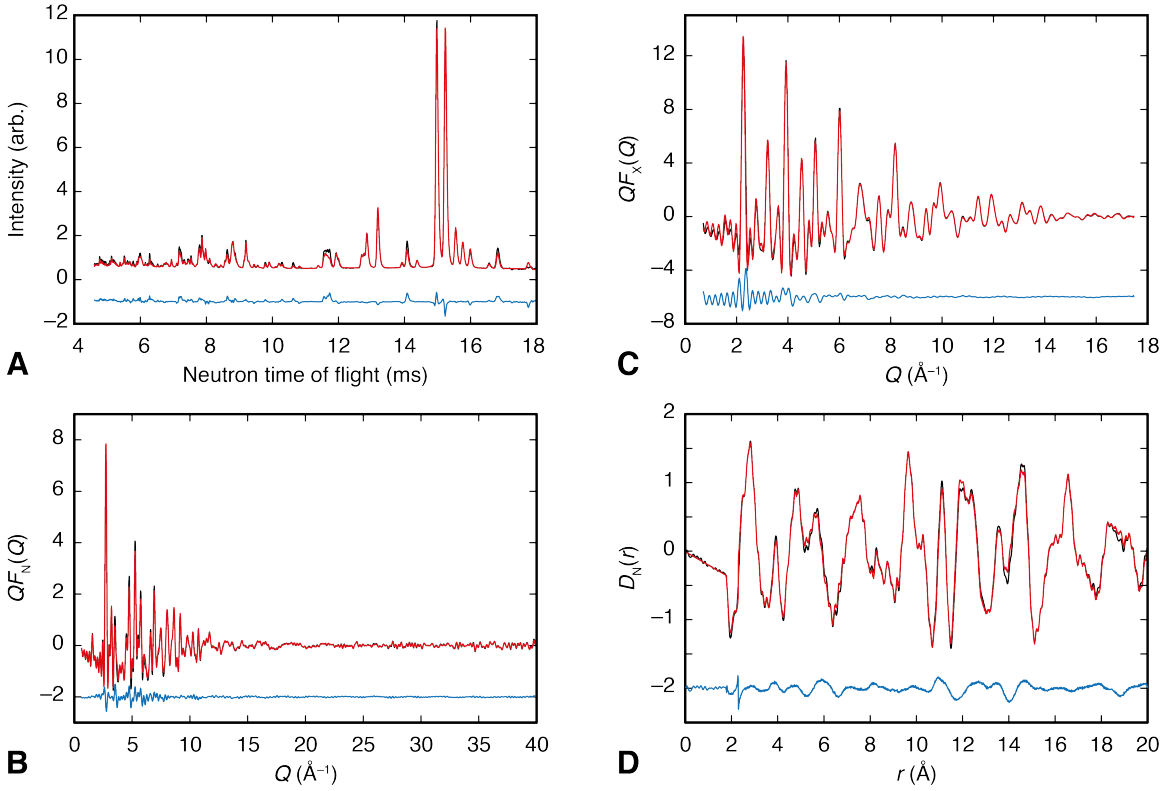

Figure A.12: RMC fits to data for the 653 K refinement: A) neutron Bragg, B) neutron $QF(Q)$, C) X-ray $QF(Q)$, and D) neutron $D(r)$.

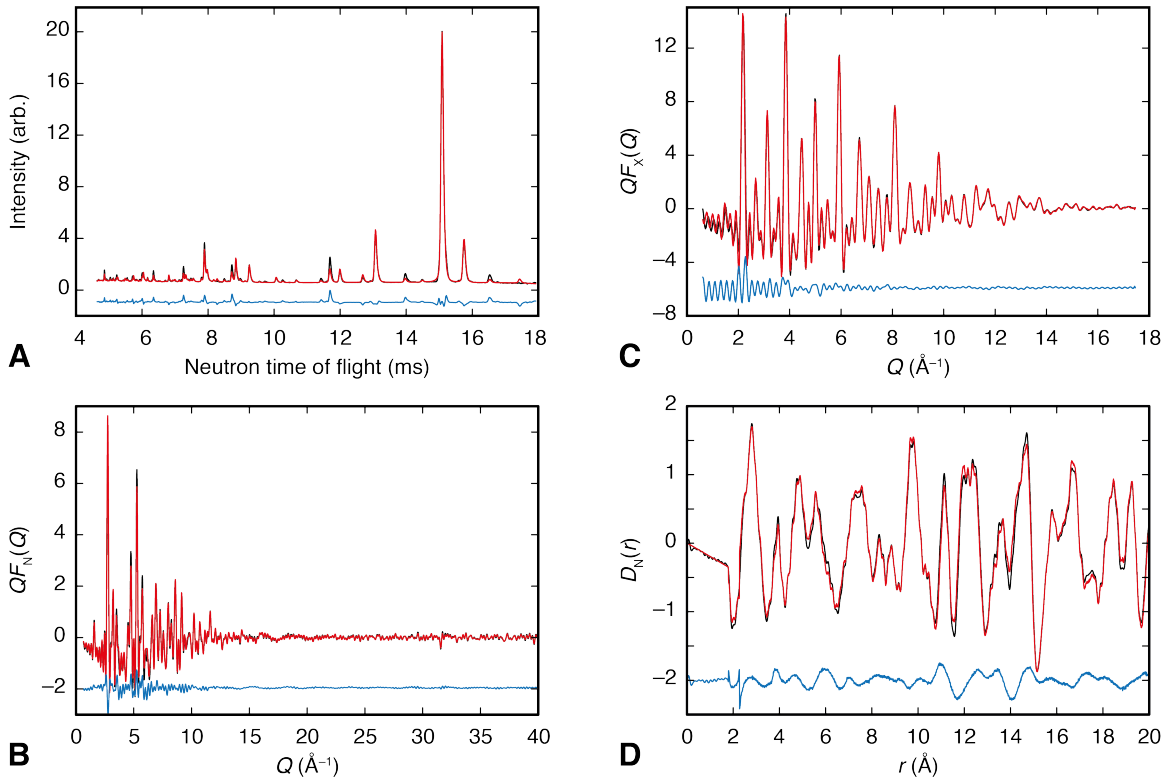

Figure A.13: RMC fits to data for the 753 K refinement: A) neutron Bragg, B) neutron $QF(Q)$, C) X-ray $QF(Q)$, and D) neutron $D(r)$.

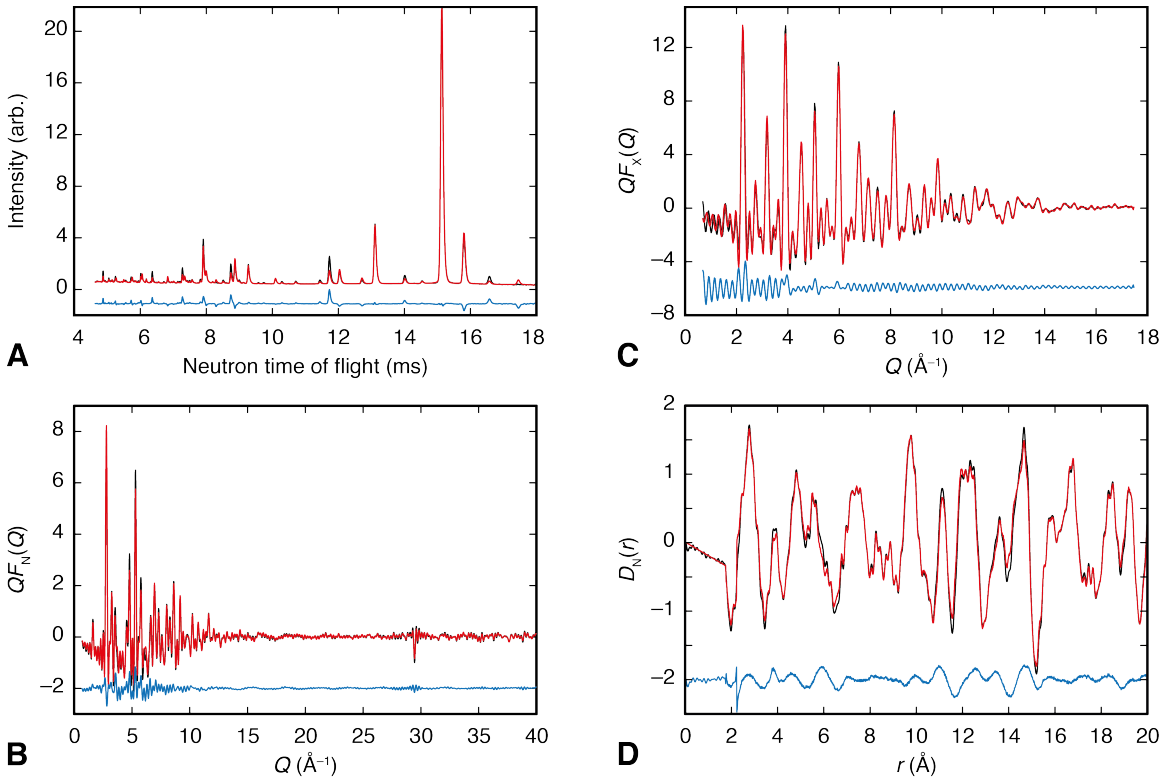

Figure A.14: RMC fits to data for the 823 K refinement: A) neutron Bragg, B) neutron $QF(Q)$, C) X-ray $QF(Q)$, and D) neutron $D(r)$.

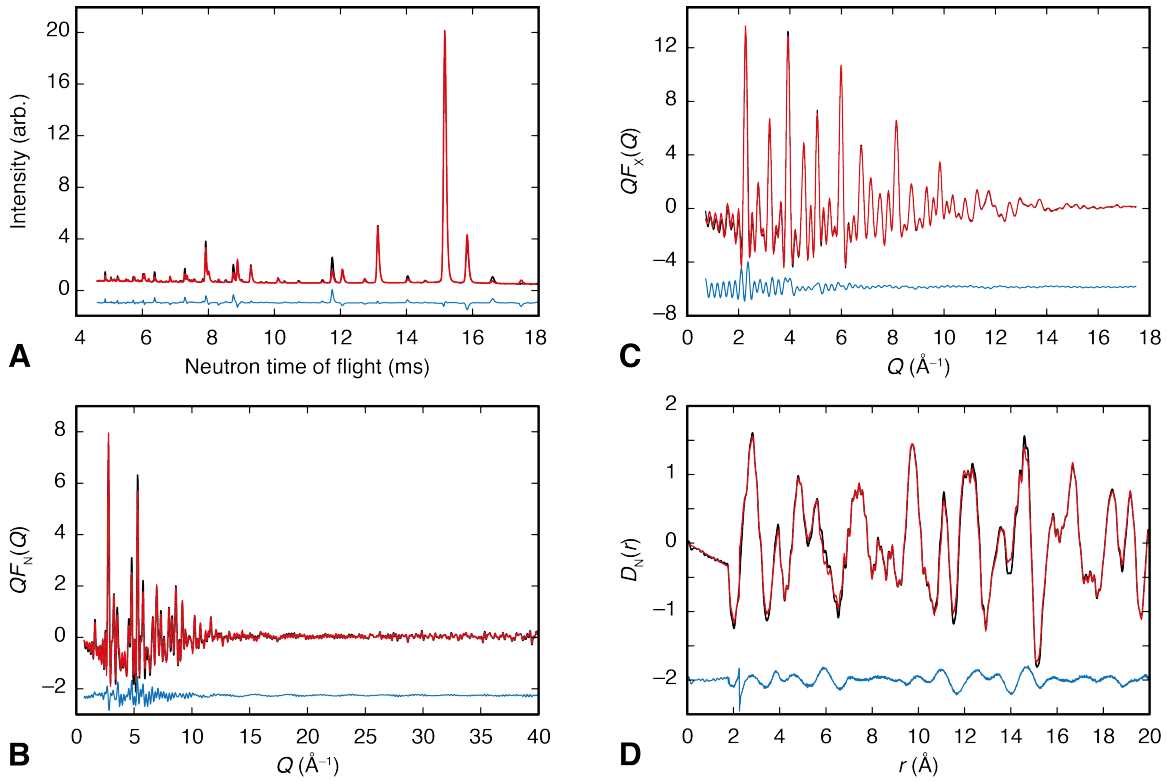

Figure A.15: RMC fits to data for the 903 K refinement: A) neutron Bragg, B) neutron $QF(Q)$, C) X-ray $QF(Q)$, and D) neutron $D(r)$.

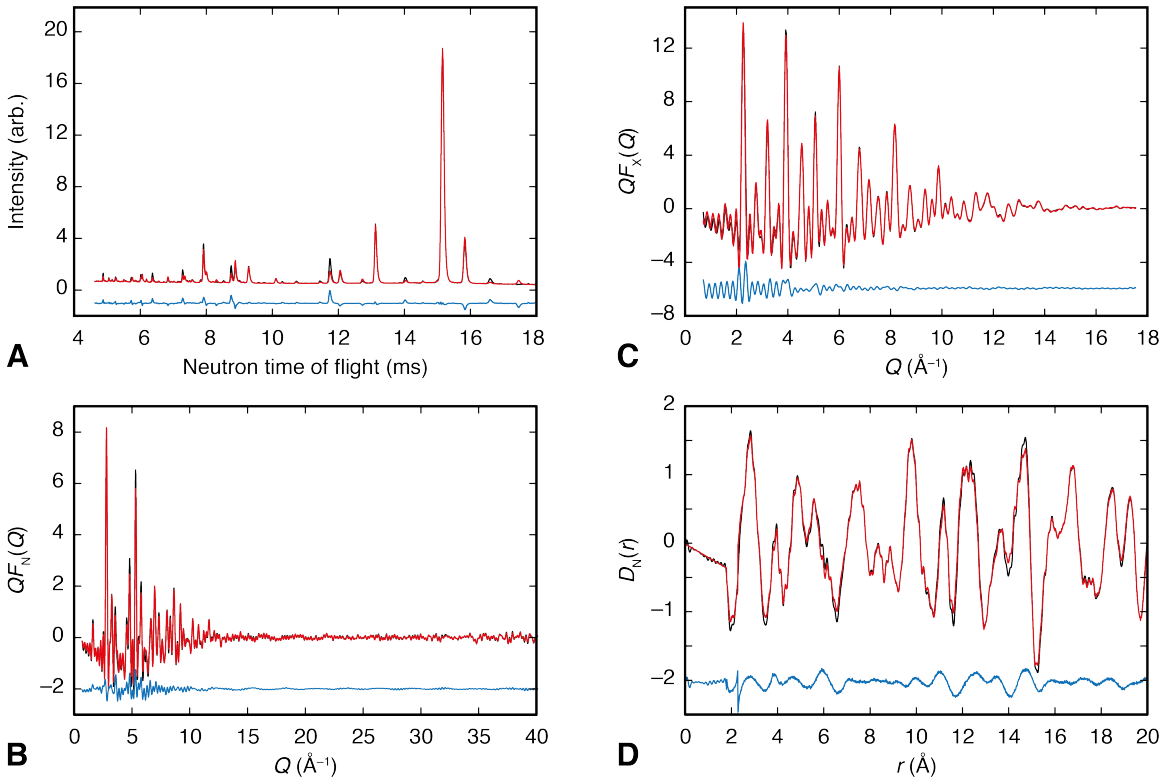

Figure A.16: RMC fits to data for the 973 K refinement: A) neutron Bragg, B) neutron $QF(Q)$, C) X-ray $QF(Q)$, and D) neutron $D(r)$.

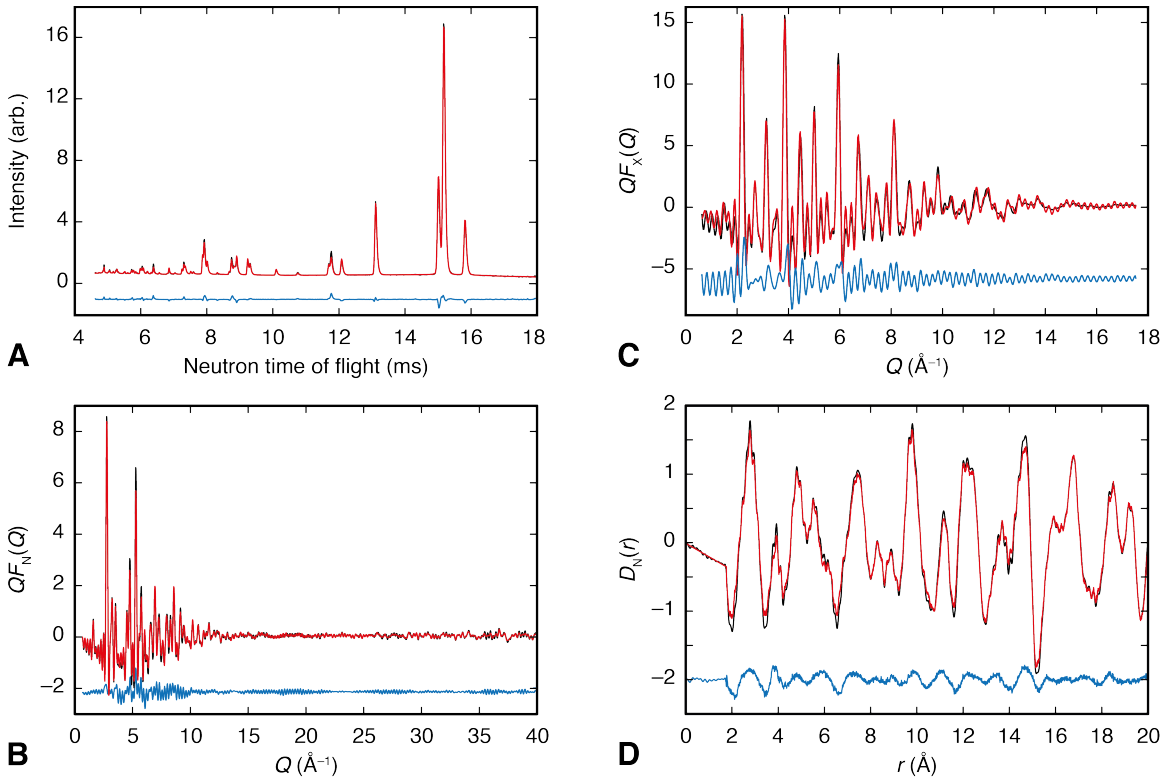

Figure A.17: RMC fits to data for the 1023 K refinement: A) neutron Bragg, B) neutron $QF(Q)$, C) X-ray $QF(Q)$, and D) neutron $D(r)$.

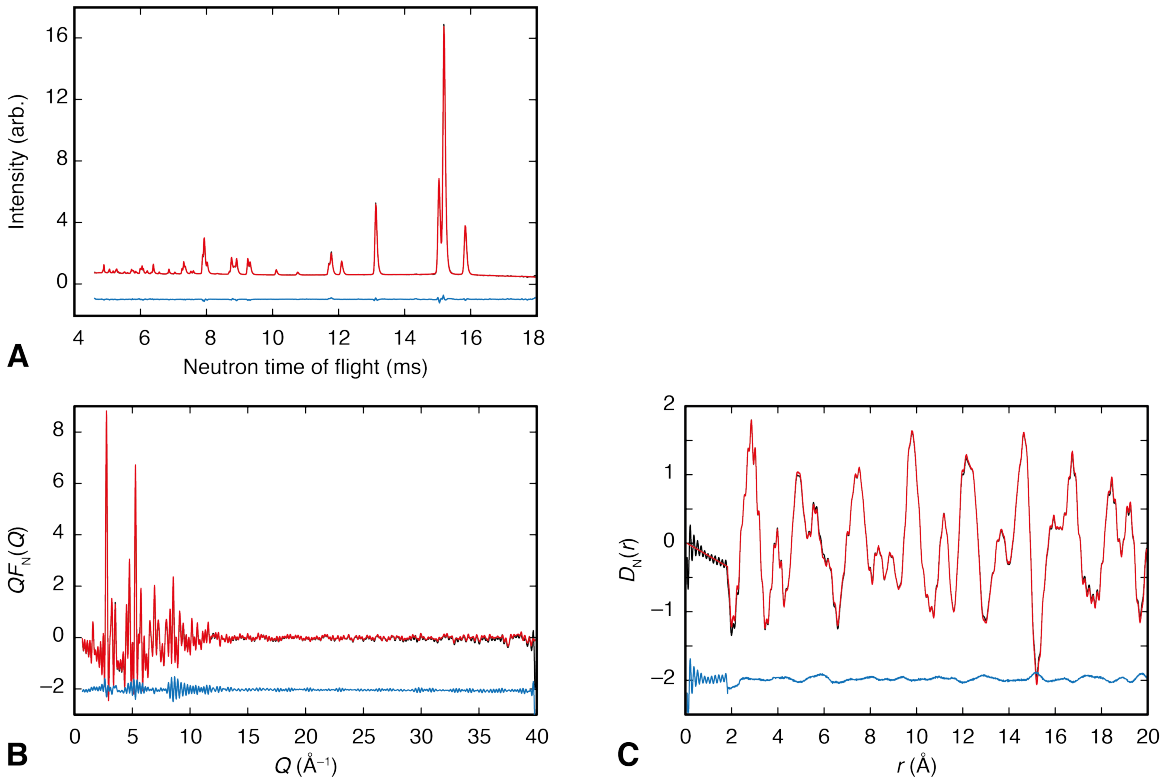

Figure A.18: RMC fits to data for the 1103 K refinement: A) neutron Bragg, B) neutron $QF(Q)$, and C) neutron $D(r)$. There is no X-ray data for this temperature.

References

[1] L. E. Cross, *Ferroelectrics* **76**, 241 (1987).

[2] E. Dagotto, *Science* **309**, 257 (2005).

[3] J. A. M. Paddison, A. L. Goodwin, *Phys. Rev. Lett.* **108**, 017204 (2012).

[4] J. Breger, N. Dupre, P. J. Chupas, P. L. Lee, T. Proffen, J. B. Parise, C. P. Grey, *J. Am. Chem. Soc.* **127**, 7529 (2005).

[5] R. Withers, *Z. Kristallogr.* **220**, 1027 (2005).

[6] M. Misawa, D. L. Price, K. Suzuki, *J. Non-Cryst. Solids* **37**, 85 (1980).

[7] M. T. Dove, M. G. Tucker, D. A. Keen, *Eur. J. Mineral.* **14**, 331 (2002).

[8] D. A. Keen, *J. Appl. Crystallogr.* **34**, 172 (2001).

[9] T. E. Faber, J. M. Ziman, *Philos. Mag.* **11**, 153 (1965).

[10] O. Masson, P. Thomas, *J. Appl. Cryst.* **46**, 461 (2013).

[11] S. J. L. Billinge, M. G. Kanatzidis, *Chem. Commun.* pp. 749–760 (2004).

[12] S. J. L. Billinge, *J. Solid State Chem.* **181**, 1695 (2008).

[13] T. Proffen, H. Kim, *J. Mater. Chem.* **19**, 5078 (2009).

[14] C. A. Reiss, A. Kharchenko, M. Gateshki, *Z. Kristallogr.* **227**, 257 (2012).

[15] M. A. Newton, K. W. Chapman, D. Thompsett, P. J. Chupas, *J. Am. Chem. Soc.* **134**, 5036 (2012).

[16] M. A. Beno, C. Kurtz, A. Munkholm, U. Rütt, M. Engbretson, G. Jennings, J. Linton, G. S. Knapp, P. A. Montano, *Nucl. Instrum. Meth. A* **467–468**, 694 (2001).

[17] P. J. Chupas, K. W. Chapman, P. L. Lee, *J. Appl. Cryst.* **40**, 463 (2007).

[18] K. W. Chapman, P. J. Chupas, G. J. Halder, J. A. Hriljac, C. Kurtz, B. K. Greve, C. J. Ruschman, A. P. Wilkinson, *J. Appl. Cryst.* **43**, 297 (2010).

[19] C. A. Young, E. O. R. Beake, F. D. Romero, L. D. Connor, T. E. Proffen, M. G. Tucker, D. A. Keen, M. A. Hayward, A. L. Goodwin, *Acta Cryst. A* **A69**, s176 (2013).

[20] W. G. Williams, R. M. Ibberson, P. Day, J. E. Enderby, *Physica B* **241-243**, 234 (1997).

[21] P. Day, J. Enderby, W. Williams, L. Chapon, A. Hannon, P. Radaelli, A. Soper, *Neutron News* **15**, 19 (2004).

[22] A. C. Hannon, *Nucl. Instrum. Methods Phys. Res. Sect. A-Accel. Spectrom. Dect. Assoc. Equip.* **551**, 88 (2005).

[23] S. Hull, R. I. Smith, W. I. F. David, A. C. Hannon, J. Mayers, R. Cywinski, *Physica B* **180 & 181**, 1000 (1992).

[24] K. Page, T. Proffen, H. Terrones, M. Terrones, L. Lee, Y. Yang, S. Stemmer, R. Seshadri, A. K. Cheetham, *Chem. Phys. Lett.* **393**, 385 (2004).

[25] A. L. Goodwin, M. G. Tucker, M. T. Dove, D. A. Keen, *Phys. Rev. Lett.* **93**, 075502 (2004).

[26] A. L. Goodwin, M. G. Tucker, E. R. Cope, M. T. Dove, D. A. Keen, *Physica B* **385**, 285 (2006).

[27] H. E. Fischer, A. C. Barnes, P. S. Salmon, *Rep. Prog. Phys.* **69**, 233 (2006).

[28] A. C. Hannon, *Encyclopedia of Spectroscopy and Spectrometry* (Academic Press, 2000), vol. 2, chap. Neutron Diffraction, Instrumentation, pp. 1479–1492.

[29] G. Placzek, *Phys. Rev.* **86**, 377 (1952).

[30] J. G. Powles, *Mol. Phys.* **26**, 1325 (1973).

[31] R. N. Sinclair, A. C. Wright, *Nucl. Instrum. Meth.* **114**, 451 (1974).

[32] I.-K. Jeong, J. Thompson, T. Proffen, A. Perez, S. J. L. Billinge, *J. Appl. Cryst.* **34**, 536 (2001).

[33] P. F. Peterson, M. Gutmann, T. Proffen, S. J. L. Billinge, *J. Appl. Cryst.* **33**, 1192 (2000).

[34] A. K. Soper, GudrunN and GudrunX: Programs for correcting raw neutron and x-ray diffraction data to differential scattering cross section, *Tech. rep.*, Rutherford Appleton Laboratory, Didcot, UK. (2011).

[35] T. Proffen, S. J. L. Billinge, *J. Appl. Cryst.* **32**, 572 (1999).

[36] C. L. Farrow, P. Juhas, J. W. Liu, D. Bryndin, E. S. Bozin, J. Bloch, T. Proffen, S. J. L. Billinge, *J. Phys.: Condens. Matter* **19**, 335219 (2007).

[37] A. K. Soper, *Chemical Physics* **202**, 295 (1996).

[38] A. K. Soper, *Mol. Phys.* **99**, 1503 (2001).

[39] C. A. Young, A. L. Goodwin, *J. Mater. Chem.* **21**, 6464 (2011).

[40] J. S. O. Evans, *J. Chem. Soc., Dalton Trans.* pp. 3317–3326 (1999).

[41] G. D. Barrera, J. A. O. Bruno, T. H. K. Barron, N. L. Allan, *J. Phys.-Condes. Matter* **17**, R217 (2005).

[42] K. W. Chapman, P. J. Chupas, C. J. Kepert, *J. Am. Chem. Soc.* **127**, 15630 (2005).

[43] M. G. Tucker, A. L. Goodwin, M. T. Dove, D. A. Keen, S. A. Wells, J. S. O. Evans, *Phys. Rev. Lett.* **95**, 255501 (2005).

[44] J. S. O. Evans, W. I. F. David, A. W. Sleight, *Acta Cryst. B* **55**, 333 (1999).

[45] J. S. O. Evans, T. A. Mary, T. Vogt, M. A. Subramanian, A. W. Sleight, *Chem. Mat.* **8**, 2809 (1996).

[46] A. K. A. Pryde, K. D. Hammonds, M. T. Dove, V. Heine, J. D. Gale, M. C. Warren, *Phase Transit.* **61**, 141 (1997).

[47] D. Cao, F. Bridges, G. R. Kowach, A. P. Ramirez, *Phys. Rev. Lett.* **89**, 215902 (2002).

[48] C. A. Perottoni, J. A. H. da Jornada, *Science* **280**, 886 (1998).

[49] S. Kohara, K. Kato, S. Kimura, H. Tanaka, T. Usuki, K. Suzuya, H. Tanaka, Y. Moritomo, T. Matsunaga, N. Yamada, Y. Tanaka, H. Suematsu, M. Takata, *Appl. Phys. Lett.* **89**, 201910 (2006).

[50] T. Matsunaga, J. Akola, S. Kohara, T. Honma, K. Kobayashi, E. Ikenaga, R. O. Jones, N. Yamada, M. Takata, R. Kojima, *Nat. Mater.* **10**, 129 (2011).

[51] R. J. Speedy, *J. Phys.: Condens. Matter* **8**, 10907 (1996).

[52] A. K. Arora, V. S. Sastry, P. C. Sahu, T. A. Mary, *J. Phys.: Condens. Matter* **16**, 1025 (2004).

[53] A. K. A. Pryde, M. T. Dove, V. Heine, *J. Phys.: Condens. Matter* **10**, 8417 (1998).

[54] D. A. Keen, A. L. Goodwin, M. G. Tucker, M. T. Dove, J. S. O. Evans, W. A. Crichton, M. Brunelli, *Phys. Rev. Lett.* **98**, 225501 (2007).

[55] H. F. Hamann, M. O'Boyle, Y. C. Martin, M. Rooks, K. Wickramasinghe, *Nat. Mater.* **5**, 383 (2006).

[56] A. V. Kolobov, P. Fons, J. Tominaga, T. Uruga, *J. Non-Cryst. Solids* **352**, 1612 (2006).

[57] Z. M. Sun, J. Zhou, R. Ahuja, *Phys. Rev. Lett.* **96**, 055507 (2006).

[58] M. A. Paesler, D. A. Baker, G. Lucovsky, *J. Non-Cryst. Solids* **354**, 2706 (2008).

[59] L. Pauling, P. Pauling, *Proc. Natl. Acad. Sci.* **60**, 362 (1968).

[60] B. F. Abrahams, B. F. Hoskins, R. Robson, *Chem. Commun.* pp. 60–61 (1990).

[61] D. J. Williams, D. E. Partin, F. J. Lincoln, J. Kouvetakis, M. O'Keeffe, *J. Solid State Chem.* **134**, 164 (1997).

[62] S. J. Hibble, A. C. Hannon, S. M. Cheyne, *Inorg. Chem.* **42**, 4724 (2003).

[63] S. J. Hibble, A. M. Chippindale, A. H. Pohl, A. C. Hannon, *Angew. Chem.-Int. Edit.* **46**, 7116 (2007).

[64] A. L. Goodwin, C. J. Kepert, *Phys. Rev. B* **71**, 140301 (2005).

[65] A. Kumar, S. M. Yusuf, L. Keller, J. V. Yakhmi, *Phys. Rev. Lett.* **101**, 207206 (2008).

[66] A. L. Goodwin, *Phys. Rev. B* **74**, 134302 (2006).

[67] A. L. Goodwin, M. T. Dove, A. M. Chippindale, S. J. Hibble, A. H. Pohl, A. C. Hannon, *Phys. Rev. B* **80**, 054101 (2009).

[68] A. G. Sharpe, *The Chemistry of Cyano Complexes of the Transition Metals* (Academic Press, London, England, 1976).

[69] Y. Mo, E. Kaxiras, *Small* **3**, 1253 (2007).

[70] A. L. Goodwin, M. Calleja, M. J. Conterio, M. T. Dove, J. S. O. Evans, D. A. Keen, L. Peters, M. G. Tucker, *Science* **319**, 794 (2008).

[71] M. G. Tucker, D. A. Keen, M. T. Dove, A. L. Goodwin, Q. Hui, *J. Phys.: Condens. Matter* **19**, 335218 (2007).

[72] A. L. Goodwin, M. G. Tucker, E. R. Cope, M. T. Dove, D. A. Keen, *Phys. Rev. B* **72**, 214304 (2005).

[73] A. L. Goodwin, D. A. Keen, M. G. Tucker, M. T. Dove, L. Peters, J. S. O. Evans, *J. Am. Chem. Soc.* **130**, 9660 (2008).

[74] M. J. Conterio, A. L. Goodwin, M. G. Tucker, D. A. Keen, M. T. Dove, L. Peters, J. S. O. Evans, *J. Phys.: Condens. Matter* **20**, 255225 (2008).

[75] A. J. Fletcher, K. M. Thomas, M. J. Rosseinsky, *J. Solid State Chem.* **178**, 2491 (2005).

[76] R. Banerjee, A. Phan, B. Wang, C. Knobler, H. Furukawa, M. O'Keeffe, O. M. Yaghi, *Science* **319**, 939 (2008).

[77] Y. H. Hu, L. Zhang, *Adv. Mater.* **22**, E117 (2010).

[78] J. E. Readman, P. M. Forster, K. W. Chapman, P. J. Chupas, J. B. Parise, J. A. Hriljac, *Chem. Commun.* pp. 3383–3385 (2009).

[79] T. D. Bennett, A. L. Goodwin, M. T. Dove, D. A. Keen, M. G. Tucker, E. R. Barney, A. K. Soper, E. G. Bithell, J.-C. Tan, A. K. Cheetham, *Phys. Rev. Lett.* **104**, 115503 (2010).

[80] A. K. Cheetham, G. Ferey, T. Loiseau, *Angew. Chem.-Int. Edit.* **38**, 3268 (1999).

[81] T. Wakihara, S. Kohara, G. Sankar, S. Saito, M. Sanchez-Sanchez, A. R. Overweg, W. Fan, M. Ogura, T. Okubo, *Phys. Chem. Chem. Phys.* **8**, 224 (2006).

[82] Y. N. Huang, E. A. Havenga, *Chem. Phys. Lett.* **345**, 65 (2001).

[83] J. Haines, C. Levelut, A. Isambert, P. Hebert, S. Kohara, D. A. Keen, T. Hammouda, D. Andrault, *J. Am. Chem. Soc.* **131**, 12333 (2009).

[84] K. W. Chapman, G. J. Halder, P. J. Chupas, *J. Am. Chem. Soc.* **131**, 17546 (2009).

[85] C. A. Schröder, I. A. Baburin, L. van Wüllen, M. Wiebcke, S. Leoni, *CrystEngComm* **15**, 4036 (2013).

[86] S. A. Moggach, T. D. Bennett, A. K. Cheetham, *Angew. Chem.-Int. Edit.* **48**, 7087 (2009).

[87] K. W. Chapman, P. J. Chupas, C. J. Kepert, *J. Am. Chem. Soc.* **127**, 11232 (2005).

[88] K. W. Chapman, P. J. Chupas, E. R. Maxey, J. W. Richardson, *Chem. Commun.* pp. 4013–4015 (2006).

[89] K. L. Mulfort, O. K. Farha, C. D. Malliakas, M. G. Kanatzidis, J. T. Hupp, *Chem.-Eur. J.* **16**, 276 (2010).

[90] I. K. Jeong, T. W. Darling, J. K. Lee, T. Proffen, R. H. Heffner, J. S. Park, K. S. Hong, W. Dmowski, T. Egami, *Phys. Rev. Lett.* **94**, 147602 (2005).

[91] V. A. Bokov, I. E. Mylnikova, *Sov. Phys-Solid State-Engl. Tran.* **3**, 613 (1961).

[92] V. Westphal, W. Kleemann, M. D. Glinchuk, *Phys. Rev. Lett.* **68**, 847 (1992).

[93] I. K. Jeong, J. K. Lee, *Appl. Phys. Lett.* **88**, 262905 (2006).

[94] A. L. Goodwin, S. A. T. Redfern, M. T. Dove, D. A. Keen, M. G. Tucker, *Phys. Rev. B* **76**, 174114 (2007).

[95] B. P. Burton, E. Cockayne, S. Tinte, U. V. Waghmare, *Phase Transit.* **79**, 91 (2006).

[96] K. Page, T. Proffen, M. Niederberger, R. Seshadri, *Chem. Mater.* **22**, 4386 (2010).

[97] K. Page, T. Kolodiazhnyi, T. Proffen, A. K. Cheetham, R. Seshadri, *Phys. Rev. Lett.* **101**, 205502 (2008).

[98] C. Laulhe, F. Hippert, R. Bellissent, A. Simon, G. J. Cuello, *Phys. Rev. B* **79**, 064104 (2009).

[99] E. Aksel, J. S. Forrester, J. C. Nino, K. Page, D. P. Shoemaker, J. L. Jones, *Phys. Rev. B* **87**, 104113 (2013).

[100] S. Y. Chong, R. J. Szczecinski, C. A. Bridges, M. G. Tucker, J. B. Claridge, M. J. Rosseinsky, *J. Am. Chem. Soc.* **134**, 5836 (2012).

[101] A. Sartbaeva, S. A. Wells, M. F. Thorpe, E. S. Bozin, S. J. L. Billinge, *Phys. Rev. Lett.* **97**, 065501 (2006).

[102] X. Y. Qiu, T. Proffen, J. F. Mitchell, S. J. L. Billinge, *Phys. Rev. Lett.* **94**, 177203 (2005).

[103] E. S. Bozin, A. Sartbaeva, H. Zheng, S. A. Wells, J. F. Mitchell, T. Proffen, M. F. Thorpe, S. J. L. Billinge, *J. Phys. Chem. Solids* **69**, 2146 (2008).

[104] E. S. Bozin, X. Qiu, M. Schmidt, G. Paglia, J. F. Mitchell, P. G. Radaelli, T. Proffen, S. J. L. Billinge, *Physica B* **385**, 110 (2006).

[105] E. S. Bozin, M. Schmidt, A. J. DeConinck, G. Paglia, J. F. Mitchell, T. Chatterji, P. G. Radaelli, T. Proffen, S. J. L. Billinge, *Phys. Rev. Lett.* **98**, 137203 (2007).

[106] T. Proffen, S. J. L. Billinge, *Appl. Phys. A-Mater. Sci. Process.* **74**, S1770 (2002).

[107] S. J. L. Billinge, V. Petkov, T. Proffen, G. H. Kwei, J. L. Sarrao, S. D. Shastri, S. Kycia, *MRS Proceedings* **602**, 177 (1999).

[108] D. P. Shoemaker, J. Li, R. Seshadri, *J. Am. Chem. Soc.* **131**, 11450 (2009).

[109] V. K. Hestermann, R. Hoppe, *Z. Anorg. Allg. Chem.* **367**, 249 (1969).

[110] R. Berger, L. E. Tergenius, *J. Alloy. Compd.* **203**, 203 (1994).

[111] S. D. Guest, J. W. Hutchinson, *J. Mech. Phys. Solids* **51**, 383 (2003).

[112] R. G. Pearson, *Proc. Natl. Acad. Sci.* **72**, 2104 (1975).

[113] I. Levin, T. G. Amos, J. C. Nino, T. A. Vanderah, C. A. Randall, M. T. Lanagan, *J. Solid State Chem.* **168**, 69 (2002).

[114] D. P. Shoemaker, R. Seshadri, A. L. Hector, A. Llobet, T. Proffen, C. J. Fennie, *Phys. Rev. B* **81**, 144113 (2010).

[115] A. L. Goodwin, R. L. Withers, H.-B. Nguyen, *J. Phys.: Condens. Matter* **19**, 335216 (2007).

[116] S. T. Bramwell, M. J. P. Gingras, *Science* **294**, 1495 (2001).

[117] A. P. Ramirez, A. Hayashi, R. J. Cava, R. Siddharthan, B. S. Shastry, *Nature* **399**, 333 (1999).

[118] Y. Tabata, H. Kadowaki, K. Matsuhira, Z. Hiroi, N. Aso, E. Ressouche, B. Fak, *J. Magn. Magn. Mater.* **310**, 1311 (2007).

[119] D. K. Singh, J. S. Helton, S. Chu, T. H. Han, C. J. Bonnoit, S. Chang, H. J. Kang, J. W. Lynn, Y. S. Lee, *Phys. Rev. B* **78**, 220405 (2008).

[120] T. Fennell, P. P. Deen, A. R. Wildes, K. Schmalzl, D. Prabhakaran, A. T. Boothroyd, R. J. Aldus, D. F. McMorrow, S. T. Bramwell, *Science* **326**, 415 (2009).

[121] D. A. Keen, R. L. McGreevy, *J. Phys.: Condens. Matter* **3**, 7383 (1991).

[122] J. R. Stewart, K. H. Andersen, *Phys. Rev. B* **78**, 014428 (2008).

[123] G. Ehlers, J. E. Greedan, J. R. Stewart, K. C. Rule, P. Fouquet, A. L. Cornelius, C. Adriano, P. G. Pagliuso, Y. Qiu, J. S. Gardner, *Phys. Rev. B* **81**, 224405 (2010).

[124] J. E. Greedan, D. Gout, A. D. Lozano-Gorrin, S. Derahkshan, T. Proffen, H. J. Kim, E. Bozin, S. J. L. Billinge, *Phys. Rev. B* **79**, 014427 (2009).

[125] T. E. Saunders, J. T. Chalker, *Phys. Rev. Lett.* **98**, 157201 (2007).

[126] A. M. Hallas, J. A. M. Paddison, H. J. Silverstein, A. L. Goodwin, J. R. Stewart, A. R. Wildes, J. G. Cheng, J. S. Zhou, J. B. Goodenough, E. S. Choi, G. Ehlers, J. S. Gardner, C. R. Wiebe, H. D. Zhou, *Phys. Rev. B* **86**, 134431 (2012).

[127] J. A. M. Paddison, J. R. Stewart, P. Manuel, P. Courtois, G. J. McIntyre, B. D. Rainford, A. L. Goodwin, *Phys. Rev. Lett.* **110**, 267207 (2013).

[128] W. L. Roth, *Phys. Rev.* **110**, 1333 (1958).

[129] H. Shaked, J. Faber, R. L. Hitterman, *Phys. Rev. B* **38**, 11901 (1988).

[130] A. L. Goodwin, M. G. Tucker, M. T. Dove, D. A. Keen, *Phys. Rev. Lett.* **96**, 047209 (2006).

[131] G. Shirane, *Acta Cryst.* **12**, 282 (1959).

[132] A. Mellergård, R. L. McGreevy, A. Wannberg, B. Trostell, *J. Phys.: Condens. Matter* **10**, 9401 (1998).

[133] A. L. Goodwin, M. T. Dove, M. G. Tucker, D. A. Keen, *Phys. Rev. B* **75**, 075423 (2007).

[134] S. J. L. Billinge, I. Levin, *Science* **316**, 561 (2007).

[135] V. Petkov, *Mater. Today* **11**, 11, 28 (2008).

[136] P. J. Chupas, K. W. Chapman, G. Jennings, P. L. Lee, C. P. Grey, *J. Am. Chem. Soc.* **129**, 13822 (2007).

[137] V. Petkov, P. D. Cozzoli, R. Buonsanti, R. Cingolani, Y. Ren, *J. Am. Chem. Soc.* **131**, 14264 (2009).

[138] J. Becker, M. Bremholm, C. Tyrsted, B. Pauw, K. M. O. Jensen, J. Eltzholt, M. Christensen, B. B. Iversen, *J. Appl. Crystallogr.* **43**, 729 (2010).

[139] K. M. Ø. Jensen, M. Christensen, P. Juhas, C. Tyrsted, E. D. Bøjesen, N. Lock, S. J. L. Billinge, B. B. Iversen, *J. Am. Chem. Soc.* **134**, 6785 (2012).

[140] R. Harrington, D. B. Hausner, N. Bhandari, D. R. Strongin, K. W. Chapman, P. J. Chupas, D. S. Middlemiss, C. P. Grey, J. B. Parise, *Inorg. Chem.* **49**, 325 (2010).

[141] A. L. Goodwin, F. M. Michel, B. L. Phillips, D. A. Keen, M. T. Dove, R. J. Reeder, *Chem. Mater.* **22**, 3197 (2010).

[142] L. Addadi, S. Raz, S. Weiner, *Adv. Mater.* **15**, 959 (2003).

[143] S. Weiner, I. Sagi, L. Addadi, *Science* **309**, 1027 (2005).

[144] Y. Politi, Y. Levi-Kalisman, S. Raz, F. Wilt, L. Addadi, S. Weiner, I. Sagi, *Adv. Funct. Mater.* **16**, 1289 (2006).

[145] E. Shalaev, G. Zografi, *Amorphous Food and Pharmaceutical Systems*, H. Levine, ed. (The Royal Society of Chemistry, 2002), pp. 11–30.

[146] S. J. L. Billinge, T. Dykhne, P. Juhas, E. Bozin, R. Taylor, A. J. Florence, K. Shankland, *CrystEngComm* **12**, 1366 (2010).

[147] A large number of studies on pharmaceuticals have been performed in which the authors take the Fourier transform of diffraction patterns obtained using laboratory Cu Kα x-ray sources. These sources do not have a sufficiently short wavelength to reliably distinguish peaks in the corresponding PDF, and there is the strong likelihood that Fourier ripples may be misinterpreted as peaks.

[148] H. Kim, K. Sakaki, H. Ogawa, Y. Nakamura, J. Nakamura, E. Akiba, A. Machida, T. Watanuki, T. Proffen, *J. Phys. Chem. C* **117**, 26543 (2013).

[149] K. Ohara, Y. Kawakita, L. Pusztai, L. Temleitner, S. Kohara, N. Inoue, S. Takeda, *J. Phys.: Condens. Matter* **22**, 404203 (2010).

[150] S. Hull, S. T. Norberg, S. G. Eriksson, C. E. Mohn, *J. Phys.: Condens. Matter* **25**, 454205 (2013).

[151] S. T. Norberg, S. G. Eriksson, S. Hull, *Solid State Ionics* **192**, 409 (2011).

[152] D. Dambournet, K. W. Chapman, M. V. Koudriachova, P. J. Chupas, I. Belharouak, K. Amine, *Inorg. Chem.* **50**, 5855 (2011).

[153] A. Abouimrane, D. Dambournet, K. W. Chapman, P. J. Chupas, W. Weng, K. Amine, *J. Am. Chem. Soc.* **134**, 4505 (2012).

[154] M. Scavini, M. Coduri, M. Allieta, M. Brunelli, C. Ferrero, *Chem. Mater.* **24**, 1338 (2012).

[155] J. J. Biendicho, M. Roberts, C. Offer, D. Noréus, E. Widenkvist, R. I. Smith, G. Svensson, K. Edström, S. T. Norberg, S. G. Eriksson, S. Hull, *J. Power Sources* **248**, 900 (2014).

[156] P. Du, O. Kokhan, K. W. Chapman, P. J. Chupas, D. M. Tiede, *J. Am. Chem. Soc.* **134**, 11096 (2012).

[157] J. Huang, J. D. Blakemore, D. Fazi, O. Kokhan, N. D. Schley, R. H. Crabtree, G. W. Brudvig, D. M. Tiede, *Phys. Chem. Chem. Phys.* **16**, 1814 (2014).

[158] A. K. Soper, E. R. Barney, *J. Appl. Cryst.* **45**, 1314 (2012).

[159] V. Krayzman, I. Levin, *J. Appl. Cryst.* **45**, 106 (2012).

[160] K. Nemeth, K. W. Chapman, M. Balasubramanian, B. Shyam, P. J. Chupas, S. M. Heald, M. Newville, R. J. Klingler, R. E. Winans, J. D. Almer, G. Sandi, G. Srajer, *J. Chem. Phys.* **136**, 074105 (2012).

[161] T. Weber, A. Simonov, *Z. Kristallogr.* **227**, 238 (2012).

[162] M. J. Cliffe, M. T. Dove, D. A. Drabold, A. L. Goodwin, *Phys. Rev. Lett.* **104**, 125501 (2010).

[163] P. Juhas, D. M. Cherba, P. M. Duxbury, W. F. Punch, S. J. L. Billinge, *Nature* **440**, 655 (2006).

[164] W. S. Howells, A. C. Hannon, *J. Phys.: Condens. Matter* **11**, 9127 (1999).

[165] R. L. McGreevy, L. Pusztai, *Mol. Simulat.* **1**, 359 (1988).

[166] R. L. McGreevy, M. A. Howe, *Annu. Rev. Mater. Sci.* **22**, 217 (1992).

[167] R. L. McGreevy, *Nucl. Instrum. Meth. A* **354**, 1 (1995).

[168] R. L. McGreevy, A. Mellergård, *AIP Conference Proceedings*, M. R. Johnson, G. J. Kearley, H. G. Buttner, eds. (1999), vol. 479, pp. 19–27.

[169] R. L. McGreevy, *J. Phys.: Condens. Matter* **13**, R877 (2001).

[170] D. A. Keen, R. L. McGreevy, W. Hayes, K. N. Clausen, *Philos. Mag. Lett.* **61**, 349 (1990).

[171] D. A. Keen, W. Hayes, R. L. McGreevy, *J. Phys.: Condens. Matter* **2**, 2773 (1990).

[172] A. Mellergård, R. L. McGreevy, *Acta Cryst. A* **55**, 783 (1999).

[173] M. G. Tucker, M. T. Dove, D. A. Keen, *J. Appl. Cryst.* **34**, 630 (2001).

[174] V. M. Nield, D. A. Keen, R. L. McGreevy, *Acta Cryst. A* **51**, 763 (1995).

[175] G. Evrard, L. Pusztai, *J. Phys.: Condens. Matter* **17**, S1 (2005).

[176] M. T. Dove, G. Rigg, *J. Phys.: Condens. Matter* **25**, 454222 (2013).

[177] A. K. Soper, *Phys. Rev. B* **72**, 104204 (2005).

[178] N. Metropolis, A. W. Rosenbluth, M. N. Rosenbluth, A. H. Teller, E. Teller, *J. Chem. Phys.* **21**, 1087 (1953).

[179] W. K. Hastings, *Biometrika* **57**, 97 (1970).

[180] S. T. Norberg, M. G. Tucker, S. Hull, *J. Appl. Cryst.* **42**, 179 (2009).

[181] I. A. Blech, B. L. Averbach, *Physics* **1**, 31 (1964).

[182] M. T. Dove, *Eur. J. Mineral.* **14**, 203 (2002).

[183] H. Kamerlingh Onnes, *Comm. Phys. Lab. Univ. Leiden* **120b** (1911).

[184] H. Kamerlingh Onnes, *Comm. Phys. Lab. Univ. Leiden* **122b** (1911).

[185] H. Kamerlingh Onnes, *Comm. Phys. Lab. Univ. Leiden* **124c** (1911).

[186] J. G. Bednorz, K. A. Müller, *Z. Phys. B Con. Mat.* **64**, 189 (1986).

[187] M. K. Wu, J. R. Ashburn, C. J. Torng, P. H. Hor, R. L. Meng, L. Gao, Z. J. Huang, Y. Q. Wang, C. W. Chu, *Phys. Rev. Lett.* **58**, 908 (1987).

[188] T. Tohyama, *Jpn. J. Appl. Phys.* **51**, 010004 (2012).

[189] S. E. Sebastian, N. Harrison, F. F. Balakirev, M. M. Altarawneh, P. A. Goddard, R. Liang, D. A. Bonn, W. N. Hardy, G. G. Lonzarich, *Nature* **511**, 61 (2014).

[190] W. Hu, S. Kaiser, D. Nicoletti, C. R. Hunt, I. Gierz, M. C. Hoffmann, M. Le Tacon, T. Loew, B. Keimer, A. Cavalleri, *Nat. Mater.* **13**, 705 (2014).

[191] L. E. Hayward, D. G. Hawthorn, R. G. Melko, S. Sachdev, *Science* **343**, 1336 (2014).

[192] L. N. Cooper, *Phys. Rev.* **104**, 1189 (1956).

[193] J. Bardeen, L. N. Cooper, J. R. Schrieffer, *Phys. Rev.* **106**, 162 (1957).

[194] J. Bardeen, L. N. Cooper, J. R. Schrieffer, *Phys. Rev.* **108**, 1175 (1957).

[195] J. Franck, D. Lawrie, *J. Supercond.* **8**, 591 (1995).

[196] G.-m. Zhao, M. B. Hunt, H. Keller, K. A. Muller, *Nature* **385**, 236 (1997).

[197] A. Mourachkine, *Supercond. Sci. Tech.* **17**, 721 (2004).

[198] A. J. Leggett, *Nat. Phys.* **2**, 134 (2006).

[199] D. M. Newns, C. C. Tsuei, *Nat. Phys.* **3**, 184 (2007).

[200] D. Reznik, L. Pintschovius, M. Ito, S. Iikubo, M. Sato, H. Goka, M. Fujita, K. Yamada, G. D. Gu, J. M. Tranquada, *Nature* **440**, 1170 (2006).

[201] J. Orenstein, A. J. Millis, *Science* **288**, 468 (2000).

[202] J. M. Tranquada, B. J. Sternlieb, J. D. Axe, Y. Nakamura, S. Uchida, *Nature* **375**, 561 (1995).

[203] C. Gadermaier, A. S. Alexandrov, V. V. Kabanov, P. Kusar, T. Mertelj, X. Yao, C. Manzoni, D. Brida, G. Cerullo, D. Mihailovic, *Phys. Rev. Lett.* **105**, 257001 (2010).

[204] A. S. Alexandrov, *Phys. Scr.* **83**, 038301 (2011).

[205] C. Q. Jin, Q. Q. Liu, H. Yang, L. X. Yang, R. C. Yu, F. Y. Li, *Physica C* **460-462**, 178 (2007).

[206] S. D. Conradson, I. D. Raistrick, *Science* **243**, 1340 (1989).

[207] J. Mustre de Leon, S. D. Conradson, I. Batistić, A. R. Bishop, *Phys. Rev. Lett.* **65**, 1675 (1990).

[208] J. Mustre de Leon, S. D. Conradson, I. Batistić, A. R. Bishop, I. D. Raistrick, M. C. Aronson, F. H. Garzon, *Phys. Rev. B* **45**, 2447 (1992).

[209] E. A. Stern, M. Qian, Y. Yacoby, S. M. Heald, H. Maeda, *Physica C* **209**, 331 (1993).

[210] C. H. Booth, F. Bridges, J. B. Boyce, T. Claeson, B. M. Lairson, R. Liang, D. A. Bonn, *Phys. Rev. B* **54**, 9542 (1996).

[211] T. A. Tyson, J. F. Federici, D. Chew, A. R. Bishop, L. Furenlid, W. Savin, W. Wilber, *Physica C* **292**, 163 (1997).

[212] J. D. Sullivan, P. Bordet, M. Marezio, K. Takenaka, S. Uchida, *Phys. Rev. B* **48**, 10638 (1993).

[213] P. Schweiss, W. Reichardt, M. Braden, G. Collin, G. Heger, H. Claus, A. Erb, *Phys. Rev. B* **49**, 1387 (1994).

[214] M. François, A. Junod, K. Yvon, A. W. Hewat, J. J. Capponi, P. Strobel, M. Marezio, P. Fischer, *Solid State Commun.* **66**, 1117 (1988).

[215] A. Williams, G. H. Kwei, R. B. Von Dreele, I. D. Raistrick, D. L. Bish, *Phys. Rev. B* **37**, 7960 (1988).

[216] G. H. Kwei, A. C. Larson, W. L. Hults, J. L. Smith, *Physica C* **169**, 217 (1990).

[217] G. H. Kwei, A. C. Lawson, W. L. Hults, J. L. Smith, *Physica C* **175**, 615 (1991).

[218] D. Louca, G. H. Kwei, B. Dabrowski, Z. Bukowski, *Phys. Rev. B* **60**, 7558 (1999).

[219] M. Gutmann, S. Billinge, E. Brosha, G. Kwei, *Phys. Rev. B* **61**, 11762 (2000).

[220] A. I. Liechtenstein, I. I. Mazin, O. K. Anderson, O. Jepsen, *Philos. Mag. B* **70**, 643 (1994).

[221] M. Arai, K. Yamada, S. Hosoya, A. C. Hannon, Y. Hidaka, A. D. Taylor, Y. Endoh, *J. Supercond.* **7**, 415 (1994).

[222] D. H. A. Blank, H. Kruidhof, J. Flokstra, *J. Phys. D: Appl. Phys.* **21**, 226 (1988).

[223] A. K. Soper, Gudrunn and gudrunx: Programs for correcting raw neutron and x-ray diffraction data to differential scattering cross section, *Tech. Rep. RAL-TR-2011-013*, Rutherford Appleton Laboratory, Didcot, UK. (2011).

[224] A. C. Larson, R. B. Von Dreele, *Los Alamos National Laboratory Report* **LAUR 86-748** (1994).

[225] J. Capponi, C. Chaillout, A. Hewat, P. Lejay, M. Marezio, N. Nguyen, B. Raveau, J. Soubeyroux, J. Tholence, R. Tournier, *Europhys. Lett.* **3**, 1301 (1987).

[226] R. P. Sharma, F. J. Rotella, J. D. Jorgensen, L. E. Rehn, *Physica C* **174**, 409 (1991).

[227] A. S. Alexandrov, N. F. Mott, *Rep. Prog. Phys.* **57**, 1197 (1994).

[228] G. H. Jonker, J. H. Van Santen, *Physica* **16**, 337 (1950).

[229] E. O. Wollan, W. C. Koehler, *Phys. Rev.* **100** (1955).

[230] J. B. Goodenough, *Phys. Rev.* **100** (1955).

[231] R. von Helmolt, J. Wecker, B. Holzapfel, L. Schultz, K. Samwer, *Phys. Rev. Lett.* **71**, 2331 (1993).

[232] S. Jin, T. H. Tiefel, M. McCormack, R. A. Fastnacht, R. Ramesh, L. H. Chen, *Science* **264**, 413 (1994).

[233] N. Mathur, *Nature* **390**, 229 (1997).

[234] Y. Tokura, *Rep. Prog. Phys.* **69**, 797 (2006).

[235] J. Rodríguez-Carvajal, M. Hennion, F. Moussa, A. H. Moudden, L. Pinsard, A. Revcolevschi, *Phys. Rev. B* **57**, R3189 (1998).

[236] G. Matsumoto, *J. Phys. Soc. Jpn.* **29**, 606 (1970).

[237] J.-S. Zhou, J. B. Goodenough, *Phys. Rev. B* **60**, R15002 (1999).

[238] Y. Tokura, A. Urushibara, Y. Moritomo, T. Arima, A. Asamitsu, G. Kido, N. Furukawa, *J. Phys. Soc. Jpn.* **63**, 3931 (1994).

[239] B. B. Van Aken, O. D. Jurchescu, A. Meetsma, Y. Tomioka, Y. Tokura, T. T. M. Palstra, *Phys. Rev. Lett.* **90**, 066403 (2003).

[240] J. M. D. Teresa, M. R. Ibarra, P. A. Algarabel, C. Ritter, C. Marquina, J. Blasco, J. Garcia, A. del Moral, Z. Arnold, *Nature* **386**, 256 (1997).

[241] C. P. Adams, J. W. Lynn, Y. M. Mukovskii, A. A. Arsenov, D. A. Shulyatev, *Phys. Rev. Lett.* **85**, 3954 (2000).

[242] J. W. Lynn, D. N. Argyriou, Y. Ren, Y. Chen, Y. M. Mukovskii, D. A. Shulyatev, *Phys. Rev. B* **76**, 014437 (2007).

[243] J. B. Goodenough, *Annu. Rev. Mater. Sci.* **28**, 1 (1998).

[244] G. H. Jonker, *Physica* **22**, 707 (1956).

[245] M. C. Sánchez, G. Subías, J. García, J. Blasco, *Phys. Rev. Lett.* **90**, 045503 (2003).

[246] R. A. Souza, N. M. Souza-Neto, A. Y. Ramos, H. C. N. Tolentino, E. Granado, *Phys. Rev. B* **70**, 214426 (2004).

[247] M. R. Ahmed, G. A. Gehring, *Phys. Rev. B* **74**, 014420 (2006).

[248] Q. Huang, A. Santoro, J. W. Lynn, R. W. Erwin, J. A. Borchers, J. L. Peng, R. L. Greene, *Phys. Rev. B* **55**, 14987 (1997).

[249] A. P. Hammersley, Fit2d: An introduction and overview, *Tech. Rep. ESRF97HA02T*, ESRF (1997).

[250] A. P. Hammersley, S. O. Svensson, M. Hanfland, A. N. Fitch, D. Häusermann, *High Press. Res.* **14**, 235 (1996).

[251] J. P. Wright, J. P. Attfield, P. G. Radaelli, *Phys. Rev. B* **66**, 214422 (2002).

[252] G. E. Assey, A. M. Butcher, R. J. Butcher, Y. Gultneh, *Acta Cryst. E* **66**, m1384 (2010).

[253] C. B. Barber, D. P. Dobkin, H. T. Huhdanpaa, *ACM T. Math. Software* **22**, 469 (1996).

[254] A. Sartbaeva, S. A. Wells, M. F. Thorpe, E. S. Božin, S. J. L. Billinge, *Phys. Rev. Lett.* **99**, 155503 (2007).

[255] S. I. Zabinsky, J. J. Rehr, A. L. Ankudinov, R. C. Albers, M. J. Eller, *Phys. Rev. B* **52**, 2995 (1995).

[256] B. J. Wood, R. G. J. Strens, *Min. Mag.* **38**, 909 (1972).

[257] R. Krüger, B. Schulz, S. Naler, R. Rauer, D. Budelmann, J. Bäckström, K. H. Kim, S.-W. Cheong, V. Perebeinos, M. Rübhausen, *Phys. Rev. Lett.* **92**, 097203 (2004).

[258] T. Chatterji, D. Riley, F. Fauth, P. Mandal, B. Ghosh, *Phys. Rev. B* **73**, 094444 (2006).

[259] J. D. Gale, *JCS Faraday Trans.* **93**, 629 (1997).

[260] J. P. Perdew, K. Burke, M. Ernzerhof, *Phys. Rev. Lett.* **77**, 3865 (1996).

[261] S. J. Clark, M. D. Segall, C. J. Pickard, P. J. Hasnip, M. I. J. Probert, K. Refson, M. C. Payne, *Z. Kristallogr.* **220**, 567 (2005).

[262] L. Wang, T. Maxisch, G. Ceder, *Phys. Rev. B* **73**, 195107 (2006).

[263] C. Franchini, R. Kováčik, M. Marsman, S. S. Murthy, J. He, C. Ederer, G. Kresse, *J. Phys.: Condens. Matter* **24**, 235602 (2012).

[264] W.-G. Yin, D. Volja, W. Ku, *Phys. Rev. Lett.* **96**, 116405 (2006).

[265] U. D. Wdowik, M. M. Koza, T. Chatterji, *Phys. Rev. B* **86**, 174305 (2012).

[266] U. D. Wdowik, B. Ouladdiaf, T. Chatterji, *J. Phys.: Condens. Matter* **23**, 245402 (2011).

[267] T. Chatterji, F. m. c. Fauth, B. Ouladdiaf, P. Mandal, B. Ghosh, *Phys. Rev. B* **68**, 052406 (2003).

[268] R. B. Potts, *Proc. Cambridge Philos. Soc.* **48**, 106 (1952).

[269] M. R. Ahmed, G. A. Gehring, *Phys. Rev. B* **79**, 174106 (2009).

[270] E. S. Bozin, C. D. Malliakas, P. Souvatzis, T. Proffen, N. A. Spaldin, M. G. Kanatzidis, S. J. L. Billinge, *Science* **330**, 1660 (2010).

[271] E. Araya-Rodriguez, A. Y. Ramos, H. C. N. Tolentino, E. Granado, S. B. Oseroff, *J. Magn. Magn. Mater.* **233**, 88 (2001).

[272] P. Mondal, D. Bhattacharya, P. Choudhury, *J. Phys.: Condens. Matter* **18**, 6869 (2006).

[273] W. Lowrie, *Fundamentals of Geophysics* (Cambridge University Press, London, 2007).

[274] M. B. Gawande, P. S. Branco, R. S. Varma, *Chem. Soc. Rev.* **42**, 3371 (2013).

[275] H. A. Lowenstam, *Science* **211**, 1126 (1981).

[276] R. Blakemore, *Science* **190**, 377 (1975).

[277] C. Walcott, J. L. Gould, J. L. Kirschvink, *Science* **205**, 1027 (1979).

[278] D. Presti, J. D. Pettigrew, *Nature* **285**, 99 (1980).

[279] F. Walz, *J. Phys.: Condens. Matter* **14**, R285 (2002).

[280] J. García, G. Subías, *J. Phys.: Condens. Matter* **16** (2004).

[281] G. S. Parks, K. K. Kelley, *J. Phys. Chem.* **30**, 47 (1926).

[282] E. J. W. Verwey, *Nature* **144**, 327 (1939).

[283] E. J. W. Verwey, P. W. Haayman, *Physica* **8**, 979 (1941).

[284] W. C. Hamilton, *Phys. Rev.* **110**, 1050 (1958).

[285] G. Shirane, S. Chikazumi, J. Akimitsu, J. Chiba, M. Matsui, Y. Fujii, *J. Phys. Soc. Jpn.* **39**, 949 (1975).

[286] G. A. Sawatzky, J. M. D. Coey, A. H. Morrish, *J. Appl. Phys.* **40**, 1402 (1969).

[287] J. M. Daniels, A. Rosencwaig, *J. Phys. Chem. Solids* **30**, 1561 (1969).

[288] R. S. Hargrove, W. Kündig, *Solid State Commun.* **8**, 303 (1970).

[289] F. J. Berry, S. Skinner, M. F. Thomas, *J. Phys.: Condens. Matter* **10**, 215 (1998).

[290] M. Rubinstein, D. W. Forester, *Solid State Commun.* **9**, 1675 (1971).

[291] P. Novák, H. Štěpánková, J. Englich, J. Kohout, V. A. M. Brabers, *Phys. Rev. B* **61**, 1256 (2000).

[292] M. Mizoguchi, *J. Phys. Soc. Jpn.* **70**, 2333 (2001).

[293] G. Subías, J. García, J. Blasco, *Phys. Rev. B* **71**, 155103 (2005).

[294] J. E. Lorenzo, C. Mazzoli, N. Jaouen, C. Detlefs, D. Mannix, S. Grenier, Y. Joly, C. Marin, *Phys. Rev. Lett.* **101**, 226401 (2008).

[295] G. Subias, J. Garcia, J. Blasco, J. Herrero-Martin, M. C. Sanchez, J. Orna, L. Morellon, *J. Synchrotron Radiat.* **19**, 159 (2012).

[296] M. Mizoguchi, *J. Phys. Soc. Jpn.* **44**, 1512 (1978).

[297] S. Iida, *Philos. Mag. B* **42**, 349 (1980).

[298] J. M. Zuo, J. C. H. Spence, W. Petuskey, *Phys. Rev. B* **42**, 8451 (1990).

[299] P. W. Anderson, *Phys. Rev.* **102**, 1008 (1956).

[300] M. Iizumi, T. F. Koetzle, G. Shirane, S. Chikazumi, M. Matsui, S. Todo, *Acta Cryst. B* **38**, 2121 (1982).

[301] J. P. Wright, J. P. Attfield, P. G. Radaelli, *Phys. Rev. Lett.* **87**, 266401 (2001).

[302] M. S. Senn, J. P. Wright, J. P. Attfield, *Nature* **481**, 173 (2012).

[303] Y. Miyamoto, S. Chikazumi, *J. Phys. Soc. Jpn.* **57**, 2040 (1988).

[304] Y. Miyamoto, M. Shindo, *J. Phys. Soc. Jpn.* **62**, 1423 (1993).

[305] C. Medrano, M. Schlenker, J. Baruchel, J. Espeso, Y. Miyamoto, *Phys. Rev. B* **59**, 1185 (1999).

[306] L. V. Gasparov, D. B. Tanner, D. B. Romero, H. Berger, G. Margaritondo, L. Forró, *Phys. Rev. B* **62**, 7939 (2000).

[307] J. García, G. Subías, M. G. Proietti, J. Blasco, H. Renevier, J. L. Hodeau, Y. Joly, *Phys. Rev. B* **63**, 054110 (2001).

[308] J. Blasco, J. Garcia, G. Subias, *Phys. Rev. B* **83**, 104105 (2011).

[309] C. G. Shull, E. O. Wollan, W. A. Strauser, *Phys. Rev.* **81**, 483 (1951).

[310] C. G. Shull, E. O. Wollan, W. C. Koehler, *Phys. Rev.* **84**, 912 (1951).

[311] L. Néel, *Ann. Phys. (Paris)* **3**, 137 (1948).

[312] L. Néel, *Proc. Phys. Soc. A* **65**, 869 (1952).

[313] E. Goering, S. Gold, M. Lafkioti, G. Schutz, *Europhys. Lett.* **73**, 97 (2006).

[314] E. Goering, M. Lafkioti, S. Gold, *Phys. Rev. Lett.* **96**, 039701 (2006).

[315] E. J. Goering, M. Lafkioti, S. Gold, G. Schuetz, *J. Magn. Magn. Mater.* **310**, e249 (2007).

[316] J. A. Duffy, J. W. Taylor, S. B. Dugdale, C. Shenton-Taylor, M. W. Butchers, S. R. Giblin, M. J. Cooper, Y. Sakurai, M. Itou, *Phys. Rev. B* **81**, 134424 (2010).

[317] I. Leonov, A. N. Yaresko, V. N. Antonov, V. I. Anisimov, *Phys. Rev. B* **74**, 165117 (2006).

[318] D. J. Huang, C. F. Chang, H. T. Jeng, G. Y. Guo, H. J. Lin, W. B. Wu, H. C. Ku, A. Fujimori, Y. Takahashi, C. T. Chen, *Phys. Rev. Lett.* **93**, 077204 (2004).

[319] Y. W. Li, P. A. Montano, B. Barbiellini, P. E. Mijnarends, S. Kaprzyk, A. Bansil, *J. Phys. Chem. Solids* **68**, 1556 (2007).

[320] E. Goering, *Phys. Status Solidi B* **248**, 2345 (2011).

[321] S. Yamaguchi, *Trans. Faraday Soc.* **58**, 1690 (1962).

[322] G. Król, W. Tabiś, J. Przewoźnik, T. Kołodziej, Z. Kąkol, A. Kozłowski, Z. Tarnawski, *J. Alloy Compd.* **480**, 128 (2009).

[323] Z. Kąkol, G. Król, W. T. T. Kołodziej, A. Wiśniewski, H. Stepankova, V. Chlan, J. Kusz, Z. Tarnawski, A. Kozłowski, J. M. Honig, *J. Phys.: Conf. Ser.* **303** (2011).

[324] P. J. Saines, M. G. Tucker, D. A. Keen, A. K. Cheetham, A. L. Goodwin, *Phys. Rev. B* **88**, 134418 (2013).

[325] H. R. Harrison, R. Aragón, J. E. Keem, J. M. Honig, J. F. Wenckus, *Single Crystal Growth of Oxides by Skull Melting: The Case of Magnetite (Fe_3O_4)* (John Wiley & Sons, Inc., 1984), pp. 43–48.

[326] R. J. Goff, J. P. Wright, J. P. Attfield, P. G. Radaelli, *J. Phys.: Condens. Matter* **17**, 7633 (2005).

[327] M. Senn, J. Wright, J. P. Attfield, *J. Korean Phys. Soc.* **62**, 1372 (2013).

[328] H. T. Stokes, D. M. Hatch, *J. Appl. Cryst.* **38**, 237 (2005).

[329] N. E. Brese, M. O'Keeffe, *Acta Cryst. B* **47**, 192 (1991).

[330] T. Egami, R. J. McQueeney, W. Dmowski, N. Seiji, H. Yamauchi, M. Arai, S. Ishihara, M. Tachiki, *Physica B* **219-220**, 145 (1996).

[331] R. A. Fisher, J. E. Gordon, N. E. Phillips, *Annu. Rev. Phys. Chem.* **47**, 283 (1996).

[332] A. Bussmann-Holder, H. Keller, J. Mustre de Leon, A. Simon, A. Bishop, K. Müller, *J. Supercond. Nov. Magn.* **23**, 295 (2010).

[333] T. A. Tyson, J. M. de Leon, S. D. Conradson, A. R. Bishop, J. J. Neumeier, H. Röder, J. Zang, *Phys. Rev. B* **53**, 13985 (1996).

[334] A. P. Ramirez, *J. Phys.: Condens. Matter* **9**, 8171 (1997).

[335] P. Dai, J. A. Fernandez-Baca, N. Wakabayashi, E. W. Plummer, Y. Tomioka, Y. Tokura, *Phys. Rev. Lett.* **85**, 2553 (2000).

[336] J. N. Reimers, J. E. Greedan, R. K. Kremer, E. Gmelin, M. A. Subramanian, *Phys. Rev. B* **43**, 3387 (1991).

[337] J. S. Gardner, B. D. Gaulin, S.-H. Lee, C. Broholm, N. P. Raju, J. E. Greedan, *Phys. Rev. Lett.* **83**, 211 (1999).